



UNIVERSIDADE FEDERAL DA PARAÍBA  
CENTRO DE CIÊNCIAS EXATAS E DA NATUREZA  
PROGRAMA DE PÓS-GRADUAÇÃO EM FÍSICA

# Problemas Direto e Inverso em Sistemas Análogos da Gravitação

Saulo Soares de Albuquerque Filho

João Pessoa - Paraíba

Julho 2024



Problemas Direto e Inverso em Sistemas Análogos da Gravitação

de

Saulo Soares de Albuquerque Filho

SUPERVISÃO:

Valdir Barbosa Bezerra (Supervisor da Universidade Federal da Paraíba, Brazil)

Iarley Pereira Lobo (Co-supervisor da Universidade Federal da Paraíba, Brazil)

Konstantinos Kokkotas (Supervisor da Universidade de Tübingen, Germany)

Tese Apresentada ao

PROGRAMA DE PÓS GRADUAÇÃO EM FÍSICA

UNIVERSIDADE FEDERAL DA PARAÍBA

Em cumprimento ao

Requisito para o Grau de

Doutor em Física

Julho 2024

# Direct and Inverse Problems for Analog Gravity Systems

by

Saulo Soares de Albuquerque Filho

## SUPERVISION:

Valdir Barbosa Bezerra (Supervisor at Universidade Federal da Paraíba, Brazil)

Iarley Pereira Lobo (Co-supervisor at Universidade Federal da Paraíba, Brazil)

Konstantinos Kokkotas (Supervisor at University of Tübingen, Germany)

A Thesis Presented to the  
PHYSICS GRADUATE PROGRAM  
UNIVERSIDADE FEDERAL DA PARAÍBA  
In Fulfillment of the  
Requirements for the Degree  
DOCTOR OF PHILOSOPHY IN PHYSICS

July 2024

**Catálogo na publicação**  
**Seção de Catalogação e Classificação**

A345p Albuquerque Filho, Saulo Soares de.

Problemas direto e inverso em sistemas análogos da gravitação / Saulo Soares de Albuquerque Filho. - João Pessoa, 2024.

255 f. : il.

Orientação: Valdir Barbosa Bezerra, Konstantinos Kokkotas.

Coorientação: Iarley Pereira Lobo.

Tese (Doutorado) - UFPB/CCEN.

1. Física. 2. Sistemas análogos da gravitação. 3. Método inverso. 4. Teoria perturbativa de buracos negros. I. Bezerra, Valdir Barbosa. II. Kokkotas, Konstantinos. III. Lobo, Iarley Pereira. IV. Título.

UFPB/BC


CDU 53(043)




Universidade Federal da Paraíba  
Centro de Ciências Exatas e da Natureza  
**Programa de Pós-Graduação *Stricto Sensu* em Física**

Ata da Sessão Pública da Defesa de Tese de Doutorado do aluno Saulo Soares de Albuquerque Filho, candidato ao Título de Doutor em Física na Área de Concentração Gravitação e Cosmologia.


Aos trinta dias do mês de julho do ano de dois mil e vinte e quatro, às 15h00, na sala virtual <https://meet.google.com/bzc-utdc-uya>, reuniram-se os membros da Banca Examinadora constituída para avaliar a tese de Doutorado, na área de Gravitação e Cosmologia, de **Saulo Soares de Albuquerque Filho**. A Banca Examinadora foi composta pelos(as) professores(as) doutores(as): Valdir Barbosa Bezerra (PPGF/UFPB), orientador e presidente da Banca Examinadora, Iarley Pereira Lobo (UFPB), coorientador, Carlos Augusto Romero Filho (PPGF/UFPB), Eugênio Ramos Bezerra de Mello (PPGF/UFPB), Geová Maciel de Alencar (UFC) e Horácio Santana Vieira (UFLA). Dando início aos trabalhos, o Prof. Valdir Barbosa Bezerra comunicou aos presentes a finalidade da reunião. A seguir, passou a palavra para o candidato para que o mesmo fizesse, oralmente, a exposição da pesquisa de tese intitulada “*Problemas direto e inverso em sistemas análogos da gravitação*”. Concluída a exposição, o candidato foi arguido pela Banca Examinadora, que emitiu o parecer “**aprovado**”. Assim sendo, deve a Universidade Federal da Paraíba expedir o respectivo diploma de Doutor em Física na forma da lei. E para constar, Widelene Menezes Tavares Santos, Assistente em Administração, redigiu a presente ata que vai assinada pelos membros da Banca Examinadora. João Pessoa, Paraíba, **30 de julho de 2024**.

Documento assinado digitalmente  
 VALDIR BARBOSA BEZERRA  
Data: 07/08/2024 16:44:32-0300  
Verifique em <https://validar.iti.gov.br>


Prof. Dr. Valdir Barbosa Bezerra  
Orientador - PPGF/UFPB

Documento assinado digitalmente  
 CARLOS AUGUSTO ROMERO FILHO  
Data: 31/07/2024 21:24:30-0300  
Verifique em <https://validar.iti.gov.br>

Prof. Dr. Carlos Augusto Romero Filho  
PPGF/UFPB

Documento assinado digitalmente  
 HORACIO SANTANA VIEIRA  
Data: 31/07/2024 13:48:36-0300  
Verifique em <https://validar.iti.gov.br>


Prof. Dr. Horácio Santana Vieira  
UFLA

Documento assinado digitalmente  
 IARLEY PEREIRA LOBO  
Data: 31/07/2024 19:38:38-0300  
Verifique em <https://validar.iti.gov.br>

Prof. Dr. Iarley Pereira Lobo  
Coorientador - UFPB



Prof. Dr. Eugênio Ramos Bezerra de Mello  
PPGF/UFPB

Documento assinado digitalmente  
 GEOVA MACIEL DE ALENCAR FILHO  
Data: 31/07/2024 13:06:52-0300  
Verifique em <https://validar.iti.gov.br>

Prof. Dr. Geová Maciel de Alencar  
UFC

# Acknowledgments

To Ana, for taking care of me and everyone else around me and for convincing me that we should always resist and stay good and emphatic. None of this would be possible without your attention and love. I love you, dear mother!

To Saulo, thank you for providing me with a light beacon, a reference, and a model to follow. For all the jokes and funny comments that kept my mind in place. I love you, dear father!

To Mateus for the brotherhood and partnership and for becoming someone I deeply admire. You have shown me that we can always improve if we stay disciplined. I love you, dear brother!

To Ruñ, for being my best friend and soul brother. Thanks for showing me what love is all about, for all the conversations and wonderful moments we had. You showed me the true beauty of life. I love you, dear friend!

To Sebastian Völkel, for almost everything related to the development of this thesis and my career in the last years. Thank you for truly believing in me and being such an illuminating and caring supervisor. Thank you for completely changing my life. Thank you so much for insisting that I give myself a chance. You have been one of the most important persons that ever I happened to meet. You convinced me that I could actually go further and thanks to you I have been given a chance for a future academic career. I will never forget all of that, and no words will ever be able to represent my gratitude to you, my friend and collaborator. In some years, I am going to say I was motivated by one of the best scientists of my time.

To Valdir Bezerra, thank you for being the first professor and supervisor to see some potential in me and patiently supervising me to guarantee that this potential could eventually flourish in real contributions. You have supervised me from the beginning of my undergrad-

uate course up until now. I will proudly be one of your last students, so thanks for finishing this great and fruitful career with me. I deeply admire you as a physicist and as a person. Nothing similar to this thesis would be possible if it weren't for you teaching me how physics works since the first years of my career. I hope I can honor your legacy.

To Kostas Kokkotas, thank you for giving me the responsibility and the motivation for taking care of this research project, which has changed my life completely. I also appreciate the great reception and hospitality provided to me in Tübingen. As a future astrophysicist, I would have had enough reasons to be grateful to you 'only' for all the knowledge you have brought to humankind itself. As someone who has met you in person, I have additional reasons to admire you as the person behind that great astrophysicist.

To Iarley Lobo for showing me how science works and for being a mind-changing supervisor. I truly believe Iarley will change the science in the next few years, and I am really excited to see that happen.

Thank you to Thiago Assis Albuquerque for introducing me to physics and inspiring me to pursue this wonderful career. You have motivated me all the way here.

I could not finish this acknowledgment section without mentioning my grandfather, "vovô" Assis, and my grandmother, "vovó" Julieta. Assis, I thank you for teaching my father everything he knows so he could teach me everything I know. I thank you for inspiring me and always showing me your deep love for us and for your books. I learned to love history and to love reading with you. I love you, Grandpa, and I always think about you daily and everywhere I go. Julieta, thank you for showing me deep love and care and teaching me how to resist the hardest days by smiling and staying strong. I thank you for teaching my mother everything she knows so she could teach me everything I know. May you rest in peace, always.

I acknowledge funding from Conselho Nacional de Desenvolvimento Científico e Tecnológico (CNPQ)-Brazil: Call N<sup>o</sup> 26/2021 – Scholarships Abroad; and Coordenação de Aperfeiçoamento de Pessoal de Nível Superior (CAPES)-Brazil.



# Table of Contents

<b>Acknowledgments</b> . . . . .	ii
<b>Resumo</b> . . . . .	vii
<b>Abstract</b> . . . . .	viii
<b>Publications</b> . . . . .	ix
<b>Chapter 1:</b>	
<b>Introduction</b> . . . . .	1
1.1 Introduction . . . . .	1
1.2 Black Holes and Exotic Compact Objects . . . . .	7
1.3 Gravitational Waves . . . . .	12
1.4 Analog Gravity Systems . . . . .	14
1.5 Inverse method with semi-analytical techniques . . . . .	17
1.6 Structure of this Thesis . . . . .	18
<b>Chapter 2:</b>	
<b>Perturbation Theory in General Relativity</b> . . . . .	22
2.1 Einstein's Field Equations and the General Relativity Theory . . . . .	22
2.2 Perturbation Theory in General Relativity . . . . .	27
2.3 Linearized Einstein Field Equations . . . . .	29
2.3.1 Perturbed Minkowski Spacetime: The Gravitational Waves Solution . . . . .	30
2.4 Linear Perturbation Theory for Schwarzschild Black Hole Spacetimes . . . . .	32
2.4.1 Test Field Perturbation on Schwarzschild Black Hole Spacetimes . . . . .	38
2.4.2 Exotic Compact Objects: Black Hole Mimickers . . . . .	43
2.4.3 Slowly Rotating Perturbed Black Holes . . . . .	44
<b>Chapter 3:</b>	
<b>Analog Gravity Systems: The Sonic Black Hole</b> . . . . .	50
3.1 The Sonic Hole as an Analog to Astrophysical Black Holes . . . . .	51
3.1.1 The Effective Acoustic Metric for an Incompressible flow . . . . .	54
3.1.2 Wave equation for acoustic perturbations in the acoustic black hole . . . . .	56
3.1.3 Experimental Findings . . . . .	59
3.2 The Imperfect Draining Vortex as an Analog to Astrophysical Exotic Compact Objects . . . . .	62

## Chapter 4:

<b>The Direct Problem: Methods for Solving the Master Wave Equations</b>	64
4.1 Solving the Linearized Field Perturbation Equations	64
4.2 Time Domain Approach	65
4.2.1 Evolving The Field Perturbation Equations in Time Domain for Black Holes	66
4.2.2 Evolving The Field Perturbation Equations in Time Domain for Static Exotic Compact Objects	68
4.3 Frequency Domain Approach	69
4.3.1 Green's function formalism for the time-independent wave equation in the black hole case	70
4.3.2 Boundary Conditions for Black Hole Solutions: The Quasinormal Modes Ringing	74
4.3.3 Boundary Conditions for Extreme Compact Objects Solutions: Trapped Quasinormal Modes and Resonant Scattering Modes	89
4.4 The BH and ECOs Scattering of Fields	99

## Chapter 5:

<b>The Inverse Problem: A Semi-analytical Approach</b>	121
5.1 Semi-analytical treatment for the direct and inverse problem	123
5.2 WKB method	124
5.2.1 Direct Bohr-Sommerfeld Rule	128
5.2.2 Direct Gamow Formulas	130
5.2.3 Three-Point Turning Points: Quasi-Stationary States	131
5.3 The Inverse WKB Formulas	134
5.3.1 Inverse Bohr-Sommerfeld Rule	134
5.3.2 Inverse Gamow Formulas	137

## Chapter 6:

<b>The Inverse Method for Analog Gravity Systems</b>	141
6.1 Introduction	141
6.2 Outline of the direct problem	142
6.3 Outline of the imperfect draining vortex model	146
6.4 Outline of the inverse problem	147
6.4.1 Analysis of the transmission	151
6.5 Application and results	157
6.5.1 Reconstruction of potential and reflectivity	157
6.6 Conclusions	165

## Chapter 7:

<b>The Inverse Method for Energy Dependent Potentials and the Extension for Rotating Analog Systems</b>	167
7.1 Inverse Method for Energy-Dependent Potentials	167
7.2 Methods	169
7.2.1 WKB method for energy-dependent potentials	169

7.2.2	Remark on turning points . . . . .	171
7.2.3	Numerical methods . . . . .	173
7.3	Application and results . . . . .	174
7.3.1	Energy-dependent quadratic potential . . . . .	175
7.3.2	Energy-dependent Pöschl-Teller potential . . . . .	179
7.4	Discussion . . . . .	184
7.4.1	Width-equivalent is not WKB-equivalent . . . . .	184
7.4.2	Accuracy of inverse methods . . . . .	184
7.5	Supplementary results . . . . .	188
7.5.1	Quadratic potential . . . . .	188
7.5.2	Pöschl-Teller potential . . . . .	190
7.5.3	Remarks on non-uniqueness . . . . .	194
7.6	Conclusions . . . . .	195
 <b>Chapter 8:</b>		
	<b>The Inverse Method for Rotating Analog Systems . . . . .</b>	<b>196</b>
8.1	Introduction . . . . .	196
8.2	Reconstructing the effective WKB-equivalent potential . . . . .	199
8.3	Reconstructing the boundary condition . . . . .	199
8.4	Application and results . . . . .	202
8.4.1	Imperfect draining vortex model . . . . .	202
8.4.2	Results for inverse problem . . . . .	203
8.5	Conclusions . . . . .	214
 <b>Chapter 9:</b>		
	<b>Final Remarks . . . . .</b>	<b>216</b>
9.1	Conclusions . . . . .	216
 <b>Bibliography . . . . .</b>		<b>220</b>

# Resumo

Modelos análogos fornecem uma promissora fonte de estudos para sistemas astrofísicos, tais como buracos negros e objetos compactos exóticos. Ao contrário dos objetos astrofísicos propriamente, os sistemas análogos podem ser adequadamente preparados para experimentos controlados em laboratório de modo a investigar sua dinâmica. As seções de choque e outras propriedades de espalhamento podem então ser mensuradas. Os resultados finais podem então ser comparados com os previstos para o caso astrofísico, e novos insights físicos podem emergir. Nesta tese, relatamos quatro resultados distintos. Primeiro, revisamos o problema direto da teoria de perturbação linear de buracos negros e objetos compactos exóticos sem horizonte, tanto no cenário astrofísico quanto em termos de seus sistemas análogos. A partir daí, deduzimos as formas de onda emitidas por esses objetos perturbados. Ao confrontar esses sinais, uma assinatura direta da refletividade do núcleo dos objetos compactos exóticos sem horizonte é deduzida, derivando uma importante *smoking-gun* para distingui-los dos buracos negros. Em segundo lugar, descrevemos um método semiclássico e não-paramétrico que permite a reconstrução do potencial efetivo a partir do conhecimento dos coeficientes de espalhamento. Terceiro, estendemos este método para potenciais dependentes da energia para resolver o problema de sistemas com rotação. Por último, aplicamos esta extensão para estudar o problema inverso de sistemas análogos que admitem rotação e condições de contorno dependentes de energia. Ao estender tais resultados, fornecemos uma receita que permite relacionar espectros de transmissão ressonante com um potencial equivalente e reconstruir a condição de contorno no núcleo da fonte de espalhamento. Para demonstrar a precisão e o escopo do nosso método, nós o aplicamos ao vórtice de drenagem imperfeito em rotação, que foi proposto como um sistema análogo para objetos astrofísicos extremamente compactos. Concluimos que a capacidade de reconstruir potenciais e condições de contorno dependentes da energia pode ser de interesse para estudos experimentais de tais sistemas.

# Abstract

Analog gravity models provide an insightful source of study for the qualitative key properties of astrophysical gravitating systems, such as black holes and exotic compact objects. Unlike distant astrophysical compact objects, analog gravity systems can be properly prepared for lab-controlled table-top experiments to investigate their dynamics. Cross-sections and other scattering properties can then be assessed by careful experiments and precise measurements. This obtained data can be compared with what was expected to be gotten from the astrophysical objects, and new physical insights can emerge. In this thesis, we report four distinct results. First, we summarize the direct problem for the linear perturbation theory of black holes and exotic horizonless compact objects, both in the astrophysical scenario and in terms of analog gravity systems. We derive the ringdown waveform signals emitted by those perturbed objects from that description. By confronting these signals, a direct signature of the exotic compact horizonless objects' core-reflectivity is detached, deriving an important smoking gun for distinguishing them from black holes. Second, we outline a semiclassical, nonparametric method that allows for the reconstruction of the effective scattering potential from the knowledge of the scattering coefficients. Third, we extend this method for energy-dependent scattering potentials to address the problem of rotating systems. Lastly, we apply this extension to study the inverse problem of analog gravity systems which admit rotation and energy-dependent boundary conditions. By extending our previous results, we provide a recipe that allows one to relate resonant transmission spectra with effective WKB-equivalent potentials and even reconstruct the boundary condition at the core of the scattering source. To demonstrate the accuracy and scope of our method, we apply it to a rotating imperfect draining vortex, which has been proposed as an analog system to astrophysical extreme compact objects. We conclude that the capability to reconstruct energy-dependent potentials and boundary conditions could be of interest to experimental studies of such systems.

# Publications

Subsection 2.4.1.1 is based on Ref. [1]: **Massless Dirac perturbations in a consistent model of loop quantum gravity black hole: quasinormal modes and particle emission rates.**

Authors: Saulo Albuquerque, Iarley P. Lobo, Valdir B. Bezerra

DOI: 10.1088/1361-6382/ace7a8 (publication)

Published in: Class.Quant.Grav. 40 (2023) 174001

Chapter 6 is based on Ref. [2]: **Inverse problem of analog gravity systems.**

Authors: Saulo Albuquerque, Sebastian H. Völkel, Kostas D. Kokkotas, Valdir B. Bezerra

DOI: 10.1103/PhysRevD.108.124053 (publication)

Published in: Phys.Rev.D 108 (2023) 12, 124053

Chapter 7 based on Ref. [3]: **Inverse problem in energy-dependent potentials using semiclassical methods.**

Authors: Saulo Albuquerque, Sebastian H. Völkel, Kostas D. Kokkotas

DOI: 10.1103/PhysRevD.109.096014 (publication)

Published in: Phys.Rev.D 109 (2024) 9, 096014

Chapter 8 is based on Ref. [4] (currently under review): **Inverse problem of analog gravity systems II: rotation and energy-dependent boundary conditions.**

Authors: Saulo Albuquerque, Sebastian H. Völkel, Kostas D. Kokkotas, Valdir B. Bezerra

e-Print: 2406.16670 [gr-qc]

# Chapter 1

## Introduction

### 1.1 Introduction

In 1915, Albert Einstein published two seminal papers, “On the General Theory of Relativity” [5] and “The Field Equations of Gravitation” [6], generalizing his special theory of relativity [7]. Through the equivalence principle, relating accelerated reference frames to reference frames experiencing a gravitational field, Einstein was able to formulate a brand new theory for the gravitational phenomenon. This theory offered a new explanation for why objects fall into the ground when we leave them in the air and why the Earth orbits around the Sun, among several phenomena of nature.

According to Einstein’s theory, gravity was no longer explained by the concept of force, such as in the Newtonian theory. Instead, the dynamical effect of gravity on the movement of bodies results from a distortion (read curvature) in spacetime. This curvature, in turn, is caused by the presence of matter and energy near that moving body. The body keeps following its free motion as described by a minimum path (read geodesic) in the background spacetime, but this background spacetime, however, is curved due to the presence of a mass-energy distribution from another massive body, readily the gravitational attractor, such as another star or planet for example.

The first success of that new gravitational theory was its ability to explain a phenomenon

that the Newtonian theory failed to describe: the precession of Mercury's orbit [8]. Nevertheless, as the history of science had already taught us at that time, for a physics fundamental theory to be the accurate scientific explanation behind any natural phenomena, it must achieve more than only explaining already existing problems. In fact, this new theory should also predict new features. Fortunately, this prediction indeed happened, and only four years later. In an observation of a total solar eclipse conducted in the Brazilian city of Sobral (situated, approximately, five hundred miles away from my university, UFPB), in 1919 [9], it was confirmed a new phenomenon predicted by Einstein's theory: the gravitational bending of light. This was the first prediction of Einstein's theory of general relativity (GR) that was experimentally demonstrated by observations.

The general relativity theory reached some other experimental proofs in the following years. In 1959, forty years later, an experiment proposed by Robert Pound and Glen Rebka [10] allowed them to measure the redshift of light caused by the acceleration of a moving rocket. The equivalence principle, the physical fundamental idea behind Einstein's theory, was fundamental for the explanation of this experiment's results. Next, sensible experiments were realized in 1976 [11], and once again in 2004 (with more accuracy) [12], confirmed another important prediction of Einstein's GR theory, which concerns the fact that the Earth's rotation warped the spacetime around the planet [13].

A few years later, recent studies on the distortion of light coming from distant galaxies [14, 15, 16], and crossing other massive astrophysical objects on their way to Earth proved another important prediction of General Relativity Theory: the gravitational lensing. The image captured by NASA's James Webb Spatial Telescope [17] in Fig. 1.1 shows us clearly this phenomenon.

Finally, the most recent pieces of evidence, accounting for General Theory of Relativity's scientific validation, were the two predictions most relevant for the research purposes of this thesis. The first one is an astrophysical object, the black Hole (BH), which is by far the most mysterious object in nature. The second is the GR prediction, which led to one of the





Figure 1.1: The combined mass of this galaxy cluster acts as a gravitational lens.  
Image Credit: **NASA, ESA, CSA, and STScI.**

most important scientific discoveries of all time: the existence of gravitational waves (GW). These waves are propagating ripples in the fabric of spacetime caused by 'violent' processes in the Universe. They were firstly detected in 2015 [18]. Since then, other gravitational wave signals from the binary merger of compact objects have also been detected [19, 20, 21, 22, 23, 24, 25]. It is expected that in the upcoming years gravitational waves astronomy will provide one of the most important tools for humankind to observe the Universe. The perspective of a prospective laser interferometer space antenna (LISA) [26] in the next few years reinforces this idea.

In the following, we will briefly introduce both black holes (BHs) and gravitational waves (GWs). Then, we shall study them conceptually in further detail in the following two chapters. Before that, however, we might need to emphasize their role in GTR phenomenology.

Black Holes and Gravitational Waves form the core of the phenomenological investigation toward testing general relativity's accuracy. We can cite, for example, the gravitational waves from merging black hole binaries [18, 27], and the images of black holes in M87\* and Sgr A\* at the center of our galaxy as important observational milestones for such phenomenological endeavor. Although much success and convincing pieces of evidence for GTR have been achieved by those observational breakthrough discoveries, the astronomical limitations imposed by the large distances between our ground-based detectors and those astrophysical sources make some key features of this theory extremely hard, if not impossible, to assess. However, it is in the physicists' interest to probe those effects and observe their

signatures to further establish the validity of general relativity theory.

On the phenomenology of black holes, for example, we can cite the quasi-thermal radiation emitted by those astrophysical objects. This radiation was theoretically predicted by Hawking [28], and it is a very relevant physical phenomenon since it lies on the interface between GR and quantum field theory, another fundamental physical theory. The study of the scattering of matter fields around black holes is another problem that is hard to assess with the currently available observational methods. Particularly within this theory, another very important prediction, which is the scattering amplification of fields around spinning black holes [29], remains missing as a fundamental piece of evidence from Einstein's theory of gravity. Lastly, a third and even more fundamental phenomenological window for testing GR with black holes comes from probing their most elementary feature. Black holes are essentially 'black' due to the existence of an intrinsically limiting surface called *event horizon*. This surface delimits a region of spacetime in which not even light can escape the strong gravitational attraction from those extremely compact objects. Probing the existence of the black hole's event horizon means probing this object's existence itself, which in turn means probing general relativity.

Aiming to tackle those phenomena and accept those observational limitations, some researchers have proposed a completely new approach for this endeavor. This phenomenological alternative consists of emulating astrophysical phenomena in a laboratory setting employing analog systems to the astrophysical ones. This brand-new field of physical investigation is called analog gravity, and it provides exciting and complementary ways to study qualitatively similar phenomena [30, 31, 32, 33], but based on much simpler underlying physics. Those analog systems are physical systems with a completely different nature, which could in principle be classical fluids [30, 34] or even mesoscopic quantum systems, such as Bose-Einstein condensates [35, 36]. Those systems are arranged in a particular way in which they reproduce key effects that were only expected to exist in the astrophysical scenario. Among key effects that we previously mentioned that could not be directly measured for astrophysical black

holes, some of them can be mimicked in analog systems. For example, we can cite: Hawking radiation [37, 38, 39, 40, 41, 42, 43, 44]; the physical profile of wave scattering through a black hole, including the superradiance on rotating black holes [45]; back-reaction effects [46]; and quasinormal modes, which have been experimentally investigated in an acoustic analog black hole setup in Ref. [47]. More than reproducing key properties of their associated actual systems in the laboratory, analog systems must also be easy to manipulate and probe with the available technologies.

Furthermore, in recent years, the question concerning the phenomenological signature of the BHs' event horizon was also formulated into the study of analog systems [48]. There are some expectations that analog systems can also qualitatively tackle this fundamental problem in an easier way. In order to understand how this problem is posed for analog gravity systems, we first need to understand its formulation in the astrophysical scenario.

We know theoretically that the major part of the key properties from black holes' scattering and emission of gravitational radiation are related to their light-ring rather than its event horizon [49]. So, the question concerning the existence of the black hole's event horizon surface was pointed out in literature in recent years [50, 51, 52, 53, 54, 55, 56, 57]. While we cannot fully assert that the event horizon is indispensable for the observational findings obtained so far, different theoretical proposals of extremely compact objects mimicking black holes' observational signatures have been proposed [58, 51, 59, 60, 61, 50], they are the so-called *exotic compact objects*, or *exotic horizonless compact objects*. Among them, we can cite the proposed models for boson stars, such as scalar stars [62, 63, 64, 65, 66] and Proca stars [67, 68, 69]; constant density stars [70, 71, 72, 73]; and more recently, black holes with quantum horizons [74, 75, 76, 77, 78], which are mainly motivated by quantum spacetime theories.

In the context of analog gravity, a system with such properties has been proposed in Ref. [48] and consists of an imperfect draining vortex. The motivation for this model came from an analog gravity experiment with a classical fluid vortex, conducted by the Gravity

Group from Nottingham [79]. The detection of a fundamental core reflectivity, due to non-vorticity effects close to the vortex’s core was pointed out by Theo Torres in Ref. [80]. While Theo’s argument could naturally disqualify the bathtub draining vortex as a natural candidate for a black hole analog gravity system, which was what it was originally meant to, some authors [48] have proposed that this core reflectivity could promote this same system as an analog gravity system to an *exotic horizonless compact object* instead. In that framework [48], the observational consequences of such a system have been studied for fluid perturbations. These include transmission and reflection coefficients and possible superradiant features. That formal treatment yields what we call the “direct problem” in the following.

This framework in Ref. [48] has added a new body to the discussion of the phenomenology of the event horizon, but now in terms of the analog gravity systems approach. Its outlining discussion provided the most important theoretical motivation for this thesis. Our main idea here, however, concerns reproducing the lab results obtained from the imperfect draining vortex and reconstructing the key properties of the analog system’s original source. For that goal, we rely on a specific set of tools, called *inverse method*. If analog exotic compact objects can be realized in laboratory experiments and transmission/reflection coefficients can be measured, how could one use them to study their properties through the inverse problem?

The inverse method referred to here consists of a set of techniques and inverted semi-analytical formulas that provide us with mathematical tools for reconstructing key properties of the scattering source. In our case here, the inverse method we develop allows us to re-obtain the associated effective scattering potentials, which produce the scattering results we use as input. In chapters 5 and 6, we describe this inverse method for energy-independent potentials, while in chapter 7, we present our extension of the same techniques for the case with energy-dependent potentials, which helps us deal with cases where the scattering source is rotating. This last application is reserved for chapter 8.

In the following section, we briefly introduce black holes and discuss the phenomeno-

logical efforts toward their observations. We also point out challenges such as testing the existence of their event horizons. Then, we also discuss gravitational waves. In the following section, analog systems are introduced as a new approach to testing GTR predictions in the laboratory. Finally, the last section discusses how we structure this thesis.

## 1.2 Black Holes and Exotic Compact Objects

Black Holes were first proposed theoretically by Schwarzschild in 1916 [81], when he obtained the first analytical solution for Einstein’s field equations. These solutions described the spacetime around a compact, static, and spherically symmetric object. The spacetime in the neighborhood of this object had a removable singularity at a spacelike spherical surface centered on the compact object. To the physicists surprise, the radius of this spherical surface happened to be a very specific value. This value was later called “Schwarzschild radius” and it defines the exact distance from the center of the massive object to which not even the light can escape from the strong gravitational pull created by this compact object. For that reason, this solution was later called by Wheeler [82] ‘the static spherical Black Hole’, and the spherical surface defined by Schwarzschild’s radius was called ‘Event Horizon’.

Later, Robert Kerr also found a theoretical model of a rotating black hole solution for Einstein’s field equation [83], which described what is called ‘the rotating Black Hole’. Together with Kerr-Newman solution [84] and Reissner-Nordstrom solution [85, 86], those mathematical solutions form the basic black hole spacetime solutions of Einstein’s field equations. They describe the equilibrium states of black holes.

Subsequently, in 1973, J. M. Bardeen, B. Carter and S. Hawking [87] formulated the basic four laws of black hole mechanics, describing the dynamics of black holes in terms of only three parameters: their mass, charge, and angular momentum. The laws of transformations for the equilibrium states of black holes were then formulated. A strong similarity between these four laws of black hole mechanics and the four laws of thermodynamics started rais-

ing some interest from physicists. Bekenstein [88] was the first to propose that this close similarity was more than an analogy. According to Bekenstein, those four laws of black hole dynamics were actually an equivalent formulation of the basic four laws of thermodynamics for black holes. Two years later, this equivalency proposed by Bekenstein was formally demonstrated by Stephen Hawking [28].

By formulating quantum field theory in the background of curved spacetimes surrounding black holes and considering the BH's formation process, Hawking showed in 1975 that black holes are not completely black. They actually emit thermal radiation. The irradiation spectrum of this thermal radiation from black holes is the same as we would have from a common black body with temperature  $T$  coinciding with the associated black hole's surface gravity. Hawking also derived the entropy of black holes, which is directly and uniquely related to their surface area.

Finally, an important line of work in theoretical physics was established: Black Hole Physics bringing several implications for astrophysics, gravitational physics, and cosmology. A widely studied branch in black hole physics is the Black Hole Perturbation Theory (BHPT), which was extensively used to theoretically demonstrate some of the above-mentioned results. A lot of important research came from this approach [82, 89]. Up to this day, this theory still furnishes a powerful method for current theoretical investigations, and it is an important tool for the research covered within this thesis.

On the other hand, while all those theoretical developments were being carried out and those mathematical solutions describing black holes were starting to become very well-established and recognized, the actual existence of black holes was still under scrutiny by the scientific community. Scientists questioned their existence theoretically and observationally.

The first reason for the theoretical distrust in the existence of black holes was the absence of a theoretical explanation for how those objects could naturally be formed. The General Theory of Relativity was able to fully describe the spacetime in the neighborhood of those massive astrophysical objects, but it was still not capable of explaining how they could be

formed in nature. In 1939, however, Oppenheimer and his student Hartland Snyder showed how black holes are formed by the collapse of certain classes of stars [90]. In 1965, Roger Penrose also showed that black hole formation was a general consequence of the GTR [91]. For this insight, Penrose was awarded with part of the 2020 Nobel Prize in Physics [92].

On the observational side of the question, however, direct and even indirect evidence of the existence of black holes was still lacking. This problem remained for a long time until the first indirect evidence emerged. Direct evidence, however, took a much longer time to appear finally.

The first piece of indirect evidence for black holes' existence emerged in 1971 [93]. It came from a binary star system within our galaxy called Cygnus X-1. The discovery of the system was allowed by the fact that this system is one of the brightest sources of X-rays. The evidence for the black hole nature of Cygnus X-1 came from the dynamical observations of its stellar components. Cygnus X-1 presented a mass of several solar masses.

Later, in 1974, astronomers also discovered that there is a supermassive black hole in the center of our galaxy. This compact object was called Sagittarius A\*. This discovery was made by Bruce Balick and Robert L. Brown [94]. They noticed a bright radio source at the center of the Milky Way galaxy. Reinhard Genzel and Andrea Ghez were the astrophysicists who tracked the motion of stars around this astrophysical object (Sagittarius A\*) [95]. Genzel and Ghez showed that those stars were orbiting a very massive and compact object. The partial orbits of many stars were observed. One of the stars, S2, made a complete revolution in an elliptical orbit around Sgr A\*, which helped Genzel and Ghez estimate the mass of this gravitational source as  $4.1 \pm 0.6$  million solar masses [96]. Accordingly, it was finally demonstrated that those stars were probably orbiting a supermassive black hole.

For the discovery of this supermassive black hole at the center of our galaxy, Reinhard Genzel and Andrea Ghez were also awarded part of the 2020 Nobel Prize in Physics. Genzel and Ghez shared this Nobel Prize with Roger Penrose [92].

In March 2022, astronomers from a global research team called Event Horizon Telescope

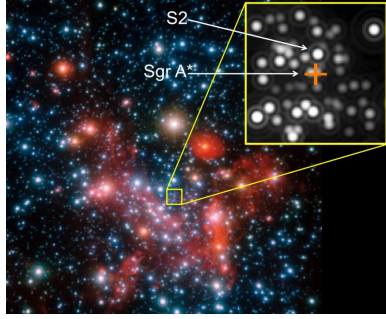


Figure 1.2: The supermassive black hole at the center of our Milky Way galaxy, Sagittarius A\*, as well as the giant star S2 is shown in this near-infrared image from the ESO’s Very Large Telescope in Chile.

Image Credit: **ESO/MPE/S; Gillessen et al.**

(EHT) Collaboration released the first image of this supermassive black hole at the center of our galaxy (Sagittarius A\*) [97]. The release of this image was another moment that we can certainly call historical for science as a whole. This image provides another strong evidence that the compact object Sagittarius A\* is indeed a black hole.

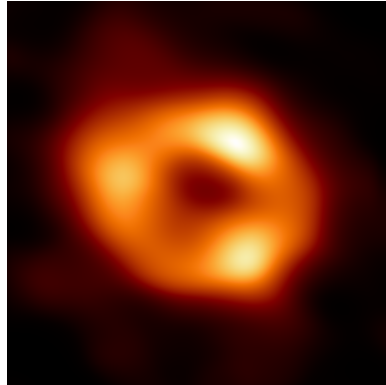


Figure 1.3: The first image of the black hole at the centre of the Milky Way galaxy (Sgr A\*).

Image Credit: **EHT Collaboration.**

*“We were stunned by how well the size of the ring agreed with predictions from Einstein’s Theory of General Relativity [...]”* said EHT Project Scientist Geoffrey Bower[98] from the Institute of Astronomy and Astrophysics, Academia Sinica, Taipei.

Finally, summing up all the evidence listed above, we can claim that black holes are a very well-established scientific fact for the scientific community nowadays. As in every



scientific case, however, even the most well-established hypothesis must always be confronted with its possible alternatives. If there are any other theoretical proposals for extremely compact objects reproducing similar or equivalent results to the ones currently attributed to black holes, the theoretical predictions from those proposals must be phenomenologically confronted with observational data until we can rule out all alternative explanations.

When it comes to black holes, the physical feature that defines their nature *a priori* and distinguishes them from the other theoretically proposed extremely compact objects is their event horizon surface. The event horizon is a particularity of black holes since it is what defines them as black holes in the first place. No other compact objects can be as compact and dense as black holes. In this sense, exotic compact horizonless objects (ECOs) can be defined as extremely compact objects that are compact enough to exhibit a photosphere but remain with a radius superior to the Schwarzschild radius's threshold.

Accordingly, a major difficulty in confronting black holes with their possible horizonless alternative models arises from the fact that astrophysical processes are usually insensitive to the spacetime geometry near the horizon. As it is well known, most of the scattering properties of perturbations in a ringing black hole spacetime are determined by its photosphere surface. Hence, the departures of the ringdown signal of extremely compact horizonless objects with a photosphere from the BHs' associated results are expected to be hidden (at least in principle). For example, a naive application of the usual quasinormal mode spectroscopy (see chapter 4) to the GW ringdown strain would not, in principle, capture a relevant difference between BHs and ECOs [59].

In the last years, however, some works claimed tentative evidence of smoking-gun signs of so-called echoes in gravitational wave data, e.g., Ref. [99]. The echo phenomenon was first studied for ultracompact constant-density stars in Refs. [100, 101, 102, 103] and, since then, for a variety of exotic compact objects (see Ref. [104] for a review of the topic). Although subsequent works cannot confirm such findings and refuse claimed significance [23, 25], the question of the existence of such objects remains intriguing.

In this thesis, beyond our main goal of developing an inverse method for reconstructing the scattering profile of BHs and ECOs, we also study and explicitly compare the ringdown waveforms from black holes and exotic compact horizonless objects. We use a frequency domain approach to demonstrate that the ECOs' waveform can be understood either as a superposition of echo pulses, added to a BH waveform [59, 58], or as a superposition of the ECO's resonant modes. In this way, we show in a straightforward way how to detach the horizonless signature of ECOs from their waveforms. We also explicitly show how those waveforms' quantitative properties are intrinsically related to the ECOs' physical features, such as their compactivity and core-reflectivity. We further develop this discussion in chapter 4.

### 1.3 Gravitational Waves

Gravitational waves were theoretically predicted in 1916 [105], by Einstein himself. He discovered that those ripples in the fabric of spacetime were a theoretical consequence of his theory of general relativity. By considering his field equations in the vacuum, Einstein found out that the perturbations in a gravitational field propagate as waves, carrying energy and momentum at the speed of light. This behavior of the gravitational field is analogous to the behavior of the electromagnetic field in a vacuum.

For a very long time, scientists had tried to propose observational methods to detect the existence of gravitational waves, indirectly and directly. After almost a century of trying to test this Einstein's prediction, on September 14 of 2015, researchers from the Laser Interferometer Gravitational-Wave Observatory (LIGO), and from the Virgo Interferometer (hosted by the European Gravitational Observatory) announced their great discovery: they had directly detected gravitational waves for the first time [18]. This finding marked one of the most important moments in the history of science. Those gravitational waves (GW150914) detected by LIGO and Virgo [18] were generated by the coalescence of a black hole binary

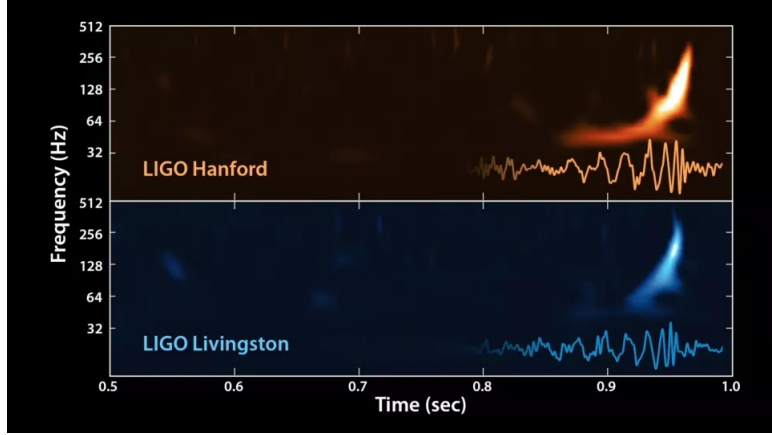


Figure 1.4: The waveform in the time and frequency domain of the gravitational waves from (GW150914), detected by LIGO and Virgo [18]. Notice that the GW frequency increases as black holes spiral closer together.

Image Credit: **LIGO**.

system. This pair of black holes spiraled together and finally merged into a unique and heavier black hole.

Since that first detection, LIGO and Virgo have detected a few other gravitational wave signals, coming from different sources [106, 27, 107]. For example, they have detected gravitational waves generated by the coalescence of other black hole binary systems [27](GW150914 [108], GW151012 [109], GW151226 [110], GW170608[111]), the merging of black holes and neutron stars [106], and the collisions within binary systems of neutron stars [107].

More than providing evidence for the General Theory of Relativity, Gravitational Wave astronomy opens a powerful new window for physicists to see the Universe. Equipped with this new tool, in the next few years, we will be able to test models and understand new features of the early universe and, most importantly, probe the behavior of black holes, neutron stars, and other astrophysical objects. For example, We can already anticipate that for every gravitational wave signal generated by an astrophysical event involving black holes, the properties of these black holes will play an important role in the behavior of that resulting gravitational wave signal. The amplitude, the decay rate, and also the frequency of the gravitational waves are all affected by some properties of the merging black holes. The black holes' masses, charges, and angular momenta are examples of those properties.

Additionally, it is worth mentioning that any modification in the BHs' description will also leave a signature in the resulting gravitational waves. These modifications in the description of black holes may arise, for example, as a result of quantum corrections introduced by modified theories of quantum gravity or quantum spacetimes.

Although a large window of observation has been opened by those interferometers, and another huge one is expected to be opened by the next generation of space-based GW interferometers [26], there is still plenty of information on the gravitational field, and about its interaction with quantum fields that will not be assessed with the GW interferometers. Examples of those properties are the superradiance [112, 113], predicted for rotating black holes; the Hawking radiation [114], which is very weak quasi-thermal radiation expected to be emitted from black holes, and a few other effects. Even the proper study of scattering properties of black holes is hard to assess without proper control of what is being 'sent' for scattering through the black hole. For the goal of exploring such questions, in the last few years, we have been trying to find analog systems to gravity systems in which such questions can be explored in lab-controlled experiments. The following section will introduce analog gravity systems and deepen the discussion on this topic.

## 1.4 Analog Gravity Systems

One of the first analog gravity systems was proposed by G. Unruh in 1980 [30], pointing out an equivalence between the hydrodynamical equations describing the evolution of acoustic perturbations in a classical hydrodynamical vortex, and the Klein-Gordon equation describing scalar field perturbations in an effective black hole spacetime. This model was later called acoustic black hole [31, 32, 34], and consists of a sonic hole created by a fast rotating and absorbing draining vortex. The idea is that the high-velocity absorption profile of this vortex will create a spatial barrier in which acoustic perturbations at the speed of sound are prevented from leaving after this limit. In some sense, this surface would be the acoustic

equivalent to the event horizon in a Schwarzschild black hole or in a Kerr black hole. That is the kinematics idea behind this model, and further details on its dynamic aspects are left for chapter 3. The equivalence between the mathematical description of those analog systems and their associated astrophysical systems allows us to carry out this investigation. The development of experiments with this analog model enabled us to detect physical analog effects that were only expected to occur in actual black hole astrophysical systems. Among the plethora of experimental findings, some of the most important are the experimental measurement of rotational superradiance in the scattering of a vortex flow [45], the experimental occurrence of quasinormal mode oscillations in analog black hole experiments [47], and the detection of Hawking radiation in an analog gravity experiment [115, 116].

Since 1980, a few new ideas for different analog gravity systems have arisen; one of them, for example, proposed an analog to a black hole with a Bose-Einstein condensate [35, 36, 42, 117, 37, 38, 39, 118]. In this system, the propagation of acoustic perturbations plays the role of "scalar" field perturbations on their associated black hole spacetimes. Similar black hole analog effects were also displayed in this system, such as Hawking radiation [37, 38, 39], superradiance [119], and even the signature of the rotating effective curved spacetimes [120]. New alternatives for analog models to gravity systems have also been proposed, such as the optical analog to black holes [121] for example.

In this framework, we focused our attention on the first and simplest tabletop experiments, repeatable in ground-based laboratories, which is the analog model of a black hole with a sonic or acoustic hole (see Fig. 1.5). We paid special attention to recent experiments conducted on this system. Among them, we can cite the detection of quasinormal mode ringing [47], the experiment that showed the superradiance in the scattering of waves around this draining vortex [79], and a recent report pointing out the possible core reflectivity of this analog system due to non-vorticity effects at its core [80]. Another recent experiment that inspired our study was the recent discovery of the rotating curved spacetime signature in the analog system consisting of a big quantum vortex [120]. This vortex was prepared by

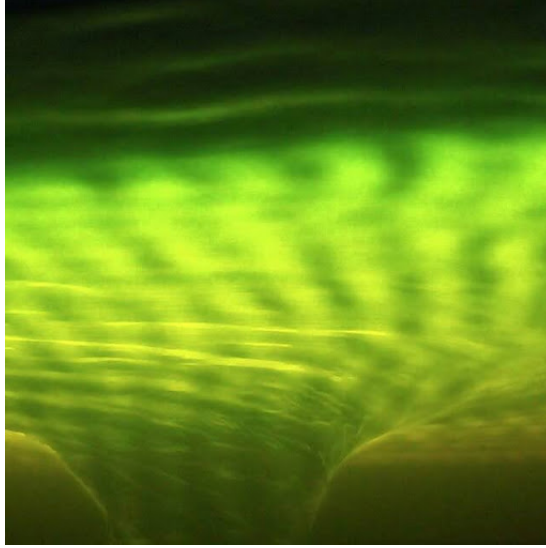


Figure 1.5: Scattering of waves by a draining vortex in a bathtub.  
Image Credit: **Gravity Group. University of Nottingham.**

combining small unstable quantum vortexes in liquid helium that would later produce a final giant vortex with macroscopic dimensions. The experiment was conducted by Nottingham’s gravity group, and it strongly motivated the extension of our results for rotating analog systems. We present this extension in chapter 7.

Among the most important advantages of carrying out our research with analog systems is the availability of accurate data on their scattering properties, including, for example, the measurement of cross-sections and reflectivity coefficients. To compute those quantities, we need previous knowledge of the incident waves and the measurement of the scattered output. The final scattering coefficients are obtained by normalizing the reflected and transmitted waves with the incident ones. Such calculations are not possible in an astrophysical scenario but are allowed for lab-controllable experimental setups. The physical identification between the scattering of perturbations in analog systems and the propagation of field perturbations around a black hole is then guaranteed by the mathematical equivalence between the master equations describing them [31, 32]. Since those equations are in the form of a Schrödinger-like wave equation, this motivates the application and extension of Wentzel–Kramers–Brillouin (WKB) based inverse problem methods. In the following, we briefly introduce this semi-

analytical inverse method. The more detailed derivation of the associated formulas is carried out in Chapter 5, while its applications are discussed in chapters 6, 7, and 8.

## 1.5 Inverse method with semi-analytical techniques

In literature, the inversion of the WKB formulas allows one to obtain a powerful inverse method for reconstructing effective potentials in the quantum scattering and bound state problems [122]. The main advantage of the inverse techniques provided by those inverse semi-analytic formulas is that they offer a parameter-free and model-agnostic inverse method based solely on the applicability of the direct WKB method. This aspect provides an important advantage when one compares it with model-dependent Bayesian techniques, such as MCMC [123], and others [124]. In Chapter 5, we introduce the WKB method in general lines, deriving its direct semi-analytic formulas and their corresponding inverted ones.

That inverse WKB method has been extended for the perturbation theory of wormholes [125], constant-density stars [126, 127, 128], and other exotic compact objects [129, 130]. In this thesis, we demonstrate that we can also apply such inverse semi-analytic formulas to analog gravity systems [2, 3]. We considered in Chapter 6, for illustration, the application of this inverse method for the analog model of exotic compact objects consisting of an imperfect draining vortex in a bathtub [2]. Among the main results we achieved in that chapter, we can mention the fact we could reconstruct the effective scattering potential associated with the effective background geometry of the imperfect draining vortex [48]. More than that, we could infer the reflectivity boundary parameter in the case it was a constant. Our application in this chapter was restricted to the non-rotating scenario of analog gravity systems. The reason for that was the fact we only have a single effective energy-independent potential if we are in a non-rotating vortex regime. Adding the rotation to this system couples an energy dependence for the scattering potential. Accordingly, distinct potentials are obtained depending on the energy of the incident wave.

In Chapter 7, and Ref. [3], however, we circumvented such difficulty in the most general case by extending the WKB techniques for energy-dependent potentials in a wave equation. To accomplish that goal, we proposed an energy-independent effective potential that reproduces the desired physical properties of the original family of energy-dependent ones. We called this reconstructed potential '*WKB-equivalent*' potential since it shares the same bound states (or transmission) that we used for its reconstruction. To illustrate how the inverse techniques would work in such cases, we considered two toy models: an energy-dependent modified harmonic oscillator and an energy-dependent Pösch-Teller potential.

Finally, in Chapter 8, we aimed to extend our inverse method for the energy-dependent scattering potentials produced by rotating analog gravity systems and for energy-dependent reflectivity parameters defined at their internal boundaries. As for the applications, we considered generalizing our results from Chapter 6 for the imperfect draining vortex with a non-zero rotation coefficient. If this method can also infer important physical properties of those systems, which we show to be the case, that potentially provides us with an auxiliary tool for treating the experimental data measured by analog systems' experiments.

## 1.6 Structure of this Thesis

We now briefly introduce the general structure of this thesis. In the next three chapters, we give a general and detailed review of the theoretical background behind the direct problem of BHs and ECOs perturbation theory, both in the astrophysical scenario and in analog gravity systems. Then, the following three chapters cover the proposal and solutions to the associated inverse problem.

In chapter 2 we introduce and discuss perturbation theory in GTR, focusing on linear perturbations in the background of black hole's and exotic compact objects' spacetimes. That chapter speculates the important distinction between black holes and other alternative exotic horizonless compact objects. We propose a simple and insightful model for ECOs in



terms of a fundamental change in the boundary conditions at the surface of these objects. That model will be extremely relevant to the upcoming discussions carried out throughout this thesis.

In chapter 3, we review the theoretical background behind analog gravity systems, paying special attention to the acoustic analog black hole and analog ECO. In that chapter, we also show the mathematical equivalence between the evolution of acoustic perturbations in a rotating draining vortex and the evolution of scalar field perturbations in the effective curved spacetime of a black hole-like metric.

In Chapter 4, we finally discuss how to solve the master wave equations describing the evolution of perturbations in the two scenarios presented in the previous chapters. For this goal, we present two main approaches; the first one consists of directly integrating those equations in the time domain, while the second one is based on Green's function formalism for integrating those equations in the frequency domain. The solutions in the frequency and time domains are connected via Fourier transformations. After presenting the methods for obtaining those solutions, we finally consider two important applications: calculating the ringdown waveforms for the evolution of perturbations, which allows us to relate the damped oscillating signal measured by a distant observer with the physical properties of their relaxing ringing sources; and also the scattering theory in these background spacetimes. We infer the main distinct predictions for black holes and other exotic compact horizonless objects for both applications. For the scattering theory, for example, we see that the reflecting boundary condition at the object's surface leads us to cavity and resonant effects. Meanwhile, for the analysis of the ringdown signal emitted by these perturbed sources, reprocessing the waves at their reflecting surface generates the so-called *echoes* in the waveform strain.

In Chapter 5, we present the semi-analytical formulas used in Nuclear physics for investigating bound states and scattering properties of quantum systems described by the Schrödinger wave equations. Since our investigated systems are dynamically described by a Schrödinger-like wave equation, we also demonstrate how we can invert those semi-analytical

formulas to obtain the inverse formulas to be used in our applications.

In Chapter 6, we explain how our previously introduced inverse method is posed for analog gravity systems to exotic compact horizonless objects. Then, we investigate how one can reconstruct the scattering effective potential, determining the scattering of perturbations for these systems in the non-rotating case. From this chapter onwards, our applications will focus on analog gravity systems, specifically, the imperfect draining vortex in a bathtub.

As we also discuss in chapter 2, the rotating behavior of astrophysical and analog gravity systems leads us to energy-dependent potentials in the master wave equations describing the evolution of perturbations. Motivated by this fact, in Chapter 7, we extend our inverse method to energy-dependent potentials by defining an effective 'WKB-equivalent' potential. We show that this effective inverse reconstructed potential reproduces the input physical properties used for its reconstruction. This way, from an energy-independent effective potential, we obtain scattering properties quasi-equivalent to the ones obtained from the original energy-dependent potentials. Finally, we discuss the achievements of our method and its limitations in terms of two toy-models potentials, the energy-dependent quadratic potential for a modified harmonic oscillator, and the energy-dependent Pöschl-Teller potential.

In Chapter 8, we use that previously developed inverse method for energy-dependent potentials to extend the applications considered in Chapter 6 for rotating analog exotic compact object (ECO) systems. In that chapter, we also study the inverse problem of analog gravity systems which admit energy-dependent boundary conditions. We contrast the inverse reconstructed effective potentials with the width-equivalent potentials and the original family of energy-dependent potentials. Lastly, we present the reconstructed scattering coefficients obtained from those WKB-equivalent reconstructed potentials, contrasting them with the original scattering coefficients used as input for our method. The accuracy of our results is discussed for different regimes of the analog ECO system.

Finally, in the last chapter 9, we finish our work by summarizing the most important conclusions and remarks obtained throughout this thesis. Future perspectives of this work

in terms of our current collaborations are also presented.

# Chapter 2

## Perturbation Theory in General Relativity

### 2.1 Einstein's Field Equations and the General Relativity Theory

While on the theoretical side, Einstein's Field Equations have unveiled the existence of previously unknown phenomena, such as gravitational waves and black holes, on the mathematical side, this new way of looking at the gravitational interaction has established an extremely complicated system of non-linear coupled equations. A closer look at the full form of those field equations quickly reveals this fact. We can summarize Einstein's field equations as in the following expression

$$R_{\mu\nu} - \frac{1}{2}g_{\mu\nu}R = \frac{8\pi G}{c^4}T_{\mu\nu}. \quad (2.1)$$

In this equation,  $R_{\mu\nu}$  is the Ricci Curvature Tensor,  $R$  is the curvature scalar,  $g_{\mu\nu}$  is the metric tensor, and  $T_{\mu\nu}$  is the energy-momentum tensor. Here, Einstein's sum convention is implicitly used. The curvature scalar is given in terms of the Ricci curvature tensor in the following way

$$R = g_{\mu\nu} R^{\mu\nu}. \quad (2.2)$$

The Ricci curvature tensor, on the other hand, can be written in terms of the metric connections

$$R_{\mu\nu} = \partial_\mu \Gamma_{\lambda\nu}^\lambda - \partial_\nu \Gamma_{\lambda\mu}^\lambda + \Gamma_{\mu\sigma}^\lambda \Gamma_{\lambda\nu}^\sigma - \Gamma_{\nu\sigma}^\lambda \Gamma_{\lambda\mu}^\sigma, \quad (2.3)$$

where those metric connections  $\Gamma_{\mu\nu}^\alpha$ , also called Christoffel symbols, are related to the metric tensor by

$$\Gamma_{\mu\nu}^\lambda = \frac{1}{2} g^{\lambda\sigma} (\partial_\mu g_{\nu\sigma} + \partial_\nu g_{\mu\sigma} - \partial_\sigma g_{\mu\nu}). \quad (2.4)$$

The energy-momentum tensor  $T_{\mu\nu}$  is determined by the mass-energy distribution in the considered space-time. In field theory, we usually define the energy-momentum tensor  $T_{\mu\nu}$  as the covariant class of objects that keep the associated action  $\mathcal{S}$  invariant under the symmetry group of transformations considered in the theory. In Einstein's general relativistic theory, this group of symmetry is the group of the diffeomorphism of a 4-dimensional differential manifold with Lorentzian structure. In mathematical terms, this is equivalent to saying that under general coordinate transformations

$$x^\mu \rightarrow x'^\mu(x). \quad (2.5)$$

The energy-momentum tensor obeys a covariant (or contravariant) transformation law such that

$$\begin{cases} T_{\alpha\beta}(x) \rightarrow T'_{\mu\nu}(x') = T_{\alpha\beta}(x) \frac{\partial x^\alpha}{\partial x'^\mu} \frac{\partial x^\beta}{\partial x'^\nu}, \\ \mathcal{S}[T_{\alpha\beta}] \rightarrow \mathcal{S}'[T_{\mu\nu}] = \mathcal{S}[T_{\alpha\beta}]. \end{cases} \quad (2.6)$$

The 4-conservation of the energy-momentum tensor is expressed by

$$\nabla_\mu T^{\mu\nu} = 0, \quad (2.7)$$

where  $\nabla_\mu$  is defined as the covariant derivative in this differential 4-dimensional manifold. For a second-rank contravariant tensor, this derivative is written as

$$\nabla_\lambda T^{\mu\nu} = \partial_\lambda T^{\mu\nu} + \Gamma_{\lambda\sigma}^\mu T^{\sigma\nu} + \Gamma_{\lambda\sigma}^\nu T^{\mu\sigma}. \quad (2.8)$$

Different mass-energy distributions define different energy-momentum tensors in the considered spacetime. For instance, if we define a spacetime embedded with an electromagnetic field, the minimal coupling states that the energy-momentum tensor on the right-hand side of Einstein's field equations shall be written as

$$T_{\mu\nu}^{\text{E.M.}} = \frac{1}{4\pi} \left( F_{\mu\rho} F_\nu{}^\rho + \frac{1}{4} g_{\mu\nu} F_{\rho\sigma} F^{\rho\sigma} \right), \quad (2.9)$$

where  $F_{\mu\nu}$  is the electromagnetic field tensor, defined in terms of the electromagnetic four-potential  $A_\mu$  as

$$F_{\mu\nu} = \nabla_\mu A_\nu - \nabla_\nu A_\mu. \quad (2.10)$$

On the other hand, if we consider our spacetime to be under the influence of a massive scalar field instead, we shall obtain the expression for the energy-momentum tensor

$$T_{\mu\nu}^\phi = \nabla_\mu \phi \nabla_\nu \phi - \frac{1}{2} g_{\mu\nu} (\nabla^\rho \phi \nabla_\rho \phi - m^2 \phi). \quad (2.11)$$

Furthermore, if we consider our spacetime to be filled with a perfect fluid with density  $\rho(x)$  and with an equation of state  $p(\rho)$ , we have

$$T_{\mu\nu}^{\text{fluid}} = (\rho + p) u_\mu u_\nu - p g_{\mu\nu}, \quad (2.12)$$

where  $u_\mu$  is the fluid 4-velocity field.

Looking at Eqs. (2.1),(2.2),(2.3),(2.4), we notice that one of the formal goals of Einstein's field equations is to describe how the spacetime geometry is affected by the presence of a mass-energy distribution specified by the energy-momentum tensor  $T_{\mu\nu}$ . This spacetime geometry is completely determined by the metric tensor  $g_{\mu\nu}$ . In other words, we can summarize by saying that one of the physical goals of Einstein's theory of relativity is solving his field equations for the metric tensor  $g_{\mu\nu}$ . This way, we address the second part of the famous Wheeler's quote:

*"Spacetime tells matter how to move; matter tells spacetime how to curve" - John Wheeler*

The first part of the above quote can be addressed once the metric tensor is finally specified  $g_{\mu\nu}$  (once we know the structure of the spacetime geometry). Formally, this could be equivalent, for example, to solving the geodesic equations for the movement of null test particles

$$\frac{d^2 x^\mu}{d\lambda^2} + \Gamma^\mu_{\alpha\beta} \frac{dx^\alpha}{d\lambda} \frac{dx^\beta}{d\lambda} = 0 \quad (2.13)$$

Solving for  $x^\mu(\lambda)$ , under a certain chosen parametrization  $\lambda$ , furnishes the cinematic description of the particle's movement under the influence of the gravitational field defined in (by) this spacetime geometry.

The problem seems intuitive and clear to understand conceptually; one could even risk claiming that it is an easy problem if it weren't for the extremely complicated form of field equations. As we see in Eqs. (2.3),(2.4), the equations for the metric tensor are coupled and highly non-linear. Considering the symmetry of the metric tensor, we are led to 10 non-linear coupled equations that could turn the easiest problems into a real nightmare! That is the reason behind the fact we do not have many exact solutions for Einstein's field equations. A highly symmetric configuration must be considered if we want to obtain exact (analytical)

solutions to these field equations. That is precisely what Schwarzschild did in 1916 [131, 132].

Considering a static and spherically symmetric configuration describing the spacetime around a massive and spherical compact object, Schwarzschild showed that the spacetime metric could be defined, in spherical coordinates, by the following line element

$$ds^2 = - \left(1 - \frac{2GM}{c^2 r}\right) dt^2 + \left(1 - \frac{2GM}{c^2 r}\right)^{-1} dr^2 + r^2(d\theta^2 + \sin^2 \theta d\phi^2). \quad (2.14)$$

In the natural units system  $c = G = 1$ , we rewrite the equation above as

$$ds^2 = - \left(1 - \frac{2M}{r}\right) dt^2 + \left(1 - \frac{2M}{r}\right)^{-1} dr^2 + r^2(d\theta^2 + \sin^2 \theta d\phi^2), \quad (2.15)$$

where  $M$  is the ADM mass of the gravitational compact object and  $r_h = 2M$  is what was later called the black hole's *event horizon*.

That highly symmetrical spacetime configuration describes the vacuum spacetime around a very compact spherical object. The high symmetries of this solution explain why it was first obtained. Schwarzschild's metric was only extended for a stationary spacetime around an axially-symmetric rotating black hole, with angular momentum, in 1967 by Roy Kerr [83]. Kerr derived the spacetime metric for an axially symmetric rotating black hole. We introduce Kerr's solution in Sec. 2.4.3.

Any spacetime deformation of those compact objects would no longer allow us to use Eq. (2.15), since these deformations cause us to depart from the highly symmetrical scenario. Numerical solutions become then indispensable. In some sense, if we are willing to describe the dynamics of spacetime analytically, we are then constrained to very symmetrical cases. However, what if we want to consider small deformation or small departures from this highly symmetric scenario? Is it possible that we can actually obtain an analytical or semi-analytical framework for the spacetime dynamics if we treat this additional deformation as a small perturbation on the (symmetrical) background spacetime? This chapter deals with these



questions, introducing the key idea of perturbation theory in GR in the following section.

## 2.2 Perturbation Theory in General Relativity

To deal with small departures or small deformations of the spacetime geometry of a symmetrical background spacetime, we must use perturbation methods in our general relativistic field equations (2.1). This defines what we call *General Relativistic Perturbation Theory*, and it is posed in the following way: assuming that we possess the metric tensor of a previous background spacetime geometry  $g_{\mu\nu}^0$ , we can describe the evolution of small deformations on this background geometry by adding a metric perturbation  $h_{\mu\nu}$  up to the desired order of perturbation. The final perturbed metric  $g_{\mu\nu}$  will be given as

$$g_{\mu\nu} = g_{\mu\nu}^0 + \epsilon h_{\mu\nu}^{(1)} + \epsilon^2 h_{\mu\nu}^{(2)} + \epsilon^3 h_{\mu\nu}^{(3)} + \mathcal{O}(\epsilon^4). \quad (2.16)$$

That perturbed metric must, once again, satisfy Einstein's field equations (2.1) until the desired order of perturbation. We can make this dynamical description as realistic as we want by increasing the perturbation order considered. That comes at the cost of making the problem formally harder to deal with. By considering second-order perturbation theory, for example, some interesting effects such as backreaction arise, but again, we are already in a non-linear regime with coupled partial differential equations.

The first-order perturbation regime is defined by fixing

$$g_{\mu\nu} = g_{\mu\nu}^0 + \epsilon h_{\mu\nu}^{(1)} + \mathcal{O}(\epsilon^2), \quad (2.17)$$

where from now on, we define  $h_{\mu\nu} = \epsilon h_{\mu\nu}^{(1)}$  for simplifying the notation.

Although some important features are missing in the first-order regime (we also call linear regime), some of the dynamical systems' most important physical properties are already attained. For some scenarios of extreme mass-ratio inspirals, the entire time evolution of such

systems can be described in terms of a first-order perturbation regime [133]. For some other systems, however, although the whole evolution cannot be attained by a linear perturbation scheme, some specific regimes can be well approached by this first-order approximation of the problem. For instance, we can cite small ratio black hole binary mergers, whose GW signals are detected by LIGO-Virgo interferometers[19, 20, 21, 22, 23, 24, 25]. Although the merger stage of the binary coalescence cannot be described in a perturbation theory, this theoretical approach can provide a good description of the late-stage ringdown signal, which is emitted by a final single perturbed black hole slowly relaxing into a final equilibrium state. In Fig. 2.1 we illustrate the relation between the gravitational waveform detected by a distant observer in the time domain, and the corresponding stages of the coalescing black hole binary, which is the irradiating source. In Fig. 2.2, we show the associated GW waveform generated by the binary merger represented in Fig. 2.1. We detach the gravitational wave signal emitted during each stage of the binary coalescence.

The initial phase, called the insparalling stage, is well described by Post-Newtonian approximation. The second stage is where the binary merger occurs, and the two initial black holes are mixed into a final highly perturbed black hole. This second stage can only be properly studied in terms of a full numerical relativistic approach. Lastly, in the third and final stage, the resulting deformed black hole slowly relaxes into a final equilibrium state of a stationary Kerr black hole. This relaxation process is carried out by the irradiation of gravitational waves towards spatial infinity and through the horizon of this ringing black hole. Note that this physical source can be dominantly regarded as a single perturbed black hole spacetime in this last stage. Accordingly, the perturbation scheme of Eq. (2.17) for this spacetime metric can be employed to describe the irradiated gravitational waves. Lastly, the final stage of the binary merger is a final single black hole's equilibrium state, well described by Kerr's metric. The final black hole has a total mass slightly smaller than the sum of the two initial black holes' masses. This difference is due to the energy irradiated through gravitational waves.

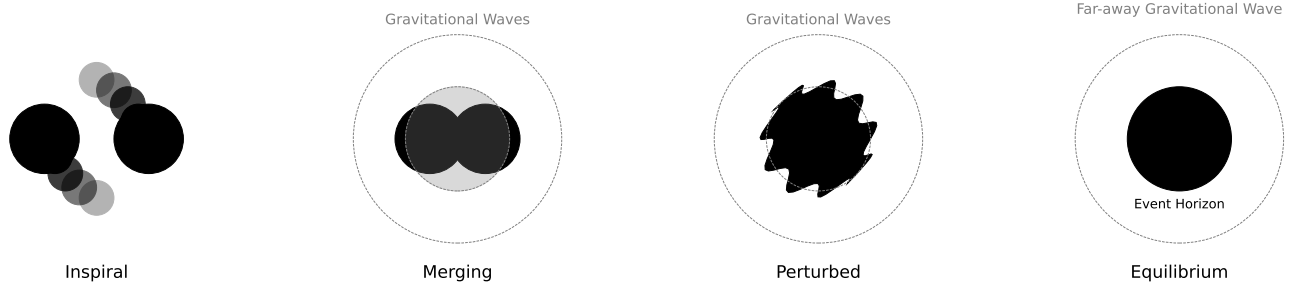


Figure 2.1: The Infographic a BH binary merger. The four stages of a black hole binary coalescence: the inspiralling initial phase, the merger, the late-ringdown phase, and the final single black hole in an equilibrium state (a Kerr black hole).

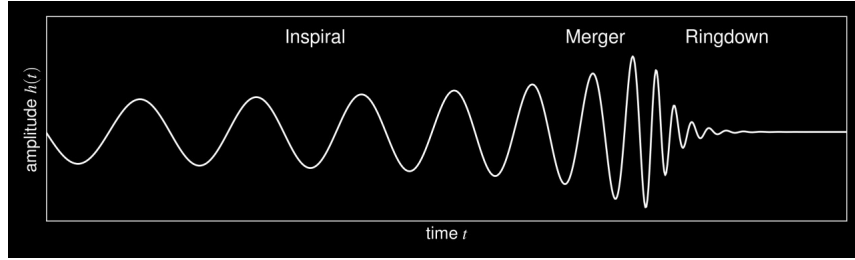


Figure 2.2: Associated GW waveform generated by the coalescence of the black hole binary pictured in Fig. 2.1. This waveform has the same three distinct phases, which are related to their respective coalescence stages. The three phases are the inspiral stage, the merger, and the ringdown phase. This waveform was generated by employing the effective-one-body waveform model and the publicly available *SEOBNRv5* code [134].

Image credit: **Sebastian Völkel**.

In the following sections, we will formally introduce the linear perturbation theory in General Relativity and discuss its mathematical details and intricacies.

## 2.3 Linearized Einstein Field Equations

To obtain the first-order perturbation regime for Einstein's field equations, we must linearize those equations. For this goal, we must first perturb the considered background metric  $g_{\mu\nu}^0$ .

$$g_{\mu\nu} = g_{\mu\nu}^0 + h_{\mu\nu}. \quad (2.18)$$

Then, we assume that the linearized version of the resulting Einstein's field equations is

also satisfied by the perturbed metric above. This leads us to the following equations for the evolution of the geometric perturbations  $h_{\mu\nu}$  in the background spacetime metric  $g_{\mu\nu}^0$ .

$$\square h_{\mu\nu} + 2R^0_{\lambda\mu\nu\sigma}h^{\lambda\sigma} - R^{0\lambda}_{\mu}h_{\lambda\nu} - R^{0\lambda}_{\nu}h_{\lambda\mu} = -16\pi T_{\mu\nu}, \quad (2.19)$$

where  $h$  is the trace of the perturbation on the spacetime of the background metric  $h = h^{\mu\nu}g_{\mu\nu}^0$ ,  $\square = \nabla_{\mu}\nabla^{\mu}$  is the contravariant version of the D'Alembertian operator defined from the background metric, and  $R^0$  is background spacetime curvature.

Those are the so-called linearized Einstein field equations. These equations describe how small perturbations in the metric propagate in the background spacetime, with  $T_{\mu\nu} = T_{\mu\nu}^0 + T_{\mu\nu}^{\text{pert.}}$ , and  $T_{\mu\nu}^{\text{pert.}}$  being the source of these perturbations.

Investigating those equations for different background metrics  $g_{\mu\nu}^0$  are the main goals for this chapter. Discussing their solutions, on the other hand, is left for Chapter 4.

### 2.3.1 Perturbed Minkowski Spacetime: The Gravitational Waves Solution

Firstly, let's consider a linear perturbation over the background of Minkowski flat spacetime, defined by the background metric in

$$\eta_{\mu\nu} = \text{diag}(1, -1, -1, -1). \quad (2.20)$$

The linearized perturbed Einstein's field equations (2.19), describing the evolution of geometric perturbations  $h_{\mu\nu}$  in this flat background spacetime yields

$$-\frac{1}{2}\square h_{\mu\nu} + \frac{1}{2}\eta_{\mu\nu}\square h - \frac{1}{2}\eta^{\alpha\beta}(\partial_{\mu}\partial_{\nu}h_{\alpha\beta} + \partial_{\alpha}\partial_{\beta}h_{\mu\nu} - \partial_{\mu}\partial_{\beta}h_{\nu\alpha} - \partial_{\nu}\partial_{\alpha}h_{\mu\beta}) = -16\pi T_{\mu\nu}, \quad (2.21)$$

and in the vacuum,

$$-\frac{1}{2}\square h_{\mu\nu} + \frac{1}{2}\eta_{\mu\nu}\square h - \frac{1}{2}\eta^{\alpha\beta}(\partial_\mu\partial_\nu h_{\alpha\beta} + \partial_\alpha\partial_\beta h_{\mu\nu} - \partial_\mu\partial_\beta h_{\nu\alpha} - \partial_\nu\partial_\alpha h_{\mu\beta}) = 0, \quad (2.22)$$

We have 10 coupled equations for our metric perturbations. The gauge freedom allows us to fix a gauge choice. So consider the following gauge transformation

$$\bar{h}_{\mu\nu} = h_{\mu\nu} - \frac{1}{2}\eta_{\mu\nu}h, \quad (2.23)$$

We choose the harmonic (Lorentz) gauge by specifying the following condition

$$\partial_\nu \bar{h}_\mu^\nu = 0, \quad (2.24)$$

The linearized Einstein's field equations for the metric perturbations yields

$$\square \bar{h}_{\mu\nu} = 0, \quad (2.25)$$

By taking the trace of this equation, we obtain  $\square h = 0$ , and finally, from Eqs. (2.23) (2.24), we also obtain

$$\square h_{\mu\nu} = 0. \quad (2.26)$$

That is a wave equation, indicating that linear perturbations evolve dynamically in this background spacetime in terms of propagating waves. Those waves travel with velocity  $c$  (equivalent to the electromagnetic case). In other words, in a vacuum flat spacetime, such as in an empty region of the deep hyperspace, small metric perturbations evolve in terms of propagating waves of gravity transmitting the spacetime perturbations through the background flat spacetime at light speed. Therefore, *there exists gravitational waves!*

This was how Einstein predicted in 1916 [105] the existence of those ripples in the fabric of spacetime. The actual observation of their existence only happened in 2016 [19] as we

already mentioned in the first chapter of this thesis.

## 2.4 Linear Perturbation Theory for Schwarzschild Black Hole Spacetimes

Extending the previous treatment from a flat background spacetime to a curved background spacetime, such as the external neighborhood of the Schwarzschild black hole, we get

$$g_{\mu\nu} = g_{\mu\nu\text{Schw.}}^0 + h_{\mu\nu} \quad (2.27)$$

where  $g_{\mu\nu\text{Schw.}}^0$  is the background Schwarzschild metric, given by Eq. (2.15), and  $h_{\mu\nu}$  is a first-order perturbation. If we input this perturbed metric into Einstein's field equations and then linearize the obtained result, we obtain the linearized Einstein's field equation for the background spacetime of Schwarzschild.

In the following, we reproduce the formal development proposed by Regge and Wheeler , in Ref. [135], Zerilli in Ref. [136] and Mathews in Ref. [137]. Namely, we apply a multi-polar angular decomposition in tensorial harmonics  $Y_l^m(\theta, \phi)$ . After some algebra, which we refer to Regge and Wheeler's seminal paper [135], we obtain for a given  $m, l$ , the following matrix form for the metric perturbations  $h_{\mu\nu}$  and parity  $(-1)^{l+1}$ , also called odd-parity

$$h_{\mu\nu} = \begin{bmatrix} 0 & 0 & -h_0(t, r)(\partial/\sin\theta\partial\phi)Y_l^m & h_0(t, r)(\sin\theta\partial/\partial\theta)Y_l^m \\ 0 & 0 & -h_1(t, r)(\partial/\sin\theta\partial\phi)Y_l^m & h_1(t, r)(\sin\theta\partial/\partial\theta)Y_l^m \\ \text{sym} & \text{sym} & h_2(t, r)(\partial^2/\sin\theta\partial\theta\partial\phi - \cos\theta\partial/(\sin\theta)^2\partial\phi)Y_l^m & \text{sym} \\ \text{sym} & \text{sym} & (1/2)h_2(t, r)(\partial^2/\sin\theta\partial\phi^2 + \cos\theta\partial/\partial\theta - \sin\theta\partial^2/\partial\theta^2)Y_l^m & -h_2(t, r)\sin\theta(\partial^2/\partial\phi^2 \\ & & & -\cotg\theta\partial/\partial\phi)Y_l^m \end{bmatrix}. \quad (2.28)$$

For even parity perturbations, on the other hand, we are led to

$$h_{\mu\nu} = \begin{bmatrix} H_0(t, r)(1 - \frac{2M}{r})Y_l^m & H_1(t, r)Y_l^m & h_0(t, r)(\partial/\partial\theta)Y_l^m & h_0(t, r)(\partial/\partial\phi)Y_l^m \\ H_1(t, r)Y_l^m & H_2(t, r)(1 - \frac{2M}{r})^{-1}Y_l^m & h_1(t, r)(\partial/\partial\theta)Y_l^m & h_1(t, r)(\partial/\partial\phi)Y_l^m \\ \text{sym} & \text{sym} & r^2(K(t, r) \\ & & +G(t, r)\partial^2/\partial\theta^2)Y_l^m & \text{sym} \\ \text{sym} & \text{sym} & r^2G(t, r)(\partial^2/\partial\theta\partial\phi) & r^2[K(t, r)\sin^2(\theta) \\ & & -\cos\theta\partial/\sin\theta\partial\phi)Y_l^m & +G(t, r)(\partial^2/\partial\phi\partial\phi \\ & & & +\sin\theta\cos\theta\partial/\partial\theta)]Y_l^m \end{bmatrix}. \quad (2.29)$$

Once again, replacing this decomposition into Einstein's linearized equations, we obtain ten coupled differential equations that fully describe the perturbations, three equations for odd perturbations, and seven for even perturbations. We can reduce it further to seven equations by making use of the Gauge freedom. Indeed, the metrics above are symmetrical under gauge transformations. This freedom allows one to choose a certain gauge. It is more appropriate to fix the same gauge choice Regge-Wheeler established. In the Regge-Wheeler gauge, the canonical forms for the odd type of metric perturbations are finally

$$h_{\mu\nu} = \begin{bmatrix} 0 & 0 & 0 & h_0(t, r) \\ 0 & 0 & 0 & h_1(t, r) \\ 0 & 0 & 0 & 0 \\ h_0(t, r) & h_1(t, r) & 0 & h_0(t, r) \end{bmatrix} \left( \sin\theta \frac{\partial}{\partial\theta} \right) P_l(\cos\theta). \quad (2.30)$$

Likewise, the canonical forms for even parity perturbations are

$$h_{\mu\nu} = \begin{bmatrix} H_0(t, r)(1 - \frac{2M}{r}) & H_1(t, r) & 0 & 0 \\ H_1(t, r) & H_2(t, r)(1 - \frac{2M}{r})^{-1} & 0 & 0 \\ 0 & 0 & r^2 K(t, r) & 0 \\ 0 & 0 & 0 & r^2 K(t, r) \sin^2(\theta) \end{bmatrix} P_l(\cos \theta). \quad (2.31)$$

However, it is possible to circumvent the obtained coupled equations and combine them further into two independent second-order differential equations, one equation for each parity. For odd-parity, for example, Regge and Wheeler obtained that the radial equation describing the time evolution of the metric perturbation is written as

$$\frac{\partial^2}{\partial r_*^2} h_0(r, t) - \frac{\partial^2}{\partial t^2} h_0(r, t) - V_{\text{RG}_l}(r) h_0(r, t) = S_l(r, t), \quad (2.32)$$

where the effective scattering potential coupled to this wave equation is given by

$$V_{\text{RG}_l}(r) = \left(1 - \frac{2M}{r}\right) \left[ \frac{l(l+1)}{r^2} + \frac{6M}{r^3} \right]. \quad (2.33)$$

Following Zerilli's framework [136], we define for even parity perturbations, the wave function  $Z$ , implicitly defined in terms of  $H_0$ ,  $H_1$ , and  $K$ . Those functions describe the radial part of the evolution of even perturbations. After some algebra [136, 138], the linearized Einstein's equations yield for even parity perturbations, a radial equation describing the time evolution of metric perturbations identical to Eq. (2.32),

$$\frac{\partial^2}{\partial r_*^2} Z(r, t) - \frac{\partial^2}{\partial t^2} Z(r, t) - V_{\text{Z}_l}(r) Z(r, t) = S_l(r, t), \quad (2.34)$$

where this time the effective scattering potential coupling to this wave equation is defined as



$$V_{Z_l}(r) = \frac{2(r^2 - 2Mr)}{r^5(\Lambda r + 3M)^2} [\Lambda^2(\Lambda + 1)r^3 + 3M\Lambda^2r^2 + 9M^2\Lambda r + 9M^3]. \quad (2.35)$$

Here,  $l$  is the index of the multipolar expansion,  $\Lambda = (1/2)(l - 1)(l + 2)$  and the  $r_*$  coordinate in both equations is the tortoise coordinate of Schwarzschild spacetime, defined by the following transformation from the radial coordinate

$$r_* = r + 2M \log \left[ \frac{r}{2M} - 1 \right]. \quad (2.36)$$

The non-homogeneous terms  $S_l(r, t)$  in Eqs. (2.34) describe the perturbation sources, and they are derived from the energy-momentum tensor of the external perturbation, i.e., the rhs. of Einstein's linearized equations in Eq. (2.19), we refer the reader to Refs. [135, 136, 139] for their full form. For illustrations of this source term, we refer the reader to the application's section 4.3.2.1, where we consider the source term for the radial infall of a test particle into a Schwarzschild black hole [139, 140].

From Eqs. (2.32),(2.34), we notice that, while the angular profile of the perturbations is given by tensorial harmonics, the radial part, for both odd and even parities, describes a wave-like behavior for the propagation of the perturbations. This wave behavior is governed by those wave equations. Solving those equations determines how the external perturbations  $h$ , forced by the source term  $S(t, r)$ , dynamically evolve in this background Schwarzschild spacetime. The effect of this background spacetime is imprinted in the effective potentials  $V(r)$  coupled to the wave equations. The detailed solutions of those equations are presented in Chapter 4.

Furthermore, as originally obtained in the seminal papers from Zerilli [136] and Regge-Wheeler [135], those equations can also be formulated in the frequency domain if we apply the usual spectral decomposition from Fourier analysis. Indeed, if we write the time-domain signal in terms of its corresponding amplitude  $\tilde{\phi}(r, \omega)$  in the frequency domain

$$\phi(r, t) = \frac{1}{\sqrt{2\pi}} \int_{-\infty}^{+\infty} \tilde{\phi}(r, \omega) e^{i\omega t} dt, \quad (2.37)$$

we obtain the following time-independent master wave equations for the radial part of the perturbations

$$\frac{d^2 \tilde{\phi}(r, \omega)}{dr_*^2} + (\omega^2 - V_l(r)) \tilde{\phi}(r, \omega) = \tilde{S}(r, \omega), \quad (2.38)$$

where the source term  $\tilde{S}_l(r, \omega)$  in the frequency domain is the Fourier transformation of the time-dependent one  $S(t, x)$ , and  $V_l(r)$  is again the effective scattering potential. This general form in Eq. (2.38) for the wave equation contemplates both Eqs.(2.34) and (2.32).

Notice that these equations have a Schrödinger-like form. This similarity is a fundamental fact for the upcoming analysis to be carried out in the following chapters, since it provides us with the possibility of applying semi-analytical techniques for the study of perturbations in BH spacetimes [141, 142]. These semi-analytic techniques are imported from Schrödinger wave quantum mechanics and give us the theoretical background for our semi-analytical inverse method to be developed in this thesis. For the proper application of quantum mechanics' semi-analytical techniques here, all we need to do is to associate  $\omega^2$  with the eigenenergy  $E$  in the Schrödinger equation, and replace the quantum potential  $V(r)$  by the effective scattering potentials derived here. Namely, the Zirelli's potential, in Eq. (2.35), for even-parity perturbations, and the Regge-Wheeler's effective potential, in Eq. (2.33), for odd-parity perturbations. Those coupled effective potentials govern the propagation and scattering properties of gravitational perturbations in the background spacetime of the Schwarzschild black hole. They are plotted in Fig. 2.3 for cases.

The asymptotic decaying profile of the perturbation potentials in the wave-equations (2.34),(2.38) reveals the important fact that in a Schwarzschild background spacetime, perturbations evolve as propagating waves that are both irradiating to infinite and falling through the event horizon of the black holes. Furthermore, if we look at the position of

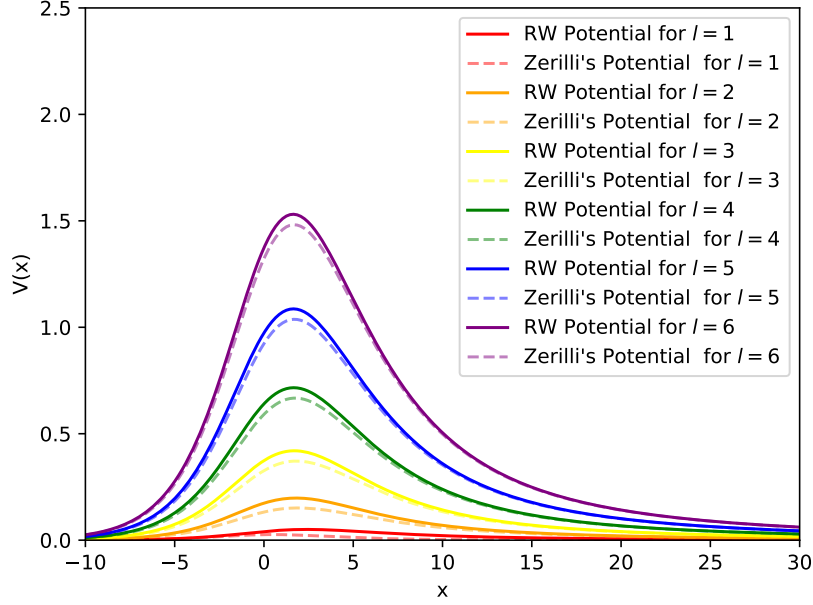


Figure 2.3: Effective scattering potentials for both Regge-Wheeler and Zerilli potentials. We show those potentials here for different multi-polar parameters  $l$ . Notice the asymptotic decaying behavior of all those potentials. Furthermore, for higher multipolar numbers  $l$ , the potentials' maximums slowly converge to  $x = 0$ , the photosphere radius in tortoise coordinate  $x$ .

this potential barrier's peak, we see that the potential barrier's center is converging to a specific fixed location, which is approximately  $r = 3M$  for the radial coordinate. That is the radius of a spatial surface called the *photosphere*. Hence, we can say that the scattering of the perturbations in the Schwarzschild spacetime occurs mainly at the photosphere surface. The contribution of the black hole's photosphere to its scattering properties is the dominant one over the entire surrounding space-time. This fact plays a major role in the phenomenology of exotic compact horizonless objects and black holes. Exotic ultra-compact horizonless objects are so compact that their delimiting surface is contained inside the photosphere but outside the 'would-be' event horizon. Accordingly, they are expected to have the same scattering properties as black holes. Equivalently, in terms of the scattering of gravitational waves or any other test-field perturbations, black holes are, in principle, indistinguishable from any other exotic ultra-compact horizonless objects. That motivated physicists to propose ECOs

as black hole mimickers in recent works [143]. In Chapter 4, however, we show how we can distinguish black holes from their associated ECO mimickers by means of their scattering properties and by studying their gravitational waveform ringdown signals.

### 2.4.1 Test Field Perturbation on Schwarzschild Black Hole Spacetimes

If instead of considering gravitational perturbations in a background Schwarzschild spacetime, one is willing to consider any other test field perturbations on this background spacetime, the minimal coupling of this field with the Schwarzschild metric must be considered. Formally, this is equivalent to transforming the usual partial derivatives into covariant derivatives into their field equations.

$$\partial_\mu \rightarrow \nabla_\mu. \quad (2.39)$$

For Electromagnetic perturbations, for instance, we have the Maxwell equations as follows

$$\nabla_\mu F^{\mu\nu} = -4\pi J^\nu, \quad (2.40)$$

$$\nabla_\mu \tilde{F}^{\mu\nu} = 0, \quad (2.41)$$

where

$$F_{\mu\nu} = \nabla_\mu A_\nu - \nabla_\nu A_\mu \quad (2.42)$$

is Maxwell's electromagnetic tensor in a curved spacetime.

Also, for Dirac field perturbations in a Schwarzschild background spacetime, the Dirac equation becomes

$$(i\gamma^\mu D_\mu - m)\psi = 0, \quad (2.43)$$

where  $\gamma_\mu$  is the tensorial form of Dirac matrices,  $m$  is the fermionic particle mass, and  $D_\mu$  is the covariant derivative acting on a Dirac field defined in a curved background spacetime. The last one is given by

$$D_\mu = \partial_\mu + \Gamma_\mu. \quad (2.44)$$

Where  $\Gamma_\mu$  includes the contribution from the connection coefficients  $\Gamma_{\mu\nu}^\lambda$  representing the curvature of the background spacetime.

Finally, for scalar field perturbations in a Schwarzschild background spacetime, we have that the Klein-Gordon equation is written as

$$\frac{1}{\sqrt{-g}}\partial_\mu(\sqrt{-g}g^{\mu\nu}\partial_\nu\phi) - m^2\phi = 0, \quad (2.45)$$

where  $m$  is the scalar mass and  $g$  is the metric tensor's determinant.

Generally, when we consider the application of those test field equations in background black hole spacetimes, the resulting radial part of those perturbation equations yields similar wave equations to Eqs. (2.34) [144, 145, 146, 147]. The only difference among them is the effective coupling potential governing the scattering of those field perturbations. For instance, in the background spacetime of Schwarzschild's black hole, the perturbation equations for those test fields are identical to Eq. (2.38), but with the effective potential replaced by

$$V_l(r) = \left(1 - \frac{2M}{r}\right) \left[ \frac{l(l+1)}{r^2} - \frac{2M(1-s^2)}{r^3} \right]. \quad (2.46)$$

where  $s$  is the spin of the considered field. For massless scalar test field perturbations,  $s = 0$ , and for electromagnetic field perturbations  $s = 1$ . Furthermore, if we set  $s = 2$  (graviton

field), we also recover the effective potential for gravitational field perturbations of odd-parity. For 1/2-spin perturbations,  $s = 1/2$ , but the potential in Eq. (2.46) must be replaced by

$$V_{\kappa}(r) = \left(1 - \frac{2M}{r}\right) \left[ m^2 \left(1 - \frac{2M}{r}\right) + \frac{\kappa \left(\kappa - \sqrt{1 - \frac{2M}{r}}\right)}{r^2} \right], \quad (2.47)$$

where  $m$  is the fermion mass, and  $\kappa$  is the sum of angular momentum, namely  $\kappa = \pm(l+1/2)$ .

The discussions carried out in chapter 4 for the wave equation solution describing the evolution of gravitational perturbations in the Schwarzschild spacetime can equivalently contemplate the test field perturbations presented here.

#### 2.4.1.1 The Dirac field in a quantum corrected black hole

This subsection is based on the following publication: **Massless Dirac perturbations in a consistent model of loop quantum gravity black hole: quasinormal modes and particle emission rates.**

Authors: Saulo Albuquerque, Iarley P. Lobo, Valdir B. Bezerra

DOI: 10.1088/1361-6382/ace7a8 (publication)

Published in: Class.Quant.Grav. 40 (2023) 174001

In Ref. [1], the Dirac equation was investigated for massless spinor perturbations in the static and spherically symmetric spacetime of a quantum-corrected Schwarzschild black hole [148]. This quantum correction consisted of an effective polymerized quantization of Schwarzschild black hole motivated by Loop Quantum Gravity theory [149, 150, 151, 152, 153]. Its main advantage is addressing the singularity problem inside the black hole's event horizon by replacing the regular singularity at  $r = 0$  with a regular bouncing space-like surface. This bouncing spacelike transition surface topologically connects the white hole and the black hole spacetimes. The final effective quantum corrected metric as derived in

Refs.[148, 154] is written as

$$ds^2 = \frac{-4a(b)A^2B^{2/3}}{\lambda_2^2}d\tau^2 + \frac{\lambda_2^2}{4a(b)}\left(1 + \frac{1}{X(b)^2}\right)^2\left(\frac{dX}{db}\right)^2db^2 + b^2d\Omega_2^2, \quad (2.48)$$

where  $b$  is the radial coordinate,  $d\Omega_2$  is the line element of the two-dimensional unit sphere  $\mathbb{S}^2$ , and  $\lambda_{1,2}$  are quantum gravity parameters of the polymerization, such that when they go to zero, the solution reduces to the Schwarzschild spacetime. The functions of the metric are

$$a(b) \doteq a(X(b)) = \lambda_2^2 \left(\frac{X^2 + 1}{2X}\right)^2 \left(1 - \frac{3CD}{2\lambda_2} \frac{2X}{X^2 + 1}\right) \frac{1}{b^2}, \quad (2.49)$$

where

$$X(b)^3 = \frac{b^3}{2A^3B} \pm \frac{1}{2}\sqrt{\frac{b^6}{(A^3B)^2} - \frac{4}{B}}, \quad (2.50)$$

for the following integration constants

$$AB^{1/3} = \left[ \frac{\lambda_1\lambda_2 M_{BH}}{2} \left(\frac{M_{BH}}{M_{WH}}\right)^{3/2} \right]^{1/4}, \quad (2.51)$$

$$B = \left(\frac{M_{BH}}{M_{WH}}\right)^3, \quad (2.52)$$

$$CD = \frac{2}{\lambda_1} \left[ \frac{2}{3} \left(\frac{\lambda_1\lambda_2}{3}\right)^3 M_{BH}^3 \left(\frac{M_{WH}}{M_{BH}}\right)^{3/2} \right]^{1/4}. \quad (2.53)$$

This metric also presents two Dirac observables, i.e., constant on-shell quantities, identified as  $M_{BH}$  and  $M_{WH}$ . They are the masses of the associated black hole and white hole, respectively.

We showed that the resulting Dirac equation for massless spinor perturbations in this background spacetime can decouple in the 2-spinor formalism of Chandrasekhar [147]. The angular part yields

$$\left( \frac{1}{\sin \theta} \partial_\theta (\sin \theta \partial_\theta) + (\csc \theta)^2 \partial_\phi^2 + \frac{i \cot \theta}{\sin \theta} \partial_\phi + \frac{1}{2} - \frac{1}{4} (\cot \theta)^2 + \lambda_l \right) S_{l,m}(\theta, \phi) = 0, \quad (2.54)$$

where  $\lambda_l$  is the decoupling constant.

Meanwhile, the radial part of the massless spin 1/2 field equation becomes

$$\frac{\partial}{\partial b_*^2} \psi(b) + [\omega^2 - V_\pm(b(b^*))] \psi(b) = 0, \quad (2.55)$$

where  $\partial/\partial b_*$  denotes the derivative with respect to the tortoise coordinate  $b^*$  in this effective modified spacetime.

Finally, in this framework, we have demonstrated that the radial part of the Dirac equation for massless spinor perturbations in the background spacetime of the BMM loop quantum corrected black hole also leads to a Schrödinger-like wave equation, equivalent to Eq. (2.38). This time, however, the effective potential governing the scattering of perturbation is written as

$$V_\pm(b) = \frac{4}{\lambda_2^2} \left[ \frac{\lambda_1 \lambda_2 M_{BH}}{2} \left( \frac{M_{BH}}{M_{WH}} \right)^{\frac{3}{2}} \right]^{\frac{1}{2}} \quad (2.56)$$

$$\times \left[ (l(l+1) + 1/4) \frac{a(b)}{b^2} \pm \sqrt{l(l+1) + 1/4} \left( \frac{2}{\lambda_2} \right) \frac{a(b)}{\left( 1 + \frac{1}{X^2(b)} \right) \frac{dX}{db}} \left( \frac{\sqrt{a(b)}}{b} \right)' \right]. \quad (2.57)$$

In Fig. 2.4 we compare this effective potential with Schwarzschild's for different values of the quantum correction parameter  $\lambda$ . Notice that it converges to Schwarzschild's potential when we consider  $\lambda \rightarrow 0$



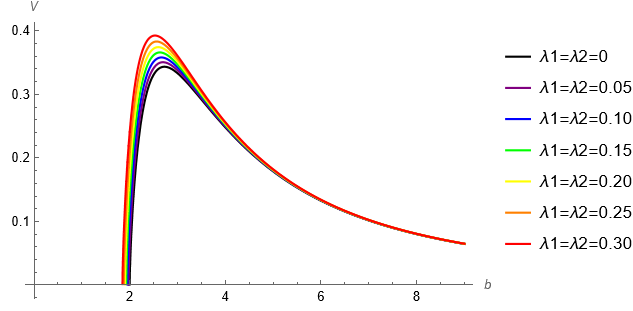


Figure 2.4: Effective potential for massless Dirac perturbations around the quantum corrected BMM black hole for different values of the quantum correction parameter  $\lambda = \lambda_1 = \lambda_2$ . The effective potential for massless Dirac perturbations in the Schwarzschild background spacetime is also shown in black for comparison. Notice that they converge when  $\lambda \rightarrow 0$ .

### 2.4.2 Exotic Compact Objects: Black Hole Mimickers

In recent years, the study of exotic compact objects has received much attention. As we have already discussed, investigating these astrophysical alternatives to black holes provides us with a prompt template for phenomenologically probing the existence and nature of black holes' event horizon surface.

There are many different proposals for horizonless alternatives to black holes in literature. Among them, we can cite gravastars [155], boson stars [156], wormholes [157], fuzz balls [158], and even quantum black holes [159, 160]. For many of those ECO models, their physical predictions, such as the ringdown waveforms, are expected to be very similar to the black hole's, at least in principle. Recent works, however, have demonstrated the existence of a smoking-gun phenomenon for differentiating those horizonless astrophysical objects from the black holes, that is, the so-called *echoes* in gravitational wave data, e.g., Ref. [74]. In order to have a better understanding of those echoes and how they help us distinguish the ECO's ringdown waveform from BH's, we must first define our exotic horizonless compact object model here, and how we describe them.

In this thesis framework, we model our exotic horizonless compact object by proposing a parameterized reflecting boundary condition into a BH spacetime. This reflecting boundary condition is defined at the objects' surface radius  $r_0$ , defined as  $r_0 = r_h(1 + \epsilon)$ , where  $0 \lesssim \epsilon$ .

Indeed, when the ECO is very compact, such that this surface radius  $r_0$  satisfies

$$\frac{r_0}{2M} - 1 \ll 1, \quad (2.58)$$

we can model our ECO by replacing the BH boundary condition at the horizon with a reflecting boundary condition at the ECO surface  $x_0 = r_*(r_0)$ . Namely, near the ECO's radius, the potential is  $V \approx 0$ , and the perturbation field  $\psi$  in the frequency domain is a linear combination of the incoming wave  $e^{-i\tilde{\omega}x}$  and the reflected wave  $Re^{i\tilde{\omega}x}$ . Therefore, near the ECO surface  $x_0$ , we must now have

$$\tilde{\psi} \propto e^{-i\tilde{\omega}(x-x_0)} + Ke^{-2i\tilde{\omega}x_0}e^{i\tilde{\omega}(x-x_0)}, \quad (2.59)$$

for some frequency-dependent reflectivity  $K$ .

That model leads us to a simple template for the ECO's description, where we can study wave propagation and emission using a Schwarzschild BH equipped with a different reflecting boundary. In Fig. 2.5, we graphically illustrate the potential and reflective boundary condition that conceptually represents this kinematic ECO model.

In Chapter 4, we study this ECO model and explicitly relate their ringdown waveforms with the black holes' waveforms. By determining their relationship in terms of the Green function's formalism, we find that the ECO waveform can be constructed by summing the BH's original waveform and a reprocessed version of the BH's waveform observed at its 'would-be' horizon [59]. We also show how this extra piece of the ECO waveform can be expressed as a sum of echoes in the time domain or as a superposition of the ECO's resonant modes in the frequency domain.

### 2.4.3 Slowly Rotating Perturbed Black Holes

In General Relativity theory, the extension of Schwarzschild's black hole solution to an axial symmetric rotating black hole was only obtained in 1963 by Roy Kerr [83]. This metric

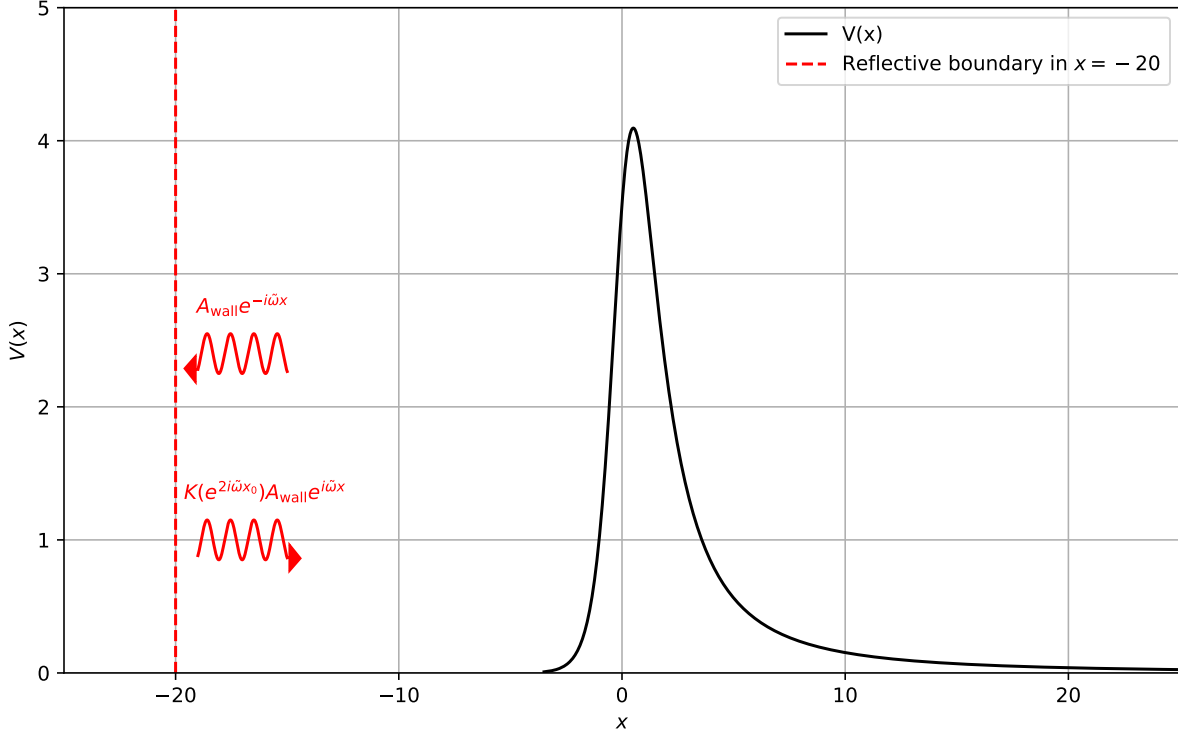


Figure 2.5: Effective scattering potential for a typical ECO and its reflective boundary condition at a certain  $x_0$  in tortoise coordinate. Notice that due to this reflective boundary condition, a certain portion of the incoming wave is now reflected at the ECO's core. For the black hole case, this reflectivity is null by definition.

describes what is called Kerr spacetime, and it is given by the following line element in Boyer-Lindquist coordinates

$$ds^2 = - \left( 1 - \frac{2Mr}{\rho^2} \right) dt^2 - \frac{4Mar \sin^2(\theta)}{\rho^2} dt d\phi \quad (2.60)$$

$$+ \frac{\rho^2}{\Delta} dr^2 + \rho^2 d\theta^2 \quad (2.61)$$

$$+ \frac{\sin^2(\theta)}{\rho^2} ((r^2 + a^2)^2 - \Delta a^2 \sin^2(\theta)) d\phi^2 \quad (2.62)$$

where

$$\rho^2 = r^2 + a^2 \cos^2(\theta), \quad (2.63)$$

$$\Delta = r^2 - 2Mr + a^2. \quad (2.64)$$

That line element describes the spacetime at the external neighborhood of a massive rotating black hole, where its mass is given by  $M$  and its angular momentum per mass unity is  $a$ . The radius that defines the outer boundary of the event horizon is given by

$$r_+ = M + \sqrt{M^2 + a^2}, \quad (2.65)$$

The shape of this event horizon is not a perfect sphere. Instead, it is an oblate spheroid due to the black hole's rotation.

Among the plethora of new physical features that Kerr spacetime description has revealed, some of the most interesting are the frame-dragging effect (or Lense-Thirring effect) [161], the Penrose process [162], and the superradiant scattering of perturbation fields [112, 113]. Those phenomena are not reported in Schwarzschild's static black hole and are a physical consequence of the spacetime 'twisting' caused by Kerr's black hole rotation.

The evolution of gravitational perturbations at the background spacetime of Kerr's metric leads to a much more complex scenario, even in linear order perturbation theory. The description of those perturbations around a rotating black hole in the context of linearized gravity typically involves the Teukolsky equation [144]. This equation governs the behavior of gravitational perturbations on Kerr's background spacetime in the frequency domain, describing specifically the perturbations to the Weyl scalar  $\Psi_4$ . The separated angular part of this equation is given by

$$\left[ \frac{1}{\sin \theta} \frac{\partial}{\partial \theta} \left( \sin \theta \frac{\partial S_{lm}}{\partial \theta} \right) + a^2 \omega^2 \cos^2 \theta - \frac{m^2}{\sin^2 \theta} - s^2 \cot^2 \theta - \frac{2ms \cos \theta}{\sin^2 \theta} - 2ams\omega \cos \theta + s + A \right] S_{lm_s}(\theta) = 0 \quad (2.66)$$

Likewise, the radial profile of gravitational perturbations around a Kerr black hole is described in the frequency domain by the following equation

$$\left[ \frac{1}{\Delta^{s+1}} \frac{d}{dr} \left( \Delta^s \frac{dR_{lm}}{dr} \right) + \frac{K^2 - 2is(r-M)K}{\Delta} + 4is\omega r - \lambda \right] R_{lm_s}(r) = 0 \quad (2.67)$$

where

$$\Delta = r^2 - 2Mr + a^2, \quad (2.68)$$

$$K = (r^2 + a^2)\omega - am, \quad (2.69)$$

$$\lambda = a^2\omega^2 - 2am\omega + A(a\omega), \quad (2.70)$$

$$m = \text{azimuthal eigenvalue}, \quad (2.71)$$

$$s = \text{spin-weight}. \quad (2.72)$$

$$A(a\omega) = \text{separation constant}, \quad (2.73)$$

$$\omega = \text{frequency}, \quad (2.74)$$

$$R_{lm}(r) = \text{radial function}, \quad (2.75)$$

$$S_{lm}(\theta) = \text{angular function}, \quad (2.76)$$

$$(2.77)$$

As we have done in the previous case of a static black hole, we can re-express the radial part of the Teukolsky equation into a wave equation in a Schrödinger-like form. After some algebra, we obtain

$$\frac{d^2 R}{dr_*^2} + F(r)R = 0, \quad (2.78)$$

where  $r_*$  is the tortoise coordinate for Kerr's spacetime. The effective potential  $F(r)$ , which depends on the properties of the Kerr black hole and the angular eigenvalue of the perturbation, is expressed as

$$F(r) = K^2 - 2i(r_* - M)K + \frac{\Delta(4ir\omega s - \lambda)}{(r^2 + a^2)^2} - G^2 - G_{,r_*}, \quad (2.79)$$

where

$$G(r) = \frac{s(r - M)}{(r^2 + a^2)} + r \frac{\Delta}{(r^2 + a^2)^2}. \quad (2.80)$$

Notice that this potential is complex-valued, which makes the usual analysis carried out throughout this thesis impossible. For the specific scenario in which we can assume that the BH's angular momentum is small compared to its mass, an easier approximative description is achieved [163]. Indeed, the spacetime around slowly rotating black holes can be described in terms of a first-order expansion of Kerr's metric in the angular momentum. In the weak field limit, this metric yields the following line element

$$ds^2 \approx - \left(1 - \frac{2M}{r}\right) dt^2 + \left(1 + \frac{2M}{r}\right) dr^2 + r^2 (d\theta^2 + \sin^2 \theta d\phi^2) - \frac{4a}{r} \sin^2 \theta d\phi dt. \quad (2.81)$$

For this case, the evolution of perturbations around this black hole in the slow rotation approximation can be obtained by expanding Teukolsky equation (2.67) and its effective potential Eq. (2.79) in terms of  $a$  and neglecting higher order terms. In the slow rotation approximation [164], the radial part of the Teukolsky equation describing gravitational perturbations to Weyl scalar yields for the axial sector

$$\frac{d^2 R}{dr_*^2} + [\omega^2 - V_{\text{eff}}(r)] R = 0, \quad (2.82)$$

where

$$V_{\text{eff}}(r) = V_0(r) + a^2 V_2(r), \quad (2.83)$$

and

$$V_0(r) = V_{\text{RG}}(r) = \left(1 - \frac{2m}{r}\right) \left[ \frac{l(l+1)}{r^2} + \frac{6M}{r^3} \right], \quad (2.84)$$

$$\begin{aligned} V_2(r) = & -\frac{M^2}{r^4} + M^2 \left(1 - \frac{2M}{r}\right) \left[ -\frac{24(7-6r)}{(\lambda+2)^3 r^6} - \frac{12(47-40r)}{(\lambda+2)^2 r^6} + \frac{2(6r^2-250r-315)}{(\lambda+2)r^6} + \frac{420(6-5r)}{(5+4\lambda)r^6} \right] \\ & - M^2 \left(1 - \frac{2M}{r}\right) \left[ -\frac{2(\lambda-10)}{(\lambda+2)(5+4\lambda)r^2} \omega^2 + 3 \frac{6r^2(4\lambda-19) - 26r(\lambda-13) - 231}{(\lambda+2)^2 r^{10} \omega^2} \right]. \end{aligned} \quad (2.85)$$

The effective potential is now written as an expansion, involving a zeroth order term  $V_0$  and a second order correction  $V_2$  depending explicitly on the black hole's spin parameter  $a$ . The effective zeroth order term corresponds to the effective potential in the Schwarzschild spacetime (in Eq. (2.33)), and the second order term represents the corrections due to the black hole's rotation. Equivalently, for slowly rotating black holes, gravitational perturbations are described by the Schwarzschild effective potential modified by a correction induced by the rotation contribution. Notice that this correction contributes with a frequency-dependent term. A general feature for astrophysical ultracompact objects is that the evolution of perturbations in a rotating background scenario induces energy or frequency dependence for the effective scattering potential. A similar picture is achieved for analog gravity systems, such as acoustic black holes, for example. We illustrate the last ones in the following chapter. The consequences of the energy dependence on a semi-analytical description of effective scattering potentials are discussed in Chapter 7.

# Chapter 3

## Analog Gravity Systems: The Sonic Black Hole

In this chapter, we describe the dynamics of an analog system to astrophysical black holes and exotic compact objects consisting of a classical fluid in a bathtub-draining vortex. Throughout our discussion, we highlight the similarities between the description of this simplified physical model and its astrophysical analog systems. These similarities motivate the study we carry out here. As we see in section 3.2 and on, our formalism is specifically chosen for pointing out the clear equivalence between the description of acoustic perturbations evolving around a draining vortex and the dynamics of a scalar field around an effective black hole in  $2 + 1$  dimensions. When this mathematical equivalence is clear, we explicitly derive the effective metric of this associated effective BH spacetime, which we call acoustic (or sonic) black hole. Next, we highlight some physical properties of the effective spacetime generated by this metric, such as its angular momentum and its acoustic horizon. Then, some remarkable experiments carried out with these analog models are reported. From the results of those experiments, we point out the observation of physical features that were expected to be intrinsically related to black holes and exotic compact objects.

Furthermore, we report what physically observed phenomena [79] motivated researchers to point out an equivalence between an imperfect draining vortex (IDV) and exotic compact horizonless objects (ECO). Finally, the description of those ECOs in terms of the analog



acoustic model with the IDV is introduced in section 4.3. For such a description, we employ a cinematically modified model, and discuss the preliminary physical conditions for its experimental realization. The mathematical equivalence between astrophysical ECOs and their analog model with an imperfect draining vortex is the main motivation for the investigation carried out throughout this thesis. In Chapter 4, a specific smoking gun effect, expected to arise from exotic compact objects, is suggested for our ECO's analog model. This feature is the so-called echoes in the gravitational wave signals. From Chapter 5 and on, the main subject of this thesis, the inverse method for the scattering of exotic compact objects, is introduced and applied to our ECO's analog model consisting of an imperfect draining vortex.

### 3.1 The Sonic Hole as an Analog to Astrophysical Black Holes

In 1980, Unruh pointed out for the first time the mathematical equivalence between the description of a bathtub-draining vortex (DBTV) and the dynamics of an effective black hole. This motivated the proposal of this simple classical system as an analog model to astrophysical black holes. This equivalence is drawn from the mathematical similarity between the wave equation describing acoustic perturbations around the draining vortex, and the Klein-Gordon equation governing the evolution of scalar field perturbations in an effective black hole spacetime. In order to demonstrate this equivalence, we need to derive these equations first. So, let us start by defining our analog table-top system.

Consider an inviscid and barotropic fluid flowing irrotationally on a draining vortex in a bathtub sink, as the one shown in Fig.1.5. The physical dynamics of this simple classical system are described, in first principles, by the hydrodynamical equations [165]

$$\frac{\partial \rho}{\partial t} + \nabla \cdot (\rho \mathbf{v}) = 0, \quad (3.1)$$

$$\rho \left[ \frac{\partial \mathbf{v}}{\partial t} + (\mathbf{v} \cdot \nabla) \mathbf{v} \right] = -\nabla p, \quad (3.2)$$

$$\nabla \times \mathbf{v} = 0, \quad (3.3)$$

where Eq. (3.2) is the Euler-equation governing the dynamics of a fluid of density  $\rho$  submitted to a pressure  $p$ , and flowing with a velocity field  $\mathbf{v}$ . Eq. (3.1) is the continuity equation stating the conservation of matter for this fluid, and Eq. (3.3) states that the vorticity  $\nabla \times \mathbf{v}$  of an irrotational flow is zero. Using this last equation, we can write the fluid velocity  $\mathbf{v}$  as the gradient of a scalar potential  $\psi(\mathbf{x}, t)$

$$\mathbf{v} = -\nabla \psi \quad (3.4)$$

We need to linearize the perturbed version of those equations above to obtain the wave equations governing the propagation of perturbations around this fluid flow. We use the usual procedure of Refs.[30], [31], [32] and [165], which consists of writing down the dynamics of the DBTV's as the background flow, and then adding a linear perturbation over this zeroth order dynamics. The final result must also obey the hydrodynamic equations, namely, Eqs. (3.1),(3.2),(3.3).

First, since the fluid is barotropic, we define the specific enthalpy  $h(p)$  as

$$h(p) = \int_0^p \frac{dp'}{\rho(p')} \quad (3.5)$$

Euler's equation (3.2) is now reduced to Bernoulli's equation

$$-\frac{\partial \phi}{\partial t} + \frac{1}{2}(\nabla \psi)^2 + h = 0. \quad (3.6)$$

We now perturb the basic dynamic quantities describing this fluid, namely its density,

pressure, and velocity potential.

$$\rho \rightarrow \rho + \delta\rho, \quad (3.7)$$

$$p \rightarrow p + \delta p, \quad (3.8)$$

$$\psi \rightarrow \psi + \delta\psi. \quad (3.9)$$

In linear order, the continuity equation with those perturbations yields

$$\nabla \cdot \left[ \frac{\rho_0}{c^2} \left( \frac{\partial \delta\psi}{\partial t} + \mathbf{v}_0 \cdot \nabla \delta \right) \mathbf{v}_0 - \rho_0 \nabla \delta\phi \right] \quad (3.10)$$

$$\frac{\partial}{\partial t} \left[ \frac{\rho_0}{c^2} \left( \frac{\partial \delta\phi}{\partial t} + \mathbf{v}_0 \cdot \nabla \delta\phi \right) \right] = 0, \quad (3.11)$$

The quantities with the subindex 0 are the zero-th order background quantities describing the non-perturbed fluid vortex. The quantity  $c^2$  describes the speed of sound by the derivation of the equation of state.

$$c^2 = \frac{\partial p}{\partial \rho} \quad (3.12)$$

The remarkable connection with General Relativity resides in the fact that the Eq. (3.11) can be rewritten as the Klein-Gordon equation in curved spacetimes

$$\frac{1}{\sqrt{-g}} \partial_\mu (\sqrt{-g} g^{\mu\nu} \partial_\nu \delta\phi) = 0, \quad (3.13)$$

describing the evolution of a scalar field  $\delta\psi$  perturbation on the background spacetime of the following effective metric in  $2 + 1$  dimensions

$$g_{\mu\nu} = \left(\frac{\rho_0}{c}\right)^2 \begin{bmatrix} -c^2 + v_0^2 & -\mathbf{v}_0 \\ -\mathbf{v}_0 & \mathbf{I}_{2 \times 2} \end{bmatrix} \quad (3.14)$$

Specifying our coordinate systems as the polar coordinates in 2 spatial dimensions, the background flow velocity of the fluid is given by

$$\mathbf{v}_0 = v_r(t, r, \phi)\hat{r} + v_\phi(t, r, \phi)\hat{\phi}, \quad (3.15)$$

and the metric tensor is written as

$$g_{\mu\nu} = \left(\frac{\rho_0}{c}\right)^2 \begin{bmatrix} -c^2 + v_0^2 & -v_r & -v_\phi r \\ -v_r & 1 & 0 \\ -v_\phi r & 0 & r^2 \end{bmatrix}. \quad (3.16)$$

The analog metric above admits a supersonic region where the fluid is faster than the soundwaves  $v > c$ , and the vector  $\partial/\partial t$  becomes spacelike. This draws a complete analogy between this supersonic region and the ergoregion of a Kerr black hole. Accordingly, when probing the scattering properties of this classical irrotational fluid in a bathtub-draining vortex, such as the one modeled above, effects such as superradiant scattering could also be measured [166, 167]. This experiment was proposed to be within the experimental reach [168], and its realization occurred in 2016 [79]. That experiment demonstrated the super-radiant profile of wave scattering through this rotating vortex flow. This astonishing result showed that physical phenomena only expected to happen in astrophysical black holes could be experimentally reproduced in terms of BHs' analog models.

### 3.1.1 The Effective Acoustic Metric for an Incompressible flow

An additional result that can be derived from Eq. (3.3), i.e. from the hypothesis of an irrotational fluid, is that the angular velocity of the background fluid is inversely proportional to  $r$ . So

$$v_\phi = \frac{C}{r}. \quad (3.17)$$

If we also admit that this fluid is incompressible, we must have by definition that the background density  $\rho_0$  and the speed of sounds  $c$  are constant. Consequently, from Eq. (3.1), the fluid's divergence must also be zero for the background velocity

$$\nabla \cdot \mathbf{v}_0 = 0 \quad (3.18)$$

Hence, by integrating this equation throughout the entire space, we obtain that the radial velocity is also inversely proportional to the radial coordinate for an incompressible fluid

$$v_r = -\frac{D}{r}. \quad (3.19)$$

So, the background fluid velocity is now

$$\mathbf{v}_0 = -\frac{D}{r}\hat{r} + \frac{C}{r}\hat{\phi}, \quad (3.20)$$

and the acoustic metric describing the effective background BH spacetime is defined by the following line-element

$$ds^2 = -\left(1 - \frac{C^2 + D^2}{r^2}\right) dt^2 + \frac{2D}{r} dr dt - 2C d\phi dt + dr^2 + r^2 d\phi^2. \quad (3.21)$$

On this effective BH spacetime, scalar field perturbations described by the Klein-Gordon Eq. (3.13) propagate as acoustic perturbations around a DBTV. It is useful sometimes to write this effective metric in a Boyer-Lindquist Kerr-like form, which can be achieved by transforming the polar coordinates into a new coordinate system,  $(\tilde{t}, r, \tilde{\phi})$ . Then, we find the equivalent line-element

$$ds^2 = - \left( 1 - \frac{C^2 + D^2}{c^2 r^2} \right) c^2 d\tilde{t}^2 + \left( 1 - \frac{D^2}{c^2 r^2} \right)^{-1} dr^2 - 2C d\tilde{\phi} d\tilde{t} + r^2 d\tilde{\phi}^2. \quad (3.22)$$

Notice the similarity in the form of this effective line-element with the line-element of a slowly rotating black hole spacetime in Eq.(2.81). Moreover, from this expression, we find that an ergoregion is located inside the ergo-sphere, whose radius is given by

$$r_e = \frac{(C^2 + D^2)^{1/2}}{c}, \quad (3.23)$$

This effective spacetime also admits an event horizon, as the surface on which the radial velocity of the fluid equals the speed of sound, so

$$r_h = D/c. \quad (3.24)$$

We have now summarized the analogy between the irrotational fluid model of a draining vortex in a bathtub and the astrophysical black hole.

### 3.1.2 Wave equation for acoustic perturbations in the acoustic black hole

As demonstrated previously, the evolution and propagation of acoustic perturbations in the background fluid flow of a draining vortex are described by the Klein-Gordon equation (3.13). This second-order partial differential equation can be separated through the following ansatz

$$\delta\psi(t, r, \phi) = R(r)e^{im\phi}e^{-i\omega t}. \quad (3.25)$$

The resulting radial equation is then

$$\frac{d^2 R}{dr^2} + P(r)\frac{dR}{dr} + Q(r)R = 0, \quad (3.26)$$

where

$$P(r) = \frac{d}{dr} \log \left[ r \left( c^2 - \frac{D^2}{r^2} \right) \right] - 2i \frac{Dr}{r^2 c^2 - D^2} \left( \omega - \frac{mC}{r^2} \right),$$

$$Q(r) = \frac{r^2}{r^2 c^2 - D^2} \left[ \left( \omega - \frac{mC}{r^2} \right) - \frac{m^2 c^2}{r^2} \right], \quad (3.27)$$

$$- i \left( \omega - \frac{mC}{r^2} \right)^2 \frac{Dr}{r^2 c^2 - D^2} \frac{d}{dr} \log \left( \omega - \frac{mC}{r^2} \right). \quad (3.28)$$

Here, we can implement a coordinate transformation for the radial coordinate  $r$  that is analog to the conformal transformations in GR. The new coordinate  $r_*$ , which we call tortoise coordinate, is related to the old radial coordinate by the following relations

$$\frac{dr}{dr_*} = \frac{1}{r^2} \left( r^2 - \frac{D^2}{r^2} \right), \quad (3.29)$$

$$r_* = r + \frac{D}{2c} \log \left| \frac{cr - D}{cr + D} \right|. \quad (3.30)$$

With an additional transformation on the dependent coordinate  $R(r)$  [165],

$$R(r) \rightarrow \left( r^{-1/2 + i \frac{mC}{D}} (c^2 r^2 - A^2)^{i \frac{D\omega}{2c^2} - i \frac{mC}{2D}} \right) \psi(r) \quad (3.31)$$

we are led to a new differential equation for the radial part of the perturbation field, namely

$$\frac{d^2}{dr_*^2} \psi(r) - \bar{V}(r, \omega) \psi(r) = 0. \quad (3.32)$$

If we also normalize this equation with  $D$  by taking  $D \rightarrow 1$ , the radial function  $\bar{V}(r)$  yields

$$\bar{V}(r, \omega) = -\left(\omega^2 - \frac{mC}{r^2}\right)^2 + \left(1 - \frac{1}{r^2}\right) \left(\frac{m^2 - 1/4}{r^2} + \frac{5}{4r^4}\right), \quad (3.33)$$

Expanding this radial function as

$$\bar{V}(r, \omega) = -\omega^2 - \frac{m^2 C^2}{r^4} + 2\frac{mC}{r^2}\omega - \left(1 - \frac{1}{r^2}\right) \left(\frac{m^2 - 1/4}{r^2} + \frac{5}{4r^4}\right). \quad (3.34)$$

Eq. (3.32) can then be finally rewritten as

$$\frac{d^2}{dr_*^2} \psi(r) - (\omega^2 - V(r, \omega)) \psi(r) = 0, \quad (3.35)$$

where  $V(r, \omega)$  is the effective potential given by

$$V(r, \omega) = -\frac{m^2 C^2}{r^4} + 2\frac{mC}{r^2}\omega - \left(1 - \frac{1}{r^2}\right) \left(\frac{m^2 - 1/4}{r^2} + \frac{5}{4r^4}\right), \quad (3.36)$$

In Fig. 3.1 we plot those potentials for some different values of the angular parameter  $m$ , and in the non-rotating case  $c = 0$ .

If we compare Eqs. (3.35),(3.34) above with Eqs. (2.82),(2.83) for the wave equation describing the evolution of gravitational perturbations around a slowly rotating black hole, we see the strong and remarkable similarity between those equations. This demonstrates once again the mathematical equivalence that motivates the study of astrophysical systems such as black holes and ECOs in terms of their analog gravity systems, such as the one we presented here. Furthermore, this mathematical equivalence allows us to study and simultaneously obtain the wave solutions for Eqs. (3.35) in terms of the same mathematical formalism. We introduce this formalism and we solve those master wave equations in the following chapter.



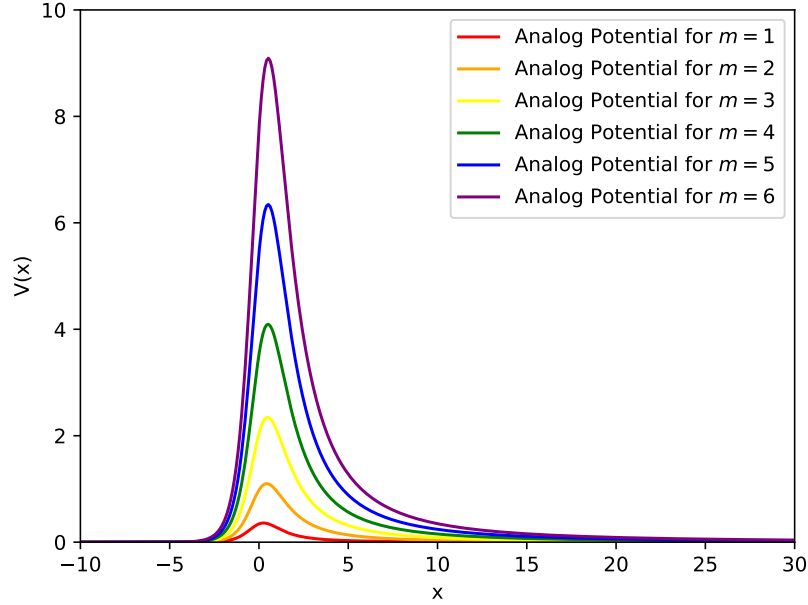


Figure 3.1: Effective analog scattering potentials from Eq. (3.36) with  $C = 0$  and for different values of the angular parameter  $m$ .

### 3.1.3 Experimental Findings

In the last years, a lot of experimental interest for analog gravity systems to astrophysical compact objects has been raised, and different lab controlled experiments were conducted by different research groups [165, 37, 118, 116, 121]. Among the many physical features these groups have searched for, the most remarkable ones reported the discovery of physical features in analog gravity systems that were initially predicted to exist in their corresponding astrophysical systems. For the analog gravity system proposed in terms of the bathtub draining vortex with a fluid, we could cite for example the detection of quasinormal modes oscillations on the free surface of the hydrodynamical vortex flow at the late stages of the relaxation process [47], and most notably, the detection of a rotational superradiant scattering in a vortex flow [79].

As we have already discussed, the superradiant behavior of scattering fields is a specific and remarkable feature of rotating black holes. The superradiant scattered waves manage to

'steal' some energy from the black hole's ergo-region, amplifying their amplitudes. We can see that by looking at the following relation for the reflection coefficient

$$|\mathcal{R}|^2 = 1 - \frac{1}{\omega} \left( \omega - \frac{mC}{r_h^2} \right) |\mathcal{T}|^2 \quad (3.37)$$

Notice that, since  $0 < |\mathcal{T}|^2 < 1$ , superradiance, i.e.  $|\mathcal{R}|^2 > 1$ , occurs whenever the frequency of the incident wave is sufficiently small (or the azimuthal number is sufficiently large).

$$\omega < \frac{mC}{r_h^2} \quad (3.38)$$

Furthermore, considerable difficulty in detecting superradiance was imposed by the fact that we need small frequencies (or big wavelengths) to probe it observationally. To circumvent this problem, the Gravity Group from Nottingham prepared a very careful experimental set-up, where extremely sensible measurements were conducted for the final result shown in Ref.[79].

From this same experiment and result, an additional and unexpected outcome was also later reported. This time, it was unrelated to the scattered waves' superradiant profile. In Ref. [80], it was pointed out that:

*"[...] while this experiment demonstrated the robustness of the superradiance process, it still lacks a complete theoretical description due to the many effects at a stage in the experiment. In this paper, we shine new light on this experiment by deriving an estimate of the reflection coefficient in the dispersive regime [...]"*

*"[...] This estimate is used to evaluate the reflection coefficient spectrum of counter-rotating modes in the Nottingham experiment. Our finding suggests that the vortex flow in the superradiance experiment was not purely absorbing, contrary to the event horizon of a rotating black hole...."*

In his same words...

*“[...] While this result increases the gap between this experimental vortex flow and rotating black hole, it is argued that it is in fact this gap that is the source of novel ideas.[...]”*

Therefore, through a careful analysis using the WKB method, Torres [80] suggested that the observations from the vortex flow experiment showed that the DBT classical vortex was not a pure absorber at its core, analogously to an astrophysical black hole. In particular, it was clear that the vorticity effects were relevant enough closer to the vortex core, so dispersive effects could no longer be neglected. However, neglecting the dispersive nature of the classical fluid is an approximation we assume *a priori* for defining the DBT vortex as an analog to black holes. So finally, a direct analogy between the DBT vortex of the Nottingham experiment [79] and a rotating black hole was impossible. While this could represent a backlash for the proposal of probing astrophysical systems with analog gravity systems, particularly for the DBT vortex model, Torres claimed that this gap could be a source of new ideas [80].

Among those new ideas, one of the most relevant for this thesis was promoting the DBT vortex to an analog model for exotic compact horizonless objects [48], rather than black holes. The framework in Ref.[47] also encouraged this idea. In Ref. [48], it was discussed how the quasinormal modes spectrum of scattering waves would be affected by the presence of vorticity effects at the vortex core. In fact, the obtained result was that the resulting quasinormal modes exhibited long-living trapped modes, also known as quasibound states. In the next section, we introduce the idea raised in Ref. [48] of proposing the draining vortex as an analog model to exotic compact objects. This idea will be extremely relevant for the applications of the inverse methods that are considered throughout this thesis.

## 3.2 The Imperfect Draining Vortex as an Analog to Astrophysical Exotic Compact Objects

In our previous discussions, we pointed out that due to the large flow velocities close to the core of a draining rotating vortex, some extra hydrodynamical effects could potentially lead to the failure of the non-vorticity and non-dispersive assumptions. In analogy to the astrophysical black hole, those approximations are assumed so that the draining vortex can become a perfect absorber. Facing this fact, it has been proposed in literature an effective model [48] of a draining vortex with a partially reflective boundary condition inside the core. Motivated by the experimental findings in [80], suggesting that this reflection occurring inside the core tends to assume the form of a finite reflectivity constant for some physical scenarios, they proposed in their model that this effective boundary condition at the center of the vortex is described by a single quantity  $\mathcal{K}$ . Moreover, in their effective model, this boundary condition is located at a small distance outside the analog horizon  $r_h$ . So, in their framework, they studied the scattering of waves by this *imperfect* draining vortex, focusing on the signature of those core reflections.

In the following, our study will be formally carried out using the equivalence between the mathematical description of analog gravity systems and their corresponding astrophysical objects. Such equivalence allows us to bring the mathematical techniques already employed in the context of compact objects' perturbation theory and use them to describe the scattering properties of their analog systems. This time, however, we can no longer rely on the black hole description of fields scattering since our DBT vortex is not a perfect absorber. Instead, the mathematical description to be used is equivalent to the techniques used for exotic compact horizonless objects.

As we have previously mentioned for some exotic ultra-compact objects, their effective boundary condition at their external surface is modeled by a reflectivity parameter defined just beyond their 'would-be' event horizon, see Fig. 2.5 for an illustration. This physical

description suits well the conceptual idea behind the imperfect draining vortex in a DBT. For this reason, we say that such vortex can now be regarded as an analog model to ECOs, rather than black holes.

As it is for the astrophysical setting, the effective description of ECOs allows one to easily relate their physical observables to associated quantities for the acoustic black hole case. We use this fact to obtain the scattering properties of our analog gravity system.

Among the plethora of results obtained in Ref.[48], the most remarkable was the presence of enhanced absorption of the waves for specific frequencies, which are visible through the presence of spectral lines in the transmission/reflection spectrum (see Fig. 4.24 for example). Those frequencies are the so-called resonant frequencies of the quasistationary modes of the system.

In the following chapters, we compute those cross-section curves, point out those enhanced spectral lines, and discuss their physical significance. The same calculations could be carried out for the astrophysical setting, where exotic compact objects surrounded by an effective boundary also exhibit sharp lines in their scattering coefficients [169, 170].

# Chapter 4

## The Direct Problem: Methods for Solving the Master Wave Equations

### 4.1 Solving the Linearized Field Perturbation Equations

As we have seen in the previous chapters, the dynamical evolution of gravitational and test field perturbations in BH's background spacetimes, as well as the evolution of acoustic perturbations around an acoustic black hole, are both radially described by the following general master wave-equation

$$\frac{\partial^2}{\partial r_*^2} \Psi(r, t) - \frac{\partial^2}{\partial t^2} \Psi(r, t) - V_l(r) \Psi(r, t) = S_l(r, t). \quad (4.1)$$

where the non-homogeneous source term  $S_l(r, t)$  specifies the perturbation profile in radial coordinate, and  $V(r)$  is the scattering potential that couples the geometrical structure of the background (or effective) spacetime into this wave equation. For odd-parity perturbations in Schwarzschild spacetime, the effective potential  $V_l(r)$  is given by

$$V_{\text{RG}_l}(r) = \left(1 - \frac{2M}{r}\right) \left[ \frac{l(l+1)}{r^2} + \frac{6M}{r^3} \right], \quad (4.2)$$

For even-parity gravitational perturbations, we get Zerilli's effective potential instead

$$V_{Zl}(r) = \frac{2(r^2 - 2Mr)}{r^5(\Lambda r + 3M)^2} [\Lambda^2(\Lambda + 1)r^3 + 3M\Lambda^2r^2 + 9M^2\Lambda r + 9M^3], \quad (4.3)$$

Lastly, for the scattering of acoustic perturbation waves around the acoustic analog of a black hole consisting of a bathtub draining vortex, the following effective potential is obtained

$$V_m(r) = \left(1 - \frac{1}{r^2}\right) \left[\frac{m^2 - 1/4}{r^2} + \frac{5}{4r^4}\right] + \frac{m^2 C^2}{r^4} - 2\frac{mC}{r^2}\omega, \quad (4.4)$$

In all cases,  $m$  and  $l$  denote the angular decomposition constants.

To study the evolution of perturbations within a considered background geometry we need to investigate and/or possibly solve this second order master wave equation. This chapter's main goal is to discuss and present solutions to these perturbation equations. We can do that through two distinct approaches: we can directly integrate this equation in the time-domain (1), evolving an initial spatial configuration for the perturbation over time; or we can also solve it in the frequency domain, after doing a spectral decomposition in terms of the Fourier transformation (2). For that last case, we rely on Green's function method. We discuss both approaches in the following sections, beginning with the time domain approach for the associated homogeneous equation.

$$\frac{\partial^2}{\partial r_*^2}\Psi(r, t) - \frac{\partial^2}{\partial t^2}\Psi(r, t) - V_l(r)\Psi(r, t) = 0. \quad (4.5)$$

## 4.2 Time Domain Approach

In order to integrate Eq. (4.5) directly in the time domain, we must evolve a certain initial configuration. Accordingly, we must specify this initial configuration at a certain initial time  $t_0$ , such as for example

$$\left\{ \begin{array}{l} \Psi(x, t_0) = g(x), \\ \frac{\partial \Psi}{\partial t}(x, t = t_0) = f(x) \end{array} \right., \quad (4.6)$$

for some certain  $g(x)$  and  $f(x)$ , and at a certain time  $t_0$ . The  $x$  coordinate here is the tortoise coordinate  $r_*$ .

We are considering here that at  $t_0$  the external perturbation  $\tilde{S}(x, t)$  gets turned off, so we have  $\tilde{S}(x, t > t_0) = 0$ . Equation (4.5) with some chosen functions  $g(x)$  and  $f(x)$  as initial conditions provides us with the formulation of our initial value problem. In the next two subsections, we show how we evolve these initial conditions in the direct time domain for Schwarzschild/analog black holes. In the following subsection, we repeat the procedure, but for their corresponding exotic compact object.

### 4.2.1 Evolving The Field Perturbation Equations in Time Domain for Black Holes

Let's consider, for example, a Gaussian pulse being sent toward the Schwarzschild or the acoustic black hole. Our initial data consists of the incoming Gaussian wave packets written as follows

$$\psi(x, t_0) = Ae^{-\frac{1}{\sigma}(x-x_3)^2} \quad (4.7)$$

with an amplitude  $A$  comparable to the maximum of the potential and widths  $\sigma$  comparable to the width of the potential. Outgoing boundary conditions are imposed (although boundaries are chosen at a distance such that possible reflections will not contaminate the observer waveforms).

With our initial value problem fully specified, we now solve Eq. (4.5) numerically via a



finite difference scheme, particularly a central in time and central in space scheme [171].

$$\Psi_j^i = 2\Psi_j^{i-1} - \Psi_j^{i-2} + \frac{\Delta t^2}{\Delta x^2}(\Psi_{j+1}^{i-1} - \Psi_j^{i-1} + \Psi_{j-1}^{i-1}) - \Delta t^2 \Psi_j^{i-1} V_j. \quad (4.8)$$

Here  $\psi_j^i = \psi(x_i, t_j)$ ,  $V_j = V(x_j)$  and  $\Delta t$  and  $\Delta x$  are the time and space resolutions respectively.

In Eq. (4.6), specifying the boundary conditions at a second space-like foliation of this spacetime,  $\Psi(x, t_0 + dt)$ , displaced by an infinitesimal time  $dt$ , is formally equivalent to providing the second initial condition for the derivative of  $\Psi(x, t_0)$ , since  $\Psi(x, t_0 + dt) \approx \Psi(x, t_0) + \frac{\partial \Psi}{\partial t}(x, t_0)dt$ . We can set the initial conditions at the two space-like foliations, infinitesimally displaced in time, as

$$\begin{cases} \psi(x, t_0) = Ae^{-\frac{1}{\sigma}(x-x_3)^2}, \\ \psi(x, t_0 + dt) = Ae^{-\frac{1}{\sigma}(x-(x_3-dt))^2}, \end{cases} \quad (4.9)$$

The specific mathematical form of the two initial conditions for the perturbation field in Eqs. (4.9) can be physically interpreted as a Gaussian pulse centered in  $x_3$  at  $t_0$  that will tend to move toward the black hole as the time increases. We can see that by noticing that after an infinitesimally small time displacement  $dt$ , the pulse's center will move to  $x_3 - dt$ . Here, we have fixed the natural unit system for which  $c = 1$ .

By evolving the initial conditions Eqs. (4.9) through Eq. (4.8) above, we evaluate and obtain the perturbation field  $\Psi$  at any future time  $t$ , while we also guarantee it satisfies the master wave equation (4.5) in every subsequent time [171]. To illustrate it, We show in Fig.4.1 some instantaneous of the evolved perturbation field for a few different time instants  $t = t_i$ , namely  $t_0 = 0$ ,  $t_1 = 10$ ,  $t_2 = 15$ ,  $t_3 = 25$  and  $t_4 = 34$ .

If we fix an observer at a certain distant position  $x_2$  from the source, which we represent as the black dashed vertical line in Fig. 4.1, this observer will measure a gravitational wave signal (or acoustic wave signal) during a certain period of time. We represent the gravitational wave

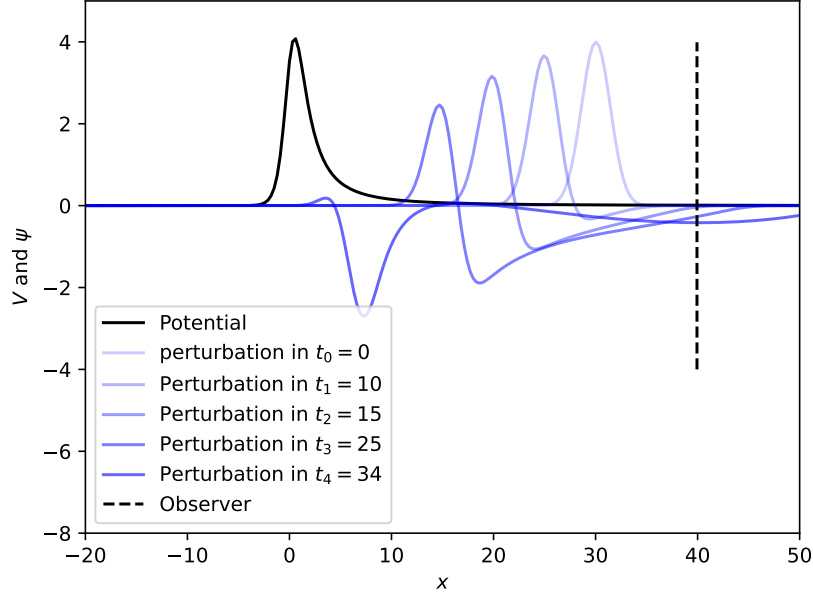


Figure 4.1: The potential in tortoise coordinate, and instantaneous of the perturbation field for 5 different times,  $t_0, t_1, t_2, t_3, t_4$ . Here we have considered the analog black hole model with  $m = 4$ , and  $C = 0$ . The initial perturbation was released from  $x_3 = 30$  with  $\sigma = 1$ .

signal (or acoustic wave signal) measured by the observer in the graphic in Fig. 4.2 for the Schwarzschild black hole, and in Fig. 4.3 for the analog acoustic black hole. We also call this detected signal gravitational-wave strain, or acoustic wave strain.

We will properly analyze and study those gravitational wave signals in Sec. 4.3.2.2, where we introduce the spectroscopy of gravitational waves from ringing perturbed black holes in terms of their quasinormal modes.

## 4.2.2 Evolving The Field Perturbation Equations in Time Domain for Static Exotic Compact Objects

For exotic compact objects, the same scheme explained above is used, with the only difference that at a certain boundary position  $x_0$ , we demand that

$$\Psi_j^i = 2\Psi_j^{i-1} - \Psi_j^{i-2} + \frac{\Delta t^2}{\Delta x^2} (\Psi_{j+1}^{i-1} - \Psi_j^{i-1} + (1 - \mathbf{K}^2)\Psi_{j-1}^{i-1}) - \Delta t^2 \Psi_j^{i-1} V_j, \quad (4.10)$$

for  $x_j = x_0$ .

That will guarantee the desired reflecting behavior for the boundary condition at the reflective surface in  $x_0$ . See some examples in Figs. 4.4, 4.5, where the signals from a Schwarzschild ECO and an analog ECO model are respectively plotted.

Notice that in all those cases, a new and more damped gravitational wave strain arises again after a fixed time interval. Those are the **echoes of gravitational waves**, produced by the reflective properties of the ECO at the boundary defined at  $x_0$ . We will study in detail those echoes in section 4.3.3.2, right after we introduce the mathematical properties of waveforms in the frequency domain for ECOs.

### 4.3 Frequency Domain Approach

From now on, we focus on integrating Eq. (4.1) in the frequency domain. For that goal, we employ Green's function formalism. This formalism gives us the fundamental tools to analyze waveforms emitted by perturbed black holes (Sec. 4.3.1) and exotic compact objects (Sec. 4.3.3), both for the astrophysical scenario and for analog gravity systems. This formalism also provides us with the basic mathematical foundation for investigating the scattering problem in Sec. 4.4.

As we see throughout our study (4.3.2), the resonant modes (or the poles of Green's function) of the solutions in the frequency domain play an important role in the upcoming analysis. Those modes are called *quasinormal modes* for the black hole case and *trapped quasinormal modes* for the ECO scenario.

In order to integrate Eq. (4.1) in the frequency domain, we first need to do the usual spectral decomposition, which is carried out in terms of a Fourier transformation on the

wavefunction  $\Psi(x, t)$

$$\tilde{\Psi}(r, \omega) = \frac{1}{\sqrt{2\pi}} \int_{-\infty}^{+\infty} \Psi(r, t) e^{-i\omega t} dt. \quad (4.11)$$

This will lead us to a time-independent wave equation for the radial profile of the perturbations, which is parametrized by the frequency  $\omega$ .

$$\frac{d^2 \tilde{\Psi}(r, \omega)}{dr_*^2} + (\omega^2 - V_l(r)) \tilde{\Psi}(r, \omega) = \tilde{S}_l(r, \omega) \quad (4.12)$$

where  $\tilde{S}(r, \omega)$  is the Fourier transformation of the perturbation source term. This second-order master equation must have two linearly independent wave solutions.

Once we solve this time-independent wave equation (4.12), we obtain the wave function in the frequency domain, also called amplitude  $\tilde{\Psi}(x, \omega)$ . From this amplitude, we can obtain the time-dependent solution  $\Psi(x, t)$  for the time evolution of the perturbations employing the inverse Fourier transformation

$$\Psi(x, t) = \frac{1}{\sqrt{2\pi}} \int_{-\infty}^{+\infty} \tilde{\Psi}(x, \omega) e^{i\omega t} dt \quad (4.13)$$

Therefore, all we need to do is to solve the non-homogeneous time-independent wave equation (4.12) for the frequency-domain amplitude  $\tilde{\Psi}(x, \omega)$ . That is accomplished in terms of Green's function formalism, which we introduce now for two distinct important cases: perturbed black holes (and acoustic analogs) (Sec. 4.3.1); and perturbed exotic compact objects (and analog models) (Sec. 4.3.3).

### 4.3.1 Green's function formalism for the time-independent wave equation in the black hole case

In order to obtain the general wave solution of the time-independent wave-equation (4.12), within the Green's function formalism, we must firstly obtain two linear-independent wave

solutions  $\tilde{\Psi}_1(x, \omega)$ ,  $\tilde{\Psi}_2(x, \omega)$  of the associated time-independent homogeneous wave-equation, readily

$$\frac{d^2 \tilde{\Psi}(r, \omega)}{dr_*^2} + (\omega^2 - V_l(r)) \tilde{\Psi}(r, \omega) = 0. \quad (4.14)$$

As we have seen in Sec. 4.2, when we solve the wave equation (4.5) directly in the time domain, we obtain an evolving perturbation, such that for a very distant observer in  $x_2 \gg 0$ , outgoing damped-harmonic oscillations are scattered out by the potential  $V_l(x)$ . The same happens in  $x_0 \ll 0$ , except that we now have incoming damped waves. If we look at the potential structure in general  $V_l(x)$ , we see that it vanishes at the two extremities in tortoise coordinate  $x$ . So

$$V_l(x) \rightarrow \begin{cases} 0, & x \rightarrow -\infty, \\ 0, & x \rightarrow +\infty \end{cases}, \quad (4.15)$$

$$\text{for non-rotating cases; and} \quad (4.16)$$

$$V_l(x) \rightarrow \begin{cases} -\omega_{\text{sr}}^2 + 2\omega\omega_{\text{sr}}, & x \rightarrow -\infty, \\ 0, & x \rightarrow +\infty, \end{cases}, \quad (4.17)$$

$$\text{for rotating cases.} \quad (4.18)$$

where  $\omega_{\text{sr}}$  is the superradiance threshold frequency, which indicates the limiting superior frequency for superradiant scattering effects. It is given by

$$\omega_{\text{sr}} = \begin{cases} a\Omega_{s,l}, & \text{for Kerr's black hole;} \\ \frac{mc}{r_h^2}, & \text{for the acoustic rotating sonic hole.} \end{cases} \quad (4.19)$$

For Kerr's black hole,  $\Omega_{s,l}$  depends on the perturbed field's spin, as shown in Refs.[164, 172].

Hence, the time-independent homogeneous wave equation (4.14) at those two extremities  $x \rightarrow \pm\infty$  is asymptotically written as

$$\begin{cases} \frac{d^2 \tilde{\Psi}(x, \omega)}{dx^2} - \tilde{\omega}^2 \tilde{\Psi}(x, \omega) = 0, & x \rightarrow -\infty \\ \frac{d^2 \tilde{\Psi}(x, \omega)}{dx^2} - \omega^2 \tilde{\Psi}(x, \omega) = 0, & x \rightarrow \infty \end{cases} \quad (4.20)$$

The homogeneous wave solutions must satisfy the following general conditions at the two extremities

$$\begin{cases} \tilde{\Psi}(x, \omega) \rightarrow e^{\pm i\tilde{\omega}x}, & x \rightarrow -\infty; \\ \tilde{\Psi}(x, \omega) \rightarrow e^{\pm i\omega x}, & x \rightarrow \infty, \end{cases} \quad (4.21)$$

where  $\tilde{\omega} = \omega - \omega_{\text{sr}}$  for rotating cases, and simply  $\tilde{\omega} = \omega$  for non-rotating ones.

This motivates us to choose, as the two linearly-independent solutions of Eq. (4.14), the pair of wave functions  $\tilde{\Psi}_h(x, \omega), \tilde{\Psi}_\infty(x, \omega)$  which, by definition, satisfy the boundary conditions

$$\tilde{\Psi}_h(x, \omega) = \begin{cases} e^{-i\tilde{\omega}x}, & x \rightarrow -\infty, \\ A_\infty^- e^{-i\omega x} + A_\infty^+ e^{+i\omega x}, & x \rightarrow +\infty, \end{cases} \quad (4.22)$$

and

$$\tilde{\Psi}_\infty(x, \omega) = \begin{cases} A_h^- e^{-i\tilde{\omega}x} + A_h^+ e^{+i\tilde{\omega}x}, & x \rightarrow -\infty, \\ e^{+i\omega x}, & x \rightarrow +\infty. \end{cases} \quad (4.23)$$

The Wrosnkian of those two linearly-independent solutions is defined as

$$W_{\text{BH}} \equiv W(x; \tilde{\Psi}_h(x, \omega), \tilde{\Psi}_\infty(x, \omega)) = \tilde{\Psi}_h(x, \omega) \frac{\partial \tilde{\Psi}_\infty}{\partial x}(x, \omega) - \tilde{\Psi}_\infty(x, \omega) \frac{\partial \tilde{\Psi}_h}{\partial x}(x, \omega) \quad (4.24)$$

The general solution  $\tilde{\Psi}(x, \omega)$  of the **homogeneous** associated wave equation (4.14) must be, everywhere in  $x$ , a linear superposition of the two independent solutions above. Furthermore, with this chosen pair of linearly-independent wave solutions for the **homogeneous** equation, we can also write the general solution of the **NON-homogeneous** time-independent wave-equation (4.12). In the frequency domain, this is carried out employing the Green's function formalism. We are mainly interested in the frequency domain waveform of the wave solution at the two extremities  $x \rightarrow \pm\infty$ . One represents the wave amplitude 'swallowed' by the BH's event horizon  $x \rightarrow -\infty$ , and the other represents the wave amplitude measured by a distant observer in  $x \rightarrow \infty$ . Green's function formalism states that the general form of the wave solution for the **NON-homogeneous** time-independent wave-equation (4.12), as measured at both extremities ( $x \rightarrow \pm\infty$ ), is

$$\tilde{\Psi}_{\text{BH}}(x, \omega) = \begin{cases} \tilde{Z}_{\text{BH}}^\infty(\omega) e^{i\omega x}, & x \rightarrow \infty, \\ \tilde{Z}_{\text{BH}}^h(\omega) e^{-i\omega x}, & x \rightarrow -\infty. \end{cases} \quad (4.25)$$

This is the wave amplitude in the frequency domain, representing the black hole response at spatial infinities to the perturbation source  $\tilde{S}(x, \omega)$ . It describes an irradiating wave solution for each frequency  $\omega$ , and its amplitude of irradiation is given by

$$\tilde{Z}_{\text{BH}}^\infty(\omega) = \int_{-\infty}^{\infty} dx' \frac{\tilde{\Psi}_1(x', \omega) \tilde{S}(x', \omega)}{W_{\text{BH}}}, \quad (4.26)$$

$$\tilde{Z}_{\text{BH}}^h(\omega) = \int_{-\infty}^{\infty} dx' \frac{\tilde{\Psi}_2(x', \omega) \tilde{S}(x', \omega)}{W_{\text{BH}}}. \quad (4.27)$$

And that is the black hole response for the perturbation source term  $\tilde{S}(x, \omega)$  as measured at the black hole's horizon  $x \rightarrow -\infty$  and by a distant observer in spatial infinity  $x \rightarrow \infty$ . This solution describes the wave amplitude in the frequency domain for a certain frequency  $\omega$ , and at those two extremities.

In theory, the problem is now fully posed in the frequency domain. As we have now obtained the wave solution amplitude, we can state that we have completed the formal procedure for solving the non-homogeneous time-independent wave equation (4.12) in the frequency domain. If we want the time evolution of our perturbation at the distant observer  $x \rightarrow \infty$ , all we have to do now is to calculate  $\Psi(x \rightarrow \infty, t)$  through the inverse Fourier transformation

$$\Psi(x \rightarrow \infty, t) = \frac{1}{\sqrt{2\pi}} \int_{-\infty}^{+\infty} \tilde{\Psi}(x \rightarrow \infty, \omega) e^{i\omega t} dt \quad (4.28)$$

In the following, we consider some applications of this formalism to illustrate how it works in practice. Before that, however, we need to pay special attention to an important and insightful feature of those wave amplitudes in frequency domain (4.26), mainly when it comes to calculating their inverse Fourier transformation in Eq. (4.28) for obtaining the time evolution of those perturbations. We discuss those special features in the following subsection.

### 4.3.2 Boundary Conditions for Black Hole Solutions: The Quasi-normal Modes Ringing

Notice that in Eq. (4.26), in the definition of the frequency domain amplitude, the Wronskian of the two L.I. homogeneous solutions appears in the denominator. Accordingly, our obtained wave solutions might admit poles for certain frequencies  $\omega$ . Those poles are essentially the roots of the Wronskian ( $W_{\text{BH}} = 0$ ), and they may arise for certain frequency values  $\omega$ .

For our case here, both in the black hole case and its analog system's scenario, the wave



function  $\tilde{\Psi}(x, \omega)$  admits poles for a certain discrete set of complex frequencies [173]

$$\omega_n = \omega_{R_n} + i\omega_{i_n}. \quad (4.29)$$

Those frequencies are called *quasinormal frequencies*, and the wave modes  $\tilde{\Psi}_n(x, \omega_n)$  associated with them are called *quasinormal modes*. The set of all quasinormal modes frequencies is called *quasinormal spectra*. Those poles do not lie on the real axis of the complex frequency plane [173], which is the case when we have a closed non-dissipative system, such as a confining quantum mechanical potential, for example, or the classical oscillations of string tied between two knots. In these two last examples, the bound states are simply the normal modes of this potential, with an associated eigen-spectrum of real energies (or real frequencies for the classical string).

But what are those quasinormal modes after all, how is their physical behavior? To answer that, we need to look, first of all, at their associated wave function in the frequency domain

$$\Psi_n(x, \omega_n) = A_n e^{i\omega_n x}. \quad (4.30)$$

Since their frequencies are complex, they have a fixed oscillating frequency, defined by the real part of  $\omega_n$ . Moreover, due to the additional imaginary part  $\omega_{i_n}$ , these quasinormal oscillations in open systems are also damped by the spatial irradiation of those modes. This exponential damping happens with a fixed decaying time, which is determined by the inverse of the imaginary part of  $\omega_n$ .

Furthermore, for the L.I. wave solution we considered below, namely  $\tilde{\Psi}_h(x, \omega)$ ,  $\tilde{\Psi}_\infty(x, \omega)$ , we can obtain the following demonstrable identity [59]

$$W(x; \tilde{\Psi}_h(x, \omega), \tilde{\Psi}_\infty(x, \omega)) = 2\tilde{\omega} A_h^+ = 2\omega A_\infty^- \quad (4.31)$$

from where we see that for the frequencies of the quasinormal modes  $\omega_n$ , Eq. (4.31) yields

$$\tilde{\omega}_n A_h^+(\omega_n) = \omega_n A_\infty^-(\omega_n) = 0 \quad (4.32)$$

So, finally, considering our homogeneous general solution  $\tilde{\Psi}(\omega, x)$  as a linear combination of the two fundamental L.I. solutions  $\tilde{\Psi}_h(\omega, x)$  and  $\tilde{\Psi}_\infty(\omega, x)$ , we see that for those quasinormal modes, we have the following common behavior at the two extremities.

$$\tilde{\Psi}_n(x, \omega_n) \sim \begin{cases} e^{-i\tilde{\omega}_n x}, & x \rightarrow -\infty, \\ e^{+i\omega_n x}, & x \rightarrow +\infty. \end{cases} \quad (4.33)$$

Physically this can be interpreted as stating that:

**Quasinormal modes are damped oscillating wave modes that are purely outgoing in spatial infinity and purely incoming at the BH's horizon.**

The importance of the quasinormal modes for our study can be better seen when taking the inverse Fourier transformation to obtain the time evolution of the perturbations (Eq. (4.28)). To understand this importance, we need to recall complex analysis.

In complex analysis, the Cauchy theorem states that the integration of an analytic function over a closed circle enlacing complex poles of this function is equivalent to summing the residues of those poles. Accordingly, we transform the Fourier inverse integral, giving us the time evolution of the perturbation in Eq. (4.13), into a Cauchy integral of the same integrand. This integrand has its poles defined by the complex QNMs frequencies. The integral contour is the curve  $\mathcal{C}$  in the complex frequency plane presented in Fig. 4.6. This Cauchy integral is now written as:

$$\Psi(x, t) = \frac{1}{\sqrt{2\pi}} \int_{\mathcal{C}} \tilde{\Psi}(x, \omega) e^{i\omega t} d\omega \quad (4.34)$$

There are three main contributions to that Cauchy integral:

- The integral along the quarter-circles, which is related to the prompt response, i.e. perturbation propagating from the source directly to the observer at lightspeed [174, 175, 176, 177]. This contribution dominates the early stage of the time evolution of the perturbation, as we see in the Fig. 4.7. We say that our template signal at this stage is “contaminated” by our initial conditions for the perturbation. It lasts for as long as the perturbation is “switched-on”, and ends a certain time after the perturbation is ‘turned off’.
- The branch-cut path’s contribution, which produces an effect called late-time tails, or later time power-decay. Late-time tails are physically related to backscattering off the background curvature. Mathematically, the branch cut arises to prevent  $\omega = 0$  from lying inside the integration contour. This contribution dominates the latest stage of the time evolution of the perturbation, as we see in the Fig. 4.7. This phase terminates driving the relaxation of the previously perturbed black hole (or analog black hole) into its final equilibrium phase. After having irradiated all of the externally produced perturbation to spatial infinity and toward the BH horizon.
- The contribution from the sum-over-residues at the poles (the QNMs frequencies). That is the most important contribution in general, and it is the most relevant for us. They represent the QNMs contribution to the response far from the source [175]. This contribution dominates the intermediate later stage of the time evolution of the perturbation, as we see in fig. 4.7. We call this intermediate stage *ringdown phase*.

If we calculate the residues of the poles of the integrand in Cauchy integral (4.34), we obtain that they are essentially the superposition of the quasinormal modes wave-functions. In other words, the most important contribution to the Cauchy integral in Eq. (4.34) and hence to the wave function  $\Psi(x, t)$ , in time-domain, is the sum of the quasinormal modes wave-functions. Since the Spectrum of QNMs frequencies is a discrete set of complex frequencies  $\omega_n$ , the time evolution of the irradiated perturbation as seen by a distant observer

in  $x \rightarrow \infty$  is then dominated by

$$\Psi(x \rightarrow \infty, t) \approx \sum_{n=0}^{\infty} \text{Re} \left[ (A_n \tilde{\Psi}_n(\omega_n, x) e^{i\omega_n t}) \right]. \quad (4.35)$$

In Eq. (4.35), each one of those QNMs describes a damped oscillation mode, with oscillation frequency  $\omega_{R_n}$  and damping time  $(\omega_{i_n})^{-1}$ . The  $A_n$  are called quasinormal excitation coefficients and they quantify the QNM content on the waveform [175]. The relative values of those complex amplitudes  $A_n$  are determined by how much each mode was excited at the perturbation stage. The quasinormal modes spectrum itself is independent of the initial perturbation and only depends on the background geometry, i.e., the QNMs spectrum is independent of the initial perturbation. This sum over the quasinormal modes then produces a final damped ringing response, mixing all the modes into a final signal. This signal is the dominant strain measured by the distant observer in  $x \rightarrow \infty$ .

#### 4.3.2.1 Black Hole Spectroscopy with Gravitational Waves and Quasinormal Modes

Finally, summarizing the insights from the previous subsection, the evolution of the irradiating perturbation measured by a distant observer in  $x$  is a combination of three different stages. The intermediate ringdown stage is the most important one for our BH spectroscopy.

The ringdown phase is the intermediate late-time response from the black hole to the previously externally produced perturbation. It lasts from the retarded-moment in which the perturbation is 'turned off' until its complete evanescence, when all perturbation is irradiated. As we had previously discussed, that is the phase of the BH response in which the signal is dominated by the sum over the quasinormal modes of the ringing black hole. Then, the signal measured by the distant observer in  $x \rightarrow \infty$  evolves in time as the superposition of the quasinormal modes ringing damped oscillations

$$\Psi_n(x, t) = A_n e^{-i\omega_n(x-t)} \quad (4.36)$$

As we have stated, although the complex amplitude  $A_n$  values are determined by how much each of those modes were excited at the previous perturbation phase, the QNMs spectrum is independent of the perturbation configuration. This fact is the main motivation behind our study of BH spectroscopy here.

For most astrophysical applications, the BH response to any initial perturbation during the late ringdown stage, and measured by a distant observer, can be approximated as a superposition of QNMs. That motivates our study of quasinormal modes for applying it to the spectroscopy of gravitational waves from black holes.

For example, consider the coalescence of a binary of black holes (BBH). The perturbation scheme discussed here cannot be considered a very reliable approximation for the realistic description of the binary merger phase. For that stage, numerical relativity is indispensable. However, for the late-ringdown stage, the relaxing deformed black hole resulting from the BBH merger can be well approximated as a perturbed black hole. That is when our approximation for the ringdown process of the black hole is valid (see Fig. 2.1). And since linear black hole perturbation theory dominates the description of relaxing perturbed black holes, we can state that:

**For a distant observer, the late-times response of a ringing black hole (or analog black hole) is mainly dominated by the superposition of its excited quasinormal modes, which are independent of the initial perturbation and only depend on the background geometry of the final resulting black hole.**

In the following, we apply those ideas to the QNMs spectral decomposition of some examples of ringdown signals. Those ringdown signals are measured by distant observers, and are obtained as a response to certain perturbation source terms  $\tilde{S}(x, \omega)$ . For the black hole case, we consider a head-on collision of the BH with a smaller object, which could be another smaller black hole, or a small star, for example. For the acoustic black hole, on the other hand, we apply our discussion for the scattering of a pulsating Gaussian source.

In both cases, we use Green’s function formalism to derive these waveform amplitudes in the frequency domain, and then we compute their time-domain counterpart signals using the inverse Fourier transformation. We can apply the spectral decomposition discussed here once we have the time-domain signal in our hands.

#### 4.3.2.2 Applications of Spectral Decomposition

To illustrate Green’s function formalism for BH Perturbation Theory and for acoustic perturbations around the analog model of a BH, we consider two simple but insightful applications in the following. The first example describes the gravitational perturbation caused by the plunge of a smaller mass into a larger black hole. This smaller mass follows a radial time-like geodesic in the background static and spherically symmetric spacetime of this Schwarzschild BH. During the plunge, the black hole absorbs the minor mass, while the perturbed gravitational field around it tends to relax by ringing and emitting gravitational radiation toward infinity. We calculate the gravitational waveform detected by a distant observer both in the time and frequency domain. This application was considered by Zerilli in Ref.[178], still in 1970. Next, we consider Gaussian periodic pulses perturbing an acoustic analog of a black hole. In the initial time, the source of these Gaussian pulsations is ‘turned off’, and the perturbations evolve in this effective background spacetime by irradiating themselves to infinity and towards the sonic hole. We also calculate the waveforms of the acoustic waves detected by a distant observer, both in frequency and time domain. At the end, we discuss how we can read out the excited quasinormal modes from the final waveform in the time domain.

- **Head-on collision of a large black hole with a smaller mass.**

In Ref.[135], Regge-Wheeler considered the very insightful problem of studying the stability of Schwarzschild metric for odd-parity perturbations. In Ref.[136] , Zerilli, has extended this analysis for even-parity perturbations. As a first application for this formalism, Zerilli considered in Ref.[178] the gravitational radiation pulse given off when a small mass falls into a black hole.

Here, we review this problem of a small particle radially infalling in a Schwarzschild black hole in linear perturbation theory. For this goal, we describe the infalling particle as a  $\delta$ -function source term describing a geodesic motion in the background Schwarzschild geometry. This problem is decomposed into tensor harmonics, and each harmonic drives its corresponding perturbation.

As in Ref. [136], the radial part of the polar perturbations of a Schwarzschild black hole are given by Zirelli sourced equation in Eq. (4.12), where the effective scattering potential  $V(r)$  is given by Eq. (2.35). The source term  $S$  corresponding to a test particle with mass  $\mu$  radially infalling from infinity with zero starting velocity is explicitly given by

$$S_l(r, \omega) = \mu \left(1 - \frac{2M}{r}\right) \left[ \frac{4\sqrt{5}e^{i\omega T(r)} \left(3\omega\sqrt{M^3r} - 2i\sqrt{2}\Lambda M + \Lambda\omega\sqrt{Mr^3} + i\sqrt{2}\Lambda r\right)}{r\omega(3M + \Lambda r)^2} \right] \quad (4.37)$$

$$- \frac{2\sqrt{10}(2M - r)e^{i\omega T(r)}T'(r)}{r(3M + \Lambda r)} \Bigg], \quad (4.38)$$

where the function  $T(r)$  and its derivative, for this orbital configuration are respectively given by [140]:

$$T(r) = M \left( -4\sqrt{\frac{r}{2M}} - \frac{4}{3} \left(\frac{r}{2M}\right)^{3/2} + 2 \log \left( \frac{\sqrt{\frac{r}{2M}} + 1}{\sqrt{\frac{r}{2M}} - 1} \right) \right), \quad (4.39)$$

and

$$T'(r) = -\frac{\frac{1}{\sqrt{\frac{2M}{r}}}}{1 - \frac{2M}{r}}. \quad (4.40)$$

Now, using the Green function's formalism, we find the numerical solution for the wavefunction amplitudes  $Z_{\text{BH}}^\infty$  and  $Z_{\text{BH}}^h$  in frequency domain given by Eq. 4.26, where here  $\tilde{\Psi}_h$  and  $\tilde{\Psi}_\infty$  are the solutions of the homogeneous problem Eq. (4.14) which satisfy the correct boundary conditions at infinity and at the horizon.

The gravitational wave energy spectrum emitted by this gravitational plunge of a smaller mass by a larger black hole in the frequency domain is the combination of each multipolar contribution  $l$

$$\left(\frac{dE}{d\omega}\right)_{2^l\text{-pole}} = \frac{1}{32\pi} \frac{(l+2)!}{(l-2)!} \omega^2 |Z_\infty^{\text{BH}}(\omega)|^2. \quad (4.41)$$

We show the energy spectrum of gravitational radiation for each multi-polar number  $l$  and their total combination in Fig. 4.8 below. The first two modes  $l = 0, 1$  have their multipolar contribution gauged away [179]. The following multipolar contributions are shown in Fig. 4.8.

As theoretically expected, the quadrupolar contribution  $l = 2$  is the dominant one and corresponds to the major contribution to the final spectrum of irradiated energy. Furthermore, its contribution, in the frequency domain, is centered around the real value of the fundamental quasinormal mode frequency. This result already anticipates the physical fact that the major part of the gravitational wave signal, as detected by a distant observer, will come as the ringing oscillation from the excitation of the fundamental quasinormal mode. The following multipolar contributions ( $l = 3, 4, 5, \dots$ ), as well as their overtones' contributions for the energy-spectrum of gravitational radiation are weaker in comparison to the fundamental quasinormal mode of  $l = 2$ .

Finally, the time-dependent gravitational waveform can be obtained by the inverse Fourier transformation of the amplitude. Computing the integral in Eq. (4.28), we numerically obtain the time-domain waveform of the gravitational waves measured by a distant observer. We show these time-domain waveforms in Fig. 4.9.

A closer look at Fig. 4.9 shows that the major part of the intermediate ringing oscillation in the time interval is very similar to the waveform of the fundamental quasinormal mode, i.e.

$$\text{Re}(\Psi_{n=0}(x \rightarrow \infty, t)) = \text{Re}(A_{n=0} e^{i\omega_{n=0}(t-t_0)}) = a_{n=0} e^{-i\omega_{i_{n=0}}(t-t_0)} \cos \omega_{R_{n=0}}(t - t_0) \quad (4.42)$$



- **Periodic Gaussian Pulses from a distant source in an acoustic black hole**

Finally, we discuss the problem of periodic Gaussian pulsations radially injected far away from a bathtub draining vortex. In the effective background spacetime of an acoustic black hole, the wave equation describing the evolution of acoustic perturbations from an external source  $S$  is, in the frequency domain, given by the same Eq. (4.12). This time, the effective potential is  $V(r, \omega)$  in Eq. (4.4), and  $\tilde{S}(r, \omega)$  is the source term in the frequency domain.

We take the external source to be some radially symmetric and periodic Gaussian pulsations that are 'turned-off' at the initial time  $t_0 = 0$ .

$$\tilde{S}_l(x, \omega) = A_l e^{-\frac{(x-x_3)^2}{\sigma}} \quad (4.43)$$

where  $x_3$  denotes the center of the Gaussian perturbation. This perturbation source is plotted in Fig. 4.10 for a few different scenarios we consider here. This initial behavior for the perturbation can be seen in Fig. 4.12 if we look at the first arcs for the initial times. Those arcs represent the harmonic oscillatory behavior of the Gaussian pulsations before the perturbation is 'turned-off'.

Now, we can obtain the acoustic black hole response for the perturbation source above in the frequency domain from the Green function's formalism. This response is given by Eq. (4.26), where again  $W$  is the Wronskian of the two L.I. solutions for the homogeneous associated equation.

This waveform amplitude in the frequency domain is shown in Fig. 4.11 for different values of the Gaussian's width parameter  $\sigma$ .

For the larger considered pulse width, namely  $\sigma = 2$ , the Gaussian packet is so wide that it does not experience the barrier's reflectivity. Instead, it completely passes through the barrier, being transmitted to the acoustic hole's interior. We can see that by looking at the response signal measured by a distant observer in  $x \rightarrow \infty$ . Its time-domain profile is dominated by the initial Gaussian arcs, generated by the initial perturbation. No quasinormal

mode oscillations are measured, and the time evolution of the perturbation quickly switches its behavior into the late-tail decay for later times. On the other hand, as we narrow the width of the Gaussian perturbative pulses, the relative excitation of the quasinormal mode overtones is increased when compared to the fundamental mode. From Fig. 4.11, we notice that narrower Gaussian pulses tend to excite higher QNMs overtones.

We can compute the time evolution of the waveform amplitudes in the frequency domain that are presented in Fig. 4.11. For that goal, we take the inverse Fourier transformation of those amplitudes. Indeed, in Fig. 4.12, we show the associated waveform signals in the time domain.

Notice that when higher QNMs overtones are excited, the resulting signals tend to increasingly mix more damped oscillation modes with smaller wavelengths and different decaying times. Those additional oscillation modes are added to the waveform strain dominated by the fundamental QNM mode oscillation, which is shown in Fig.4.12.

- **Spectral Decomposition of the GW Signal into the BHs' quasinormal modes**

Finally, in this section, we aim to decompose the final time-domain waveform into its quasinormal modes' oscillations

$$\text{Re}(\Psi_{n=0}(x \rightarrow \infty, t)) = A_{n=0} e^{-i\omega_{i_n=0}(t-t_0)} \cos \omega_{R_{n=0}}(t - t_0). \quad (4.44)$$

This way, we can obtain the complex frequency values of those quasinormal modes  $\omega_n = \omega_{R_n} + i\omega_{i_n}$ , and their relative excitation coefficient  $A_n$ .

We clarify again that the same procedure applied for the quasinormal modes' spectroscopy of the final wave signal is equally valid for both previous examples: the GW ringing radiation emitted by the gravitational plunge of a small mass into a larger black hole (Fig. 4.9); and the acoustic waves emitted by a ringing perturbed acoustic black hole (Fig. 4.12). The mathematical equivalence between their description is what allows for this equivalent treatment. For simplicity, we choose the acoustic waves around the perfect draining vortex (black hole

analog model) as the prototypical example to illustrate how this procedure works.

The main conclusion that can be drawn from this treatment is that the frequencies of the quasinormal modes should not depend on the initial perturbation injected into our system but only on the background effective spacetime. Hence, by determining those quasinormal frequencies, we fully characterize the acoustic or astrophysical black hole background spacetime.

To accomplish our spectral decomposition for the spectroscopy of gravitational (or acoustic) waves in terms of their composing quasinormal modes, a standard algorithm is usually prescribed.

- 1 Firstly, we select an intermediate time interval for our analysis. We choose an interval that better fits the features described for the second stage/ ringdown phase described previously for the waveform signal [171]. We show one example of this time interval in Fig. 4.13. Notice that the dominant physical behavior for the waveform within this interval is a quasi-periodic damped oscillation, exactly as we expect from the quasinormal modes' dominated phase.
- 2 The second step consists of fitting the quasinormal modes parameter with this time domain waveform. We start with the fundamental quasinormal mode. By fitting the three parameters  $A_{n=0}$ ,  $\omega_{i_{n=0}}$ , and  $\omega_{R_{n=0}}$ , we can infer with reasonable accuracy the complex frequency of the fundamental quasinormal mode, and its quasinormal excitation coefficient  $A_n$ . We illustrate this step in Fig. 4.14.
- 3 Then, we subtract the resulting fundamental quasinormal mode contribution from the full signal waveform in the time domain. With this waveform strain, we can repeat the procedure discussed above to obtain the complex frequency of the quasinormal mode first overtone.
- 5 We can continue this procedure for as long as our resolution permits. It is a widely known fact [180] that the initial time  $t_0$  we use slightly contaminates our inferred

quasinormal modes' frequencies. That is one of the limitations of the gravitational waves' spectroscopy with quasinormal modes, as explained in Ref.[180]. We cannot fully remove the contribution from the initial prompt signal associated with the initial perturbation.

With this example, we have successfully illustrated how to apply gravitational wave spectroscopy in terms of quasinormal modes for the time domain signal of a certain gravitational waveform. Although our injected waveforms are obtained here from the linear order perturbation theory of acoustic and astrophysical black holes, this procedure can be extended to any waveform strain. This extension is guaranteed by the fact that for a final relaxing black hole emerging from the collapse of a relativistic star or a binary merger, the late-stage dynamics of this perturbed background BH spacetime can be successfully described by linear perturbation theory.

#### **4.3.2.3 Numerical and semi-analytical methods for calculating the QNMs spectra**

In the previous subsection, we presented an example that illustrated how we can compute the quasinormal modes of a certain black hole by decomposing its ringdown signal into its oscillating quasinormal modes. This procedure is very insightful from the physical point of view, since in some sense we are emulating the observational efforts of astrophysicists when analyzing a certain gravitational wave signal measured by the GW interferometers. On the other hand, approaching the computation of quasinormal modes with this method adds a large and unnecessary complexity to the problem, since now, we are not only computing the frequency-domain waveform amplitude, but also its associated signal in time-domain. Finally, after all of those calculations, we decomposed the final GW strain into its composing decaying oscillations, namely the quasinormal modes. Furthermore, this approach also added some uncertainties that can be avoided by a more direct approach. In fact, the initial perturbation source  $S$  can still 'contaminate' our results for the late-stage ringdown signal.

The inference methods used for fitting the signal with its quasinormal modes are also a source of uncertainty.

To avoid those problems, we list here some different approaches for calculating the quasinormal modes of a black hole spacetime or for the effective spacetime of a black hole analog system. The first one is the numerical procedure, based on the formal definition of quasinormal modes derived from Green’s function formalism, which we discussed throughout this section. The second approach is an iterative procedure, also based on the Green’s function formalism. The third and final method presented here is a semi-analytical method based on the WKB approximation for quantum mechanical scattering potentials. This last approach is motivated by the Schrödinger-like form of the wave equations describing the evolution of perturbation in those background spacetimes.

### • Numerical Approach for Evaluating Quasinormal Modes

As we have introduced in Sec. 4.3.2.1, the quasinormal modes are formally defined as the discrete set of poles of Eq. (4.26) in the frequency complex plane. For each pole, we have a complex frequency  $\omega_n = \omega_{R_n} + i\omega_{i_n}$  such that the frequency domain amplitude in Eq. (4.26) diverges. From Eq. (4.26), we notice that those divergences are determined by the roots of the Wronskian  $W$ . So, in other words, to find the discrete set of complex frequencies of the QNMs  $\omega_n$ , we must develop a *rootfinding* code for the Wronskian of the two LI solutions of the homogeneous equation. A *shooting method*’s code does this trick. For that, we only need to set the initial boundary conditions of the two wave solutions at the asymptotic extremities, and then we look for the complex values of  $\omega$  that annul  $W$ .

That numerical method provides us with one of the most reliable and accurate approaches for finding the quasinormal modes of any black hole’s spacetime, including rotating black holes, for example. Its main disadvantage concerns the calculating time. Depending on the overtone order, the waiting time for finding an associated frequency can last from some seconds (lower overtones) to some hours (higher overtones).

- **Iterative Method for Evaluating Quasinormal Modes**

The Leaver method [181] is considered one of the most accurate approaches to evaluate quasinormal modes' frequencies. The idea consists of inputting an initial guess for the wave solution that satisfies at the same time both the asymptotic behavior of the solution at the singular points of the equation (Eq. (4.33)). The following step is to identify the mathematical function that vanishes at the black hole horizon and then define a power series of that function. By multiplying our initial guess by the obtained power series, we must get an ansatz to be inserted in the perturbation master wave equation. We must then be able to find a recurrence relation for the coefficients of the series, and the solution can be written in terms of continued fractions. This method finds the frequencies of the quasinormal modes up to any desired accuracy order.

- **Semi-analytical Method for Evaluating Quasinormal Modes**

Finally, our last approach for finding the frequencies of the quasinormal modes relies on the WKB approximation for the Schrödinger equation in quantum mechanics. We can use this approach here since our master wave equation describing the evolution of gravitational/test field perturbations in the frequency domain is a Schrödinger-like equation.

To accomplish the calculation of BH's quasinormal frequencies with the WKB method [182], we employ a small adaptation of the method for our context here. This adaptation of the WKB method was proposed initially by Iyer and Will [183] up to third order, and posteriorly upgraded to sixth order by Konoplya [182]. From those frameworks, we are led to a semianalytic technique for determining black holes' complex quasinormal mode frequencies for any kind of field perturbation, including gravitational ones. It already incorporates the boundary conditions

$$\Psi \sim e^{+i\omega x}, \quad x \rightarrow +\infty, \quad (4.45)$$

$$\Psi \sim e^{-i\omega x}, \quad x \rightarrow -\infty. \quad (4.46)$$

The formula for the frequencies in the sixth-order WKB method is the following

$$\frac{i(\omega^2 - V(r_{max}))}{\sqrt{-2\partial_*^2 V|_{r_{max}}}} - \sum_{i=1}^6 \Lambda_i = n + \frac{1}{2}, \quad (4.47)$$

where  $n$  is the overtone number,  $r_{max}$  is the point at which the potential reaches its maximum and the corrections  $\Lambda_i$  contain the derivatives of the potential evaluated at  $r_{max}$  up to the 12th order and are reported in [182, 184]. This formula is an improvement over the third-order formula obtained in [183].

With equation (4.47), we can finally evaluate the quasinormal frequencies of any perturbation field for the Black Hole spacetime under investigation. For this purpose, we only need to replace the potential  $V$  in that formula with one of the potentials derived in the previous section. This approach provides very accurate results [184] when compared to the previously introduced calculation procedures introduced. In Ref.[1], we considered the application of this method for the calculation of the quasinormal modes of Dirac perturbation in the LQG polymerized effective spacetime proposed by BMM [148, 154].

### 4.3.3 Boundary Conditions for Extreme Compact Objects Solutions: Trapped Quasinormal Modes and Resonant Scattering Modes

In this section, we discuss how we address the solution of Eq. (4.12) in the frequency domain for the case of perturbed exotic compact objects (ECOs). For ECOs, the boundary conditions for the perturbation field at one of the extremities must be changed. Indeed, for the reflective surface at  $x_0$ , the boundary conditions must now be re-defined by adding a reflecting condition for the perturbation field. In the frequency domain, the boundary conditions that need to be incorporated at the reflective surface  $x_0$ , replacing Eq. (4.25) from the black holes, must be given by

$$\tilde{\Psi}(x \approx x_0, \omega) = A^{\text{wall}} [e^{-i\tilde{\omega}x} + K e^{-2i\tilde{\omega}x_0} e^{i\tilde{\omega}x}] , \quad (4.48)$$

where  $\tilde{\omega} = \omega - \Omega_{s,l}a$ , for astrophysical ECOs, and  $\tilde{\omega} = \omega - mC/r_h^2$  for the imperfect draining vortex. The reflectivity parameter at the wall in  $x_0$  is specified by the function  $K = K(\omega)$ .

The  $e^{-2i\tilde{\omega}x_0}$  factor for the outgoing waves in  $x_0$  encompasses the phase-change experienced by the reflected wave as it crosses the potential barrier and travels back and forth from the barrier to the reflective boundary.

For spatial infinity, the boundary conditions are exactly the same as for the BHs

$$\tilde{\Psi}(x \rightarrow \infty, \omega) = A^{\text{in}} e^{-i\omega x} + A^{\text{out}} e^{+i\omega x}. \quad (4.49)$$

In order to solve the time-independent wave equation with the specific BCs defined above for ECOs, we must use Green's function formalism again. Since the master wave equation for the radial perturbation remains the same, i.e., Eq. (4.12), and the only changes are in the boundary conditions, the two L.I. solutions of the associated homogeneous wave equation are the same as the one obtained in the black hole case, namely  $\tilde{\Psi}_h(x, \omega)$  and  $\tilde{\Psi}_\infty(x, \omega)$ , defined in Eqs. (4.22), (4.23). For the general solution, however, the waveform in the frequency domain will be different. The presence of the reflecting boundary conditions drastically changes the evolution of perturbation in the background spacetime. Mark et al [59] have shown that for ECOs, the solution of Eq. (4.12) for a distant observer in  $x \rightarrow \infty$ , in the freq. domain, is given as

$$\tilde{\Psi}_{\text{ECO}}(x \rightarrow \infty, \omega) = \tilde{Z}_{\text{ECO}}^\infty(\omega) e^{i\omega x} \quad (4.50)$$



This time, however, the amplitude in the frequency domain is given by

$$\tilde{Z}_{\text{ECO}}^{\infty}(\omega) = \tilde{Z}_{BH}^{\infty}(\omega) + \mathcal{K}(\omega)\tilde{Z}_{BH}^h(\omega) \quad (4.51)$$

Where  $\tilde{Z}_{BH}^{\infty}$  is the asymptotic waveform amplitude for the associated BH case at infinity, as defined in Eq. (4.26). Likewise,  $\tilde{Z}_{BH}^h$  is the BH's asymptotic waveform amplitude calculated at the objects' surface, close to the associated event horizon. This ECO's surface  $x_0$  is where the boundary condition is expected to be defined. Hence, the ECO frequency domain amplitude of the waveform at a distant observer is a combination of the associated black hole response, with the black hole's wave amplitude at its 'would-be' horizon. This black hole's waveform amplitude at  $x_0$  modulates another function  $\mathcal{K}$  of  $\omega$ , for the ECO response, called the transfer function. This function completely details our ECO model, and it is defined [59, 185, 58] as

$$\mathcal{K} = \frac{T_{BH}R_{BH}e^{-2i\omega x_0}}{1 - R_{BH}Ke^{-2i\omega x_0}} \quad (4.52)$$

where  $K = K(\omega)$  is the reflectivity at  $x_0$  boundary.

Qualitatively, Eq. (4.52) states that the ECO'S waveform in the frequency domain, measured by distant observers, can be understood as the sum of the same equivalent BH's response, along with an additional signal  $\mathcal{K}\tilde{Z}_{BH}^h$ . This additional emission arises from the reflection of the radiation that would normally enter the horizon and is reprocessed by the transfer function  $\mathcal{K}$  at the reflective boundary in  $x_0$ .

The power of Eq. (4.51) is that it allows us to compute the total asymptotic waveform in an ECO spacetime with the corresponding waveforms from the associated black hole spacetime. For that, all we need to do is to specify a particular choice of  $K(\omega)$ , which corresponds to a particular model of the reflectivity properties at the ECO's surface, and  $x_0$ , which specifies the ECO's compactness.

The poles of this new amplitude for the ECO in the frequency domain, however, are

different from those of the associated BH, which means that the ECOs' QNMs will be different from the BH's. The additional quasinormal modes of the ECOs are the poles of the transfer function  $\mathcal{K}(\omega)$ , and we call them trapped quasinormal modes, since they obey the boundary conditions in Eqs. (2.59). We also refer to the poles of the ECO's waveform amplitude as resonant modes, since they are 'quasi-bound' by the cavity between the boundary  $x_0$  and the potential barrier, see Fig. 2.5.

In Fig. 4.15, we plot the intrinsic ECO transfer function for a few different analog ECO models defined by an imperfect draining vortex. If we look at the transfer function in the frequency domain, we can see the resonant modes of the ECO as the narrow spikes. Each peak of the transfer function  $\mathcal{K}$  on the real frequency axis corresponds to a resonant state. The real part of the trapped quasinormal mode is related to its peak location, while the imaginary part is related to the width of this peak.

As we see in Fig. 4.15, by increasing the boundary reflectivity  $K(\omega)$  in  $x_0$  we make the resonant peaks narrower and more pronounced in the frequency domain. Modes with narrower peaks have smaller frequency imaginary parts, which will in turn increase the damping time of the resonant mode  $\mathcal{T}_n = (\omega_n)^{-1}$ . Hence, the associated resonant modes are longer-living. This is physically expected in a potential well created between a reflective surface and a potential barrier. As we see in those results, increasing the reflectivity of the reflective wall tends to amplify the lifetime of the trapped modes. Since a 'higher portion' of the wave is being reflected by the compact object's surface, rather than absorbed, those waves will be trapped in the well for a longer time before they actually manage to escape the well (being absorbed by the object, or being sent back to infinity). Therefore, larger reflectivity on the surface of the compact object implies exponentially smaller imaginary parts for the modes, which in turn leads to narrower widths in the transmission plots. For the waveform amplitude of a black hole, we see that the black hole QNMs have more broad and wide resonant "peaks" in the frequency domain. So the imaginary part is larger, and accordingly, the BHs's quasinormal modes decay more quickly.

Furthermore, we can also see how the transfer function depends on  $x_0$  in Fig. 4.16. In the frequency domain, we see that the effect of increasing  $x_0$  corresponds to reducing the distance between each resonant mode, while also increasing the number of resonant modes. Physically, increasing  $x_0$  corresponds to enlarging the cavity size, so we can expect a longer time between each reflection of the transmitted waves. As a consequence, we can fit more half-wavelengths traveling within the cavity's size. In a Fourier analysis [59], increasing the number of resonant modes and decreasing the frequency spacing between the resonant modes in the freq. domain implies a larger period of time between each wave reflection. For resonant modes with an approximately uniform frequency spacing between them, such as we have here, this frequency spacing will be related to the period of time according to

$$\Delta\omega \approx \frac{2\pi}{2T}. \quad (4.53)$$

Where we have here that

$$T = 2|x_0|. \quad (4.54)$$

The time period in Eq. (4.54) corresponds to a round trip of the wave from the potential barrier to the reflective surface in  $x_0$ . The derivation of those formulas is presented in the appendix of Ref. [59].

Finally, the time evolution of the perturbation at the distant observer can be obtained by taking the inverse Fourier transformation of the FD waveform defined in Eq. (4.50).

$$\Psi_{\text{ECO}}(x, t) = \frac{1}{\sqrt{2\pi}} \int_{-\infty}^{\infty} \tilde{\Psi}_{\text{ECO}}(x, \omega) e^{i\omega t} dt \quad (4.55)$$

However, replacing the Eq. (4.51) into Eq. (4.55), we get that

$$\Psi_{\text{ECO}}(x \rightarrow \infty, t) = \Psi_{\text{BH}}(x \rightarrow \infty, t) + \Psi_{\text{reproc.}}(x \rightarrow \infty, t) \quad (4.56)$$

where

$$\Psi_{\text{reproc.}}(x \rightarrow \infty, t) = \frac{1}{\sqrt{2\pi}} \int_{-\infty}^{\infty} \mathcal{K}(\omega) \tilde{Z}_{BH}^h(\omega) e^{i\omega t} dt \quad (4.57)$$

That is a key result here. It shows that the waveform both in time and frequency domain can be seen as the sum of the usual emission in a BH spacetime, along with an additional signal coming from  $\mathcal{K} \tilde{Z}_{BH}^h$ . As we discussed earlier, this additional emission arises from the reflection of the radiation that would normally enter the BH horizon, but it is reprocessed by the transfer function  $\mathcal{K}(\omega)$  at  $x_0$ . To make this qualitative discussion of Eq. (4.56) even more clear, we can consider in the following an application of Eqs. (4.56) and Eq. (4.51) for a Gaussian source perturbation into an ECO analog spacetime. This example will help us clarify what is the signature of the ECO's reflecting boundary condition in the final waveform detected by a distant observer. So, consider the Gaussian perturbation source  $\tilde{S}(x, \omega)$  in Eq. (4.43), into the time-independent wave equation Eq. (4.12) for an ECO from an analog acoustic effective spacetime.

$$\tilde{S}_l(x, \omega) = A_l e^{-\frac{(x-x_3)^2}{\sigma_l^2}}$$

We now use the Green function's formalism, namely Eq. (4.26), to solve for the black hole waveforms in the frequency domain. With those BHs' waveforms, we obtain the ECO waveform in the frequency domain through Eq. (4.51).

We divide our results into two scenarios: the regime of small cavities and large cavities. They are represented in Fig. 4.17, where we plot an effective potential for scattering perturbations around the analog ECO with two distinct scenarios for  $x_0$ . The resulting waveforms in the frequency domain, for analog acoustic black holes are shown in Figs. 4.18. In the following, we also present the results for the associated ECO scenarios, contrasting them with their associated black hole case. We organize those graphics in the following way: the BH asymptotic waveform at infinity  $x \rightarrow \infty$  is represented by a solid black line, the BH asymp-

otic waveform at the reflecting boundary  $x \rightarrow x_0$  is represented by a dashed black line, the ECO waveform in FD  $\tilde{\Psi}_{\text{ECO}}$  are shown as colored dashed lines. For all cases considered in the following, the Gaussian perturbation source's parameter is fixed at  $\sigma = 0.5$ .

#### 4.3.3.1 Small cavities scenario

For  $x_0 = -3$ , we only get a few additional ECO's resonant modes, or additional trapped quasinormal modes. This is expected since the cavity is too small. In Fig.4.16, we see those extra few resonant modes contrasting with the large number of extra resonant modes arising in a large cavity scenario  $x_0 = -20$ . The waveform amplitudes in the frequency domain for those two distinct scenarios are shown in Fig. 4.19. Their associated waveforms in the time domain, as given by Eq.(4.57), are shown in fig. 4.20.

For the case with  $x_0 = -3$ , the time evolution of the perturbation appears as a single decaying sinusoidal wave packet. This behavior can be interpreted as the excitation of only a few resonant modes of  $\tilde{K}(\omega)$ . This case is slightly similar to the BHs' QNM ringdown, except that it decays slower. In some sense, we can physically interpret this result as picturing the incoming perturbation, which eventually encounters the barrier peak. While major part of this perturbation is directly reflected by the barrier, other part transmits to inside the cavity. Inside the small cavity, this perturbation wave will quickly bounce back and be transmitted through the barrier again. Finally, after that, this signal will encounter the firstly major reflected portion of the perturbation wave and they will mixture themselves into a single final decaying sinusoidal wave packet.

#### 4.3.3.2 Large cavities and the Echoes

For  $x_0 = -20$ , we have that the cavity size and the phase factor  $2\omega x_0$  is larger. Accordingly, the wave takes longer to travel from the potential barrier to the reflective boundary. As we have seen, this leads to more resonant modes, and a shorter frequency-spacing between the modes (see 4.19) . To stress special attention to the role played by a large cavity size, we fix

its value at  $x_0 = -20$ , and contrast two distinct reflectivity scenarios, one for  $K = 0.5$  and the other for  $K = 0.75$ . We see the associated waveforms in the frequency domain for those two scenarios in Fig. 4.21. The time-domain associated signals are presented in Fig. 4.22.

At first sight, we see that the  $Z_{\text{BH}}^\infty$  is dominant over small frequencies, explaining why we have the BHs' ringdown signal dominating in small times, which is precisely where the BH's fundamental QNM is located (see Eq. (4.60)). That explains why the first part of the time domain signal is very similar to the black hole's signal in Fig. 4.22.

For intermediate and high frequencies,  $Z_{\text{BH}}^h(\omega)$  starts playing a more significant role, modulating the transfer function into the final signal  $\tilde{K}$ . As we know,  $\tilde{K}$  carries the trapped quasinormal modes and all the information about the ECOs. So the ECOs' parameter will dictate the behavior of the waveform over intermediate and high frequencies. At this intermediate/high-frequency regime, the ECO's total wavefunction in the frequency domain is composed of a group of very peaky resonant cliffs, with an approximately constant spacing between them, given approximately by  $\delta\omega \approx 2\pi/2x_0$ . As we know from Fourier analysis (see appendix of Ref. [59]) when we have a combination of equally-spaced narrow peaks, the time domain associated signal is expected to be a periodic repetition of a damped-oscillation. And that is why we see the following pattern for the time domain signal in Figs. 4.20 and 4.22. For large values of the cavity parameter  $x_0$ , the final ECO's waveform, as detected by a distant observer, appears as a sum of distinct echo pulses following the first ringdown signal.

The time decay of those echoes, similarly to a single mode in the frequency domain, is related to the reflective parameter  $K$ , while the time periodicity of those echoes, and equivalently the frequency-spacing between the modes, is dictated by the cavity size  $x_0$ .

Another insightful way to visualize and understand the nature of those echoes can be achieved if we consider the time evolution of the perturbation in this ECO spacetime, given by Eq. (4.56), and we expand the transfer function as a geometric series:

$$\mathcal{K}(\omega) = \frac{T_{BH}R_{BH}e^{-2i\omega x_0}}{1 - R_{BH}Ke^{-2i\omega x_0}} = T_{BH}R_{BH}e^{-2i\omega x_0} \sum_{n=1}^{\infty} (R_{BH}K)^{(n-1)} e^{-2i(n-1)\omega x_0}. \quad (4.58)$$

This shows that the additional signal takes the form of a series of terms, each reprocessing the waves that impinge on the boundary condition with a different 'sub-transfer' function.

The zeroth order ray is the  $\tilde{Z}_{BH}$  term, representing the radiation that would also be detected by the distant observer in the black hole case. Its time evolution  $\Psi_{BH}(x \rightarrow \infty, t)$  is the same as we would obtain in the BH case. The additional terms  $\Psi_{\text{reproc.}}$  are described by  $\mathcal{K}$  expanded as in Eq. (4.58), which gives us

$$\begin{aligned} \mathcal{K}(\omega) &= \frac{T_{BH}R_{BH}e^{-2i\omega x_0}}{1 - R_{BH}Ke^{-2i\omega x_0}} = T_{BH}R_{BH}e^{-2i\omega x_0} \sum_{n=1}^{\infty} (R_{BH}K)^{(n-1)} e^{-2i(n-1)\omega x_0} = \\ &T_{BH}R_{BH}e^{-2i\omega x_0} + T_{BH}R_{BH}e^{-2i\omega x_0} (R_{BH}K)e^{-2i\omega x_0} + T_{BH}R_{BH}e^{-2i\omega x_0} (R_{BH}K)^2 e^{-2 \cdot 2i\omega x_0} + \dots \end{aligned} \quad (4.59)$$

As we can see in Ref. [59], this first term of the expansion is, qualitatively, the result of the primary reflection of  $\Psi$  off of the boundary at  $x_0$ , which generates the factor  $R_{BH}$ , along with the phase change factor  $e^{-2i\omega x_0}$ . The phase change corresponds to a time delay between the first pulse reflected by the potential barrier, with the main burst due to the pulse's extra round trip journey between the boundary at  $x_0$  and the potential barrier. When reaching the angular momentum barrier, the pulse is partially transmitted by the barrier  $T_{BH}$ , which adds this additional term  $T_{BH}$ . The remaining part is partially reflected inside the cavity again, which explains an additional  $R_{BH}$  term for the following term in the expansion. This following term is associated with the second pulse. The successive terms are obtained by an integer number of bounces between the potential barrier, and the reflective boundary, each one adding a  $R_{BH}$  and a  $K$  respectively. After that, they are all partially transmitted through the potential barrier, which contributes with  $T_{BH}$ . The trip back and forth of the

wave inside the cavity adds a propagation delay described by the phase change term of  $e^{-2i\tilde{\omega}x_0}$ .

This picture of the successive echoes is made even more apparent by transforming the FD domain waveform into its time-domain associated wave function. For a distant observer, we have

$$\Psi_{\text{ECO}}(x \rightarrow \infty, t) = \Psi_{\text{BH}}(x \rightarrow \infty, t) + \Psi_{\text{reproc.}}(x \rightarrow \infty, t) \quad (4.60)$$

where  $\Psi_{\text{reproc.}}$  is given by

$$\begin{aligned} \Psi_{\text{reproc.}}(x \rightarrow \infty, t) &= \frac{1}{\sqrt{2\pi}} \int_{-\infty}^{\infty} dt \tilde{Z}_{\text{BH}}^h(\omega) e^{i\omega t} T_{\text{BH}} R_{\text{BH}} e^{-2i\omega x_0} \sum_{n=1}^{\infty} (R_{\text{BH}} K)^{(n-1)} e^{-2i(n-1)\omega x_0} = \\ &= \frac{1}{\sqrt{2\pi}} \int_{-\infty}^{\infty} dt \tilde{Z}_{\text{BH}}^h(\omega) e^{i\omega t} T_{\text{BH}} R_{\text{BH}} e^{-2i\omega x_0} + \frac{1}{\sqrt{2\pi}} \int_{-\infty}^{\infty} dt \tilde{Z}_{\text{BH}}^h(\omega) e^{i\omega t} T_{\text{BH}} R_{\text{BH}} e^{-2i\omega x_0} (R_{\text{BH}} K) e^{-2i\omega x_0} \\ &+ \frac{1}{\sqrt{2\pi}} \int_{-\infty}^{\infty} dt \tilde{Z}_{\text{BH}}^h(\omega) e^{i\omega t} T_{\text{BH}} R_{\text{BH}} e^{-2i\omega x_0} (R_{\text{BH}} K)^2 e^{-2.2i\omega x_0} + \dots \end{aligned} \quad (4.61)$$

After the  $\Psi_{\text{BH}}$  time evolution contribution, each additional term corresponds to a successive echo in the time domain. We illustrate this qualitative analysis in the graphics in Fig. 4.23.

We have now finally concluded our discussion on the ringdown waveforms for ECOs, black holes, and their analog models. We studied here their amplitudes in the frequency domain and their time evolution as measured by a distant observer in infinity  $x \rightarrow \infty$ . This section opened a vast range of possibilities for the phenomenology of black holes, exotic compact objects, and analog gravity systems for compact objects. In the next sections, we will focus on studying the scattering properties of BHs, ECOs, and analog systems in the physical regime in which we can control the input waves.



## 4.4 The BH and ECOs Scattering of Fields

Since this thesis mainly focuses on introducing an inverse problem from the transmission and reflection coefficients, we conclude this chapter by studying the numerical setup for solving the direct problem of obtaining those scattering quantities numerically. The results of the direct study then provide us with the starting point for our investigation of the inverse problem. Our entire discussion is based on the frequency domain formalism presented previously.

The equation describing the scattering of fields in both BHs and ECOs spacetime is the homogeneous associated time-independent wave equation, Eq. (4.14), since we are not considering any additional external perturbation. Accordingly, our L.I. wave solutions are, once again, the pair  $\Psi_h(x, \omega)$ ,  $\Psi_\infty(x, \omega)$ , defined in Eqs. (4.22),(4.23). The general solution, in turn, is a linear combination of those two L.I. wave solutions, both for the BHs and ECOs spacetimes. The main difference in the description of the scattering properties of those distinct objects is then provided by the boundary conditions at the extremities.

For black holes, we have that

$$\tilde{\Psi}_{\text{BH}}(x, \omega) = A^{\text{wall}} e^{-i\tilde{\omega}x}, \quad \text{for } x \rightarrow -\infty, \quad (4.62)$$

$$\tilde{\Psi}_{\text{BH}}(x, \omega) = A^{\text{in}} e^{-i\omega x} + A^{\text{out}} e^{+i\omega x}. \quad \text{for } x \rightarrow +\infty \quad (4.63)$$

For exotic compact objects, on the other hand, we have

$$\tilde{\Psi}_{\text{ECO}}(x, \omega) = A^{\text{wall}} [e^{-i\tilde{\omega}x} + K e^{-2i\tilde{\omega}x_0} e^{i\tilde{\omega}x}], \quad \text{for } x \approx x_0, \quad (4.64)$$

$$\tilde{\Psi}_{\text{ECO}}(x, \omega) = A^{\text{in}} e^{-i\omega x} + A^{\text{out}} e^{+i\omega x}. \quad \text{for } x \rightarrow +\infty \quad (4.65)$$

As we see, at spatial infinity, the boundary conditions are equally defined. The main difference between these two cases is the core reflectivity of the ECOs' spacetime, incorporated at their reflective surface in  $x_0$ . That difference in the boundary conditions drastically changes their scattering properties compared to the black hole case, as we later see within this framework.

From the amplitudes  $(A_{\text{in}}, A_{\text{out}})$ , we can define the reflection and transmission coefficients as

$$|T|^2 = \frac{|A^{\text{wall}}|^2}{|A^{\text{in}}|^2} (1 - |K|^2), \quad (4.66)$$

$$|R|^2 = \frac{|A^{\text{out}}|^2}{|A^{\text{in}}|^2}. \quad (4.67)$$

They relate to each other by

$$|R|^2 = 1 - \frac{\tilde{\omega}}{\omega} |T|^2. \quad (4.68)$$

We also assume the notation  $|T|^2(E) = t(E)$ .

By expressing our general solution  $\Psi$  decomposed into this basis of solutions  $\Psi_h(x, \omega)$ ,  $\Psi_\infty(x, \omega)$ , we can obtain the following relations between the coefficients

$$A_h^+ = \frac{\omega}{\tilde{\omega}} A_\infty^-, \quad (4.69)$$

$$\frac{A^{\text{in}}}{A^{\text{wall}}} = \frac{\tilde{\omega}}{\omega} (A_h^+ - A_h^- K e^{-2i\tilde{\omega}x_0}), \quad (4.70)$$

$$A^{\text{wall}} = \frac{\omega}{\tilde{\omega}} \frac{(A_\infty^- A^{\text{out}} - A_\infty^+ A^{\text{in}})}{K e^{-2i\tilde{\omega}x_0}}. \quad (4.71)$$

These are the basic relations that are needed for the direct scattering problem calculation and further discussions about their derivation can be found in Ref.[48].

Finally, for the direct problem, we first need to evaluate the set of coefficients  $(A_h^+, A_h^-, A_\infty^+, A_\infty^-)$ . This is accomplished by numerically evolving the  $\Psi_h(x, \omega)$  solution from the reflective surface at  $x_0$  to infinity, and vice versa with the  $\Psi_\infty(x, \omega)$  solution. With the evaluated coefficients, and by using Eqs. (4.69), (4.70) and (4.71), we can then determine the coefficients  $A^{\text{wall}}, A^{\text{in}}, A^{\text{out}}$  and, accordingly, the transmission and reflection coefficients  $T$  and  $R$ , for both BHs and ECOs scenarios respectively.

Finally, the transmission and reflection coefficients, calculated here by means of the direct numerical problem, provide the starting point to study the inverse method that we consider within this thesis. While not observationally available for astrophysical observations, in principle, these are the observables that could be obtained through laboratory experiments of analog gravity systems [79]. In Fig. 4.24, we show a few examples of those coefficients for analog ECO systems.

Notice here that, analogously to the transfer function in the previous section, the transmission and reflection present resonant peaks associated with the resonant modes defined by the cavity. As we usually get in the context of extreme compact objects perturbation theory,  $E_{0_n}$  describes the location of the peak associated with the  $n$ -th mode, while the imaginary part  $E_{1_n}$  is proportional to its width.

To investigate the role of the wall's reflectivity in the resulting scattering coefficients (transmission), in Fig. 4.24 we chose some different physical scenarios to investigate by fixing different values for our reflectivity constant associated with the reflective wall, namely  $(K = 0.5, 0.75)$  and two different values for the boundary condition's location  $x_0$ . Meanwhile, we have fixed a value for the harmonic constant  $m$  ( $m = 4$ ), and  $C = 0$  for the rotation constant. The role of the harmonic constant  $m$ , and the rotation constant  $C$  will be investigated in Chapter 6, and Chapter 8, respectively.

As we can see in the graphics on Fig. 4.24 above, as we increase the values of the reflectivity parameter  $(K)$ , the intensity of the transmission/reflection at the resonant peaks gets higher. On the other hand, the peaks tend to get exponentially narrower. This means

that increasing the reflectivity of the wall amplifies the effect of the resonance, both in the transmission/reflection, and it also increases the damping time of the trapped modes. That is physically plausible, since those waves are being more reflected by the wall, and hence being more strongly trapped and confined within the cavity between the wall and the barrier, those modes tend to live longer. Moreover, the asymptotic behavior of the transmission coefficient tends to be diminished as the wall's reflectivity increases, since for high energies, the transmission through the potential barrier becomes dominant over the absorption through the wall. In Fig. 4.24 we also detach the role played by the location of the reflective boundary  $x_0$  which mainly controls the number of resonance peaks, and strongly impacts their spacing.

We have now finished our analysis of the direct problem in perturbation theory for both astrophysical and analog models of black holes and ECOs. In the following chapter, we develop our inverse method, introducing its formulas and explaining how it works. Then, we apply this method to the transmission coefficients we shall. From now on, we will focus on analog black hole and ECO systems, since those are the only ones we can experimentally obtain the scattering coefficients from. As we have seen, there is a mathematical equivalence between the description of the evolution of linear perturbations in BH/ECO's spacetimes and the evolution of perturbation in their analog systems. In theory, the inverse method to be developed within this thesis could be successfully applied to both cases. The unique availability of the experimental data for scattering coefficients in analog gravity systems motivated us to choose those systems as the main prompt model for applying our inverse method developed within this thesis.

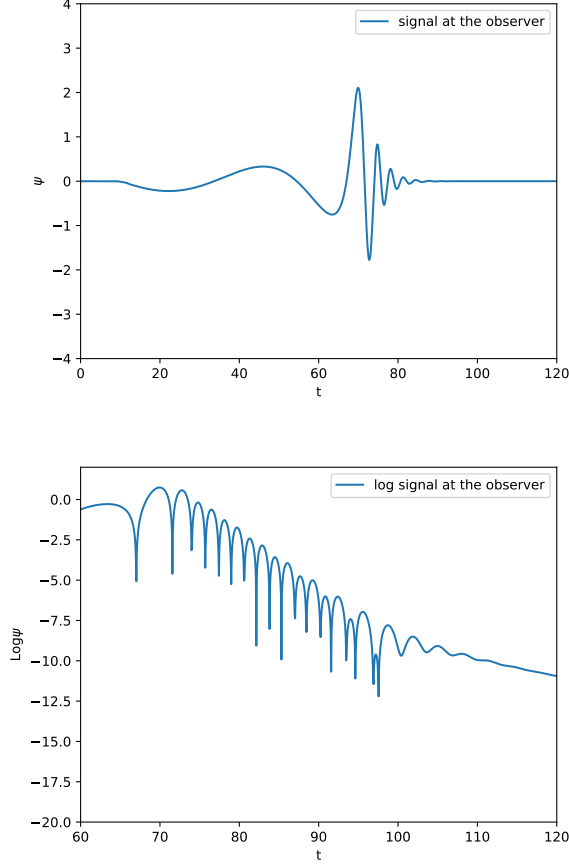


Figure 4.2: GW Strain measured by a distant observer in  $x_2$  (tortoise coordinate) from a Schwarzschild astrophysical black hole, and generated by the prompt perturbation in (4.9). We directly evolved this perturbation (an inwards propagating Gaussian pulse) in the time domain via the finite difference scheme in Eq. (4.8). In the upper panel, we see a plot of the time evolution of a gravitational wave signal measured by a distant observer in  $x_2$ . In the lower panel, we see the logarithmic plot of this same signal. Here we have considered the Schwarzschild black hole with  $L = 2$ , and  $M = 1$ . The initial perturbation was released from  $x_3 = 30$  with  $\sigma = 3$ .

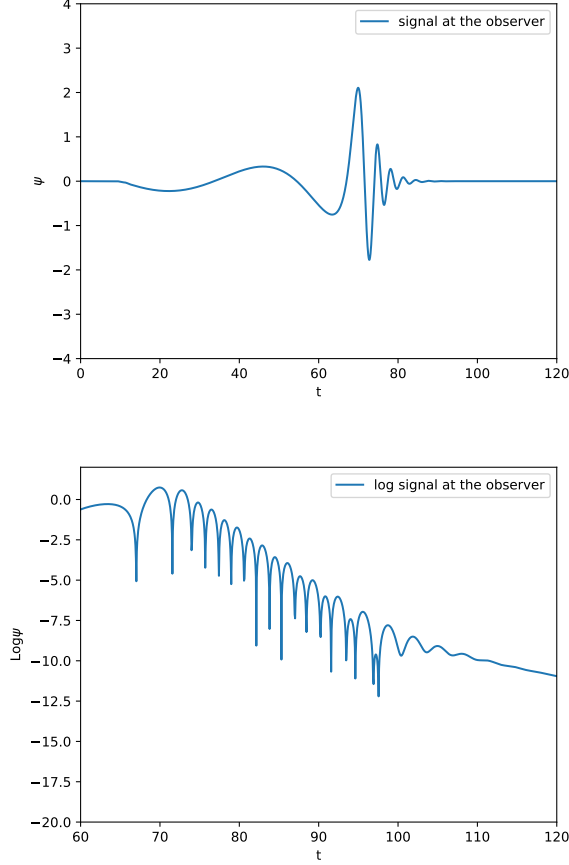


Figure 4.3: Waveform measured by a distant observer in  $x_2$  (tortoise coordinate) from the acoustic analog to a black hole, namely the sonic hole, and generated by the prompt perturbation in (4.9). We directly evolved this perturbation (an inwards propagating Gaussian pulse) in the time domain via the finite difference scheme in Eq. (4.8). In the upper panel, we see a plot of the time evolution of a acoustic wave signal measured by a distant observer in  $x_2$ . In the lower pannel we see the logarithmic plot of this same signal. Here we have considered the analog model to a black hole with  $m = 4$ . The initial perturbation was released from  $x_3 = 30$  with  $\sigma = 1$ .

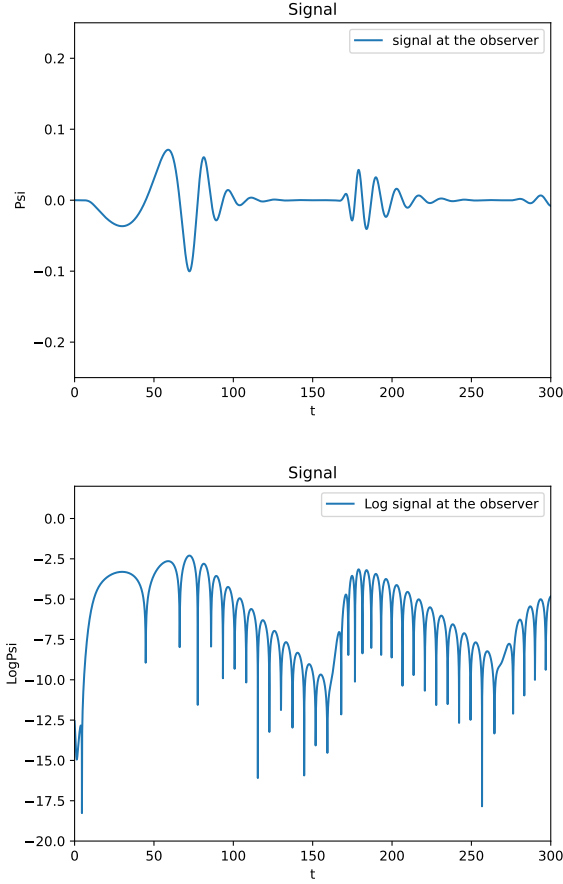


Figure 4.4: GW Strain measured by a distant observer in  $x_2$  (tortoise coordinate) from a Schwarzschild exotic compact object, and generated by the prompt perturbation in (4.9). We directly evolved this perturbation (an inwards propagating Gaussian pulse) in the time domain via the finite difference scheme in Eq. (4.10). In the upper panel, we see a plot of the time evolution of a gravitational wave signal measured by a distant observer in  $x_2$ . In the lower panel, we see the logarithmic plot of this same signal. Here we have considered the Schwarzschild black hole with  $L = 2$ , and  $M = 1$ . The initial perturbation was released from  $x_3 = 30$  with  $\sigma = 3$ . The reflective boundary was imposed at  $x_0 = -40$

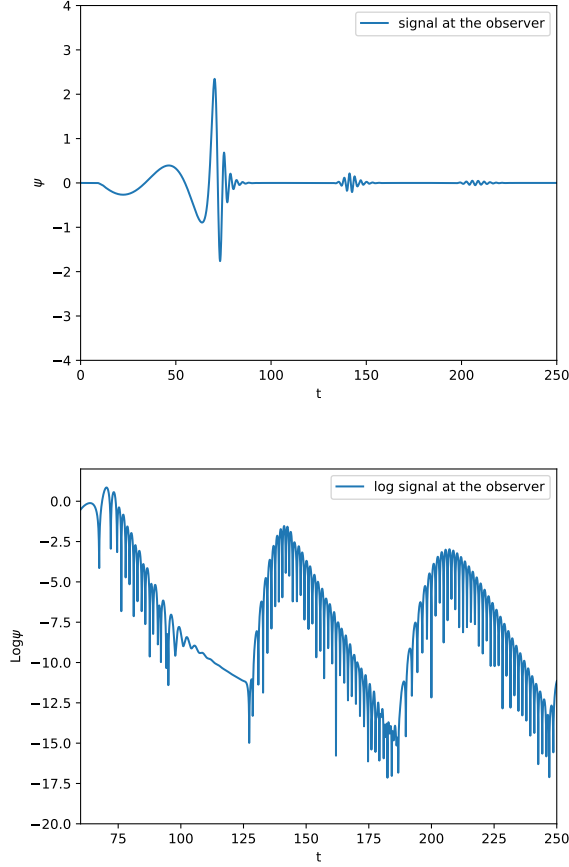


Figure 4.5: Waveform measured by a distant observer in  $x_2$  (tortoise coordinate) from the acoustic analog to an exotic compact object, namely the imperfect draining vortex, and generated by the prompt perturbation in (4.7). We directly evolved this perturbation (an inwards propagating Gaussian pulse) in the time domain via the finite difference scheme in Eq. (4.10). In the upper panel, we see a plot of the time evolution of a gravitational wave signal measured by a distant observer in  $x_2$ . In the lower panel, we see the logarithmic plot of this same signal. Here we have considered the analog model to a black hole with  $m = 4$ . The initial perturbation was released from  $x_3 = 30$  with  $\sigma = 1$ . The reflective boundary was imposed at  $x_0 = -30$



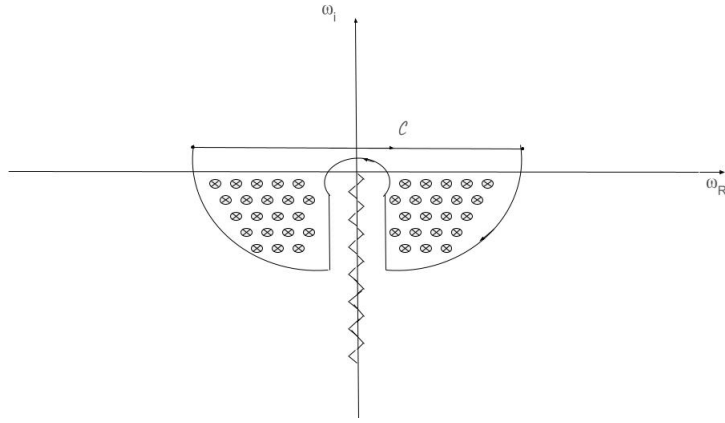


Figure 4.6: The integral contour  $\mathcal{C}$  for the Cauchy integral in Eq. (4.34). The crosses are the positions of the quasinormal frequencies in the complex plane. The hatched area is the branch cut.

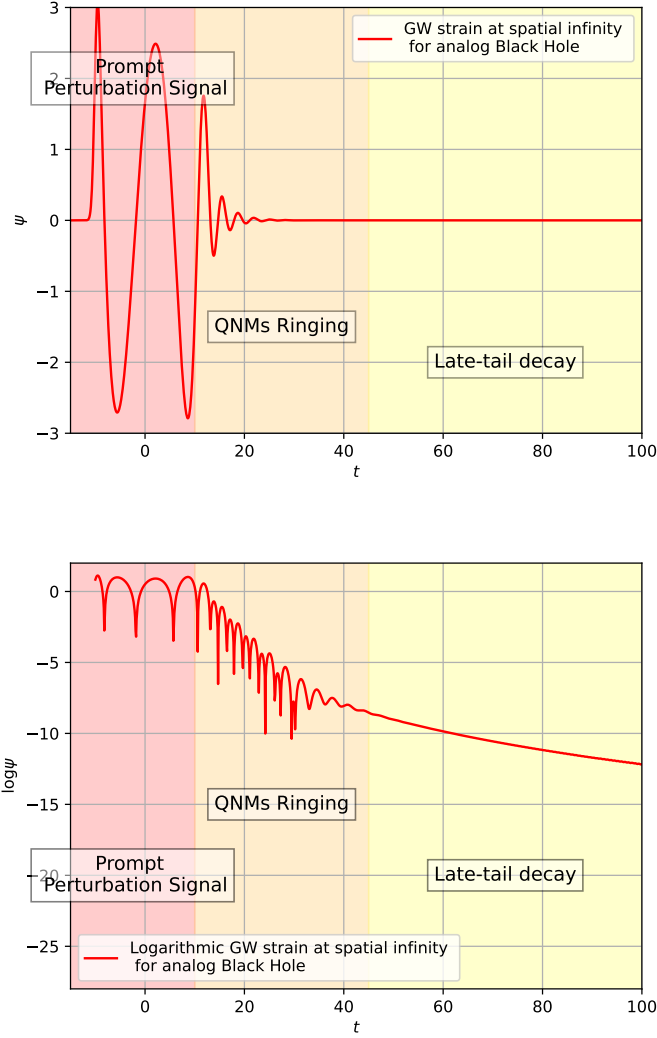


Figure 4.7: Waveform strain measured by a distant observer far away from the source in an analog black hole spacetime. The three different stages of the time evolution of this signal are: perturbation stage (1), ringdown phase (2), late tail stage(3). In the upper panel, we see the time evolution of this wave signal. In the lower panel, we see the logarithmic plot of that same signal.

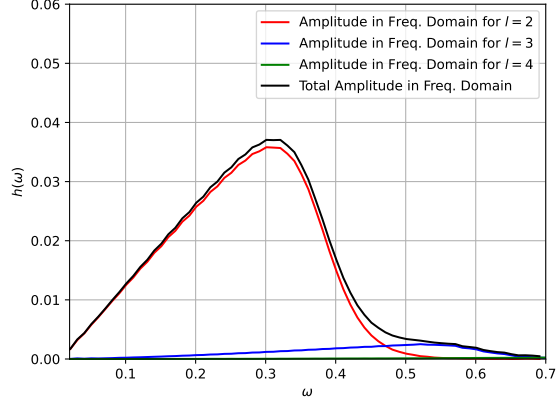


Figure 4.8: The energy spectrum of gravitational radiation emitted by the radial infall of a smaller mass into a larger black hole for each multipolar number  $l$ . The total combination of all multipolar contributions is the solid black curve. Notice the difference in contribution between each mode.

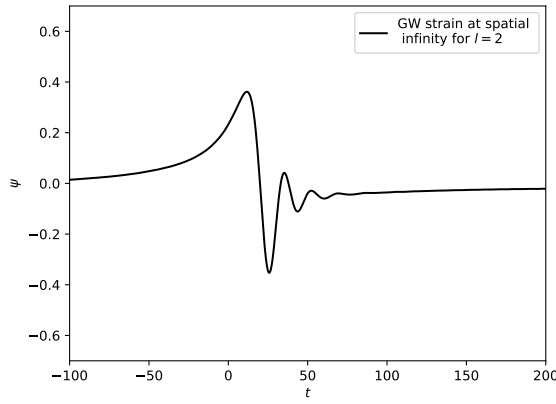


Figure 4.9: Time domain gravitational wave signal emitted by a plunge of a small star into a larger black hole as measured by a distant observer in  $x \rightarrow \infty$ .

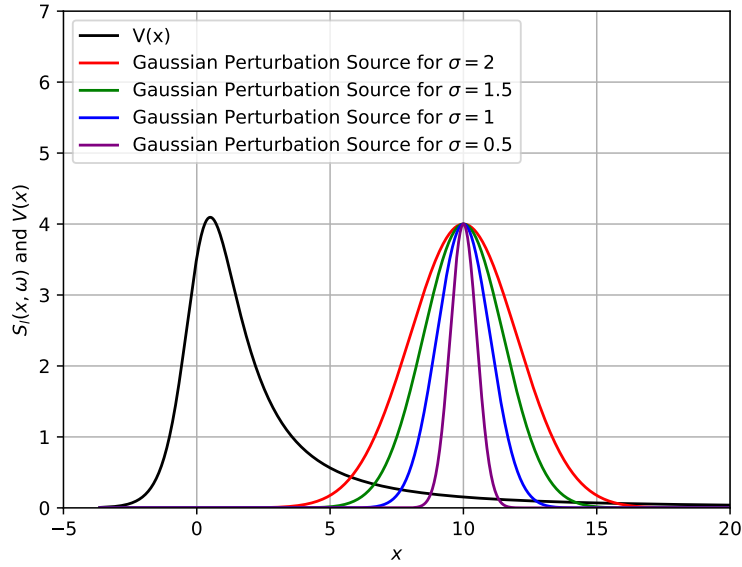


Figure 4.10: Potential versus the perturbation sources from Eq. (4.43) for a few different  $\sigma$  scenarios.

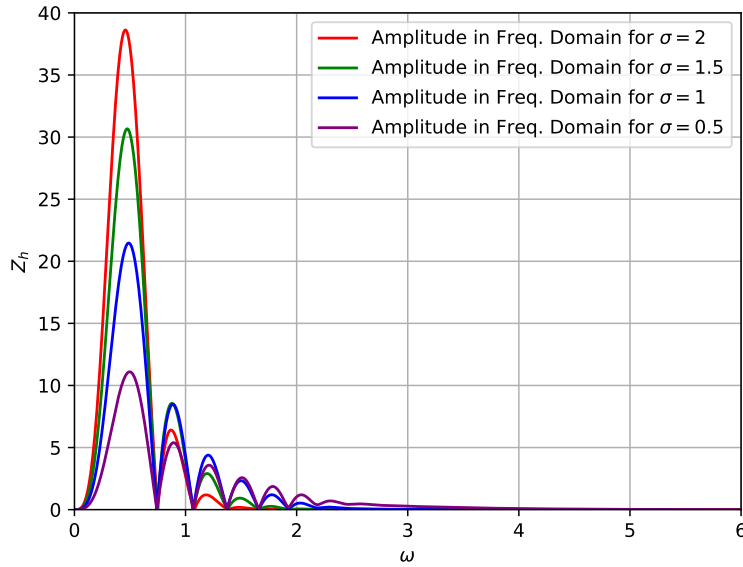


Figure 4.11: Frequency domain waveform amplitudes for Gaussian acoustic perturbations in the background effective spacetime of an acoustic black hole for the different  $\sigma$  scenarios represented in Fig. 4.10. Notice that narrower Gaussian perturbations excite higher QNMs overtones.

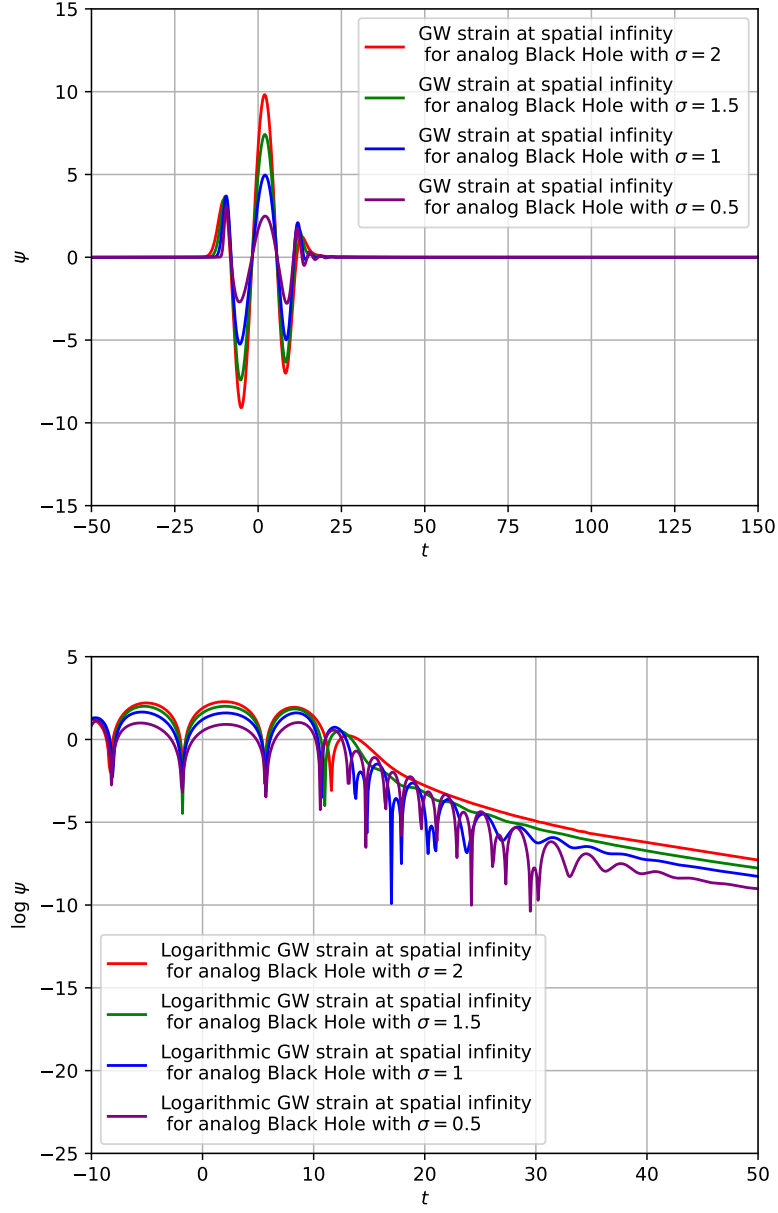


Figure 4.12: Time domain waveform signals emitted by an acoustic black hole in response to Gaussian acoustic perturbations in Eq. (4.43). Those signals for the different  $\sigma$  scenarios represented in Fig. 4.10 are measured by distant observers.

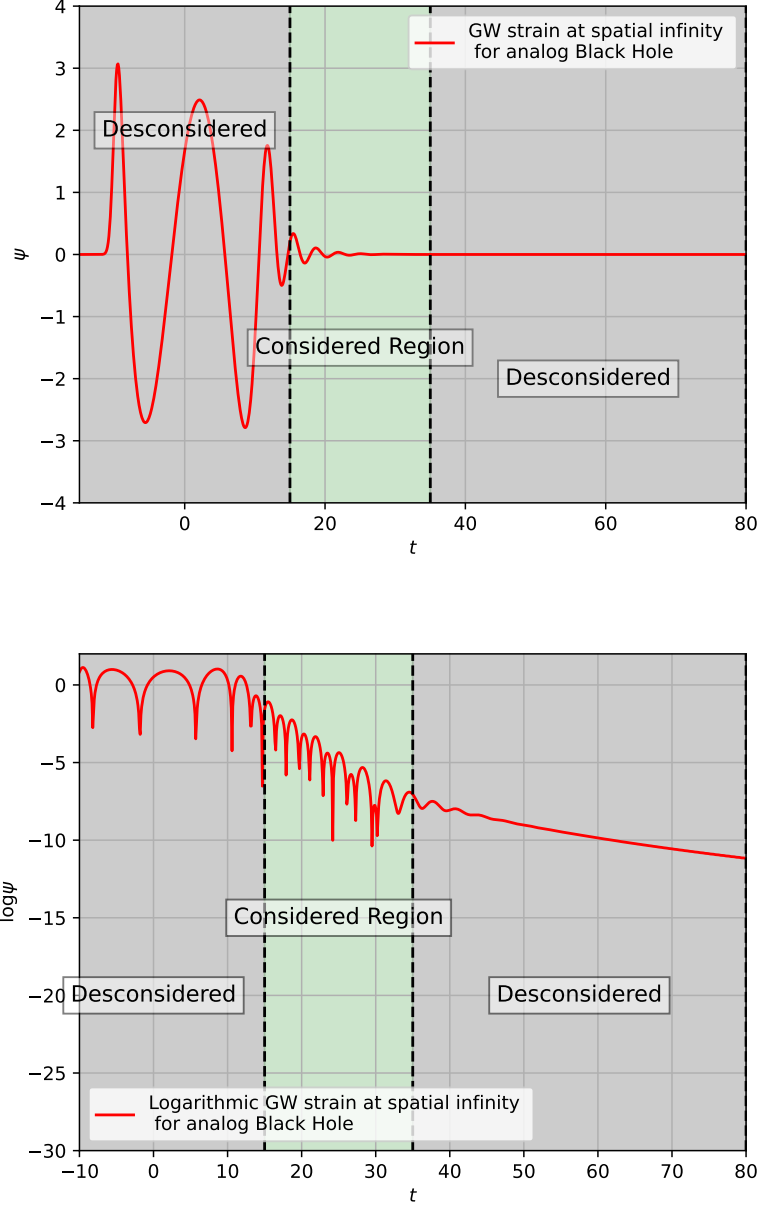


Figure 4.13: Time domain waveform signals emitted by an acoustic black hole in response to Gaussian acoustic perturbations in Eq. (4.43) for  $\sigma = 0.5$ . The upper panel represents the direct signal in the time domain measured by a distant observer, while the lower panel represents the logarithmic version of this signal. In those graphics, we delimited the region of interest for our waveform spectroscopy in terms of QNMs. This region is chosen by looking for a time interval that better represents the intermediate stage of QNM ringing oscillations.

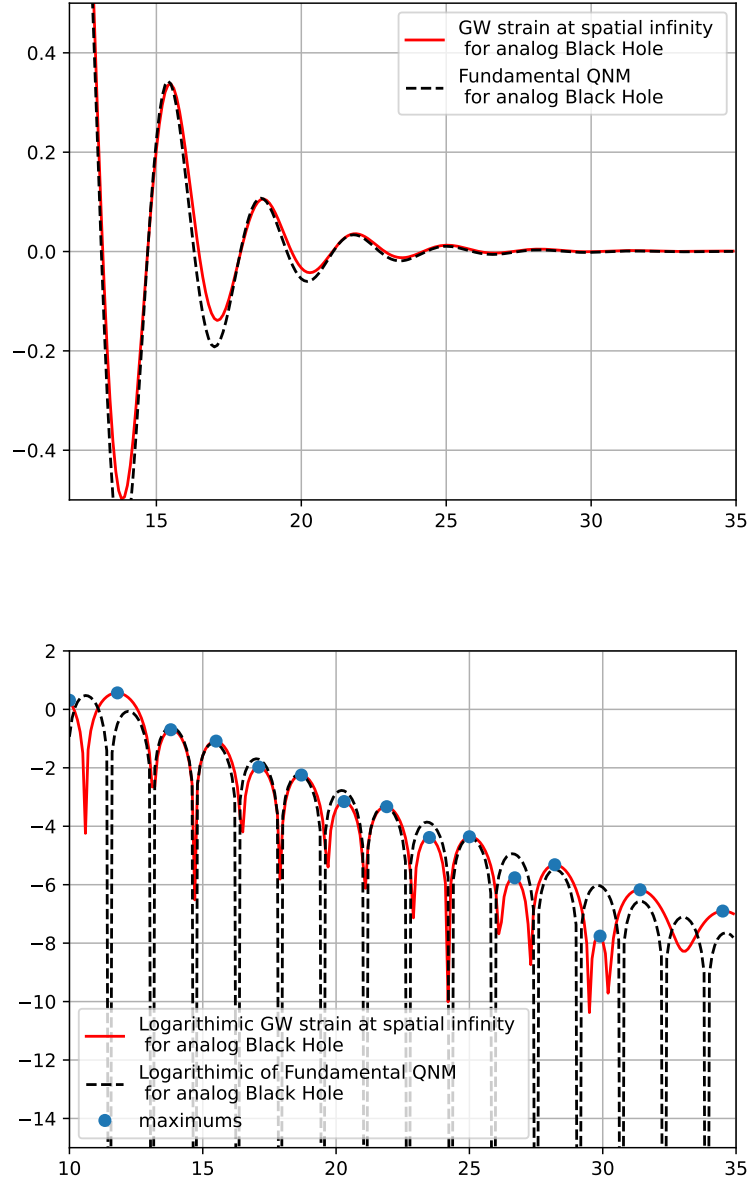


Figure 4.14: We contrast the waveform signal in Ref. 4.13 with the inferred fundamental quasinormal mode whose parameters better fit the input signal

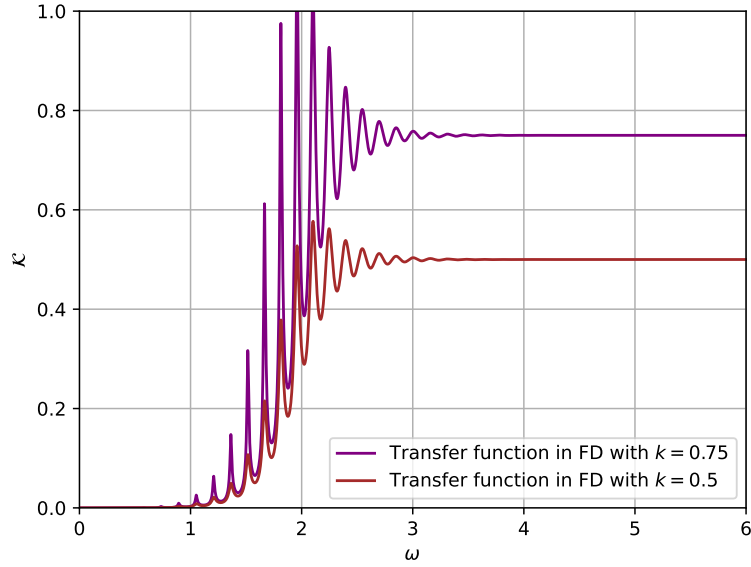


Figure 4.15: Transfer functions for two different ECOs' analog models, generated by  $x_0 = -20$ , and  $K = 0.5$  (red) and  $K = 0.75$  (purple). Notice that the frequency spacing is equivalent, but the peaks are more pronounced for the case with the largest reflectivity.

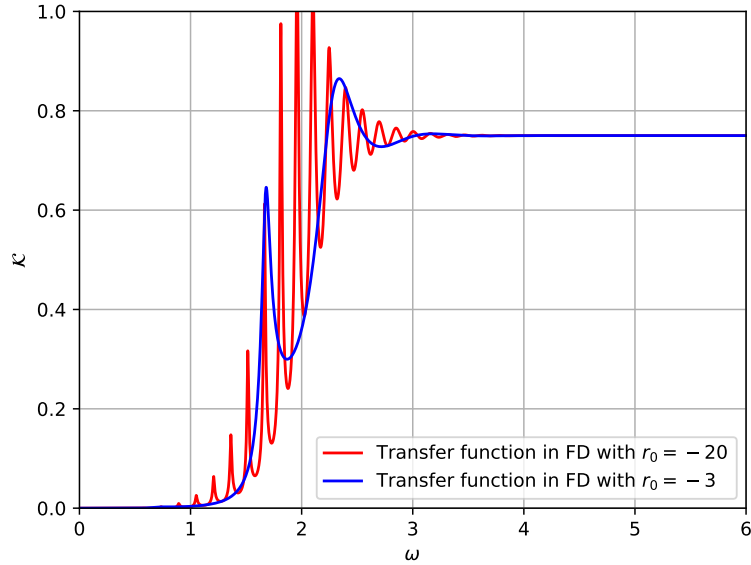


Figure 4.16: Transfer functions for a few different ECOs' analog models, generated by  $K = 0.75$ , and  $x_0 = -3$ , and (red) and  $x_0 = -20$  (blue). Notice that larger cavities are associated with more resonant modes, which in turn are separated by smaller frequency spacings.



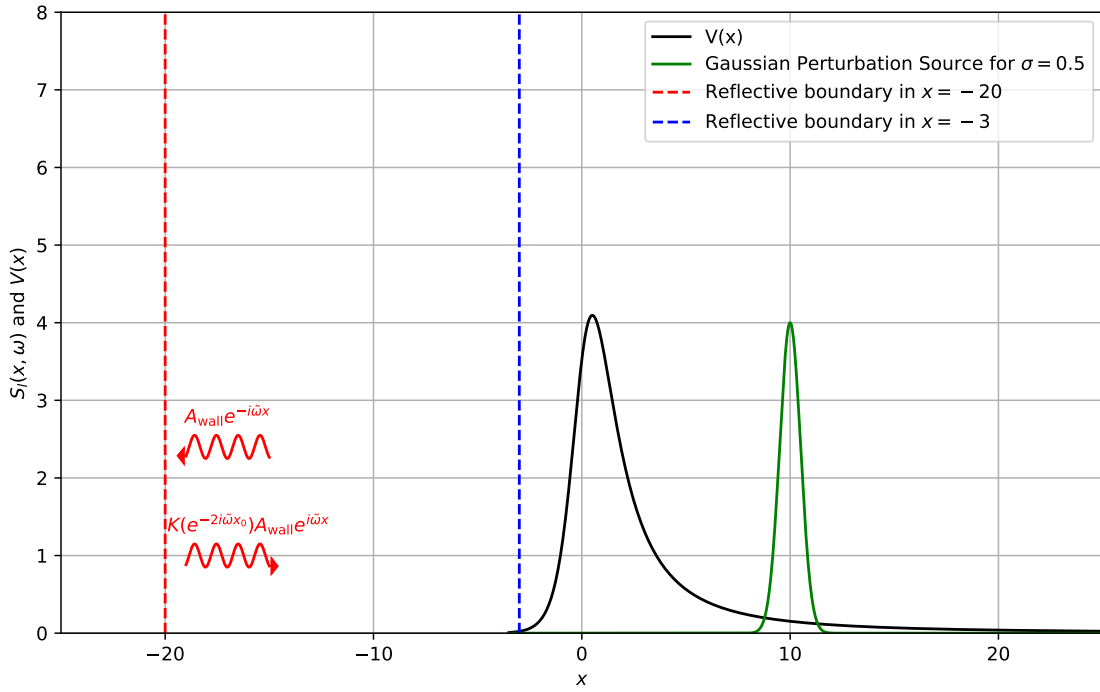


Figure 4.17: Effective potential for the imperfect draining vortex with  $M = 4$  and  $C = 0$ . The reflectivity boundary location  $x_0$  yields two distinct scenarios, namely  $x_0 = -3$  (blue) representing the regime of small cavities, and  $x_0 = -20$  (red) representing a large cavity case.

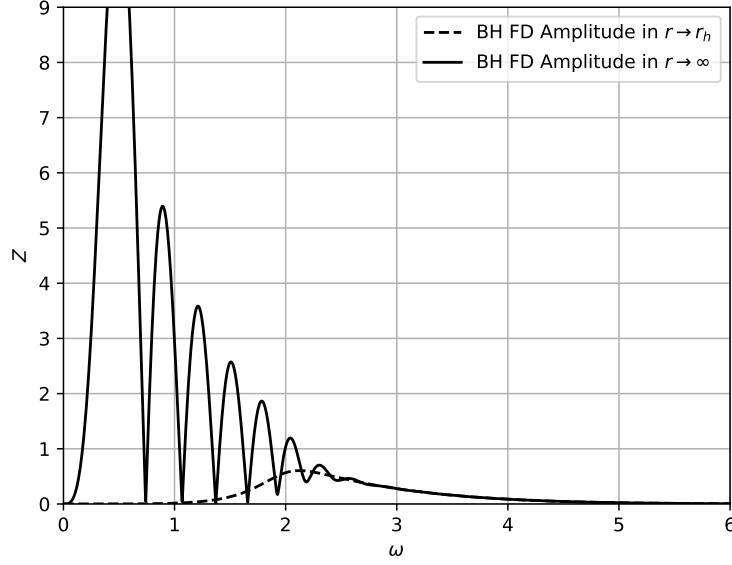


Figure 4.18: Waveform amplitudes in the frequency domain for acoustic perturbations generated by the Gaussian source term in Eq. (4.43) on the perfect draining vortex. Those are the FD amplitudes at the horizon and at the infinity, respectively

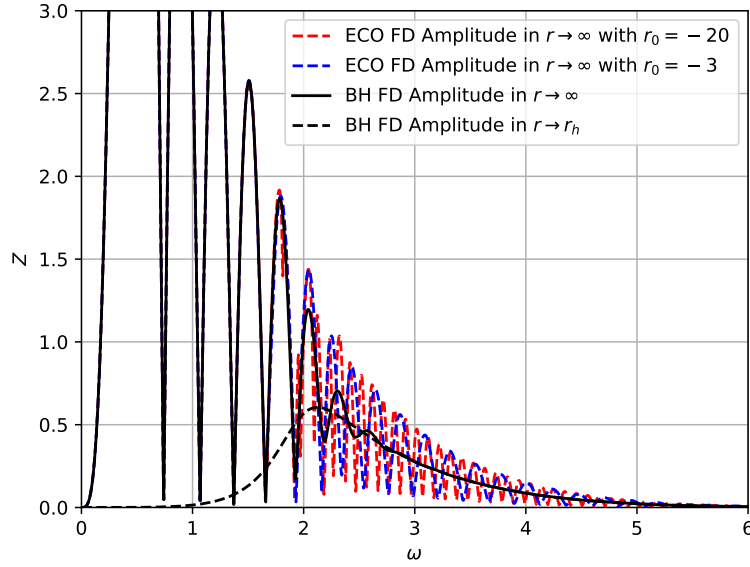


Figure 4.19: Waveform amplitudes in the frequency domain for acoustic perturbations generated by the Gaussian source term in Eq. (4.43) on the perfect and imperfect draining vortex. At infinity  $r \rightarrow \infty$  we contrast the acoustic black hole waveform amplitude with two distinct ECO models, one for a small cavity  $x_0 = -3$  (red-dashed) and the other for a large cavity  $x_0 = -20$  (blue-dashed). Notice the difference in the frequency spacing between the modes.

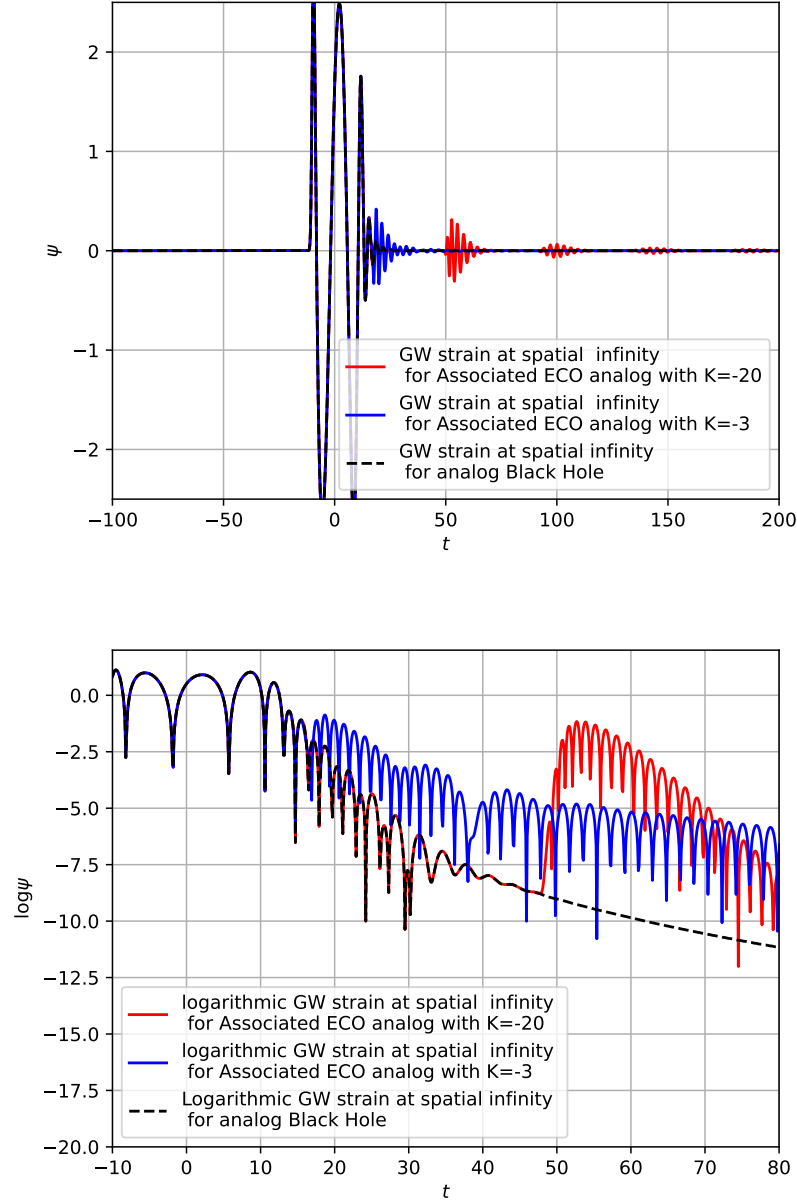


Figure 4.20: Waveform strain in the time domain for acoustic perturbations generated by the Gaussian source term in Eq. (4.43) on the perfect and imperfect draining vortex. We contrast the acoustic black hole waveform signal detected by a distant observer (black-dashed) from those two distinct ECO models, one for a small cavity  $x_0 = -3$  (blue) and the other for a large cavity  $x_0 = -20$  (red).

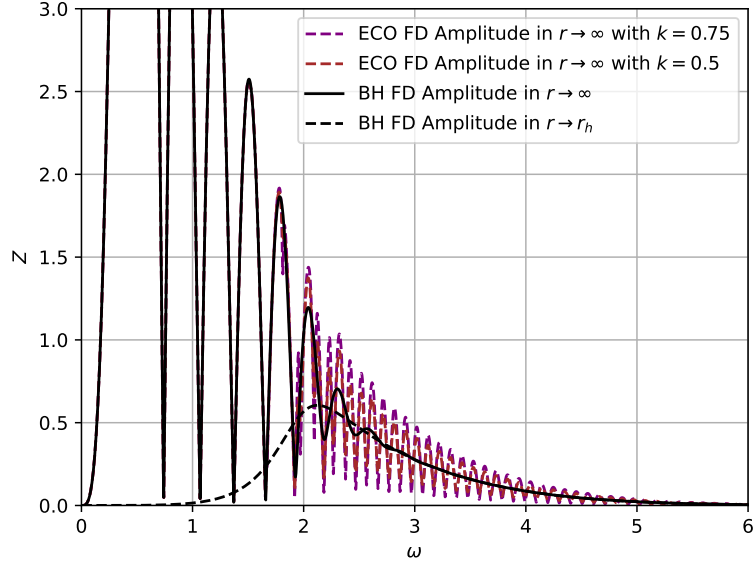


Figure 4.21: Waveform amplitudes in the frequency domain for acoustic perturbations generated by the Gaussian source term in Eq. (4.43) on the perfect and imperfect draining vortex. At infinity  $r \rightarrow \infty$  we contrast the acoustic black hole waveform amplitude with two distinct large cavity ( $x_0 = -20$ ) ECO models, namely  $K = 0.5$  (red-dashed) and  $K = 0.75$  (purple-dashed). Notice that for higher reflectivities  $K$  yields narrower and higher peaks at the resonant modes. Notice that the frequency spacing is the same, but higher reflectivities yield higher peaks.

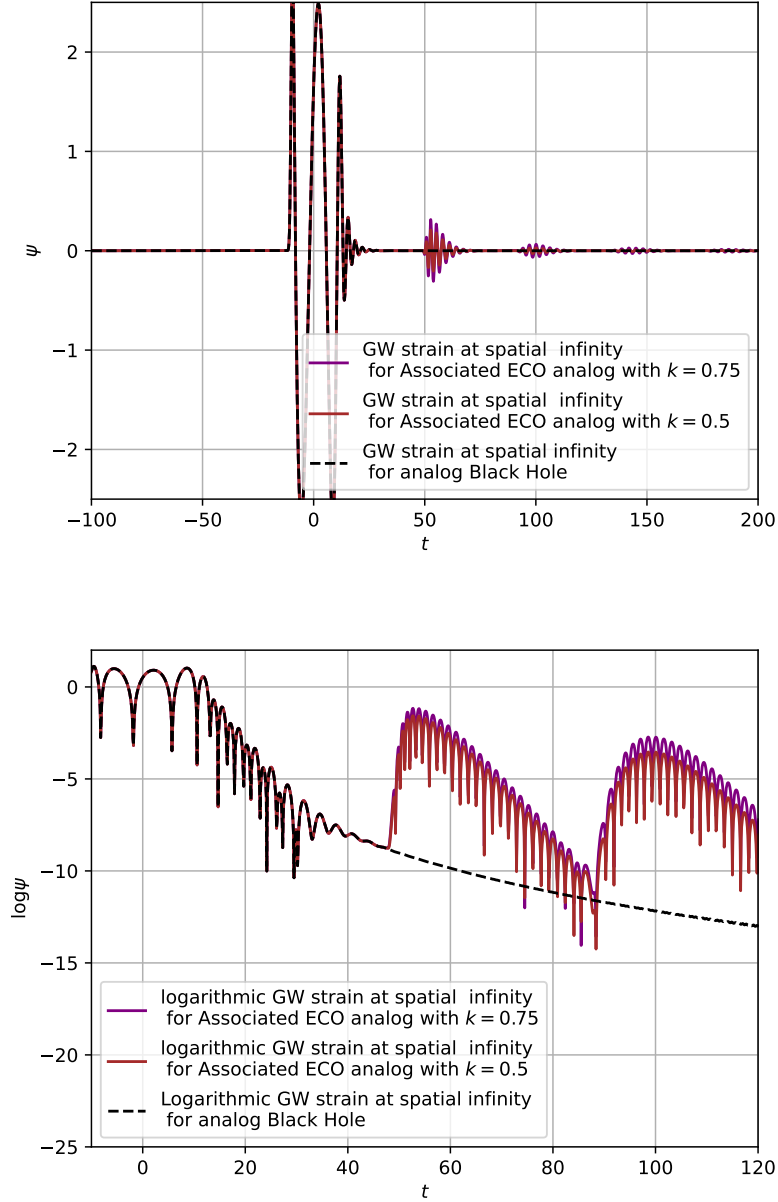


Figure 4.22: Waveform strain in the time domain for acoustic perturbations generated by the Gaussian source term in Eq. (4.43) on the perfect and imperfect draining vortex. We contrast the acoustic black hole waveform signal detected by a distant observer (black-dashed) from those two distinct large cavity ECO models, the one from  $K = 0.5$  (red) and the other from  $K = 0.75$  (purple).

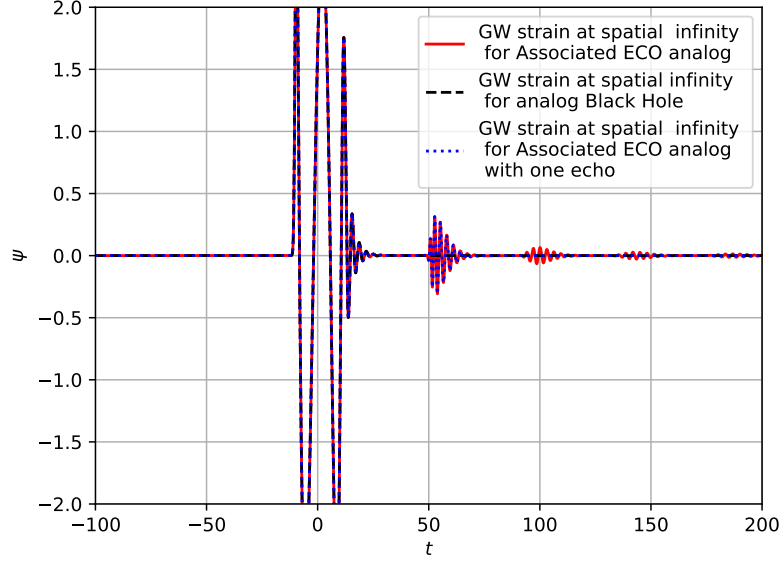


Figure 4.23: Waveform strain in the time domain for acoustic perturbations generated by the Gaussian source term in Eq. (4.43) on the perfect and imperfect draining vortex. We present the acoustic black hole waveform signal detected by a distant observer (black-dashed), and we contrast it with the time domain signal from Eq. (4.61) in two scenarios: considering only the two first terms of this expansion, which corresponds to the BH signal and the first echo (blue-dotted line) and the signal from the entire expansion itself (red solid line).

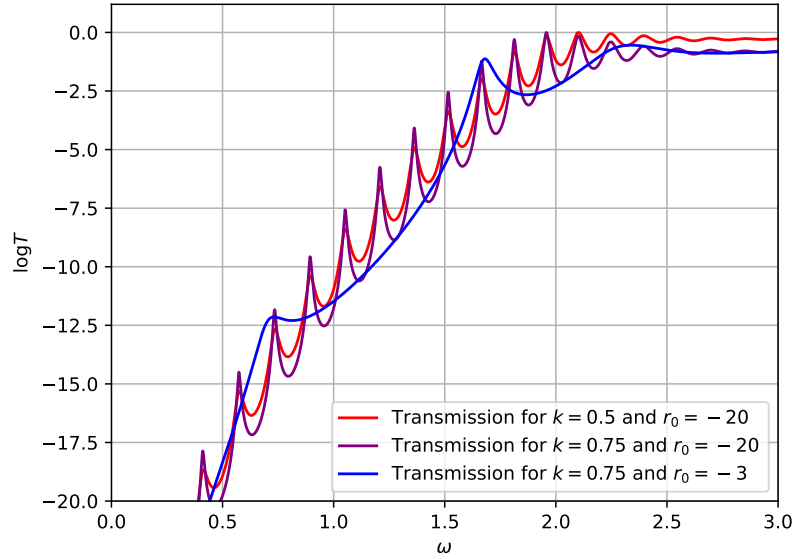


Figure 4.24: Comparison between the logarithmic plot of the transmission for scenarios where  $x_0 = -20$  and the reflectivity constant is  $K = 0.5, 0.75$ ; and for the case with  $x_0 = -3$  and  $K = 0.75$ .

# Chapter 5

## The Inverse Problem: A Semi-analytical Approach

The WKB method [186, 187, 188, 189] is the group of theoretical concepts behind the semi-classical theory of wave quantum mechanics. It is used in general for finding approximate solutions to linear differential equations, but it has gained a lot of notoriety for its applications in the context of Schrödinger wave equation. Since its first presentations [190, 191, 192], many extensions have been proposed, making this set of techniques a handy and reliable tool for semi-analytic treatment of many other physical problems. Among them, we can cite the application to the direct problem of linear perturbation theory of compact objects, such as black holes [182, 193, 194, 195, 196, 197, 198, 199]. This chapter presents the most important mathematical formulas behind the WKB method and its application for the perturbation theory of compact objects and analog systems. In section 5.2, we introduce the formal theory behind this semi-analytic approach and the direct equations used for such treatment.

On the other hand, the corresponding problem of starting with the radiation spectrum or with the scattering properties of a certain physical system (possibly measured in an experiment, for example) and then reconstructing their underlying physics is a completely different problem. In contrast to deriving a source's spectrum or scattering properties when its underlying physics is known, doing the “reverse engineering” of reconstructing the source from its spectrum/scattering properties is generally a much more difficult problem. That

formulates what we call *the inverse scattering problem* [122], or simply, *the inverse problem*.

In terms of an exact/numerical treatment from the analytical equations describing these systems, that inverse problem becomes extremely difficult, if not formally impossible to tackle with the techniques currently known. For this reason, applying semi-analytic techniques by inverting the usual WKB formulas can become very useful and might reveal important insights concerning the underlying structure of this physical problem. These inverted WKB formulas, which form the theoretical foundation of the inverse problem, are presented in Sec. 5.3 of this chapter.

The inverse method we develop in this thesis consists of a novel method that is based on a semianalytic analysis of the underlying wave equation, and that does not require the specification of specific details of the underlying model. Formally, it embodies a set of techniques and inverted semi-analytical formulas that provide us with a mathematical setting for reconstructing key properties of the scattering source. In our case here, the developed inverse method allows us to obtain the coupled effective scattering potentials that produce the measured results we use as input for the inverse reconstruction.

Note that this is very different from standard inference approaches, in which one reconstructs the parameters of a model using statistical tools. Instead, we show how Wentzel-Kramers-Brillouin (WKB) theory-based results known for quasistationary states of astrophysical exotic compact objects [200] can be extended to recover main properties of the effective potential, as well as absorption properties at the surface of the objects.

In general, although once we specify the underlying physics of a certain scattering object, its spectrum is uniquely determined. Formally, at least in principle, we cannot do the other way around for the same problem and find a unique solution, but only a class of possible solutions. That is the main goal of the inverse problem. If an additional well-motivated hypothesis concerning the physical properties of the scattering source is also provided, the joint application of this hypothesis with the inverse method can get us closer to an approximative solution for the inverse problem. That is the line of reasoning we follow through this thesis.



For exotic compact objects, this problem was already addressed in the literature [125, 126, 127, 128, 129, 130] employing the same semi-analytic techniques we introduce here. Among the plethora of questions investigated, the reconstruction of perturbation scattering potentials from exotic compact objects from their QNMs spectra was achieved for many different cases. The question that remained was whether we would have been as lucky had we started from the scattering properties of analog gravity systems. That problem is what we aimed to address with this thesis. As proof of principle, in Chapter 6, we apply it to the imperfect draining vortex model studied in Ref.[48], for which we compute the relevant observables with standard, accurate numerical methods.

## 5.1 Semi-analytical treatment for the direct and inverse problem

As we discuss in this chapter, the application of the semi-analytic techniques based on the WKB [186, 187, 188, 189] method allows us to obtain a powerful tool for the direct problem of obtaining the scattering properties and the irradiated spectrum of ringing compact objects [200]. The same can be said about their analog gravity systems [48] and the inverse problem of using their scattering properties to reconstruct their intrinsic effective potentials.

Furthermore, we show that the problem for which the spectrum of a source or its scattering properties is known, but the physical parameters that describe those sources are not, also called *inverse problem*, can also be posed in terms of those semi-analytical equations in their inverse formulations. The solution for the inverse problem might not be unique, and since inverse problems are often not uniquely solvable, we argue how physically motivated constraints allow one to reconstruct the relevant potential. The quality of the reconstruction, due to its relation to WKB theory, is very good for large angular numbers. Furthermore, as shown in the following chapters, we can also reconstruct the sources' boundary reflectivity, for which results become more accurate the more the object reflects incoming waves.

In this chapter, we introduce the direct and inverse WKB method for energy-independent potentials, applying for non-rotating analog gravity systems in chapter 6. In chapter 7, we present our extension of the same techniques for the case with energy-dependent potentials, which tackles cases where the scattering source is rotating. This last application is left for chapter 8.

## 5.2 WKB method

We start our discussion with the time-independent Schrödinger-like wave equation in Eq.(4.14).

$$\frac{d^2\Psi(r, E)}{dx^2} + (E - V(x))\Psi(r, E) = 0. \quad (5.1)$$

Where  $V(x)$  is the potential and  $E$  is the continuous or discrete set of eigenvalues for the energy. The main approximation hypothesis behind the WKB method is that the potential does not appreciate drastic changes when compared to the considered wavelength dimensions in one's desired application regime [201, 202]. That is the so-called Eikonal approximation.

The WKB theory makes the following ansatz for the wave solution of Eq. (5.1)

$$\Psi(x) \approx \exp \frac{1}{\epsilon} \sum_{n=0}^{\infty} \epsilon^n S_n(x), \quad (5.2)$$

where  $S_n(x)$  is the phase, and  $\epsilon$  is the small expansion parameter controlling the approximation order desired. If we write the Schrödinger equation in terms of the function  $Q(x, E)$ , where

$$Q(x, E) = E - V(x), \quad (5.3)$$

and we insert the Ansatz in Eq. (5.2), we obtain the following expansion

$$\left( \sum_{n=0}^{\infty} \epsilon^n S'_n(x) \right)^2 + \epsilon \sum_{n=0}^{\infty} \epsilon^n S''_n(x) = Q(x). \quad \text{for } Q(x, E) \neq 0. \quad (5.4)$$

The first-order term yields the so-called Eikonal equation

$$S_0'^2 = Q(x, E). \quad (5.5)$$

which is solved by

$$S_0(x) = \pm \int^x \sqrt{Q(x')} dx'. \quad (5.6)$$

The following order of expansion gives us the transport equation,

$$2S_0' S_1' + S_0'' = 0, \quad (5.7)$$

whose solution is

$$S_1(x) = -\frac{1}{4} \ln Q(x, E) \quad (5.8)$$

For terms with higher orders than  $n \geq 2$ , we get

$$2S_0' S_{n-1}'' + \sum_{j=1}^{n-1} S_j' S_{n-j}' = 0. \quad (5.9)$$

As reported by Bender and Orszag [203], the solutions  $S_n$  for the equations above are, up to the 5-th order, given by the following expressions

$$\Psi(x) = c_1 Q^{-1/4}(x) e^{\frac{1}{\epsilon} \int_a^x \sqrt{Q(x')} dx'} + c_2 Q^{-1/4}(x) e^{-\frac{1}{\epsilon} \int_a^x \sqrt{Q(x')} dx'}, \quad \text{for } \epsilon \rightarrow 0, \quad (5.10)$$

where  $c_1, c_2$  are integration constants, and  $a$  is a fixed integration point.

We are assuming that  $Q(x, E) \neq 0$ , therefore we cannot expect our solutions here to be valid at the turning points. The standard approach to circumvent this limitation is splitting the domain into three different regions. The so-called classically allowed region with  $E < V(x)$ , where the wave solution presents an oscillatory behavior, and the classically forbidden region with  $E > V(x)$ , where the wave function exponentially decays with distance. The third region takes place around the turning point, and it consists of the overlapping region between the classically allowed and classically forbidden regions. To approach the wave solution around this region in our semi-analytic treatment we need to solve the Schrödinger equation for a Taylor expansion of  $V(x)$ . In the overlap interval between the two solutions, the relations between the WKB solutions and the wave solutions obtained for the linear expansion of the potential around the turning point are called Kramer's matching relations or matching conditions. The two possible cases for one turning point are illustrated in Fig. 5.1.

The WKB solutions around these turning points  $(x_0, x_1)$  can be derived by considering the linear Taylor expansion of the potential  $V(x)$  around them.

$$V(x) \approx V(x_{0,1}) + \left[ \frac{dV}{dx} \right]_{x=x_{0,1}} (x - x_{0,1}) \quad (5.11)$$

In that way, we can then obtain the solutions at the matching regions in terms of Airy functions. After that, we match these wave solutions around the turning points with the WKB wave solutions for the classically allowed/forbidden regions, given by Eqs. (5.10). The final form of those matched WKB solutions is finally presented in the following, for a detailed derivation of those results, we refer the interested reader to Ref.[200]. The WKB solutions around the turning points are given by

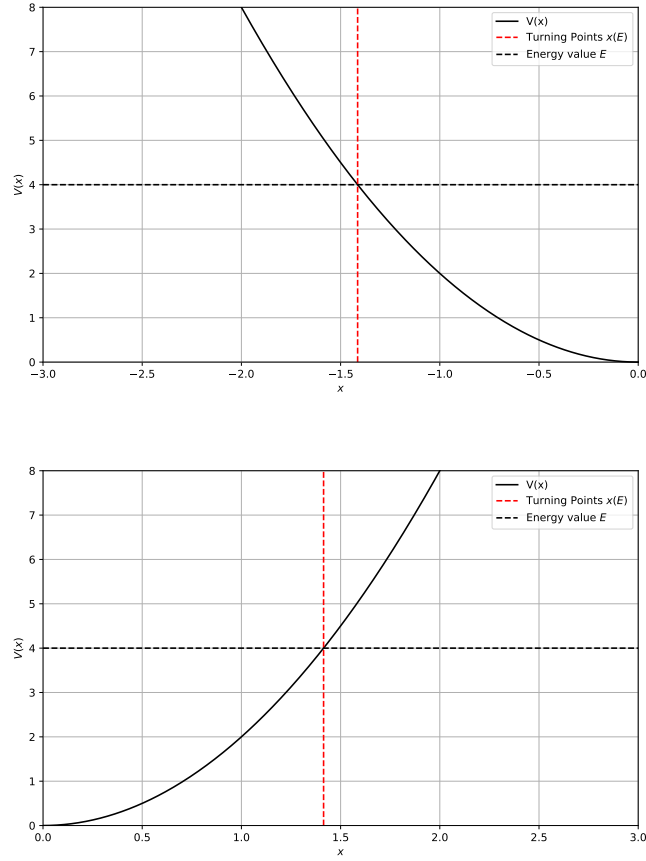


Figure 5.1: Two possible cases for the problem of one turning point. For the upper panel, we have  $x_0(E)$  and for the lower panel, we have  $x_1(E)$ .

$$\psi_I(x) = B_I \frac{1}{\sqrt{|p(x)|}} \exp \left( - \int_x^{x_0} |p(x')| dx' \right), \quad x < x_0, \quad (5.12)$$

$$\psi_I(x) = B_I \frac{2}{\sqrt{p(x)}} \sin \left( \int_{x_0}^x p(x') dx' + \frac{\pi}{4} \right), \quad x > x_0, \quad (5.13)$$

for  $x$  around  $x_0$  as in the upper pannel of Fig. 5.1, and

$$\psi_I(x) = A_{III} \frac{2}{\sqrt{p(x)}} \sin \left( \int_x^{x_1} p(x') dx' + \frac{\pi}{4} \right), \quad x < x_1, \quad (5.14)$$

$$\psi_{III}(x) = A_{III} \frac{2}{\sqrt{|p(x)|}} \exp \left( - \int_{x_1}^x |p(x')| dx' \right), \quad x > x_1, \quad (5.15)$$

for  $x$  around  $x_1$  as in the lower pannel of Fig. 5.1.

Eqs. (5.12),(5.13),(5.14),(5.15) are the so-called Kramer's matching relations or matching conditions. They are important for the derivation of the direct Bohr-Sommerfeld rule and the direct Gamow formulas in the following.

### 5.2.1 Direct Bohr-Sommerfeld Rule

For realistic one-dimensional potentials describing physical confining systems, it is technically very difficult to find exact solutions for the energy eigenvalues and their associated eigenfunctions in the wave equation (4.14). For such a goal, we need to directly integrate this equation, which depending on the potential  $V(x)$  can lead to an extremely complex mathematical problem. In such situations, WKB theory can help to find approximate solutions for our problem. For a potential well with two turning points, such as the one shown in Fig. 5.2 for example, the WKB solutions in Eqs. (5.12),(5.13),(5.14),(5.15) can be used to derive an integral equation for the spectrum  $E_n$  itself, which can be computed without knowing the eigenfunctions explicitly. That gives us the so-called Bohr-Sommerfeld rule:

$$\int_{x_0}^{x_1} \sqrt{E_n - V(x)} dx = \pi \left( n + \frac{1}{2} \right), \quad (5.16)$$

where  $(x_0, x_1)$  are the classical turning points for an associated energy eigenvalue  $E_n$ . This result is valid for potential wells in general with two classical turning points and vanishing asymptotic boundary conditions in the two extremes. In such a case, the spectrum of

energies  $E_n$  is real-value and describes bound states.

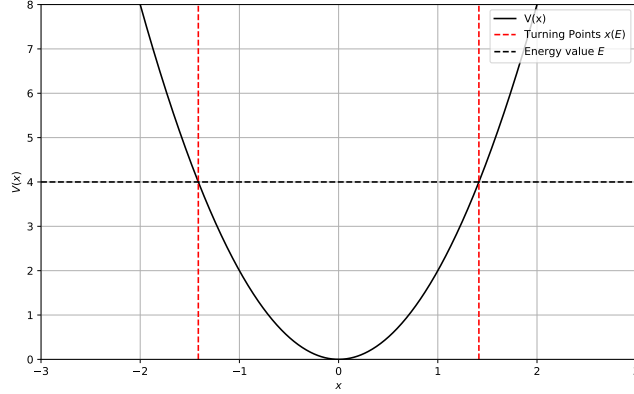


Figure 5.2: Potential well in a confining system. For each energy  $E$  we have two turning points associated  $x_0(E)$  and  $x_1(E)$ .

Deriving the Bohr-Sommerfeld rule is in principle straightforward if we use the WKB integral equations (5.12),(5.13),(5.14),(5.15) describing the wave functions around turning points. To accomplish this derivation, we split up the interval in Fig. 5.2 into 2 classically forbidden regions ( $x < x_0$ ), ( $x_1 < x$ ), and one classically allowed region ( $x_0 < x < x_1$ ). There is an overlap region around each one of the two turning points. The WKB solutions in the classically forbidden regions have two different constants, that will be determined by matching the two oscillatory WKB solutions in the classically allowed region. Following the explicit calculation in [202] we rewrite

$$B_I \frac{2}{\sqrt{p(x)}} \sin \left( \int_{x_0}^x p(x') dx' + \frac{\pi}{4} \right) = -B_I \frac{2}{\sqrt{p(x)}} \sin \left( \int_{x_0}^x p(x') dx' + \frac{\pi}{4} - \left[ \int_{x_0}^{x_1} p(x') dx' + \frac{\pi}{2} \right] \right). \quad (5.17)$$

Comparing with Eq. (5.14), we notice there is a strong similarity to the relation for the other solution. Indeed, these equations coincide if the extra term within the square brackets equals to  $\pi k$ . This implies the following

$$\int_{x_0}^{x_1} p(x') dx' = \pi \left( n + \frac{1}{2} \right) \quad (5.18)$$

where we restricted the  $n$  values to be positive integers, since the integral is positive in this range.

The classical Bohr-Sommerfeld rule in Eq. (5.16) can be further improved by including higher-order terms of the WKB method. The results are shown in [202].

### 5.2.2 Direct Gamow Formulas

Another important result that can be derived from WKB formulas in Eqs. (5.12),(5.13),(5.14), and Eq. (5.15) is the Gamow formula [204]. This formula approximates the transmission coefficient of a wave function through a potential barrier, and the result is given as a function of the energy. As we have shown in chapter 3 and 4, potential barriers in the context of this thesis appear for astrophysical and analog systems to astrophysical black holes, as well as for exotic compact objects. In the first case, one finds a two-turning point potential barrier, while the second one combines this potential barrier with a potential well, leading to quasi-stationary states. That second case is very important for the goals of this thesis, and we discussed it separately in the following subsection.

The Gamow formula describing the semi-classical approximation for transmission of waves with energies below the barrier maximum is

$$T_2(E) = \exp \left( 2i \int_{x_1}^{x_2} \sqrt{E_n - V(x)} dx \right), \quad (5.19)$$

Between the two turning points  $x_1$  and  $x_2$ , we have  $E < V(x)$  (see Fig. 5.3), so the final transmission is real.

In the literature, the Gamow formula has been inverted in order to address the inverse problem. For such cases, the transmission is provided and we want to find the potential



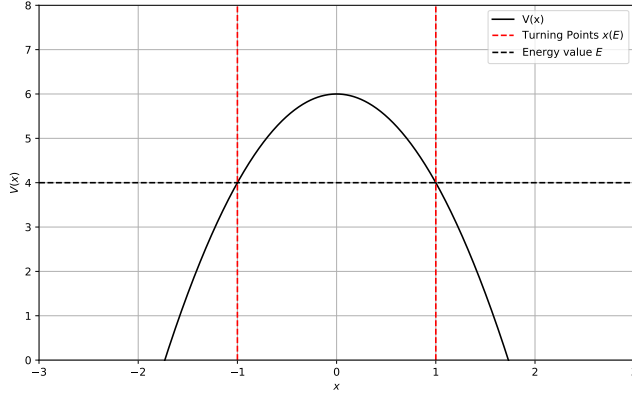


Figure 5.3: Potential barrier in a scattering system. For each energy  $E$  we have two turning points associated  $x_0(E)$  and  $x_1(E)$ .

instead [205, 206, 207]. We explore the inversion of Gamow formula in Sec. 5.3.2.

Besides that, the Gamow formula is important for quasi-stationary states, which arise for different exotic compact objects, and for their analog systems as well. This last scenario gives rise to the most important application considered in this thesis. We explore their general description in terms of the semi-analytic WKB method in the following subsections. Their applications, on the other hand, are considered in Chapters 6,8.

### 5.2.3 Three-Point Turning Points: Quasi-Stationary States

A similar but more intricate physical scenario arises if the potential barrier considered previously possesses an additional turning point. This is the case for potentials shown in Fig. 5.4.

For such potentials, the spectrum of eigenenergies is complex-valued, and we call them quasi-bound states or quasi-stationary states. In [208], it has been shown that it is possible to extend the Bohr-Sommerfeld rule to describe the energy values of quasi-stationary states located in the lower part of this potential by a higher-order correction to Eq. (5.16). This extension is approximately written as

$$\int_{x_0}^{x_1} \sqrt{E_n - V(x)} dx = \pi \left( n + \frac{1}{2} \right) - \frac{i}{4} \exp \left( 2i \int_{x_1}^{x_2} \sqrt{E_n - V(x)} dx \right), \quad (5.20)$$

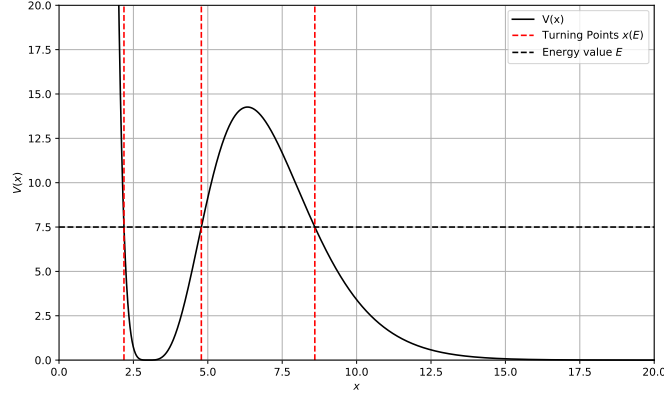


Figure 5.4: Potential with three turning points, respectively,  $x_0(E)$ ,  $x_1(E)$ , and  $x_2(E)$ .

For the quasistationary states, the imaginary part of their energy eigenvalues is exponentially small, so we can further expand the lhs. formula for those energies in the following way

$$\int_{x_0}^{x_1} \sqrt{E_n - V(x)} dx \approx \int_{x_1}^{x_2} \sqrt{E_{0_n} - V(x)} dx + \frac{iE_{1_n}}{2} \int_{x_0}^{x_1} \frac{1}{\sqrt{E_{0_n} - V(x)}} dx, \quad (5.21)$$

where

$$E_n = E_{0_n} + iE_{1_n} \text{ with } |E_{1_n}| \ll |E_{0_n}|. \quad (5.22)$$

Similarly, for the rhs.:

$$\begin{aligned} & \pi \left( n + \frac{1}{2} \right) - \frac{i}{4} \exp \left( 2i \int_{x_1}^{x_2} \sqrt{E_{0_n} + E_{1_n} - V(x)} dx \right) \\ & \approx \pi \left( n + \frac{1}{2} \right) - \frac{i}{4} \exp \left( 2i \left[ \int_{x_1}^{x_2} \sqrt{E_{0_n} - V(x)} dx + \frac{iE_{1_n}}{2} \int_{x_1}^{x_2} \frac{1}{\sqrt{E_{0_n} - V(x)}} dx \right] \right) \end{aligned} \quad (5.23)$$

The last term in the exponential can be neglected, since it only contributes with the ex-

ponential of an already exponentially small term. This property is used to expand Eq. 5.23 into two equations, one for the real part and the other for the imaginary part of those equations. This leads us to the final equations shown bellow, which are going to be extensively used throughout this thesis

$$\int_{x_0}^{x_1} \sqrt{E_{0n} - V(x)} dx = \pi \left( n + \frac{1}{2} \right), \quad (5.24)$$

and

$$E_{1n} = -\frac{1}{2} \exp \left( 2i \int_{x_1}^{x_2} \sqrt{E_{0n} - V(x)} dx \right) \left( \int_{x_0}^{x_1} \frac{1}{\sqrt{E_{0n} - V(x)}} dx \right)^{-1} \quad (5.25)$$

Here  $x_0, x_1, x_2$  are the classical turning points defined by  $E_{0n} = V(x)$ . Notice that comparing this last equation with Gamow formula Eq. (5.19), we notice that the exponential term in the rhs. of Eq. (5.25) below is the semi-analytical approximation for the transmission through the potential barrier, between the turning points  $x_1$  and  $x_2$ . That is a very important result. Its beauty lies in the two-step approach for evaluating the real and imaginary parts of  $E_n$ . While the real part is determined by the classical Bohr-Sommerfeld rule applied to the cavity of this potential, the imaginary part is directly connected with the transmission through the barrier of this same potential.

A further extension of this result can be considered when the wave solution is not decaying at the classically forbidden region for  $x < x_0$ . For example, if there is a partial wave transmission at the turning point  $x = x_0$ , then, we have

$$E_{1n} = -\frac{1}{2} (T_1(E) + T_2(E)) \left( \int_{x_0}^{x_1} \frac{1}{\sqrt{E_n - V(x)}} dx \right)^{-1}. \quad (5.26)$$

where  $T_1(E)$  is defined in terms of boundary conditions at the objects 'surface' located at  $x_0$  and discussed in Sec. 8.4.1.

The inverse problem related to reconstructing properties of  $V(x)$  given the spectrum of quasi-stationary states was studied in Refs. [127, 125] and is explained in more detail in Sec. 8.4.

## 5.3 The Inverse WKB Formulas

Now we discuss the inversion of the different WKB formulas we derived in the previous section. We start by deriving the inverse formula for the Bohr-Sommerfeld rule, which allows us to reconstruct the cavity width of a certain potential well assuming we know its spectra. Next, we derive the inverse Gamow formula, which gives us an effective method to reconstruct the width of a potential barrier providing that we have a previous knowledge of the transmission through this potential barrier.

### 5.3.1 Inverse Bohr-Sommerfeld Rule

We motivate the explicit theoretical proposal behind the inverse problem considered here by the following question:

**Can we find the potential well that yields a given spectrum of bound states?**

To address this question from a semi-analytical perspective, we would need an equation that could, in principle, work inversely as of Eq. (5.16). Instead of giving us the energies of the bound states from a given potential well, we want it to give us some enlightening information about this potential well, provided we already know the normal modes spectra. This inverted version of the Bohr-Sommerfeld rule does exist, and here in this section, we summarize how one can derive it. We refer the more interested reader to Ref. [200] for a more detailed derivation of this formula.

We start by defining the so-called inclusion

$$I(E) \equiv \int_{x_0}^{x_1} (E - V(x)) dx, \quad (5.27)$$

which delimits the area enclosed by the horizontal line intersecting the energy-axis at the  $E$  value, and the function that describes the potential  $V(x)$ , between the two turning points  $(x_0, x_1)$ .

The second definition we need is the so-called excursion,

$$\mathcal{L}(E) \equiv \int_{x_0}^{x_1} dx = x_1 - x_0. \quad (5.28)$$

This quantity defines the width of the potential well as a function of energy. It is the most important quantity to be obtained from our inverse problem in terms of the inverse BS rule.

Now, let's assume that we could have a continuous function connecting  $E_n$  and the mode number  $n$  with the following features. This function  $E(n)$  reproduces the discrete values of  $E_n$  at the integer values  $n$ , while it remains defined for the real values between them. For example, a numerical interpolation  $E(n)$  can achieve this goal. Since  $E_n$  is usually monotonically connected with its mode number  $n$  for the problems we consider, we can also invert this relation to obtain  $n = n(E)$ . Finally, we can write the Bohr-Sommerfeld rule for the continuous case

$$\pi \left( n(E) + \frac{1}{2} \right) = \int_{x_0}^{x_1} \sqrt{E - V(x)} dx \quad (5.29)$$

Note that this interpolation  $n = n(E)$  might not be unique. The minimum  $E_{\min}$  of the potential well  $V(x)$  can be defined as the extrapolation where the change in the phase is zero. This implies in

$$n(E_{\min}) = -\frac{1}{2}. \quad (5.30)$$

The inversion of the Bohr-Sommerfeld rule connecting the inclusion, Eq. (5.27), and the exclusion, Eq. (5.28), is then derived as follows. We multiply both sides of Eq. (5.29) with  $1/(E - E')^{1/2}$  and integrate over  $E'$ .

$$\int_{E_{\min}}^E \frac{\pi(n(E) + 1/2)}{\sqrt{E - E'}} dE' = \int_{E_{\min}}^E \frac{1}{\sqrt{E - E'}} \left( \int_{x_0}^{x_1} \sqrt{E - V(x)} dx \right) dE' \quad (5.31)$$

The integral on the right-hand side can be split into two parts

$$\begin{aligned} \int_{E_{\min}}^E \frac{1}{\sqrt{E - E'}} \left( \int_{x_0}^{x_1} \sqrt{E - V(x)} dx \right) dE' &= \int_{E_{\min}}^{V(x)} \frac{1}{\sqrt{E - E'}} \left( \int_{x_0}^{x_1} \sqrt{E - V(x)} dx \right) dE' \\ &\quad + \int_{V(x)}^E \frac{1}{\sqrt{E - E'}} \left( \int_{x_0}^{x_1} \sqrt{E - V(x)} dx \right) dE' \end{aligned} \quad (5.32)$$

The first term is identically zero, since the  $x$  integration does not contribute for  $E' < V(x)$ . For the second part, we can integrate explicitly noticing that the turning points depend on  $E$  and not  $E'$ . We obtain

$$\int_{V(x)}^E \frac{1}{\sqrt{E - E'}} \left( \int_{x_0}^{x_1} \sqrt{E - V(x)} dx \right) dE' = \frac{\pi}{2} \int_{x_0}^{x_1} (E - V(x)) dx. \quad (5.33)$$

where this last integral is the definition of inclusion as written in Eq. (5.27).

Now we must replace this result with Eq. (5.31), multiply it by  $2/\pi$ , and differentiate the final result. The result we obtain is

$$\begin{aligned} \frac{d}{dE} \int_{x_0}^{x_1} (E - V(x)) dx &= \left( \frac{\partial}{\partial E} + \frac{dx_0}{dE} \frac{\partial}{\partial x_0} + \frac{dx_1}{dE} \frac{\partial}{\partial x_1} \right) \int_{x_0}^{x_1} (E - V(x)) dx \\ &= \left( \frac{\partial}{\partial E} + \frac{dx_0}{dE} \frac{\partial}{\partial x_0} + \frac{dx_1}{dE} \frac{\partial}{\partial x_1} \right) \left( E(x_1 - x_0) - \int_{x_0}^{x_1} (V(x)) dx \right) \\ &= (x_1 - x_0) + E \left( -\frac{dx_0}{dE} + \frac{dx_1}{dE} \right) + \left( \frac{dx_0}{dE} V(x_0) - \frac{dx_1}{dE} V(x_1) \right) \\ &= (x_1 - x_0). \end{aligned} \quad (5.34)$$

We have used the fact that the term  $E - V(x_{1,2})$  vanishes on the turning points and we

have also taken into account the implicit dependence of the turning points on the energy.

Finally, the final result for the inversion of the Bohr-Sommerfeld rule is written as:

$$\mathcal{L}(E) = x_1 - x_0 = 2 \frac{d}{dE} \int_{E_{\min}}^E \frac{n(E) + 1/2}{\sqrt{E - E'}} dE' \quad (5.35)$$

This inverse formula for the Bohr-Sommerfeld rule reveals that given a spectrum of bound states  $E_n$ , it is in principle possible to reconstruct the width of the potential well  $L(E)$ . This does not mean that we reconstruct the potential  $V(x)$  itself and does not necessarily imply a failure of our inverse method, but simply a natural limitation that asserts to us that the connection between the spectrum of the bound states and the geometrical configuration of a potential well is in general not unique. Infinitely different potentials can admit the same spectrum. Eq. (5.35) tells us that all potentials sharing the same width also admit the same spectrum. That is an important result for energy-independent potentials, since to construct a family of isospectral potentials all we need to do is provide a valid function for one of the two turning points. We illustrate this last fact in the following chapter.

In chapter 7, we show that for energy-dependent potentials, however, this statement that tells us that all potentials sharing the same width admit the same spectrum no longer holds. Indeed, when the potential also varies with the energy  $V(x, E)$ , width-equivalent potentials do not reproduce in general the same energy-spectrum of their associated energy-dependent potentials. In such cases, although the problem becomes more complex, we show that the inverse formulas provided in this chapter are still reliable for obtaining an associated energy-independent effective potential, which we call WKB-equivalent potential.

### 5.3.2 Inverse Gamow Formulas

Finally, the inversion of the Gamow formula (Eq. (5.19)) is discussed in the following. Here, we follow the derivation reported in Refs. [200], but summarizing some of the intermediate steps.

We start with the derivative of  $T(E)$  with respect to  $E$ . Using Eq. (5.19) and exchanging the signal of the argument of the square root, we are led to

$$\frac{dT(E)}{dE} = \left( \frac{\partial}{\partial E} + \frac{dx_0}{dE} \frac{\partial}{\partial x_0} + \frac{dx_1}{dE} \frac{\partial}{\partial x_1} \right) e^{-2 \int_{x_0}^{x_1} \sqrt{V(x)-E} dx} \quad (5.36)$$

$$= \left( \int_{x_0}^{x_1} \frac{1}{\sqrt{V(x)-E}} dx - \frac{dx_0}{dE} \sqrt{V(x_0)-E} + \frac{dx_1}{dE} \sqrt{V(x_1)-E} \right) e^{-2 \int_{x_0}^{x_1} \sqrt{V(x)-E} dx} \quad (5.37)$$

$$= \left( \int_{x_0}^{x_1} \frac{1}{\sqrt{V(x)-E}} dx \right) e^{-2 \int_{x_0}^{x_1} \sqrt{V(x)-E} dx} \quad (5.38)$$

Similar to the previous case, terms with  $V(x_{1,2})-E$  vanish at the turning point. Dividing the resulting equation with  $T(E)$  yields

$$\frac{1}{T(E)} \frac{dT(E)}{dE} = \int_{x_0}^{x_1} \frac{1}{\sqrt{V(x)-E}} dx. \quad (5.39)$$

Now, we replace  $E \rightarrow E'$ , multiply with  $1/\sqrt{E'-E}$  and integrate over  $E'$  from  $E$  to  $E_{\max}$ .

$$\int_E^{E_{\max}} \frac{1}{\sqrt{E'-E}} \left( \frac{1}{T(E)} \frac{dT(E')}{dE'} \right) dE' = \int_E^{E_{\max}} \frac{1}{\sqrt{E'-E}} \left( \int_{x_0}^{x_1} \frac{1}{\sqrt{V(x)-E'}} dx \right) dE'. \quad (5.40)$$

$E_{\max}$  is the maximum of the potential barrier. Similar to the Bohr-Sommerfeld case it has to be extrapolated. Employing physical arguments, we choose  $E_{\max}$  to be defined as the energy value in which

$$T(E_{\max}) = \frac{1}{2}. \quad (5.41)$$

As in the previous section, we can split up the  $E'$  integration into two intervals, the first



interval for  $E' < V(x)$ , while the second goes from  $V(x)$  until  $E_{\max}$ . The first integral does not add any contribution for the total integral, so we obtain

$$\int_E^{E_{\max}} \frac{1}{\sqrt{E' - E}} \left( \int_{x_0}^{x_1} \frac{1}{\sqrt{V(x) - E'}} dx \right) dE' = \pi \int_{x_0}^{x_1} dx = \pi(x_1 - x_0). \quad (5.42)$$

Replacing Eq. (5.42) into Eq. (5.40), we obtain that the solution to the inverse transmission problem is the following inverted Gamow formula

$$\mathcal{L}(E) = (x_1 - x_0) = \frac{1}{\pi} \int_E^{E_{\max}} \frac{1}{\sqrt{E' - E}} \left( \frac{1}{T'(E)} \frac{dT(E')}{dE'} \right) dE'. \quad (5.43)$$

It is interesting to notice the same question concerning the non-uniqueness of the solution of our inverse problem can be raised here, in a similar fashion to the Bohr-Sommerfeld case. Eq. (5.19) tells us that all classes of width-equivalent potential share the same transmission. Accordingly, a given transmission  $T(E)$  cannot reconstruct a unique potential barrier. If we are willing to determine a unique potential barrier, we need to provide an additional relation for one of the two classical turning points. For the interesting case of a three turning points potential consisting of a cavity merged with a subsequent potential barrier, the previous reconstruction of the cavity already provides a relation for one of the two turning points from the potential barrier. The second turning point is then obtained by summing the reconstructed barrier width to the first one. We illustrate this specific case in the following chapter.

In chapter 7, we show that the uniqueness in the relation between the transmission and the width of a certain barrier is also lost for energy-dependent potential barriers. For a potential varying with the energy, the transmission associated with width-equivalent potentials is not equivalent to the actual transmission from the associated energy-dependent potentials. Nevertheless, as for the Bohr-Sommerfeld rule, the inverted Gamow formula provided here remains reliable for obtaining an associated energy-independent effective barrier, which we

call WKB-equivalent potential barrier.

In the following chapters, we only consider potentials for which WKB theory is valid and that the results in Eqs. (5.16),(5.19) are accurate enough. Due to the very nature of approximate methods, this might imply some quantitative restrictions on the potential shapes, but it does not affect the qualitative scope of the underlying method.

# Chapter 6

## The Inverse Method for Analog Gravity Systems

This Chapter is based on the following publication: **Inverse problem of analog gravity systems**.

Authors: Saulo Albuquerque, Sebastian H. Völkel, Kostas D. Kokkotas, Valdir B. Bezerra

DOI: 10.1103/PhysRevD.108.124053 (publication)

Published in: Phys.Rev.D 108 (2023) 12, 124053

### 6.1 Introduction

In this chapter, we present our novel inverse method. This nonparametric method is based on a semianalytic analysis of the underlying wave equation and does not require the specification of the details of the underlying model. As we show, it allows for the reconstruction of the effective perturbation potential from the knowledge of transmission and reflection coefficients for certain types of potentials in the Schrödinger wave equation admitting resonant tunneling. Note that this method differs greatly from standard inference statistical approaches. Instead, we show how the (WKB) theory-based results known for quasistationary states of astrophysical exotic compact objects [127, 125, 129] can be extended to recover the main properties of the effective potential, as well as absorption properties at the surface

of analog gravity systems.

We show how to use our method by applying it to an imperfect draining vortex, which has been suggested as an analog of extreme compact objects [48]. Although the inverse problem is, in general, not unique, choosing physically motivated assumptions and requiring the validity of the semiclassical theory, we demonstrate that the method provides efficient and accurate results.

In Chapters 2, 3, and 4, we outlined the fundamentals of the direct problem, introducing the numerical methods for computing the transmission curves from our scattering problem. Then, in Chapter 5 we presented the inversion of the WKB-based methods, and the inverse formulas to solve the inverse problem for given transmission and reflection coefficients. In this chapter, we finally discuss how these coefficients need to be further analyzed to provide the input for the analysis presented in the following sections. We then apply these methods to the imperfect draining vortex model and discuss our results in Sec. 6.5. Our conclusions can be found in Sec. 6.6.

## 6.2 Outline of the direct problem

Throughout this work, the main properties of the systems we consider can be obtained by studying the effective one-dimensional wave-equation (4.14). Here  $V(x)$  is, in general, an energy-independent potential that captures the dynamical properties of the object under consideration. Exotic astrophysical systems [104], as well as the analog systems we study in Sec. 6.5 can be best described by a potential barrier with model-dependent reflection properties on one side of the barrier. To understand the description of the inverse problem, let us first review the key concepts of the direct one.

There are two common scenarios in which Eq. (4.14) is typically studied. One of them is an eigenvalue problem for discrete values of  $E_n$  that are determined from suitably chosen boundary conditions. In its most basic form, this can either give bound states (purely

real eigenvalues of potential wells) or quasinormal modes (complex eigenvalues of potential barriers). The second scenario is the scattering problem of transmission and reflection coefficients, which is more commonly studied in quantum mechanics or in the context of black holes for Hawking radiation calculations. Both scenarios are not independent of each other, and in fact, our framework requires a joint analysis to address the inverse problem.

For those astrophysical or analog systems for which the outlined method here is valid, the typical structure of the potential yields the so-called quasistationary states as an eigenvalue problem. The spectrum  $\omega_n^2 = E_n = E_{0n} + iE_{1n}$  of those modes is characterized by real-valued bound states  $E_{0n}$ , together with a very small imaginary part  $E_{1n}$  reflecting the transmission through the barrier and “surface” thus measuring the respective mode’s lifetime. In the astrophysical context, these modes have first been found for ultracompact constant density stars in Refs. [209, 210] and are also known as trapped modes. Accordingly, as we usually have in the context of compact object perturbation theory, the real part of  $\omega_n$  describes the frequency of the  $n$  th mode, while the imaginary part of  $\omega_n$  is inversely proportional to the damping time of that respective mode. Therefore, exponentially small imaginary parts imply long-living trapped modes. This is physically expected in a potential well created between a reflective surface and a potential barrier. We show such a typical case in Fig. 6.1.

As we see later in the results, increasing the reflectivity of the reflective wall tends to increase the lifetime of the trapped modes. Since a “larger portion” of the wave is being reflected by the compact object’s surface, rather than being absorbed, those waves will be trapped in the well for a longer time before they actually manage to escape the well (being absorbed by the object, or being sent back to infinity). Therefore, larger reflectivity on the surface of the compact object implies exponentially smaller imaginary parts for the modes, which in turn leads to narrower widths in the transmission plots, as we discuss and illustrate later.

A semianalytic treatment of astrophysical exotic compact objects with such properties has been studied in Ref. [126], which combined the classical Bohr-Sommerfeld rule

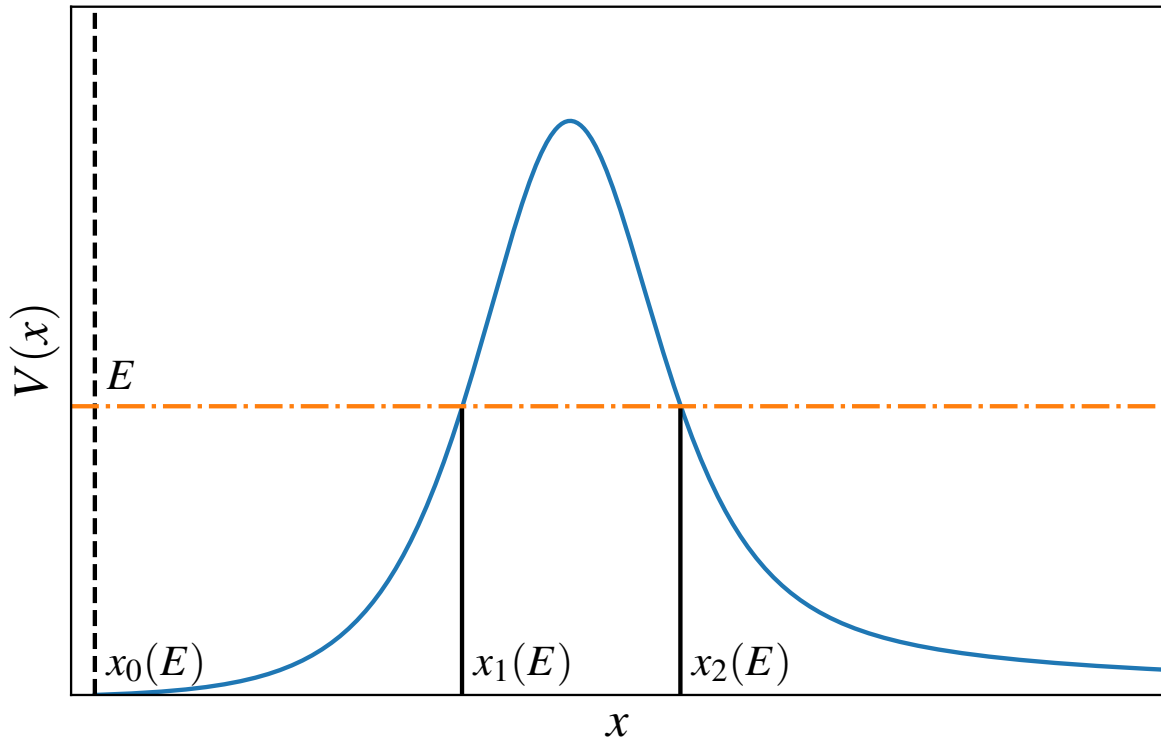


Figure 6.1: Here we show a typical potential barrier  $V(x)$  (blue) with turning points  $x_0(E)$ ,  $x_1(E)$ , and  $x_2(E)$  for a given value of  $E$  (orange dot-dashed line). The location of the reflective core's surface coincides with  $x_0(E)$  (black dotted line).

$$\int_{x_0}^{x_1} \sqrt{E_{0n} - V(x)} dx = \pi \left( n + \frac{1}{2} \right), \quad (6.1)$$

and the Gamow formula

$$E_{1n} = -\frac{1}{2} (T_1(E) + T_2(E)) \left( \int_{x_0}^{x_1} \frac{1}{\sqrt{E_n - V(x)}} dx \right)^{-1}. \quad (6.2)$$

Here  $x_0, x_1, x_2$  are the classical turning points defined by  $E_{0n} = V(x)$ . The semiclassical approximations for the transmissions  $T_2(E)$  through a potential barrier is given by Eq. (5.19), while  $T_1(E)$  is defined in terms of boundary conditions at the object's surface located at  $x_0$  and given by  $(1 - |K|^2)$ . See also Ref. [211] for a very similar approach to the direct problem. The inverse problem related to reconstructing properties of  $V(x)$  given the spectrum of quasistationary states was studied in Refs. [127, 125] by inverting the Bohr-Sommerfeld rule and Gamow's formula.

For the direct problem, we first need to evaluate the set of coefficients  $(A_h^+, A_h^-, A_\infty^+, A_\infty^-)$  from Eqs. (4.69). This is done by numerically evolving the  $\tilde{\Psi}_h$  solution from the wall at  $x_0$  to infinity, and vice versa, with the  $\tilde{\Psi}_\infty$  solution. With the evaluated coefficients, and by using Eqs. (4.69),(4.70) and, we can then determine the coefficients  $(A^{\text{wall}}, A^{\text{in}}, A^{\text{out}})$ , and, accordingly, the transmission and reflection coefficients  $T$  and  $R$ , respectively.

Finally, the transmission and reflection coefficients, calculated here by means of the direct numerical problem, provide the starting point to study the inverse method that we consider within this framework. In principle these are the observables that could be obtained through future laboratory experiments of analog gravity systems.

### 6.3 Outline of the imperfect draining vortex model

In chapter 3, we summarized the main details of the imperfect draining vortex as an analog of an extremely compact object. For more details, we refer the reader to Ref. [48], where this model was outlined in more depth. The effective wave equation, which is the central piece of our analysis, is given by Eq. (3.35).

The rotational properties of the vortex are characterized by the constant  $C$ , and  $m$  labels the harmonic decomposition used in the derivation of the effective wave equation for the radial part of the wave function. The latter one has a similar meaning as in the case of the Schwarzschild black hole. Note that, as in the case of rotating black holes, the potential becomes nontrivially  $\omega$  dependent for rotating configurations (for  $C \neq 0$ ). The absorption at the core of the vortex is modeled by defining a reflectivity  $K$  through the interface surface, and it is defined by the boundary conditions at  $r = r_h(1 + \epsilon)$ , where  $\epsilon$  is a very small number; we normalize our acoustic horizon radius with  $r_h = 1$ .

As applications for our inverse method, we have used the numerical setup described in Chapter 4 to generate transmission curves as a function of energy. From now on, we assume that the reflective wall is defined as the cylindrical surface (since we are in a 2+1-dimensional scenario) with a radial distance of the center defined by the value  $(1 + \epsilon)$ , where  $\epsilon = 2e^{-20}$ . According to Eq. (3.29), this implies that the tortoise coordinate is given by  $x_0 = -9$  at the reflective wall.

In order to study different analog system realization, we choose several reflectivity values  $K = [0, 0.75, 0.9, 0.99, 0.999]$ , several harmonics  $m = [4, 6, 8, 10]$ , and  $C = 0$ . To make the impact of each parameter more clear and to avoid a plethora of various combinations, we vary only one of the parameters at a time and set the other ones to default values. The transmission curves for different reflectivity values are shown in Fig. 6.2. As one would expect, the resonance peaks become more dominant for  $K \rightarrow 1$  and vanish in the limit  $K \rightarrow 0$ , but their location remains extremely similar. Varying the harmonic parameter



$m$  yields transmission curves provided in Fig. 6.3. Note that  $m$  changes the height of the potential barrier, which mainly controls the number of resonance peaks, but only mildly impacts their separation.

## 6.4 Outline of the inverse problem

With the numerical results for reflection and transmission coefficients available now, we will outline the different steps of the inverse problem method. We start with a high-level description of the main idea, and explain more specific details afterward.

The first step is to identify the location of resonance peaks as an approximation for the energies of the quasistationary states  $E_{0n}$ . Assuming that the Bohr-Sommerfeld rule Eq. (5.16) is a good approximation, it is known [212, 122] that it can be used to reconstruct the “width”  $L_1(E)$  of the potential well as a function of the energy via Eqs. (6.1) Here, however,  $E_{\min}$  is the minimum of the potential defined by extrapolating where  $n(E)+1/4 = 0$ . Note that the potential cannot be uniquely reconstructed, but instead there are infinitely many potentials sharing the same width between their turning points. For this reason, a well-motivated physical hypothesis must be additionally formulated for the turning points. As we later see, this hypothesis corresponds to fixing  $x_0$  as a constant value.

The second step is to combine the inversion of Gamow’s formula for a two-turning point potential barrier with the information about the potential well, which has been derived in Ref. [127] for a single barrier next to a reflective boundary condition and in Ref. [125] for quasistationary states trapped between two potential barriers. The inversion of the Gamow formula allows one to connect the transmission through a single potential barrier with the width of the barrier. This was first shown in [213, 214] and is given by Eq. (5.43). Note, however, that  $T(E)$  in this equation here is not the same as the full measured transmission coefficient, as the latter one includes the net result of the potential and the reflective wall combined together.

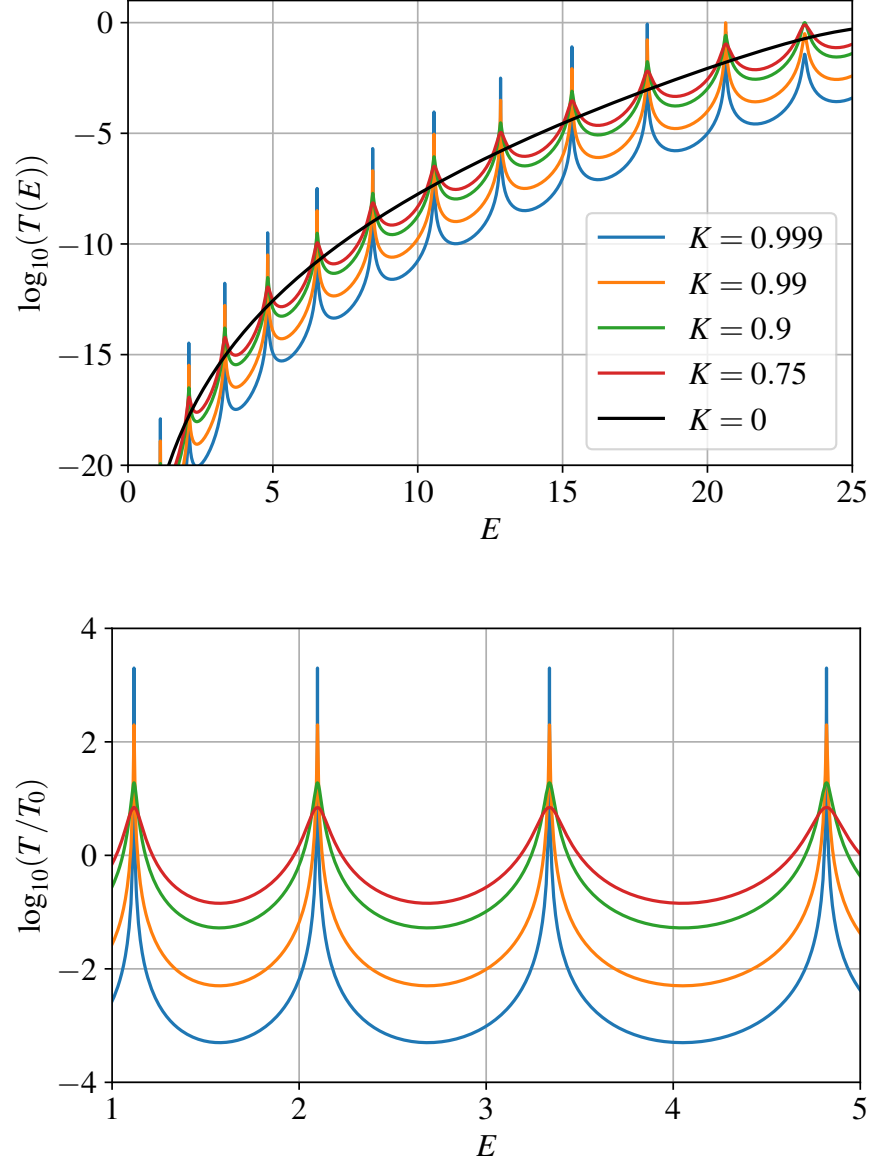


Figure 6.2: Here we show different aspects of the transmission  $T(E)$ . Top: transmission for different values of  $K = [0, 0.75, 0.9, 0.99, 0.999]$ ,  $C = 0$  and  $m = 10$ . Bottom: same transmissions as before (same colors), but normalized with the one for no reflectivity  $K = 0$  denoted with  $T_0$  and in a smaller  $E$  range for better visibility of the resonance peaks.

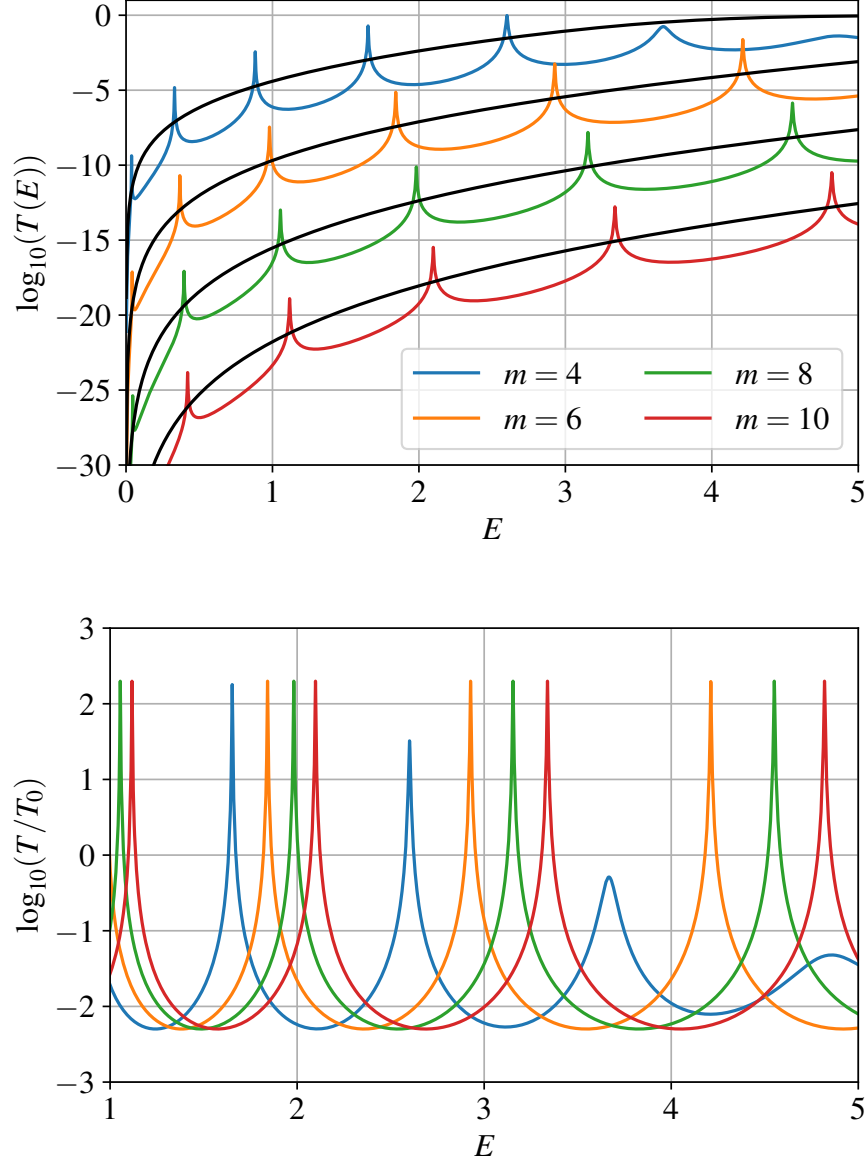


Figure 6.3: Here we show different aspects of the transmission  $T(E)$ . Top panel: transmission for different values of  $m = [4, 6, 8, 10]$ ,  $C = 0$ , and  $K = 0.99$ . The  $K = 0$  case for each  $m$  is shown for comparison (black lines). Bottom: same transmissions as before (same colors), but normalized with the ones for no reflectivity  $K = 0$  denoted with  $T_0$  and in a smaller  $E$  range for better visibility of the resonance peaks.

To circumvent this limitation, we developed a numerical fitting procedure that provides an effective transmission through the potential barrier individually, which can then be used for the reconstruction of the barrier. This numerical procedure starts from the total transmission through the barrier and reflective wall and isolates the pure effect of the potential barrier. The final result obtained by this procedure is what one could use as the input for the inversion of the Gamow formula, given by Eq. (5.43) to reconstruct the barrier with the additional information coming from the potential well. However, in order to obtain robust results, one needs to slightly modify the transmission for energies close to the peak of the barrier, which we outline in the sequence. Finally, although we have not faced problems from possible low-energy inaccuracies from the WKB method, it could be a problem in other cases. In that case, it may be useful to extrapolate the low-energy transmission with analytic functions that do not cause so-called “overhanging cliffs” in the corresponding potentials; see Ref. [128] for a related study on such analytic extensions.

#### 6.4.0.1 Treatment at energies close to the barrier peak

Because of the reduced validity of the Bohr-Sommerfeld rule and Gamow formula for energies around the peak of the barrier, we complement the close vicinity of the maximum of the potential barrier with a parabolic approximation

$$V_{\text{parabolic}}(x) = E_{\text{max}} + a(x - x_{\text{max}})^2. \quad (6.3)$$

Here the two relevant free parameters ( $E_{\text{max}}$  and  $a$ ) are directly obtained from fitting the analytic form of the transmission to the numerical one; see Appendix of Ref. [129]. With the estimate of  $E_{\text{max}}$ , one can now compute  $L_2(E)$  to obtain width-equivalent potentials  $V_{L_2}(x)$ . Finally, we define the effective reconstructed barrier to be a smooth interpolation between

the two potentials

$$V_{\text{eff}}(x; x_{\text{int}}, \lambda) = V_{\text{parabolic}}(x) \left( \frac{1}{2} - \frac{1}{2} \tanh[\lambda(x - x_{\text{int}})] \right) + V_{L_2}(x) \left( \frac{1}{2} + \frac{1}{2} \tanh[\lambda(x - x_{\text{int}})] \right), \quad (6.4)$$

where  $\lambda$  controls the “smoothness” of the transition between the two connected curves  $V_{\text{parabolic}}(x)$  and  $V_{L_2}(x)$  in  $x_{\text{int}}$ , where these two curves intersect. Directly approximating the maximum of the potential with a parabola improves the reconstruction, because the inversion of the Gamow formula used to derive  $L_2(E)$  is only valid for energies below the barrier peak. The choice of the matching point where the two curves shall intersect is done by optimizing the determination of the position of the parabola maximum in  $x$  axis, while looking for an intersection point where the functions to be matched have the same value and same slope.

### 6.4.1 Analysis of the transmission

Knowing the transmission/reflection coefficients, we now outline how exactly we analyze it to provide the necessary input for the semiclassical inversion methods. These quasistationary states, as well as the transmission, are only related to the potential barrier and the reflective wall.

#### 6.4.1.1 Extracting quasistationary states from transmission

Given the numerical transmission curve as the starting point of our analysis, we need to extract the spectrum of quasistationary modes. They are imprinted in the locations and widths of the resonance peaks. For example, the real part of the mode energies ( $E_{0n}$ ) are the energy values at the local center of the peaks (or the local center of the small “bumps”, in the low-reflectivity scenario), while the imaginary parts ( $E_{1n}$ ) are related to the widths of those peaks.

As we will discuss later, for some cases (high-reflectivity regime), the local center of the peaks are, with a very good approximation, the local maximum as well. For those cases, we extract the locations using a basic peak-finder algorithm, and then numerically fit a three parameter Lorentzian [215] in a very close vicinity to it,

$$f(E) = \frac{T(E_{\text{max}, n})\Gamma_n^2}{(E - E_{\text{max}, n})^2 + \Gamma_n^2}, \quad (6.5)$$

where  $E_{\text{max}, n}$  is the location of the resonance peak and the real part of  $E_n$ ,  $\Gamma_n$  is the half width at half maximum, and  $T(E_{\text{max}, n})$  is the peak value of the transmission at the resonant energy. The width  $\Gamma_n$  of a certain peak will be related to the imaginary part/damping time of its respective mode. To increase the accuracy and optimize the algorithm, we iteratively refine the energy resolution in a more narrow region around a given peak.

For the cases where the local maximums at the peaks are not a good approximation for the centers of the peak, a rather different approach is needed. This new approach is based on the analysis of the slope of the transmission and its variation within the peak. When passing through a peak/bump, the transmission's slope reaches a local maximum and it quickly decays into a local minimum (passing through zero, when there is a local maximum at this peak/bump). Accordingly, at the local center of the peak, the slope is decaying at the faster rate, so that the transmission's second-order derivative reaches a local minimum there. This way, we can estimate the local center of the small bumps by calculating the local minimum of their second derivative there. We further discuss the low-reflectivity scenarios in Sec. 6.5.1.2.

In all scenarios, we will be able to obtain the energies of the quasistationary modes ( $E_{0n}, E_{1n}$ ) for all different reflectivity regimes. These energies for the quasistationary states can then be solved for  $n(E_0)$ , interpolated, and then used as input for Eq. (5.35).

#### 6.4.1.2 Defining effective transmission through the barrier

As we demonstrate explicitly in the following, one can use the transmission including the resonance peaks to construct an “effective” transmission that only captures the transmission through the barrier. To isolate this effective transmission from the full transmission curve that contains the barrier and cavity effects, we need to employ a procedure we proposed. This technique consists of taking the average of the transmission’s envelopes. For applying this method, we first compute the envelopes connecting only the minima  $T_{\min}(E)$  and only the maxima  $T_{\max}(E)$  of the logarithm of the transmission curve and then construct an effective logarithmic transmission defined only by the envelopes

$$\log(T_{\text{effective}}) = \frac{1}{2}(\log(T_{\max})(E) + \log(T_{\min})(E)) \quad (6.6)$$

As it can be seen in Fig. 6.4, our technique furnishes a good approximation of the barrier transmission obtained in the case of perfect absorption at the core. Accordingly, this transmission will be the input for Eq. (5.43) to reconstruct the barrier width. In the following, we analytically demonstrate the validity of Eq. (6.6) for approximating the isolated barrier transmission.

- **Demonstrating the envelopes’ average approximation for the effective barrier transmission**

Here, we derive Eq. (6.6) and demonstrate analytically the average envelope technique’s validity. The proper application of this method is carried out in Sec. 6.5 of this chapter, and in Secs.6.5 of Chapter 8.

The boundary conditions for the wave functions  $\Psi(x, \omega)$  are given at the reflective boundary surface by Eq. (4.64). At spatial infinity, they are given by Eq. (4.64). From the amplitudes  $(A^{\text{in}}, A^{\text{out}})$  previously defined, we obtained that the transmission and reflection coefficients in terms of Eqs. (4.66). Particularly, the transmission for an imperfect draining

vortex (or for an extremely compact object), with a general reflectivity  $K$  at the boundary interface, can be rewritten if we rearrange Eq. (4.71) as

$$\frac{A^{\text{wall}}}{A^{\text{in}}} = \frac{\omega}{\tilde{\omega}} \frac{1}{A_h^+} \frac{1}{\left(1 - \frac{A_h^-}{A_h^+} K e^{-2i\tilde{\omega}x_0}\right)}, \quad (6.7)$$

So now we have a relation between  $T_{\text{ECO}}$  and  $T_{\text{BH}}$ , which is written as follows

$$T_{\text{ECO}} = (1 - |K|^2) T_{\text{BH}} \frac{1}{\left|1 - \frac{A_h^-}{A_h^+} K e^{-2i\tilde{\omega}x_0}\right|^2}, \quad (6.8)$$

where  $T_{\text{ECO}} = T_{K \neq 0}$ , and  $T_{\text{BH}} = T_{K=0}$ .

The subscript  $K$  labels the reflectivity parameter  $K$  defined for the system. If we want to consider the particular case of a perfect absorbing acoustic hole (a black hole, in the astrophysical scenario), we need to restrict ourselves to the specific regime of  $K = 0$ . This scenario leads us to

$$T_{\text{BH}} = T_{K=0} = \left(\frac{\omega}{\tilde{\omega}}\right)^2 \frac{1}{|A_h^+|^2}. \quad (6.9)$$

In other words, for a general reflective case, the transmission can be written as a product of the transmission for the sub-case with no reflectivity (perfect absorbing boundary conditions) with an extra term  $\mathcal{F}_K$

$$T_K = \mathcal{F}_K T_{K=0}, \quad (6.10)$$

where

$$\mathcal{F}_K = \frac{(1 - |K|^2)}{\left|1 - \frac{A_h^-}{A_h^+} K e^{-2i\tilde{\omega}x_0}\right|^2}. \quad (6.11)$$



That extra term  $\mathcal{F}_K$  is what we call 'normalized transmission'. It adds the cavity and reflective boundary effects on the final transmission. Since we want to find a way to estimate the effective barrier transmission  $T_{K=0}$  from the full transmission  $T_K$ , we need to find a way to isolate  $T_{K=0}$  from this extra term.

Studying  $\mathcal{F}_K$  in detail, we see that it is modulated by the transmission through the reflective surface  $(1 - |K|^2)$ , while it also oscillates according to  $e^{-2i\tilde{\omega}x_0}$ , which explains the peaks on the resonant modes. This oscillatory behavior is dictated by two times the cavity size  $(-2x_0)$ , describing the phase change of the waves as they come from the barrier to the interface, and are reflected back to the barrier; and by the complex phase of  $A_h^-/A_h^+$ . This oscillation, in turn, is modulated by  $K$  (the peaks are more pronounced for higher reflectivity) and damped by the absolute value of the 'reflection' term  $A_h^-/A_h^+$ . It is that last term that explains why around the  $E_{\text{vertex}}$ , the transmission peaks tend to decay from their 'uniform' behavior suddenly. It is known that  $|A_h^-/A_h^+| = 1$  for energies below  $E_{\text{vertex}}$ , and it quickly decays to zero around  $E \approx E_{\text{vertex}}$ . After that,  $|A_h^-/A_h^+| \rightarrow 0$ , and  $\mathcal{F}_K \rightarrow (1 - |K|^2)$ .

Finally, in the low energy regimes, we notice that  $\mathcal{F}_K$  oscillates uniformly between a maximum (the peaks) and a minimum (the valleys). The maximums happen when  $e^{(-2i\tilde{\omega}x_0 + \text{phase}(A_h^-/A_h^+))} = 1$ , and the minimums when  $e^{(-2i\tilde{\omega}x_0 + \text{phase}(A_h^-/A_h^+))} = -1$ . So we have that for energies  $E < E_{\text{vertex}}$ ,

$$\frac{(1 - |K|^2)}{|1 + K|^2} < \mathcal{F}_K < \frac{(1 - |K|^2)}{|1 - K|^2} \quad \text{for } E < E_{\text{vertex}} \quad (6.12)$$

Since we are assuming that  $0 < K < 1$ , this implies that  $\mathcal{F}_K$  maximums are  $(1 + K)/(1 - K)$ , while its minimums are  $(1 - K)/(1 + K)$ . And then,

$$\log \mathcal{F}_{K_{\text{max}}} = -\log \mathcal{F}_{K_{\text{min}}}, \quad \text{for } E < E_{\text{vertex}} \quad (6.13)$$

Therefore, taking the Log of Eq. 6.10, we get

$$\log T_K = \log \mathcal{T}_{K=0} + \log \mathcal{F}_K. \quad (6.14)$$

Finally, we can demonstrate the result we wanted from the beginning, namely, we can show that

$$\log T_{K=0} = \frac{1}{2}(\log T_{K_{\max}} + \log T_{K_{\min}}), \quad \text{for } E < E_{\text{vertex}} \quad (6.15)$$

where  $T_{K_{\max}}$  is the transmissions calculated at the peaks (maximums of  $\mathcal{F}_K$ ) and  $T_{K_{\min}}$  is the transmissions calculated at the valleys (minimums of  $\mathcal{F}_K$ ). While  $T_{K_{\max}}$  defines the superior envelope,  $T_{K_{\min}}$  defines the inferior one. Equation (6.15) states that the average of those envelopes gives the effective barrier transmission (the transmission for the purely absorbing case) for energies below  $E_{\max}$ .

For energies higher than  $E_{\max}$ , however, we see that  $|(A_h^-/A_h^+)| \rightarrow 0$ . In Eq. 6.11, this leads to

$$\mathcal{F}_K \rightarrow (1 - |K|^2), \quad \text{for } E > E_{\text{vertex}} \quad (6.16)$$

And since at this limit  $T_{K=0} \rightarrow 1$ , hence, the total transmission of our system  $T_K$  tends to plateau at the finite value  $T_K \rightarrow (1 - |K|^2)$ . This is exactly what we see in the transmission curves in Fig. 6.4. Notice that  $(1 - |K|^2)$  is the transmission through the reflective boundary, which means that for energies higher than  $E_{\max}$ , the waves are completely transmitted through the effective barrier and are only reflected by the reflective interface at the boundary  $x_0$ . Here, we have achieved a natural limitation for our technique. For energies around  $E_{\max}$  and above it, we no longer can approach the barrier transmission with the effective transmis-

sion  $T_{\text{eff}}$  defined by Eq. (6.6). As for this high energy regime, however, this methodological limitation is circumvented in this thesis by complementing the approximation of the effective barrier transmission with the Gamow points' information, taken from Eq. (6.2)

This way we have finally demonstrated Eq. (6.6) for the effective transmission through the potential barrier. We have also shown the limits of this approximation, which provides us with important insights into the asymptotic behavior of the core reflectivity in general. In the following sections, we apply this equation and its underlined technique for reconstructing the effective potential barriers.

## 6.5 Application and results

In this section, we show the results of our inverse method applied for the imperfect draining vortex.

### 6.5.1 Reconstruction of potential and reflectivity

With the transmission curves of the previous section, we now apply the inverse methods introduced in Chapter 5. We first show and discuss our results for varying the harmonic number  $m$  in Sec. 6.5.1.1 and then study the reflectivity  $K$  in Sec. 6.5.1.2.

#### 6.5.1.1 Dependency on harmonic $m$

In the following, we demonstrate the various steps that have been explained in Sec. 7.2. We start our analysis with the transmission curves from Fig. 6.3 (for  $K = 0.99$  and  $m = [4, 6, 8, 10]$ ). To obtain an accurate estimate for the location and widths of the resonance peaks, we could first normalize it with the  $K = 0$  transmission. If the  $K = 0$  transmission is not available, e.g., because such a case could not be realized in an experiment, it can also be approximated with high accuracy from constructing  $T_{\text{effective}}(E)$  from envelopes, as discussed in Sec. 6.4.1.2. In the following, we assume the latter is the case and do not make explicit

use of any  $K = 0$  knowledge. The result of the envelope construction is shown in Fig. 6.4, which clearly demonstrates the excellent agreement between the effective transmission and the  $K = 0$  transmission, at least until it reaches energies close to the maximum of the potential ( $E \approx 20 \sim 25$ ). Using the location of the resonance peaks  $E_{0n}$ , we can invert the relation for  $n(E_{0n})$ , interpolate it, and use it as input for Eq. (5.35), which then enters Eq. (5.35). This yields the width of the cavity  $L_1(E)$ , which we report in the bottom panel of Fig. 6.5, and concludes the reconstruction of the cavity properties.

Next, we use the effective transmission  $T_{\text{effective}}(E)$  to compute the width of the barrier  $L_2(E)$  via Eq. (5.43). Because  $T_{\text{effective}}(E)$  deviates from the  $K = 0$  transmission close to the potential maximum (depending on the value of  $K$ ), we use the Gamow formula Eq. (6.2) and the width of the resonance peaks  $\Gamma_n = E_{1n}$  to define  $T_2(E)$ . The Gamow formula relates those values with the sum of transmission  $T_1(E) + T_2(E)$ . Note the presence of the integral over the potential well, which can only be computed using our reconstructed width  $L_1(E)$ . Because of the nonuniqueness of the reconstructed potentials from  $L_1(E)$ , we can construct any potential with such a turning point relation to carry out the integration numerically. Since the transmission is constant through the wall  $T_1(E) = 1 - K^2$ , and the transmission through the barrier  $T_2(E)$  is exponentially smaller for lower energies, we can assert that, in the low-energy regime, the sum  $T_1(E) + T_2(E)$  tends to  $T_1(E) + T_2(E) \approx T_1(E) = 1 - K^2$ . This helps us infer the transmission through the wall  $T_1(E)$  and its associated reflectivity  $K$ . With these values, we can infer the behavior of  $T_2(E)$  for higher energies if we use  $T_2(E) = T_1(E) + T_2(E) - (1 - K^2)$ , where  $T_1(E) + T_2(E)$  is obtained by Gamow formula [Eq. (6.2)]. This procedure gives us some points slightly below the blue dots shown in Fig. 6.4. If we interpolate those points, we obtain the green dashed line, which can be used to properly continue the  $T_{\text{effective}}(E)$  in the energy domain where the envelopes' mean failed to approximate the transmission through the barrier  $T_{K=0}(E)$ .

Smoothing  $T_2(E)$  with  $T_{\text{effective}}(E)$  we capture the barrier transmission for low and maximum energies and, finally, use it in Eq. (5.43) to obtain  $L_2(E)$ , which we report in the

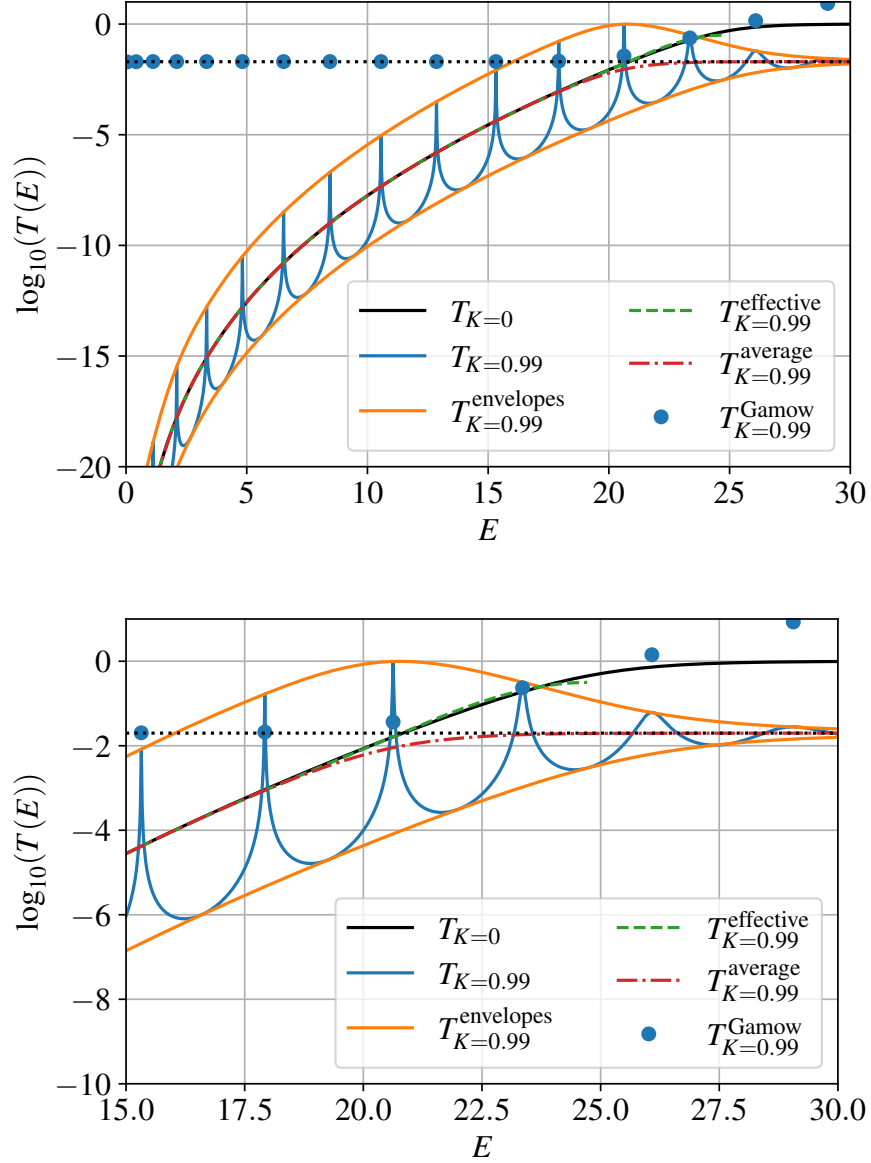


Figure 6.4: Here we compare the transmission  $T_{K=0.99}(E)$  for  $m = 10$  and  $C = 0$  (blue solid) with  $T_{K=0}(E)$  (black solid line). The corresponding envelopes  $T_{K=0.99}^{\text{envelopes}}(E)$  (orange solid line) and the average transmission  $T_{K=0.99}^{\text{average}}(E)$  (red dash-dotted line) defined by the two envelopes that are shown as well. It is evident that the average transmission is a very accurate approximation for  $T_{K=0}(E)$  until  $E \approx 20$ , where it plateaus toward around  $10^{-2}$  (black dotted line), which corresponds to  $1 - K^2$ . Here, the effective transmission  $T_{K=0.99}^{\text{effective}}(E)$  (green dashed line) follows  $T_{K=0}(E)$  closely until around the maximum of the potential barrier (around  $E = 25$ ).  $T_{K=0.99}^{\text{Gamow}}(E)$  (blue points) are the transmissions obtained from the resonance peaks and Gamow formula, see main text. Bottom: we show the same system as in the top, but for a smaller energy range for better visibility of details.

bottom panel of Fig. 6.4. Because the  $L_2(E)$  integration requires the knowledge of  $E_{\max}$ , which is not known *a priori*, we used the parabolic transmission (7.4) approximation to fit  $T_2(E)$  transmission in a range that can initially be estimated from where the transmission starts to plateau.

With two relations  $L_1(E), L_2(E)$  for three turning points  $x_0, x_1, x_2$ , one needs to provide a third relation to define a specific potential. The natural choice in our problem is to assume that the location of the reflective wall does not depend on the energy, and thus, we set  $x_0$  to be some constant. The only freedom in choosing the constant is a coordinate shift, which is not relevant for the underlying properties of the system. Finally, we report the reconstructed potentials defined by this choice in Fig. 6.6. As can be seen in both figures, the overall accuracy of the reconstruction improves with larger values of  $m$ . Because  $m$  mostly controls the height of the barrier, and thus the number of quasistationary states that appear as resonance peaks, one should expect the reconstruction to be more accurate because more information can be used for the interpolation of the spectrum and effective transmission. Furthermore, the underlying WKB-based methods are expected to be most accurate for the quasistationary states that are located not too close to the minimum of the potential, and not too close to the maximum of the barrier.

### 6.5.1.2 Dependency on reflectivity $K$

What remains is the reconstruction of the corresponding reflectivity parameters  $K$ . We assume that the wall's reflectivity  $K$  is energy independent and thus the same for all different incident wave frequencies. In this case, the transmission through the wall is also a constant and given by

$$T_1(E) = 1 - K^2. \tag{6.17}$$

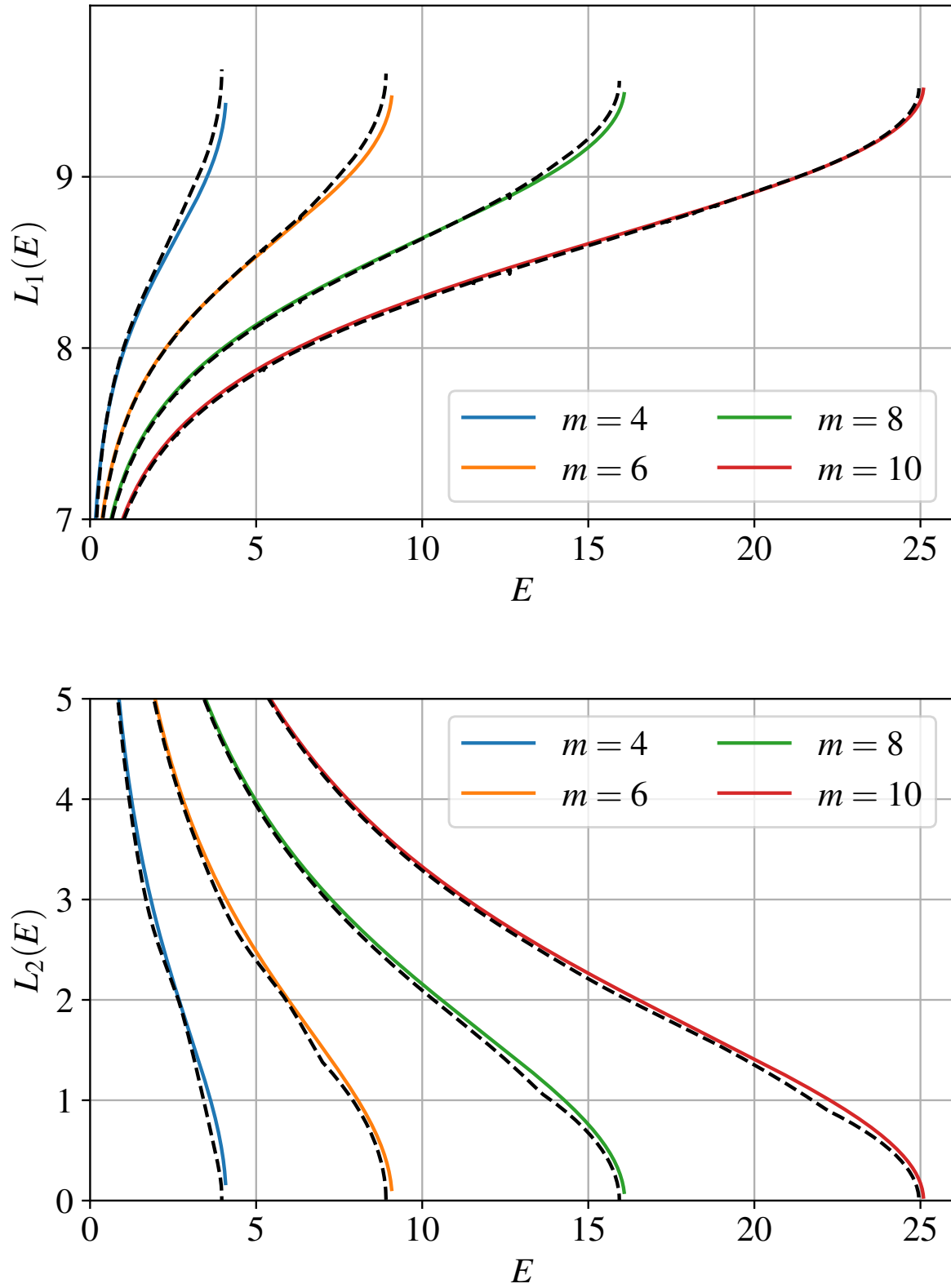


Figure 6.5: In this plot we show the exact (colored solid) and reconstructed (black dashed) widths  $L_1(E)$  (top panel) and  $L_2(E)$  (bottom panel) for  $K = 0.99$  and  $m = [4, 6, 8, 10]$ .

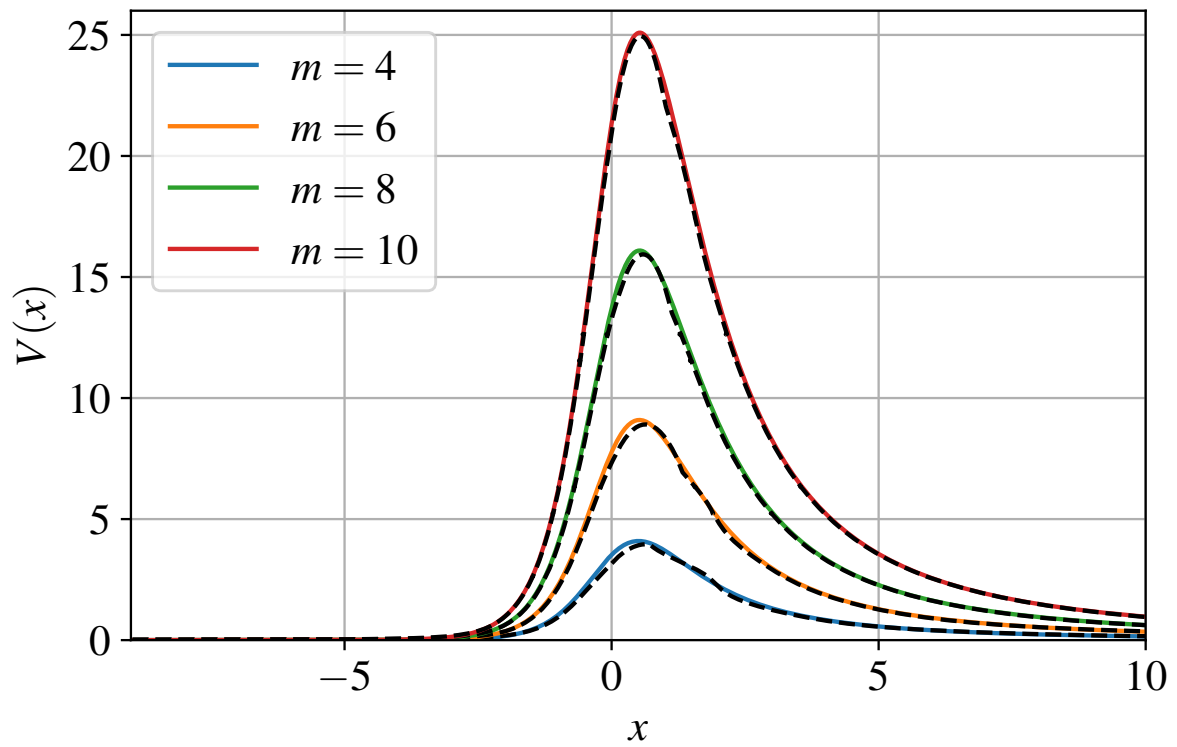


Figure 6.6: Here we show the true (colored lines) and reconstructed (black dashed) effective potentials  $V(x)$  for  $K = 0.99$  and  $m = [4, 6, 8, 10]$ . The location of the effective core's surface is at  $x = -9$ .



Accordingly, as an outcome of applying the Gamow formula Eq. (6.2), one can obtain the sum of the value above, for the transmission through the wall, with the transmission  $T_2(E)$  through the potential barrier as if the wall would be perfectly absorbing. The sum  $T_1(E) + T_2(E)$  is dominated by  $T_1(E)$  for low energies, because  $T_2(E)$  becomes exponentially small. This fact can be illustrated graphically in Fig. 6.4. If we look at the blue dots [the Gamow points  $T_1(E) + T_2(E)$ ], we can see that they start to plateau as we decrease the energy. This plateau gives us the constant value of  $T_1(E) = 1 - K^2$ .

We show the reconstructed values of  $K$  in Fig. 6.7. Here, the  $x$  axis labels the  $n$ -th quasistationary state that has been used in the Gamow formula Eq. (6.2). One can observe that for values of  $K$  close to 1, the reconstruction is very accurate. In this case the transmission through the wall is much smaller than the one through the barrier and the resonance peaks can be very accurately extracted. For smaller values of  $K$ , the reconstruction loses accuracy, and deviates from the correct injection by  $10\% \sim 20\%$  for  $K = 0.75$ . To investigate this, we tried several improvements. First, even when the  $T_2(E)$  contribution is included in the Gamow formula (by using the effective transmission extrapolated), the results for  $K = 0.75$  do not change significantly, especially not for moderate values of  $n$ , where the approximation is excellent. Second, we also checked whether fitting all resonance peaks simultaneously can give better results, because peaks start to overlap and results may get biased. However, also in this case we do not report improvements, as we fit the resonance peaks in a close vicinity around the maximum, where the impact of the other peaks is mainly absorbed by the value of the transmission at each maximum,  $T(E_{\max})$  Eq. (6.5), and does not impact  $\Gamma_n$  significantly. Finally, the alternative and more direct approach to determine  $K$  is from  $T(E)$  via Eq. (6.17) evaluated for energies beyond the maximum of the barrier, since then the effect of the barrier becomes negligible. We note that the latter approach is complementary to using the widths of the resonance peaks. Which of the two approaches yields more accurate results when applied to real data with measurement uncertainties remains for future work.

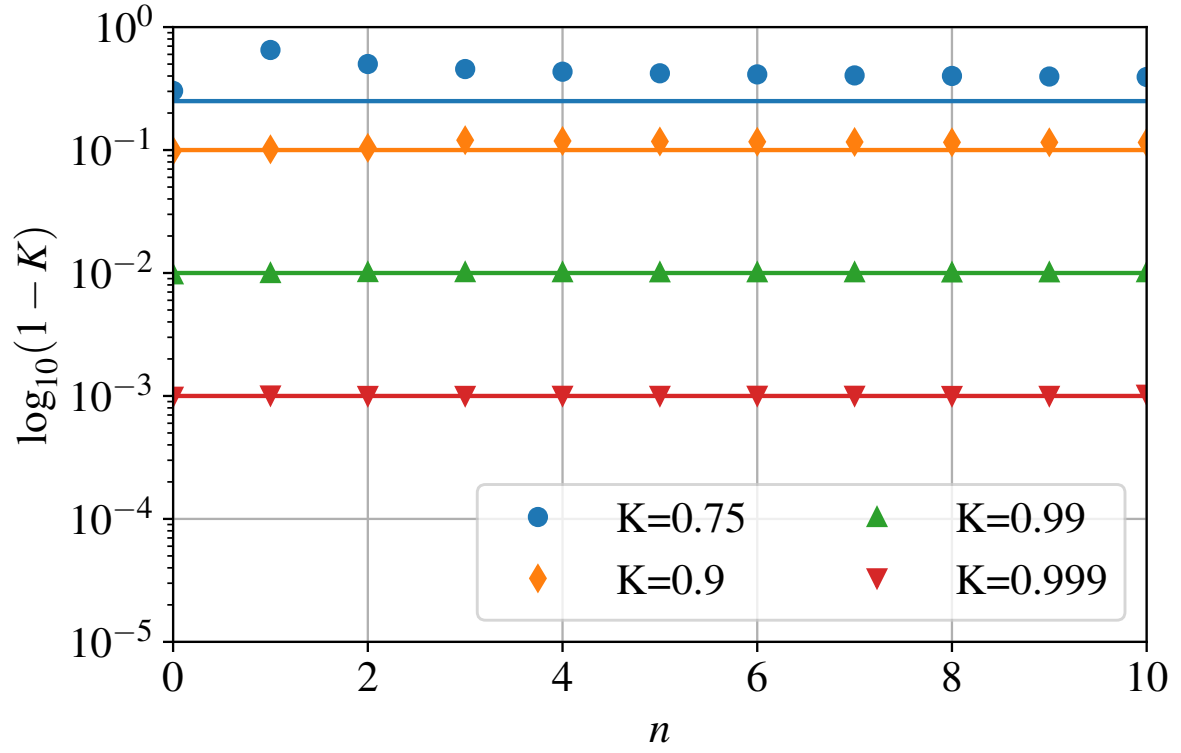


Figure 6.7: Reconstruction of the different reflectivity parameters  $K = [0.75, 0.9, 0.99, 0.999]$  with the inverse method using the resonance peaks and Gamow formula. The solid lines correspond to the exact values, while the different points are the reconstructed values using the  $n$  resonance peak.

## 6.6 Conclusions

Analog gravity systems may provide unique and controlled measurements of their key properties, which are not accessible from their astrophysical counterparts. The novel method that we developed in this work is based on the extension of semiclassical methods and is tailored to study measured transmission/reflection coefficients of analog exotic compact objects. The outcome of the method is the reconstruction of the effective potential, which captures the dynamical properties of the system, as well as the reflectivity coefficient describing the internal boundary condition. In this work, we chose the imperfect draining vortex model suggested in Ref. [48] as one example. First, we obtained the transmission/reflection coefficients with accurate (numerical) methods to explore different properties of the system, in particular, the impact of the reflectivity  $K$  and different angular numbers  $m$ . These results were then used as ideal measurements of a future experiment to demonstrate the capabilities of the new (semiclassical) method.

Our main findings for this chapter are as follows. The reconstruction of the effective potential becomes very accurate with increasing angular numbers  $m$ , which is expected from the validity of the underlying WKB theory. This is also related to the fact that for the same location of the core, increasing  $m$  yields more resonance states, and thus more information used for the interpolation of the inclusion (5.35) that is needed to reconstruct the width of cavity. The reconstruction of the reflectivity coefficient  $K$  through the width of the resonance peaks becomes more accurate when it approaches unity, which corresponds to the full reflection case. This may also be expected, because large values of the reflectivity result in more prominent resonance peaks. Although inverse problems are often not uniquely solvable (typically not limited by the chosen methods), we suggested physically motivated assumptions that allow one to reconstruct the effective potential. We want to stress that because the input of our method has been computed with accurate numerical methods, but the reconstruction is based on semianalytic results, comparing the original potential with

its reconstruction is not circular, but indeed self-consistent. Because of the explicit energy dependence of the potential for rotating configurations (for  $C \neq 0$ ), we have focused on  $C = 0$  and leave the conceptually more involved inverse problem of the energy-dependent potential for a separate work.

Since our method is based on modifying similar approaches for the inverse problem of quasistationary states [127, 125] and Hawking radiation [129], we also want to briefly compare some aspects. Although the knowledge of the transmission/reflection coefficients does not rely on the knowledge of the spectrum of quasistationary states, our method partially relies on identifying them indirectly. Thus, for specific model parameters that only provide very few such states, our method is not very accurate. However, since increasing angular numbers yields larger potential barriers, they also yield potentials with more quasistationary states. This means, if one is experimentally able to measure transmission/reflection coefficients of large enough angular numbers, our method can, even in such cases, always be used. In the context of astrophysical objects, this is not easily possible, as standard binary mergers mostly excite small angular numbers, which undermines the opportunities of studying analog gravity systems.

We conclude this chapter with a comment on measurement uncertainties. Throughout this work we assumed that the transmission/reflection coefficients can be provided with pristine accuracy. However, any real experiment will come with statistical and systematic uncertainties, which may need to be taken into account. This could, for example, be done by repeating the reconstruction procedure for different realizations of the transmission coefficient that represent the statistical uncertainties of the measurements. At the same time, these uncertainties may not be relevant for all energy ranges, since the transmission varies over many orders of magnitude.

# Chapter 7

## The Inverse Method for Energy Dependent Potentials and the Extension for Rotating Analog Systems

This Chapter is based on the following publication: **Inverse problem in energy-dependent potentials using semiclassical methods.**

Authors: Saulo Albuquerque, Sebastian H. Völkel, Kostas D. Kokkotas

DOI: 10.1103/PhysRevD.109.096014 (publication)

Published in: Phys.Rev.D 109 (2024) 9, 096014

### 7.1 Inverse Method for Energy-Dependent Potentials

Energy-dependent potentials in wave equations play an important role in many different areas of physics. They appear naturally in nuclear physics [216, 217, 218, 219, 220, 221, 222, 223, 224, 225, 226, 227, 228, 229], when studying perturbations of black holes and neutron stars [230, 231, 232, 233], and in analog gravity [234]. One popular approach to solving the wave equations is to use the Wentzel-Kramers-Brillouin (WKB) method. Among its most iconic tools are the classical Bohr-Sommerfeld rule [235] for the computation of bound states in potential wells, and the Gamow formula [236] for the computation of transmission and

reflection coefficients.

Due to their simplicity, it is known how they can be used to infer relevant information of the underlying potential in the *inverse problem*, *i.e.*, when bound states or transmission coefficients can be provided [212, 122, 213, 214]. Such an inversion is also possible for one, three or four turning point potentials with quasi-stationary states [127, 125, 130]. One of the key results is that the inversion is, in general, not unique. Instead, one can reconstruct a family of potentials with similar properties for their classical turning points. The universal property is that the separation of turning points must be unchanged. Thus, these potentials may also be called *width equivalent* potentials. In the literature, some authors have also coined such potentials as *WKB-equivalent* potentials; see Ref. [237].

To our knowledge, existing studies on the inverse problem using the Bohr-Sommerfeld rule or Gamow formula have only considered energy-independent potentials. However, many physical scenarios require one to work with energy-dependent potentials. Although WKB methods to solve the direct problem of bound states or transmission function are relatively straightforward to use, *e.g.*, see Refs. [238, 239, 240], the energy dependence may introduce additional degeneracy for the inverse problem.

In this chapter, we demonstrate how the standard methods for the inverse problem can be used to construct WKB-equivalent, energy-independent potentials from the bound states and transmission coefficients of energy-dependent potentials. As examples, we study extensions of the quadratic potential (harmonic oscillator), and the Pöschl-Teller potential [241]. Using numerical methods, we also quantify how accurately these potentials can represent their energy-dependent pendants. One of our main findings is that *energy-dependent, WKB-equivalent potentials are not width-equivalent anymore*. Another important finding is that those reconstructed, energy-independent, effective potentials capture some key properties of their associated energy-dependent ones, such as their asymptotic behavior and local behavior around their minimum or maximum.

The rest of the chapter is organized as follows. In Sec. 7.2, we apply the semi-classical

methods and our numerical scheme to two energy-dependent potentials in Sec. 8.4. We discuss our findings in Sec. 7.4, and our conclusions can be found in Sec. 8.5.

## 7.2 Methods

In the following, we first review some basics of the WKB method in Sec. 7.2.1 for energy-dependent potentials. Next, we discuss the important role played by the turning points within this framework in Sec. 7.2.2.

### 7.2.1 WKB method for energy-dependent potentials

The WKB method, also known as semi-classical approximation, is a widely used approximation to study linear differential equations. For energy-dependent potentials, this method is based on the one-dimensional wave equation

$$\frac{d^2}{dx^2}\psi(x) + Q(x, E)\psi(x) = 0, \quad (7.1)$$

where

$$Q(x, E) \equiv E - V(x, E). \quad (7.2)$$

Here,  $V(x, E)$  is an energy-dependent potential.

The WKB method is valid under several assumptions (see Refs. [201, 242] as standard references for more details), and it breaks down close to classical turning points (defined by  $Q(x, E) = 0$ , or equivalently,  $E = V(x, E)$ ). To construct solutions, one can connect exact, local solutions, *e.g.*, described by the Airy functions, with the WKB solutions using asymptotic matching. One convenient application of that approach is to derive so-called quantization conditions to compute eigenvalues  $E = E_n$  for given boundary conditions of a potential well or reflection/transmission coefficients through potential barriers. Although

the WKB method is not exact, it can be an excellent approximation. Moreover, due to the integral equations, it is also possible to study the inverse problem, in which one is interested in reconstructing properties of the potential for given eigenvalues or transmission/reflection coefficients. We have seen in Chapter 5 two of the most commonly used applications, namely the Bohr-Sommerfeld Rule in Eq. (5.16) and the Gamow Formulas in Eqs. (5.19).

The Bohr-Sommerfeld rule can be inverted to study the inverse problem, in which one is provided with some spectrum  $E_n$  and is interested in reconstructing the potential [212, 122]. Solutions to the inverse problem are, in general, not unique, and the problem itself may even be ill-posed. By inverting the Bohr-Sommerfeld rule, the non-uniqueness is imprinted in the observation that one can only reconstruct the width of the potential defined by the separation of turning points

$$\mathcal{L}_1(E) = x_1(E) - x_0(E) = \frac{\partial}{\partial E} I(E), \quad (7.3)$$

where  $I(E)$  is the so-called inclusion, given by Eq. (5.27).

The Gamow formula approximates the transmission  $T(E)$  through a two turning point via Eq. (5.19). Although more accurate WKB-based results exist, the advantage of Eq. (5.19) is that it can be inverted similarly to the Bohr-Sommerfeld rule (5.16). In Chapter 5 and in Refs. [213, 214], it was shown that it is again the separation of turning points.

### 7.2.1.1 Parabolic approximation of the potential maximum

Because the Gamow formula and its inversion formula become less accurate around the potential peak, we approximate this region of the reconstructed, energy-independent, potential barriers with a parabolic approximation

$$V_{\text{parabolic}}(x) = V_{\text{max}} + \alpha(x - x_{\text{max}})^2, \quad (7.4)$$



with  $x_{\max} = 0$ . The two other free parameters ( $V_{\max}$  and  $\alpha$ ) are then obtained by fitting the analytic form of the transmission to the numerical transmission obtained from the energy-dependent potentials; see Ref. [2], and appendix of Ref. [129] for more details. In general, we note that the value of  $V_{\max}$  obtained by this fitting procedure agrees well with  $E_{\max}$  obtained by solving  $T(E_{\max}) = 1/2$ . Once we have estimated the two parabolic parameters, we match our inverse potential barrier constructed with the inverse Gamow formula with the fitted parabola around the peak via a smooth version of the Heaviside function, given by  $\Theta_{\pm}(E; E_0, \kappa) = 1/2 \pm (1/2) \tanh[\kappa(E - E_0)]$ . Here,  $\kappa$  controls the “smoothness” of the transition between the two connected curves, while  $E_0$  determines around where the transition takes place. We choose  $E_0$  as the energy for which the two curves intersect.

### 7.2.2 Remark on turning points

Turning points of a potential, as shown in Fig. 7.1, are a concept that is well motivated beyond WKB theory. Because they play an important role in the expected validity of the WKB method (via  $Q(x, E) \equiv E - V(x, E)$ ), it is natural to generalize the definition of turning points  $x_i$  for energy-dependent potentials to  $V(x_i, E) = E$ , where the argument in  $V(x, E)$  is the same  $E$  as used on the right-hand side.

The minimum  $V_{\min}$  or maximum  $V_{\max}$  of an energy-independent, two turning point potential can be defined as the pair of values  $(x_{\text{critic}}, E_{\text{critic}})$  for which  $Q(x, E) = 0 \Leftrightarrow V(x) = E$  and  $dQ(x, E)/dx = 0 \Leftrightarrow dV(x)/dx = 0$ . Similarly, for the more general case of energy-dependent potentials  $V(x, E)$ , we define the vertex point as the pair of values  $(x_{\text{vertex}}, E_{\text{vertex}})$  for which  $Q(x_{\text{vertex}}, E_{\text{vertex}}) = 0$ , and  $dQ(x_{\text{vertex}}, E_{\text{vertex}})/dx = 0$ . Note that another way of defining  $V_{\min}$  or  $V_{\max}$  of a two turning point, energy-independent potential is by requesting that the left and right turning points converge  $x_0(E_{\text{vertex}}) = x_1(E_{\text{vertex}})$ . For energy-dependent potentials, this holds as well.

Finally, the Bohr-Sommerfeld treatment of complex-valued potentials, *e.g.*, as they appear for perturbations of the Kerr black hole, is also possible and has been investigated in

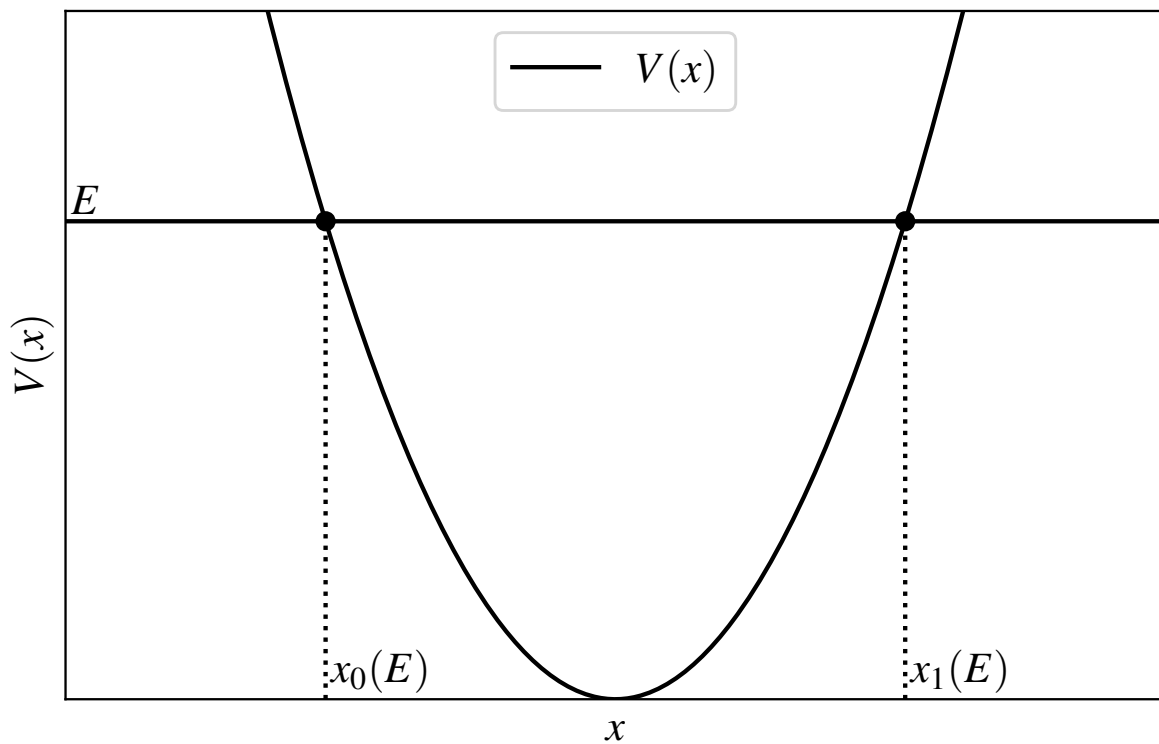


Figure 7.1: Potential well  $V(x)$  with the pair of turning points  $x_0(E), x_1(E)$  associated with the energy  $E$  denoted as points at the intersection  $E = V(x)$ .

Ref. [199]. In this case, the turning points are, in general, also complex-valued, but both cases share a non-trivial behavior of  $Q(x, E)$  with respect to  $E$ .

### 7.2.3 Numerical methods

To verify the accuracy of the WKB-based methods, we use a straight-forward shooting method to compute the bound states and numerical integration through the potential barrier to obtain the transmission. Later, we also present the approximate results obtained with the Bohr-Sommerfeld rule and Gamow formula. Such a comparison allows us to determine where the methods are reliable and where they lose accuracy.

#### 7.2.3.1 Shooting method for bound states

The shooting method is based on numerically integrating the wave-equation for given boundary conditions from both sides. For Eq. (7.1), we choose the asymptotic behavior for the solution to be given by Eqs. (4.21), for the cases where  $V(x, E)$  asymptotically goes to constant values, and for the cases where  $V(x, E)$  diverges at the two limits. The eigenvalues are then obtained by determining the roots of the Wronskian of the numerical solutions at some intermediate point.

#### 7.2.3.2 Numerical integration for transmission

Similar to the shooting method, the transmission is obtained by numerical integration, but for different boundary conditions. In this case, our *ansatz* for two independent solutions are the same wave solutions which satisfy the boundary conditions in Eqs.(4.21).

From the computational point of view, the solutions described by those solutions and  $\psi_2$  describe monochromatic plane waves numerically evolved from one end of the domain to the other. Physically, the first solution represents incoming plane waves with an incident amplitude  $A_\infty^+$  that are scattered at the energy-dependent potential  $V(x, E)$ . Those waves are partially reflected with reflection amplitude  $A_\infty^-/A_\infty^+$ , and partially transmitted with

transmission amplitude  $1/A_{\infty}^-$ . A similar interpretation can be made for  $\psi_2$ . Accordingly, the transmission coefficient can be defined as

$$T^2 = \frac{1}{A_{\infty}^{-2}} = \frac{1}{B_{-\infty}^{-2}}. \quad (7.5)$$

### 7.3 Application and results

In the following, we apply the WKB-based methods to two types of energy-dependent potentials. In Sec. 7.3.1, we study a modified quadratic potential, and in Sec. 7.3.2, we consider a modified Pöschl-Teller potential. We first consider parameters of the potentials that yield wells admitting bound states and then barriers for which we compute the transmissions.

In all applications, our approach can be explained in three main steps. First, for the given energy-dependent potential, we provide the spectrum of bound states/transmission either analytically or with the numerical method. Second, we use the spectrum/transmission as input for the WKB-based inverse method to construct the width of a family of WKB-equivalent, energy-independent potentials. Third, we use the numerical method to compute the bound states/transmission of one of the reconstructed potentials  $V_{\text{inv}}(x)$  to quantify how accurately they match the original ones. For comparison, we also use the numerical method to compute the associated properties of the energy-independent, width-equivalent potential  $V_{\text{width}}(x)$ .

Therefore, we associate with a certain energy-dependent potential  $V(x, E)$ , an energy-independent, inverse potential  $V_{\text{inv}}(x)$ , which must match the property used for its reconstruction, at least within the validity of the WKB-approximation. This allows one to describe properties of energy-dependent potentials more simply by constructing energy-independent ones.

### 7.3.1 Energy-dependent quadratic potential

As first example, we study an energy-dependent quadratic potential, given by

$$V_{\text{HO}}(x, E) = (a + bE)x^2 + cE + V_0, \quad (7.6)$$

where  $a, b, c, V_0$  are real-valued constants. In the following, we consider two scenarios that either describe potential wells in Sec. 7.3.1.1, or potential barriers in Sec. 7.3.1.2. For each of the two scenarios, we study two distinct cases for the variation of the concavity with the variation of the energy. The cases are defined by  $a/b < 0$ , which tends to increasingly open the parabola with increasing  $E$ , and by  $a/b > 0$ , which tends to close it. To make the main text more readable, but still cover comprehensive material, some of the results are reported in the appendix 7.5.

#### 7.3.1.1 Potential wells

The spectrum of bound states  $E_n$  can be computed analytically. For this we generalized results first reported for the case  $c = V_0 = 0$  in Ref. [243]. The energy of the normal modes are obtained by solving

$$E_n(1 - c) + V_0 = (2n + 1)\sqrt{a + bE_n}. \quad (7.7)$$

To test our numerical implementation of the shooting method presented in Sec. 7.2.3.1, we have verified that it agrees with the analytic results.

Varying  $E$  yields a family of curves for the potential, whose qualitative properties depends non-trivially on the chosen parameters. To illustrate that, we present the potential and the results of the inverse method for  $a/b < 0$  in Fig. 7.2, whose caption contains the numerical values of all parameters. The top panel demonstrates that the potential curves as function of  $E$  get increasingly more open until  $E_{\text{limit}} = -a/b$ . At this energy, the potential turns into

a horizontal line at  $V_0 - ca/b$  and the separation of turning points diverges. For even higher energies, the curvature of the parabola becomes negative. Qualitatively, we therefore expect that by approaching the energy limit of  $E \rightarrow E_{\text{limit}} = -a/b$ , the system starts behaving as a quasi-free particle in a constant potential, with the energy spacing of the modes becoming increasingly smaller.

Using the bound states as input for the inverse Bohr-Sommerfeld rule (7.3) yields a family of inverse potentials  $V_{\text{inv}}(x)$  sharing the same separation of turning-points. To fix one of them, we assume that the potential is symmetric around the origin ( $x_0(E) = -x_1(E)$ ). From Fig. 7.2 it is evident that  $V_{\text{inv}}(x)$  is not the same as the width equivalent potential  $V_{\text{width}}(x)$ . On the other hand, they are asymptotically converging to the same maximum energy for large values of  $x$  and are similar close to the minimum.

In the bottom panel of Fig. 7.2, we compare the bound states of the original potential Eq. (7.7) with the ones of the inverse potential and the width-equivalent potential, all computed using the numerical method. The inverse potential  $V_{\text{inv}}(x)$  is quasi-isospectral with the original energy-dependent potential. The asymptotic behavior of the overtones marks the transition from an essentially discrete spectrum to a quasi-continuum one, showing the increasing opening tendency of the energy-dependent potential. The bound states of the width-equivalent potential  $V_{\text{width}}(x)$  differ quantitatively but otherwise have a similar behavior as a function of  $n$ .

The case  $a/b > 0$  also provides interesting, but qualitatively different applications. Instead of opening with higher energy values, the potential curves become progressively more closed. We refer the reader to appendix 7.5.1 for an illustration of this scenario.

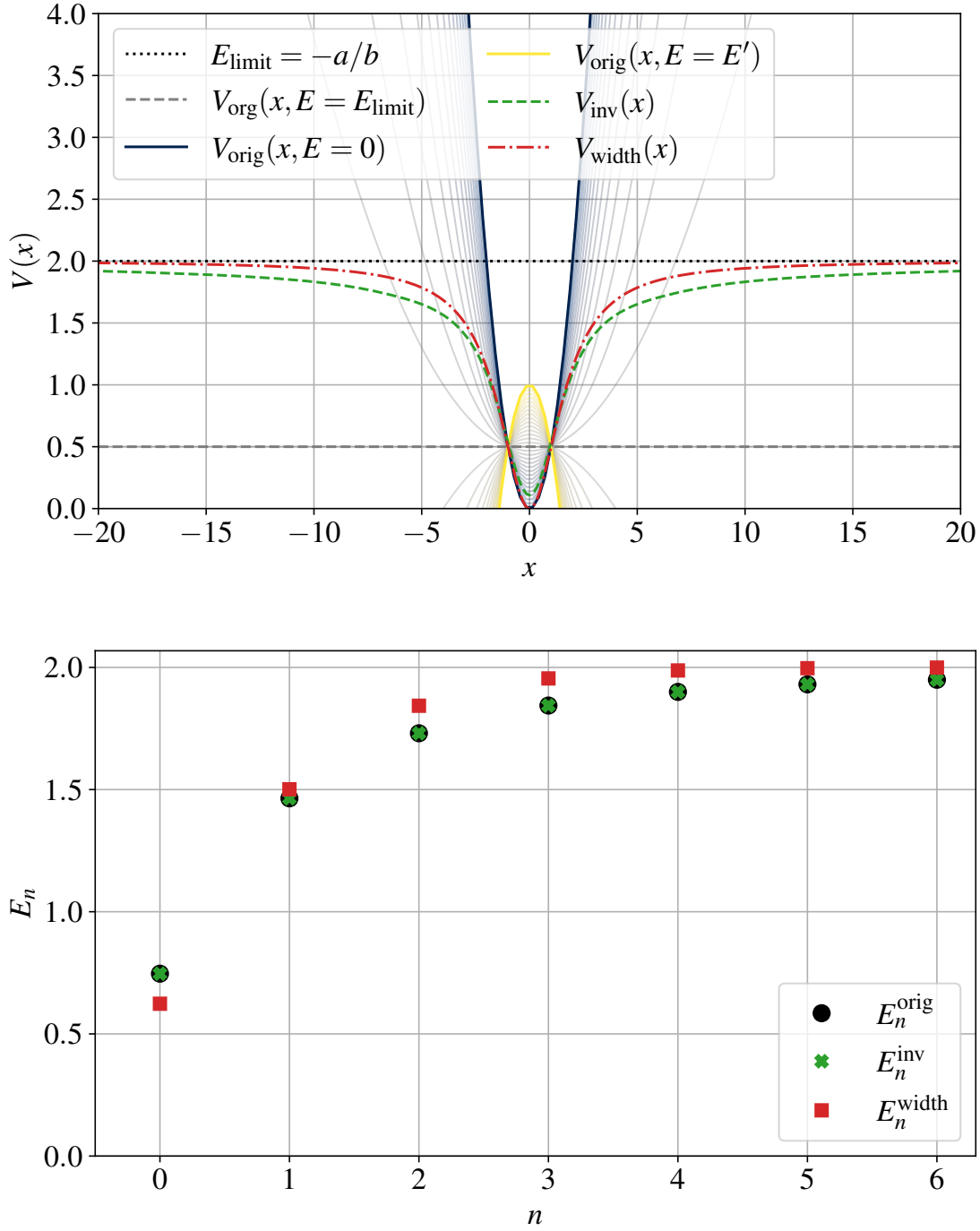


Figure 7.2: Application of the inverse method to the energy-dependent quadratic potential Eq. (7.6) for case  $a/b < 0$ , with parameters  $a = 0.5, b = -0.25, c = 0.25, V_0 = 0$ . Top panel: The series of curves of varying colors indicate the chosen value of  $E$  when computing the energy-dependent potential  $V_{\text{orig}}(x, E) = V_{\text{HO}}(x, E)$  starting from  $E = 0$  to  $E = E' = 2E_{\text{limit}}$ . The inverse potential (green dashed) is labeled as  $V_{\text{inv}}(x)$  and the width-equivalent potential (red dotted dashed) is labeled as  $V_{\text{width}}(x)$ . Bottom panel: Here we show the spectrum of bound states for the original potential  $E_n^{\text{orig}}$  (black circles), the inverse potential  $E_n^{\text{inv}}$  (green cross), and the width-equivalent potential  $E_n^{\text{width}}$  (red squares).

### 7.3.1.2 Potential barriers

To represent a more standard barrier, we re-define the original potential as follows

$$\bar{V}_{\text{HO}}(x, E) = \begin{cases} V_{\text{HO}}(x, E), & x_{i1} < x < x_{i2}, \\ 0, & \text{otherwise.} \end{cases} \quad (7.8)$$

The points  $x_{i1}$  and  $x_{i2}$  are defined by where the potential is zero, by  $V_{\text{HO}}(x_{i1,i2}, E) = 0$ , and are thus given by

$$x_{i1,i2} = \pm \sqrt{-\frac{V_0 + cE}{a + bE}}. \quad (7.9)$$

As previously, the energy dependence introduces a non-trivial behavior for the family of potential curves. The linear term  $cE$  is responsible for the vertical shift. For  $c \in (0, 1)$ , by increasing the energy, it will eventually reach a vertex point  $E_{\text{vertex}} = V_0/(1 - c)$  in which the two turning points converge to a single point at the maximum of its associated parabola  $V(x_{\text{vertex}}, E_{\text{vertex}})$ , just like a global maximum in an energy-independent potential. For  $c > 1$ , however, this scenario does not occur.

The maximum of an energy-independent potential barrier with two turning points plays an important role in the scattering of waves [142]. There the transmission changes from exponentially small values to asymptotically one. Similarly, for energy-dependent potentials, the vertex  $E_{\text{vertex}}$  for the turning points is exactly where the wave scattering of those potentials transits from almost null absorption to full transmission. After this reference value, the associated potential  $V(x, E)$  no longer possesses turning points, and the energy is above the barrier. Thus  $E_{\text{vertex}}$  characterizes a local maximum of an effective, energy-independent potential barrier with similar properties. The existence of  $E_{\text{vertex}}$ , which plays the role of  $E_{\text{max}}$  in the Gamow formula, is crucial for the inverse method when applied to energy-dependent potentials. For this reason, our discussions are limited to  $c \in (0, 1)$ .

In the following, we apply our method to a potential with  $a/b > 0$ , and report our results



in Fig. 7.3. It shows that the potential barrier curves tend to increasingly close their concavity with increasing  $E$ , which is shown in the top panel of Fig. 7.3. Here we also provide the results for the inverse potential  $V_{\text{inv}}(x)$  and the width-equivalent potential  $V_{\text{width}}(x)$ . They are both similar close to their vertex at  $E_{\text{vertex}} = V_0/(1 - c)$ , but overall deviate. The corresponding transmissions provided in the bottom panel demonstrate that  $V_{\text{inv}}(x)$  better reproduces the original transmission. The transmission of  $V_{\text{width}}(x)$  differs substantially for small energies, but becomes very similar around the maximum. In the appendix 7.5.1, we provide complementary results for a potential barrier with  $a/b < 0$ .

### 7.3.2 Energy-dependent Pöschl-Teller potential

As the second main example of energy-dependent potentials, we introduce a modified Pöschl-Teller potential given as follows

$$V_{\text{PT}}(x, E) = (a + bE)\text{sech}^2[k(x - x_0)] + cE + V_0. \quad (7.10)$$

The main reason for considering the Pöschl-Teller potentials is that it is widely used in different areas of physics, including nuclear physics [244, 245], and the perturbations of black holes and exotic compact objects [246, 247, 248].

An important difference between the energy-dependent, quadratic potential and the here presented Pöschl-Teller potential is that the latter one converges necessarily to finite asymptotic values for  $x \rightarrow \pm\infty$  given by  $V_0 + cE$ .

#### 7.3.2.1 Potential wells

In this subsection, we present the findings of the Pöschl-Teller energy-dependent potential wells. Again, we differentiate between  $a/b > 0$  and  $a/b < 0$ . Both cases provide distinct profiles for the energy-dependent variation of the potential. We show the potentials for a range of energy values for  $a/b < 0$  in the top panel of Fig. 7.4. Here, we also present the

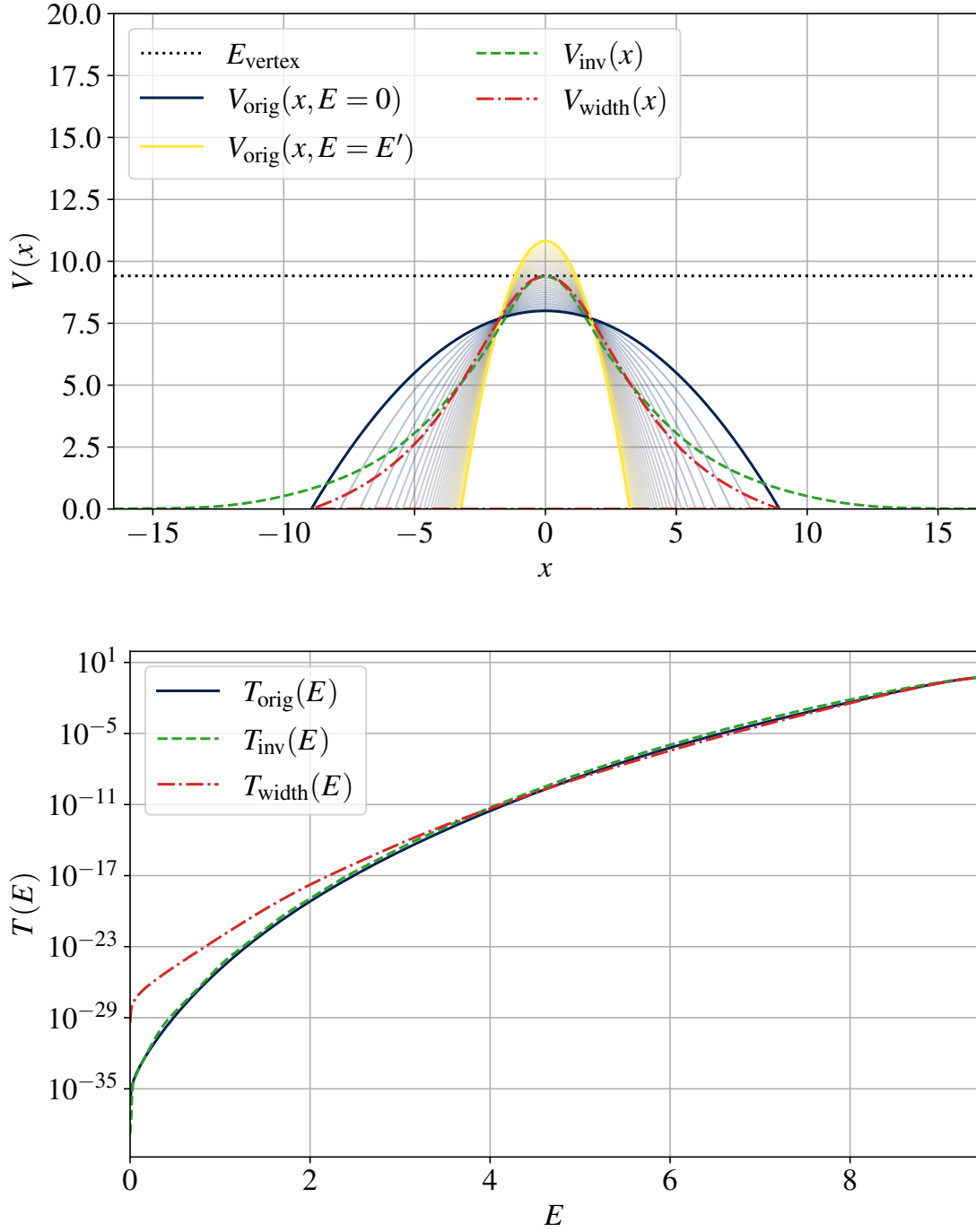


Figure 7.3: Application of the inverse method to the energy-dependent quadratic potential barrier Eq. (7.6) for case  $a/b > 0$ , with parameters  $a = -0.1$ ,  $b = -0.05$ ,  $c = 0.15$ , and  $V_0 = 8$ . Top panel: The series of curves of varying colors indicate the chosen value of  $E$  when computing the energy-dependent potential  $V_{\text{orig}}(x, E) = \bar{V}_{\text{HO}}(x, E)$  starting from  $E = 0$  to  $E = E' = 2E_{\text{vertex}}$ . The inverse potential (green dashed) is labeled as  $V_{\text{inv}}(x)$  and the width equivalent potential (red dotted dashed) is labeled as  $V_{\text{width}}(x)$ . Bottom panel: Here we show the transmission for the original potential  $T_{\text{orig}}(E)$  (black solid line), the inverse potential  $T_{\text{inv}}(E)$  (green dashed line) and the width-equivalent potential  $T_{\text{width}}(E)$  (red dot-dashed lines).

inverse potential and the width-equivalent potential. In the bottom panel, we report the associated bound states. The case  $a/b > 0$  is presented in the appendix 7.5.

We notice that  $V_{\text{inv}}(x)$  and  $V_{\text{width}}(x)$  agree in both cases very well at the minimum, as well as for their asymptotic value  $V_0/(1 - c)$  for large values of  $|x|$ . However, for intermediate energies, the two potentials differ. The bound states of the original potential agree in both cases very well with the ones of the inverse potential, while they differ for the ones of the width-equivalent one. As the energy approaches the asymptotic value of the potential, the energy spacing between the modes decreases, which indicates the transition to a quasi-continuum spectrum of a quasi-free particle, as in Sec. 7.3.1.1. Note that the energy dependence lifts the potential minimum, and thus decreases the space for bound states. The opposite is observed in case  $a/b > 0$ , which is shown in appendix 7.5.2.

### 7.3.2.2 Potential barriers

Finally, we investigate Pöschl-Teller potential barriers. In the following, we consider  $a/b < 0$ , while  $a/b > 0$  is reported in appendix 7.5. The potentials can be found in the top panel of Fig. 7.5, while the associated transmissions are reported in the bottom panel. In both cases, we find that  $V_{\text{inv}}(x)$  and  $V_{\text{width}}(x)$  agree well at their maximum value  $E_{\text{vertex}} = (a + V_0)/(1 - (c + b))$ , but not at intermediate energies. In the lower panel, we show the transmissions associated with the potentials. As expected, the transmission reconstructed from the inverse potential matches very well with the original transmission, while there are significant differences when compared to the width-equivalent potential, at least for energies below the maximum.

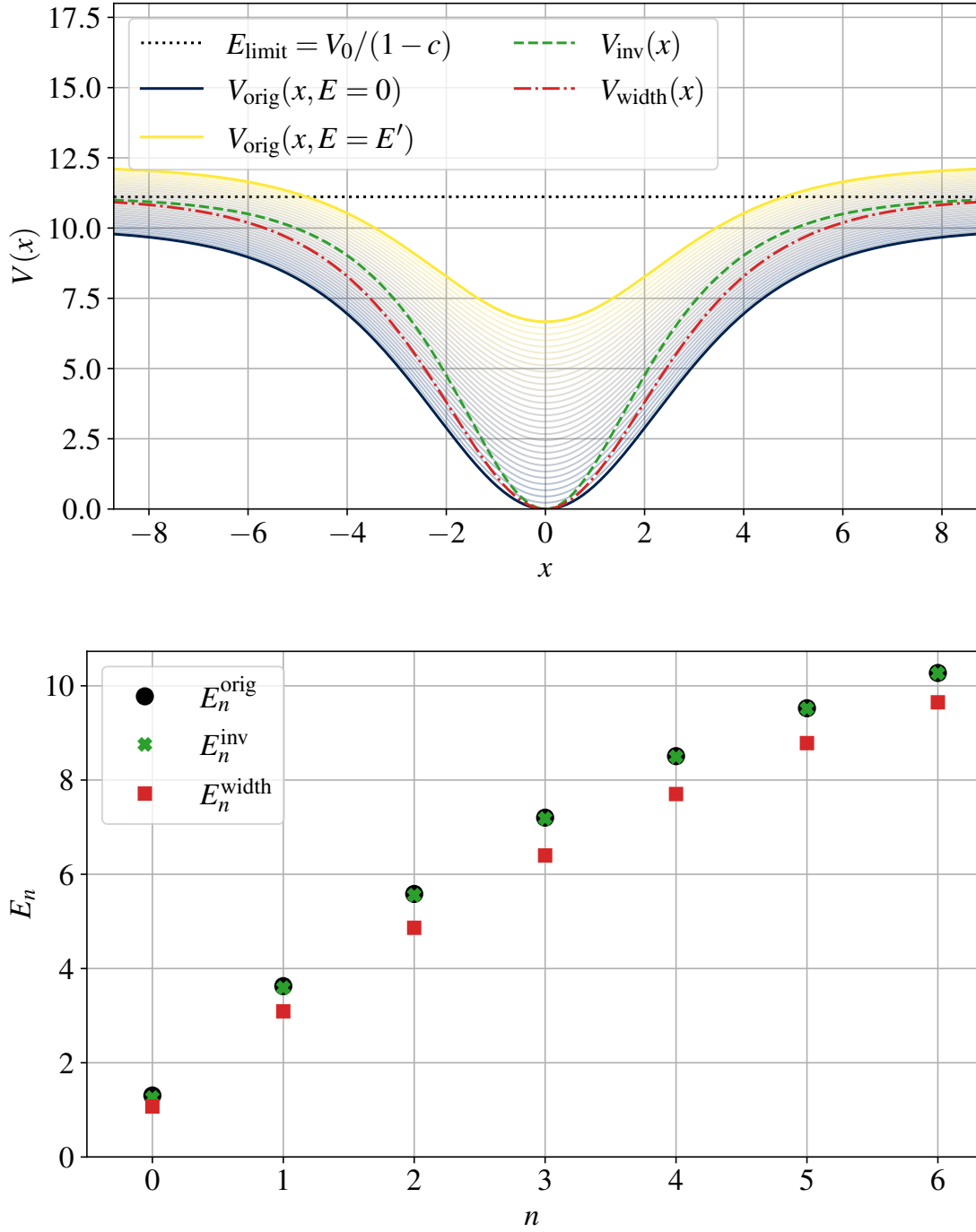


Figure 7.4: Application of the inverse method to the energy-dependent Pöschl-Teller potential Eq. (7.10) for case  $a/b < 0$ , with parameters  $a = -10$ ,  $b = 0.2$ ,  $c = 0.1$ ,  $k = 0.3$ , and  $V_0 = 10$ . Top panel: The series of curves of varying colors indicate the chosen value of  $E$  when computing the energy-dependent potential  $V_{\text{orig}}(x, E) = V_{\text{PT}}(x, E)$  starting from  $E = 0$  to  $E = E' = 2E_{\text{limit}}$ . The inverse potential (green dashed) is labeled as  $V_{\text{inv}}(x)$  and the width equivalent potential (red dotted dashed) is labeled as  $V_{\text{width}}(x)$ . Bottom panel: Here we show the spectrum of bound states for the original potential  $E_n^{\text{orig}}$  (black circles), the inverse potential  $E_n^{\text{inv}}$  (green cross), and width-equivalent potential  $E_n^{\text{width}}$  (red squares).

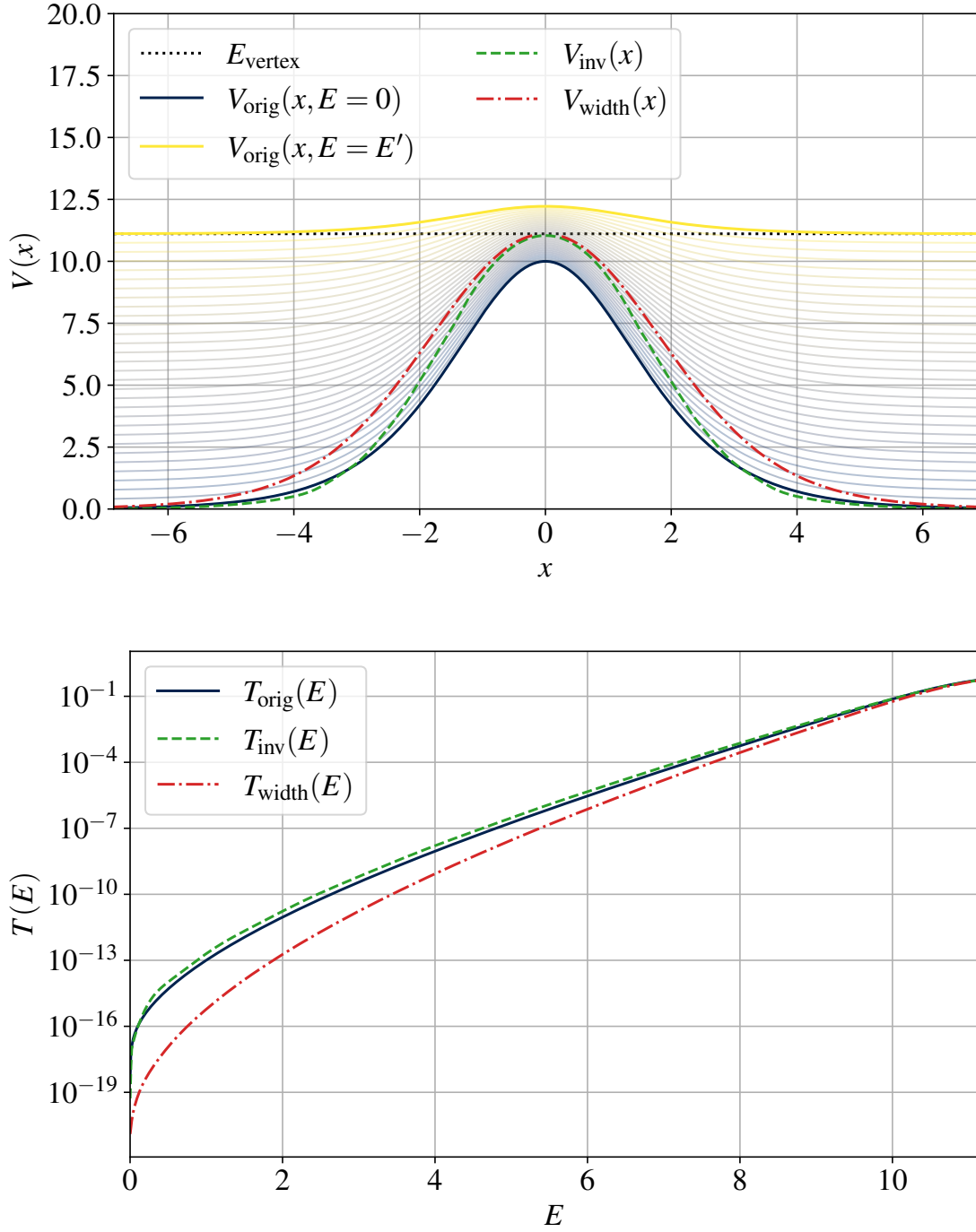


Figure 7.5: Application of the inverse method to the energy-dependent, Pöschl-Teller potential Eq. (7.6) for case  $a/b < 0$  with parameters  $a = 10$ ,  $b = -0.4$ ,  $c = 0.5$ ,  $k = 0.5$ , and  $V_0 = 0$ . Top panel: The series of curves of varying colors indicate the chosen value of  $E$  when computing the energy-dependent potential  $V_{\text{orig}}(x, E) = V_{\text{PT}}(x, E)$  starting from  $E = 0$  to  $E = E' = 2E_{\text{vertex}}$ . The inverse potential (green dashed) is labeled as  $V_{\text{inv}}(x)$  and the width equivalent potential (red dotted dashed) is labeled as  $V_{\text{width}}(x)$ . Bottom panel: Here we show the transmission for the original potential  $T_{\text{orig}}(E)$  (black solid line), the inverse potential  $T_{\text{inv}}(E)$  (green dashed line) and the width-equivalent potential  $T_{\text{width}}(E)$  (red dot-dashed lines).

## 7.4 Discussion

### 7.4.1 Width-equivalent is not WKB-equivalent

As stated previously, and demonstrated in our results, one key finding of our work is that the spectra and transmissions of width-equivalent energy-dependent potentials are, in general, not WKB-equivalent. By explicitly constructing the width-equivalent potentials and computing their spectral properties with an accurate numerical method, it is evident that they no longer correspond to those of the energy-dependent potential.

For the bound states  $E_n$ , we noticed that the deviations were typically small around  $n = 0$  and then increased. One can explain this behavior by observing that the width equivalent and inverse potentials agree well around their minimum. For the transmission  $T(E)$ , one finds that the agreement between both potentials is good around the maximum; also a consequence of the local approximation of the peak, and then deviates for smaller energies. In both cases, the spectral properties can be well understood from the local character of the Bohr-Sommerfeld rule and Gamow formula.

### 7.4.2 Accuracy of inverse methods

Because the WKB method is in general not exact, using the Bohr-Sommerfeld rule and Gamow formula for the direct problem, or their inversions for the inverse problem, can in general only provide approximate results. This is well known for energy-independent potentials and it also holds for the more general, energy-dependent ones. To demonstrate this, we vary the potential properties of some of the previous cases to further investigate the accuracy of the WKB method. We compare the WKB predictions of the bound states  $E_n$  and transmission  $T(E)$  of the original potential, with the ones of the WKB-constructed inverse potential predicted using the accurate numerical method. For the overall performance of the WKB method for the inverse potential, as one would expect from the direct problem, the

spectral properties of the inverse potentials should match the ones of the original potential more accurately for higher bound states and energies below the peak of the barrier.

In Fig. 7.6, we computed the relative errors of the bound states via

$$\delta_n^i \equiv \left| \frac{E_n^{\text{Num orig}} - E_n^i}{E_n^{\text{Num orig}}} \right|, \quad (7.11)$$

where  $i$  is either using the direct WKB prediction for the original potential or the numerical prediction for the inverse potential. For increasing bound state number  $n$ , we report that the relative errors decrease, and that the performance of the inverse potential is clearly correlated with the accuracy of the WKB method for the direct problem. We also find that in most cases, the relative errors of the direct WKB computation of the original potential are smaller than those of the numerical method of the inverse potential. Since the construction of the inverse potential requires one to interpolate the spectrum of bound states, an overall difference in accuracy should be expected from this additional source of imprecision.

Next we investigate the performance when computing the transmission  $T(E)$ , which is shown in Fig. 7.7. As previously, we vary  $k$  of one of the previous cases and leave all other parameters to be the same. Our results confirm what should be expected. For wider potential barriers (smaller values of  $k$ ), the different predictions are more similar throughout all energies. Since the inverse method does not rely on an interpolation of the transmission, both WKB related predictions should be of similar accuracy with respect to the numerical result of the original potential.

We conclude this part of the discussion by noting that the good agreement between results of the numerical original potential and the numerical inverse potential are also an independent check of the numerical method itself.

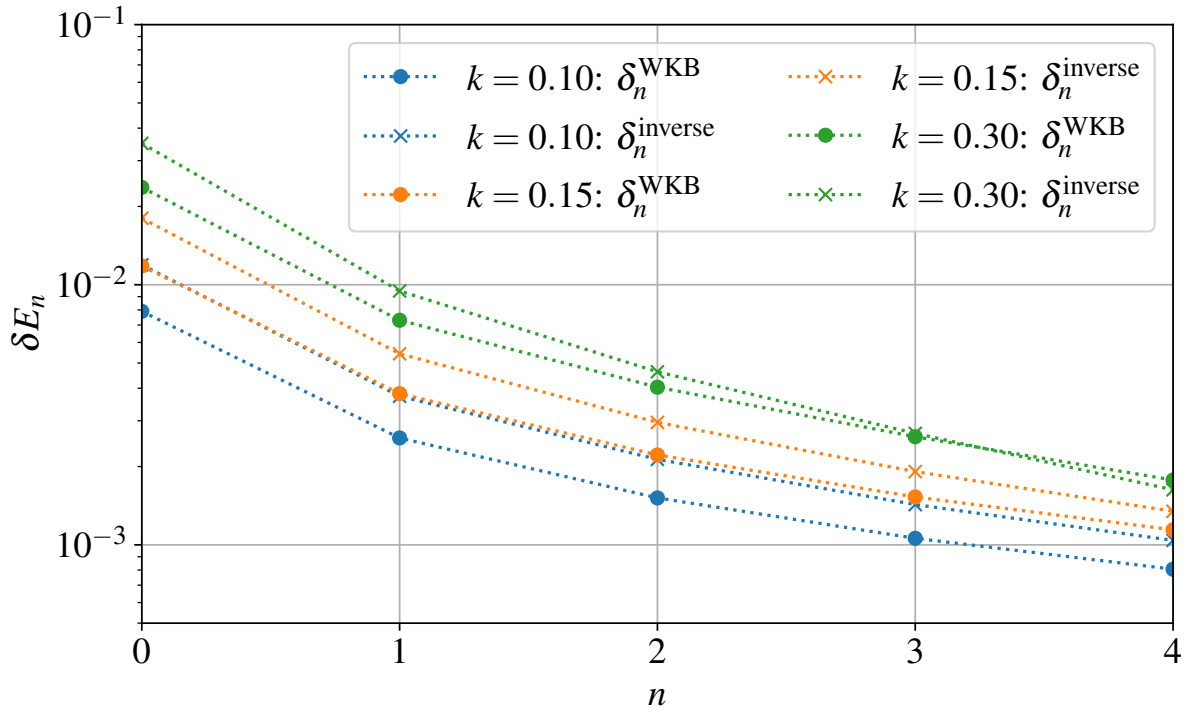


Figure 7.6: Here we show the relative error defined by  $\delta_n^i$ , where the index  $i$  stands for either the WKB prediction for the original potential (circles) or the numerical method of the inverse potential (crosses). The different colors represent different choices of  $k$ , which changes the width of the well, and thus indirectly the expected accuracy of the WKB method. All other parameters are those of Fig. 7.4.



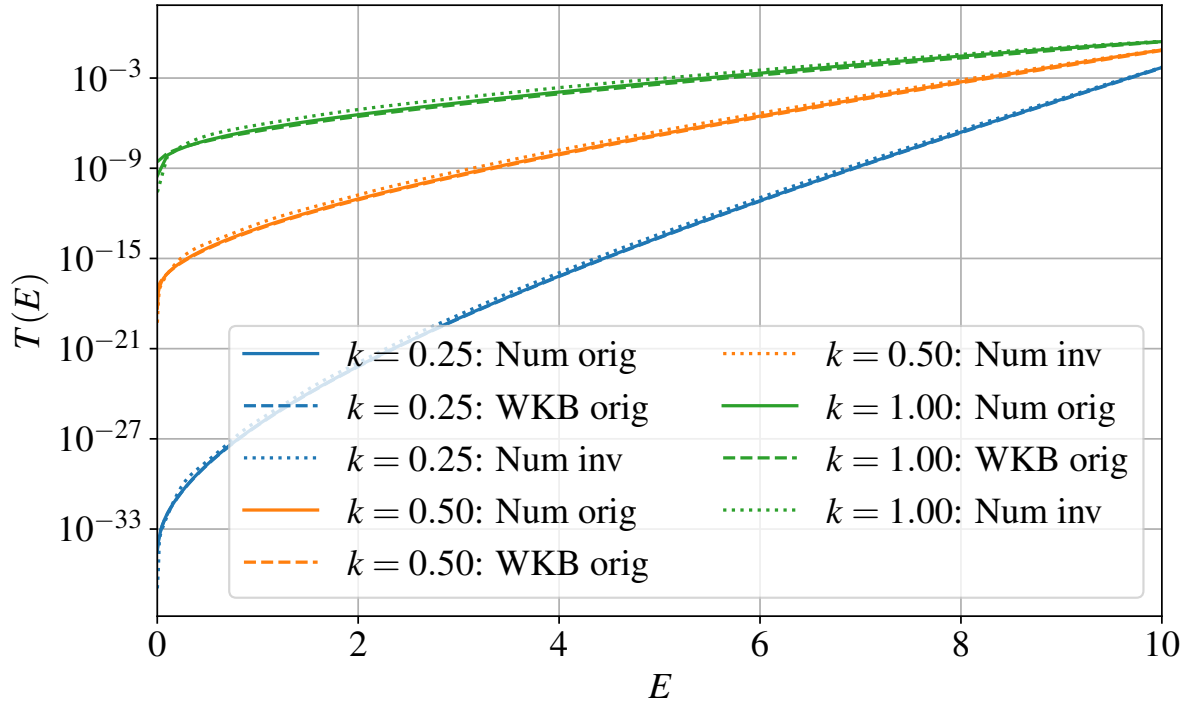


Figure 7.7: Here we show the transmission  $T(E)$  using the numerical method for the original potential (solid lines), the WKB prediction for the original potential (dashed lines), and the numerical method of the inverse potential (dotted lines). The different colors represent different choices of  $k$ , which changes the width of the barrier, and thus indirectly the expected accuracy of the WKB method. All other parameters are those of Fig. 7.5.

## 7.5 Supplementary results

Throughout this paper, we divided our study into two main cases, the energy-dependent quadratic potential and the energy-dependent Pöschl-Teller potential, with two scenarios of applications for each one: the effective inverse potential wells and the effective inverse potential barriers. In this appendix, we present complementary examples for each scenario.

### 7.5.1 Quadratic potential

Complementing the discussion made in Fig. 7.2, we present here an extra example of an energy-dependent quadratic well. This second scenario is defined by  $a/b > 0$ , for which the results and more details can be found in Fig. 7.8. As can be seen in the top panel, the potential curves get increasingly more closed with higher values of  $E$ , until at some point, the turning points become asymptotically fixed at a certain distance,  $x_{\text{limit}} = \pm\sqrt{(1-c)/b}$ . For these energies, the system behaves qualitatively like a particle in an infinite square well, which can also be seen from the bound states in the bottom panel.

As in the previous case, we use the bound states as input for the inverse Bohr-Sommerfeld rule (7.3) to construct  $V_{\text{inv}}(x)$ . The width-equivalent potential  $V_{\text{width}}(x)$  is included for comparison.

In the bottom panel of Fig. 7.8, we show the bound states for the three potentials. As in all previous cases, the bound states of the WKB-equivalent and original potentials agree very well. The asymptotic behavior of the overtones describes the transition from the spectrum of a quadratic potential to the one of a particle in an infinite square well ( $E_n \propto n^2$ ).

Finally, we complement the discussion made in Fig. 7.9 for energy-dependent quadratic barriers by considering  $a/b < 0$ . The potential barrier curves get increasingly more open with increasing energy, which can be seen in the top panel of Fig. 7.9. The WKB-equivalent and width-equivalent potentials are also presented. As in the previous case in Fig. 7.3, the difference between  $V_{\text{inv}}(x)$  and the width equivalent potential  $V_{\text{width}}(x)$  is apparent, although

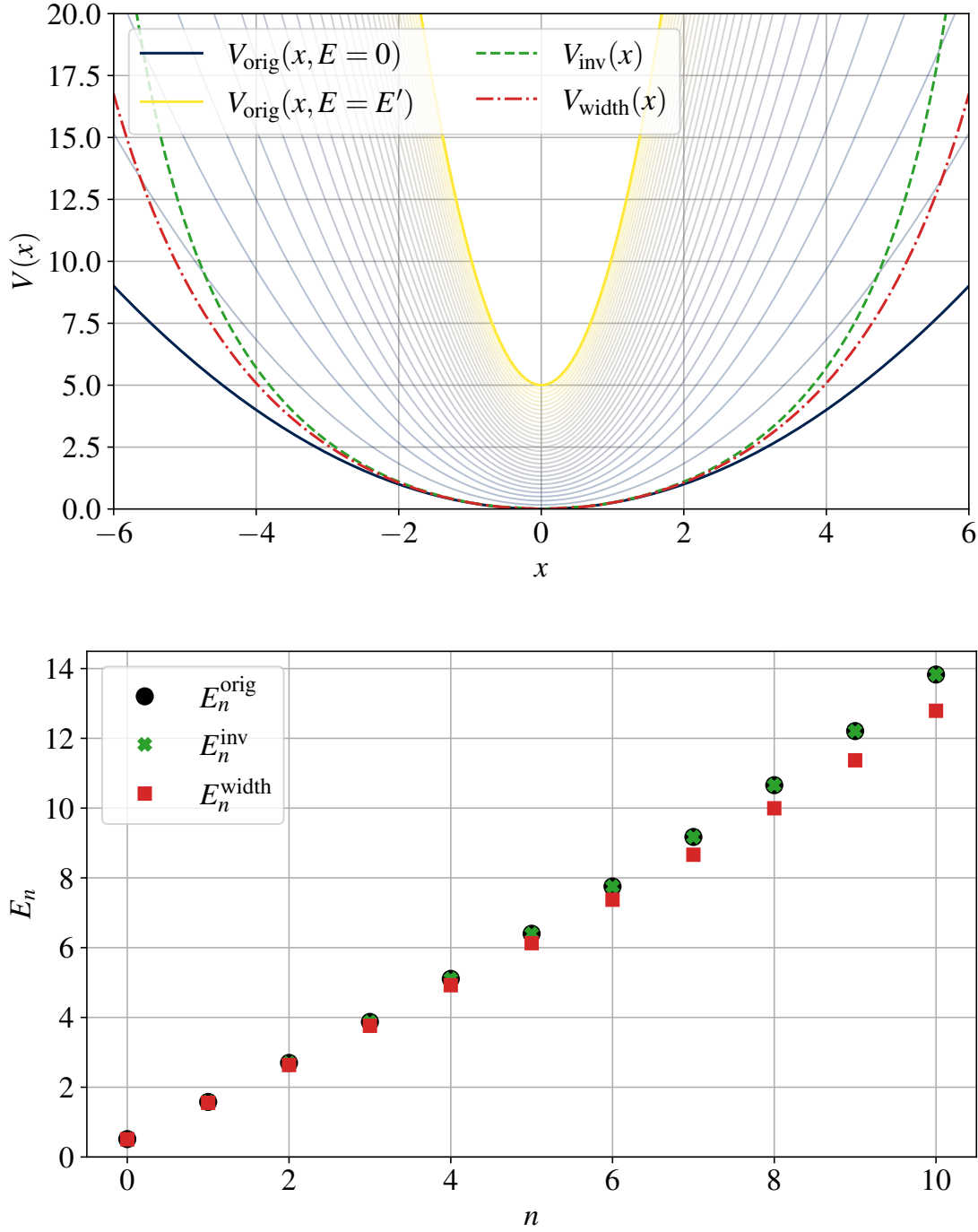


Figure 7.8: Application of the inverse method to the energy-dependent quadratic potential Eq. (7.6) for case  $a/b > 0$ , with parameters  $a = 0.25$ ,  $b = 0.0125$  and  $c = 0.0125$ . Top panel: The series of curves of varying colors indicate the chosen value of  $E$  when computing the energy-dependent potential  $V_{\text{orig}}(x, E) = V_{\text{HO}}(x, E)$  starting from  $E = 0$  to  $E = E' = 20a/b$ . The inverse potential (green dashed) is labeled as  $V_{\text{inv}}(x)$  and the width-equivalent potential (red dotted dashed) is labeled as  $V_{\text{width}}(x)$ . Bottom panel: Here we show the spectrum of bound states for the original potential  $E_n^{\text{orig}}$  (black circles), the inverse potential  $E_n^{\text{inv}}$  (green cross) and width-equivalent potential  $E_n^{\text{width}}$  (red squares).

they become similar close to  $E_{\text{vertex}}$ . In the bottom panel of the same figure, we show the transmission associated with each potential. In this case, they are all very similar to each other.

### 7.5.2 Pöschl-Teller potential

In Fig. 7.10 and Fig. 7.11 we complement the previously introduced examples for energy-dependent Pöschl-Teller potentials describing a potential well reconstruction, and a potential barrier reconstruction, respectively.

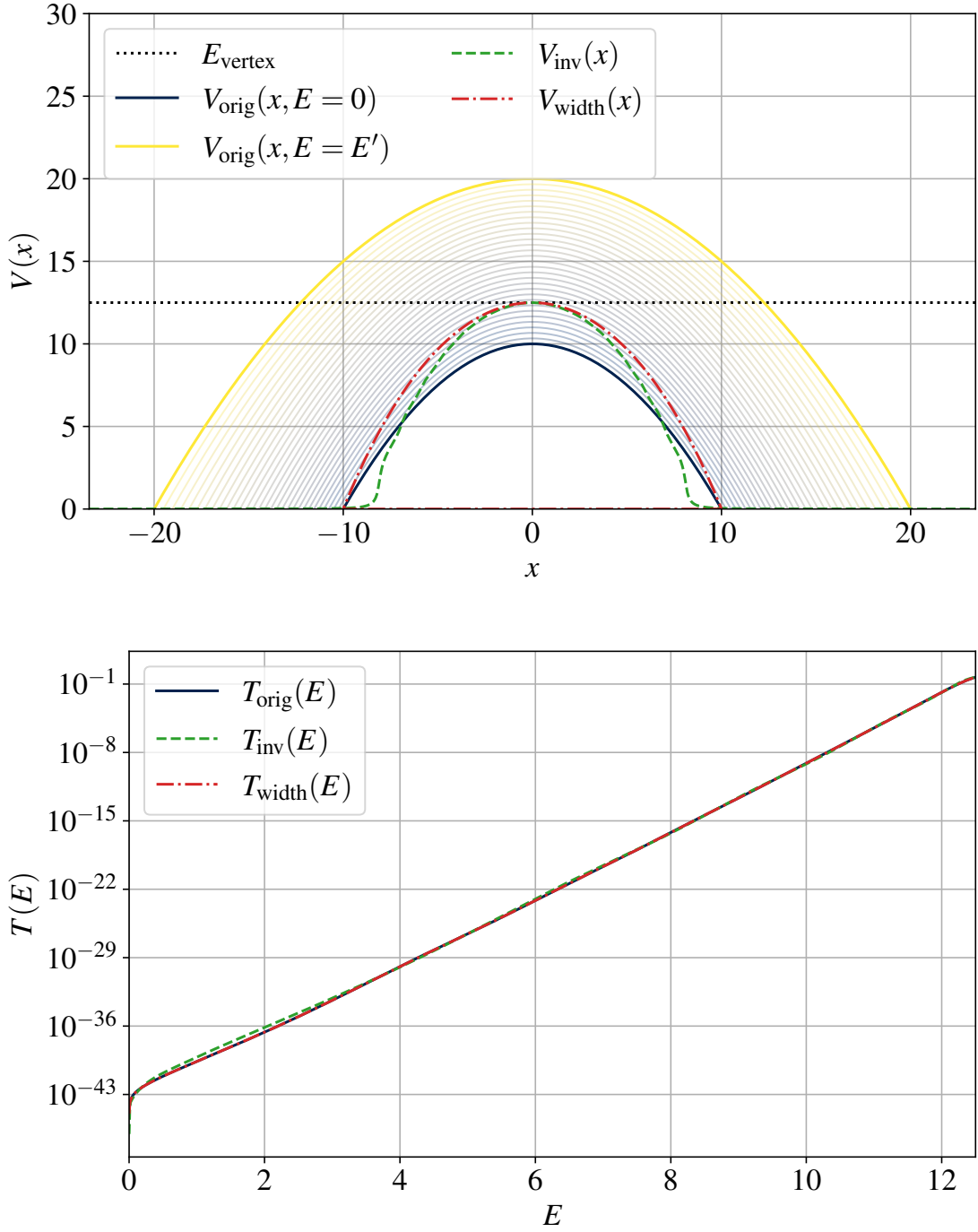


Figure 7.9: Application of the inverse method to the energy-dependent quadratic potential barrier Eq. (7.6) for case  $a/b < 0$ , with parameters  $a = -0.1$ ,  $b = 0.001$ ,  $c = 0.2$ , and  $V_0 = 10$ . Top panel: The series of curves of varying colors indicate the chosen value of  $E$  when computing the energy-dependent potential  $V_{\text{orig}}(x, E) = \bar{V}_{\text{HO}}(x, E)$  starting from  $E = 0$  to  $E = E' = 4E_{\text{vertex}}$ . The inverse potential (green dashed) is labeled as  $V_{\text{inv}}(x)$  and the width equivalent potential (red dotted dashed) is labeled as  $V_{\text{width}}(x)$ . Bottom panel: Here we show the transmission for the original potential  $T_{\text{orig}}(E)$  (black solid line), the inverse potential  $T_{\text{inv}}(E)$  (green dashed line) and the width-equivalent potential  $T_{\text{width}}(E)$  (red dot-dashed lines).

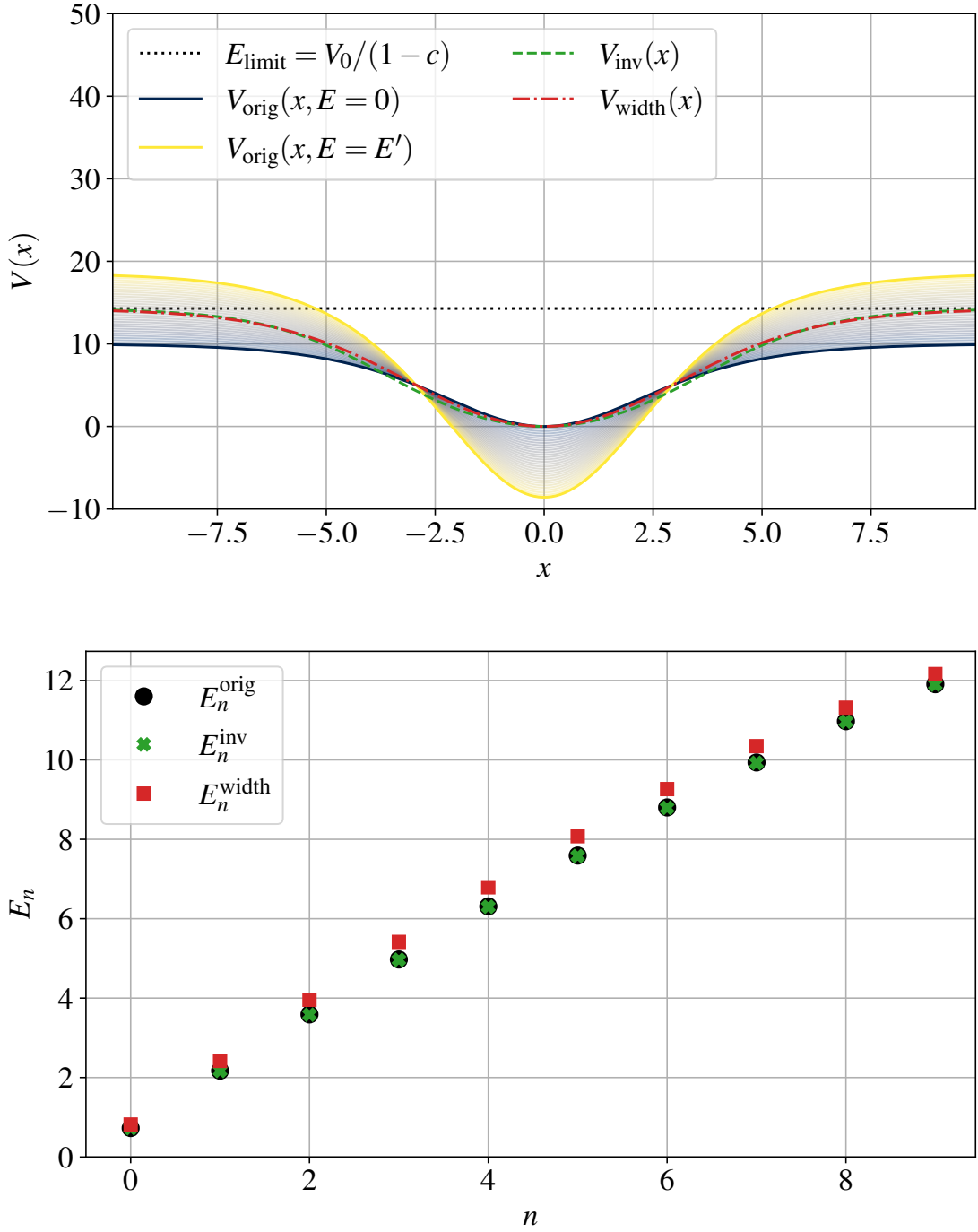


Figure 7.10: Application of the inverse method to the energy-dependent Pöschl-Teller potential Eq. (7.10) for case  $a/b > 0$ , with parameters  $a = -10$ ,  $b = -0.6$ ,  $c = 0.3$ ,  $k = 0.3$ , and  $V_0 = 10$ . Top panel: The series of curves of varying colors indicates the chosen value of  $E$  when computing the energy-dependent potential  $V_{\text{orig}}(x, E) = V_{\text{PT}}(x, E)$  starting from  $E = 0$  to  $E = E' = 2E_{\text{limit}}$ . The inverse potential (green dashed) is labeled as  $V_{\text{inv}}(x)$  and the width equivalent potential (red dotted dashed) is labeled as  $V_{\text{width}}(x)$ . Bottom panel: Here we show the spectrum of bound states for the original potential  $E_n^{\text{orig}}$  (black circles), the inverse potential  $E_n^{\text{inv}}$  (green cross) and width-equivalent potential  $E_n^{\text{width}}$  (red squares).

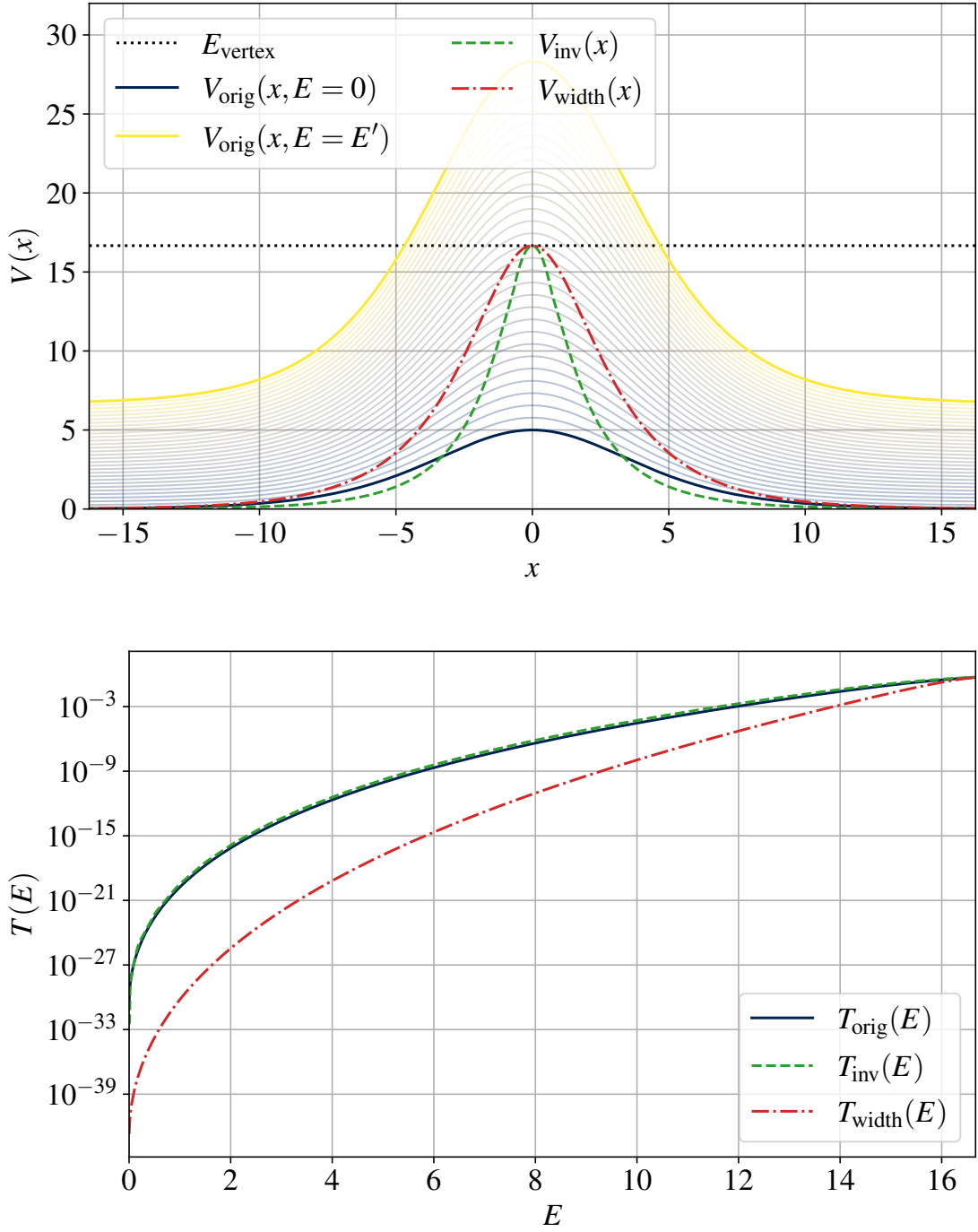


Figure 7.11: Application of the inverse method to the energy-dependent Pöschl-Teller potential Eq. (7.10) for case  $a/b > 0$ , with parameters  $a = 5$ ,  $b = 0.5$ ,  $c = 0.2$ ,  $k = 0.2$ , and  $V_0 = 0$ . Top panel: The series of curves of varying colors indicate the chosen value of  $E$  when computing the energy-dependent potential  $V_{\text{orig}}(x, E) = V_{\text{PT}}(x, E)$  starting from  $E = 0$  to  $E = E' = 2E_{\text{vertex}}$ . The inverse potential (green dashed) is labeled as  $V_{\text{inv}}(x)$  and the width equivalent potential (red dotted dashed) is labeled as  $V_{\text{width}}(x)$ . Bottom panel: Here we show the transmission for the original potential  $T_{\text{orig}}(E)$  (black solid line), the inverse potential  $T_{\text{inv}}(E)$  (green dashed line) and the width-equivalent potential  $T_{\text{width}}(E)$  (red dot-dashed lines).

### 7.5.3 Remarks on non-uniqueness

Even without energy-dependence, the inverse problem is in general not uniquely solvable. The WKB-equivalent potentials constructed from the inverse, semi-classical methods provide an intuitively clear, but approximate answer. They map a one-dimensional function of energy,  $n(E)$  or  $T(E)$ , into the width  $L(E)$  of all possible potential wells or barriers. Note that it might be possible to provide one turning point function from underlying properties of the application, which would then uniquely determine the underlying potential, *e.g.*, Refs. [127, 125].

Introducing energy dependence to  $V(x, E)$  does not translate to a family of bound states or transmission functions, but instead, only yields another one-dimensional function of energy. This is fundamentally different from introducing a free parameter, for which a family of bound states or transmissions could be mapped to a family of widths. A closer look into the Bohr-Sommerfeld and Gamow integrals reveals that potentials defined by the separation of turning points via  $E = V(x, E)$ , are in general not equivalent to the reconstructed potentials, which are instead isospectral to the energy-dependent potential. Future extensions of this work could study to what extent it may be possible to infer the energy-dependent contributions to  $V(x, E)$ , *e.g.*, if it can be treated perturbatively.

Finally, the inverse problem could in general be ill posed, and thus any inverse approach must fail. Independent of the non-uniqueness, a typical situation in which the construction of an inverse potential can fail when using the WKB-based methods, is when the width of the well/barrier is not strictly monotonically increasing/decreasing as function of  $E$ . In such a case, there are “overhanging cliffs” in the potential (see Wheeler [212]), because there is no bijective mapping from the width to a well-defined potential. For some explicit examples, we refer the interested reader to Ref. [128].



## 7.6 Conclusions

In this chapter, we have studied the direct and inverse problem of energy-dependent potentials using results from WKB theory. From the inversion of the classical Bohr-Sommerfeld rule and the Gamow formula for energy-independent potentials, it is well known in the literature that the reconstructed potentials are not unique. Instead, there is a family of infinitely many potentials that share a common property, which is the separation of their classical turning points, also known as width.

Because results of the inverse method have been limited to energy-independent potentials, but many physical applications require energy dependency, we have extended it to the inversion of such potentials. Here we have focused on introducing energy-dependent terms to the quadratic potential (harmonic oscillator) and Pöschl-Teller potentials, which serve as examples that offer a rich phenomenology.

By applying the same inversion techniques to the bound states or transmission coefficients of energy-dependent potentials, we have explicitly demonstrated that it is possible to construct a family of energy-independent potentials. We note that the bound states and transmission coefficients used for the inverse method are either known analytically or have been computed with full numerical methods, and are thus not limited to the accuracy of the WKB method. We have also used full numerical methods to verify the accuracy of the reconstructed potentials by computing their bound states and transmission coefficients, and find it is comparable to the expected accuracy of the WKB method for the direct problem.

The novelty of our findings is that the widths of the reconstructed potentials are not equivalent to the original, energy dependent ones. Thus, energy-dependent WKB equivalent potentials are not width-equivalent anymore. We utilize these findings to extend the inverse problem of analog gravity systems [2], shown in the previous chapter, to include the study of rotating analog gravity systems in the following chapter.

# Chapter 8

## The Inverse Method for Rotating Analog Systems

This Chapter is based on the following submission (currently under review): **Inverse problem of analog gravity systems II: rotation and energy-dependent boundary conditions.**

Authors: Saulo Albuquerque, Sebastian H. Völkel, Kostas D. Kokkotas, Valdir B. Bezerra

e-Print: 2406.16670 [gr-qc]

### 8.1 Introduction

As we have seen, the pioneering idea of probing astrophysical gravitating systems with lab-controlled analog experiments [30] has received much attention and significance in the last twenty years. New experimental setups and analog physical systems have been proposed together with analytical solutions [35, 36, 37, 38, 39, 249, 250, 251, 252, 42, 43, 253, 254, 255, 256], extending the horizons for state-of-the-art research within this investigation line. In particular, much experimental interest has recently been raised for analog systems that can be used, in principle, to better understand rotating astrophysical compact objects, mainly black holes. Experiments conducted with acoustic analogs to black holes have detected, for example, the analog of Hawking radiation [257, 258, 259, 260], propagation of light in optical

fibres [261], laser pulse filaments [262] and Bose–Einstein condensates [263]. In addition, superradiant effects for the scattering profile of acoustic incident waves have been studied [264, 45], as widely known, superradiance is intrinsically related to black holes’ rotation [112, 113]. Analogs of black and white hole horizons in superfluid  $^3\text{He} - B$  have been created [265], while proposals for using analog simulations of quantum gravity with fluids have been recently proposed [266]. Furthermore, in another recent experiment, the specific signature of curvature effects from rotating black hole spacetimes was measured by studying a giant rotating vortex in superfluid  $^4\text{He}$  [120].

Such experimental proposals show the rising interest of physicists in covering the qualitative description of rotating black holes in terms of analog systems. One general motivation behind that comes from the claiming that probing Kerr’s hypothesis validity is one of the routes towards probing general relativity [267, 268, 269, 270]. Compared to the static description of a spherically symmetric black hole [131, 132], Kerr’s metric adds rotation as one of the two fundamental degrees of freedom for those astrophysical compact objects [83]. Hence, probing this rotation can play an important role in gravitational physics phenomenology in general.

This chapter, and the associated Ref. [4], are an extension of the previous study in chapter 6 and in Ref. [2], in which we have demonstrated the applicability of the semi-analytic formulas to analog gravity systems. We considered, for illustration, the application of the inverse method for the analog model of exotic compact objects consisting of an imperfect draining vortex in a bathtub [48]. Our main result is the reconstruction of the effective potential associated with the effective background geometry. Moreover, we could also infer the reflectivity boundary parameter when it was an energy-independent constant.

Our application in chapter 6 was restricted to non-rotating systems because rotating systems admit an energy dependence for the scattering potential. In such cases, distinct potentials are obtained for different energies of the incident waves. In Ref. [3], we have applied the WKB techniques to energy-dependent potentials with two classical turning points.

Our method proposes an energy-independent, effective potential that reproduces the desired physical properties of the original family of energy-dependent ones. We called this reconstructed potential “*WKB-equivalent*” potential because it shares the same bound states (or transmission) we used for its reconstruction.

Finally, in this present chapter, we extend the inverse method for energy-dependent scattering potentials describing rotating analog gravity systems and for energy-dependent reflectivity parameters defined at their internal boundaries. As an application, we extend our previous work in chapter 6 by studying the imperfect draining vortex with a non-zero rotation coefficient. We can successfully reconstruct effective potentials admitting similar spectral properties as the original ones. Moreover, we can robustly infer the energy dependence of boundary conditions, which could potentially represent internal states of the core. Our approach thus provides a novel tool for exploring the experimental data measured by suitable types of analog gravity experiments.

In the following sections, we detail how that inverse method is formulated. We structure this study in the following way. First, we review how one can reconstruct the effective WKB-equivalent potential in Sec. 8.2. Then, in Sec. 8.3, we discuss how one can tackle the reconstruction of the reflectivity parameter at the boundary condition in one of the extremities. For such a goal, we discuss two effective techniques. We focus our investigation on analog gravity rotating systems in the application section 8.4, paying special attention to the rotating imperfect draining vortex proposed in Ref. [48] and introduced in Chapter 3. In the results, we show how one can compute an effective energy-independent potential reproducing the same physical properties as the energy-dependent original potentials, namely the WKB-equivalent potential. We calculate their transmission coefficients in Secs. 8.4.2.1 and 8.4.2.2 to show that they are quasi-equivalent to their original input values. In Sec. 8.4.2.3 we test how the two previously introduced effective techniques perform the reconstruction of the core reflectivity parameter at one of the boundary conditions. We contrast the results of the two methods and discuss their systematic errors. Finally, in Sec. 8.5 we finish this

chapter with the conclusions and final remarks.

## 8.2 Reconstructing the effective WKB-equivalent potential

In this chapter, we follow the procedure of Chapter 6, and our framework in Ref. [2], which starts from a transmission curve with resonances. The main steps are to identify the location of peaks and their widths to obtain the quasi-stationary states of the cavity, and to construct an average of two envelopes that can capture the direct transmission through the effective potential barriers. We illustrate the calculation of the latter in Fig. 8.1. Finally, for computing  $L_2(E)$  from this effective barrier transmission  $T_{\text{effective}}(E)$ , we assume  $E_{\text{max}} = E_{\text{vertex}}$  in Eq. (5.43) as proposed in the Sec. 7.5.2 of the previous chapter, or Sec. II C of Ref. [2].

Then, we merge the reconstructed cavity of width  $L_1(E)$  with the effective barrier, whose width is  $L_2(E)$ . Finally, we obtain the effective WKB-equivalent potentials by setting  $x_0$  as a constant. In this way, we complete the reconstruction of the effective potentials.

## 8.3 Reconstructing the boundary condition

In the following, we discuss two complementary approaches for reconstructing the boundary condition described by an energy-dependent reflectivity  $K(E)$ , as defined in Eq. (4.62).

The first method is called the “envelope method”. It is related to the method used for inferring the barrier transmission (see Fig. 8.1). In the logarithmic scaling, the transmission curves, as well as their upper and lower envelopes, can be normalized by the effective transmission through the barrier, or similarly, by the average of the envelopes when the last converges to  $T_{K=0}^{\text{effective}}$ . The normalized total transmission is a quasi-periodic oscillation with narrow peaks at the resonant frequencies and local minima between them. The values of the peaks and minima are symmetrical and uniform for energies below  $E_{\text{max}}$ , as shown in

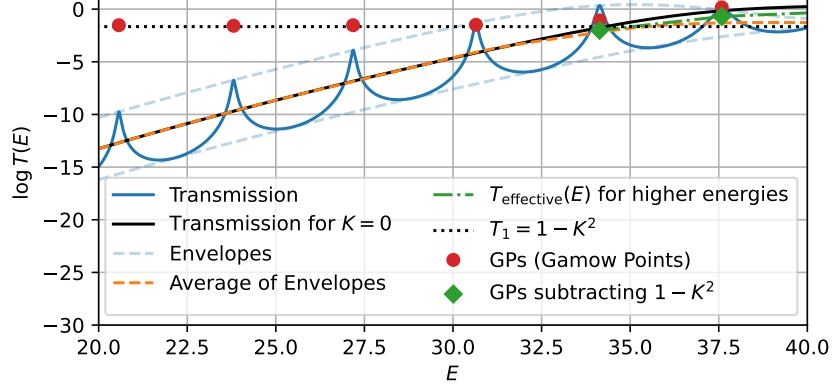


Figure 8.1: The application of the average-envelope method for obtaining the effective transmission  $T_{\text{effective}}(E)$  (red dot-dashed line) approaching the effective potential barrier's transmission (black solid line). Notice that around  $E_{\text{vertex}}$  the average-envelopes curve plateaus at the transmission through the reflective barrier  $1 - K^2$ . For this high-energy regime, the new Gamow points (green dots), obtained by subtracting  $1 - K^2$  from the original Gamow points (red dots), give us a good approximation for the remaining barrier transmission. For this scenario,  $K$  was assumed to be constant.

Fig. 3 in Ref. [2]. Their amplitudes are directly related to the reflectivity parameter  $K(E)$ . The analytical formula relating  $K(E)$  and this amplitude of oscillation for the normalized transmission is given by

$$\log(T_{\pm}^{\text{normalized}}) = \pm \log \left( \frac{1 + K(E)}{1 - K(E)} \right), \quad (8.1)$$

for the upper (+) and lower (−) envelopes. Therefore, if we normalize the logarithmic transmission by the average of its envelope, the reflectivity function can be computed by solving the difference between these envelopes for the reflectivity parameter  $K(E)$  in Eq. (8.1).

Since the envelopes are constructed by interpolating the local maxima or minima, respectively, there is an intrinsic uncertainty related to the interpolation method. As long as  $K(E)$  is changing less drastically compared to the maxima and minima, the interpolation error can be expected to be small. We quantify this error in Sec. 8.4.2.3.

The second method is called the “Gamow method” because it is based on the Gamow formula Eq. (5.19) in order to connect the width of the resonance peaks with the transmis-

sion at the boundary condition. It has previously been explained and applied in Ref. [2], where more details can be found. Due to the underlying assumption required to derive the Gamow formula from a more complex, generalized BS rule for three turning points [271], the transmission through the boundary needs to be very small. This implies that  $1 - K(E)$  needs to be small, and the accuracy of the method is expected to decrease if this condition is violated, which was also observed in Ref. [2].

To extend the range of validity also to larger values of  $1 - K(E)$ , we construct the following correction

$$K^{\text{new}}(E) = K^{\text{Gamow}}(E) + \Delta K(E) \quad (8.2)$$

$$\approx 1 + a(1 - K(E)) + b(1 - K(E))^2 \quad (8.3)$$

where  $K^{\text{Gamow}}(E)$  is the leading order earlier result obtained by the Gamow method, and  $a, b$  are constants that depend on the specific case under consideration. Note that  $K^{\text{Gamow}}(E)$  is only available at discrete values of  $E = E_n$  corresponding to the location of the resonance. By identifying

$$K^{\text{Gamow}}(E) = 1 + a(1 - K(E)), \quad (8.4)$$

$$\Delta K(E) = b(1 - K(E))^2, \quad (8.5)$$

one would expect the correction  $\Delta K(E)$  to be only depending on the functional form of  $K(E)$ , not directly on the energy. Instead of predicting  $a, b$  explicitly, which is non-trivial, we will use the envelope method to compute the correction as

$$\Delta K(E) = K^{\text{envelope}}(E) - K^{\text{Gamow}}(E), \quad (8.6)$$

and then numerically fit the constant  $b$  via Eq. (8.5) by assuming  $b$  does not depend on  $E$ , and is thus the same constant for all discrete  $K^{\text{Gamow}}(E)$ .

One remark is needed. At first, it may seem circular to use one method to compute the necessary correction of another one. However, in cases where the envelope method is applied to rapidly changing  $K(E)$ , the interpolation error can become significant in such energy ranges but very accurate where  $K(E)$  changes slowly. The numerical fitting of  $b$  can effectively average out such uncertainties, and thus make the “corrected” prediction Eq. (8.2) more robust. We illustrate this in Sec. 8.4.2.3.

## 8.4 Application and results

### 8.4.1 Imperfect draining vortex model

As proposed in Ref. [48], an imperfect draining vortex can be regarded as an analog model of an astrophysical extremely compact object. The evolution of small acoustic perturbations in its surroundings is described by a wave equation, which can be separated into a radial and an angular equation. The radial part can be written as in Eq. (3.34), where the effective potential is given by

$$V(r, E) = -\frac{(mC)^2}{r^4} + \left(1 - \frac{1}{r^2}\right) \left(\frac{m^2 - \frac{1}{4}}{r^2} + \frac{5}{4r^4}\right) + 2\frac{mC\sqrt{E}}{r^2}. \quad (8.7)$$

Here  $m$  is an integer number that labels the harmonic decomposition of the angular coordinate (azimuthal number), while  $C$  characterizes the tangential velocity profile of the vortex. In Eq. (3.34),  $x(r)$  is the so-called tortoise coordinate. Notice that the energy dependency couples to the effective potential through the rotation parameter  $C$ .

To complete the physical model, we introduce an energy-dependent reflectivity  $K(E)$  defined at the boundary surface in  $r_0 = r_h(1 + \epsilon)$ , where  $r_h$  is the acoustic horizon radius in radial coordinate, and  $\epsilon$  is a very small parameter. Physically, this reflective boundary condition is defined as a cylindrical interface radially displaced by a small radial distance  $\epsilon$



from the horizon surface  $r_h$ . From now on, we assume that  $\epsilon = 2e^{-20}$ , which implies that the tortoise coordinate at this reflective boundary is given by  $x_0 = x(r_0) = -9$ . For more details, we refer the interested reader to Ref. [48].

## 8.4.2 Results for inverse problem

In the following, we apply the inverse method introduced in Chapter 7 and Sec. 8.3 to the various transmission curves of the imperfect draining vortex from Sec. 8.4.1. In Sec. 8.4.2.1, we analyze the impact of the rotation parameter  $C$  by varying it until we reach our method's applicability limit. Then, in Sec. 8.4.2.2, we discuss how the value of the harmonic constant  $m$  impacts the accuracy of the method. Finally, in Sec. 8.4.2.3, we demonstrate the performance of our method to infer the energy-dependent reflectivity parameter  $K(E)$  by investigating a set of non-trivial examples.

### 8.4.2.1 Dependency of rotation profile $C$

We consider different applications for varying rotational velocity profiles  $C$ . Our analysis starts from transmission curves numerically obtained for cases with  $K = 0.9$  and  $m = 10$ .

We report some examples of those reconstructions in Fig. 8.2, where we compare the effective reconstructed potentials with the corresponding family of energy-dependent potential curves  $V(x, E)$  for a certain range of energy values. Furthermore, for each energy value, we also present the associated pair of turning points  $x_1(E)$  and  $x_2(E)$ .

As discussed in Ref. [3], the effective WKB-equivalent potentials and the width-equivalent curves are not supposed to be similar for the method to work. While the effective WKB-equivalent potential succeeds in approximately reproducing the physical properties used for its reconstruction, the width equivalent potentials, obtained by continuously connecting the turning points  $x_1(E)$  and  $x_2(E)$  for each energy  $E$ , do not provide similar results. However, although those curves are increasingly different for increasing values of the rotation parameter  $C$ , there is still a remarkable agreement between the original value of  $E_{\text{vertex}}$ , obtained

analytically from Eq. (8.7), with the  $E_{\text{vertex}}$  value inferred by the turning points' analysis from Sec. 7.2.2.

Notice in Fig. 8.2 that, for higher rotations, e.g.,  $C = 0.2$ , there is an “overhanging cliff” [212] behavior on the width of the cavity with  $E$ , which comes from a non-monotonic dependence of  $L_1$  with  $E$ . This problematic behavior of  $L_1$  is explained by the fact that the inverse BS rule Eq. (5.35) is reading a  $n$ -dependence of  $E_{0n}$  that grows faster than  $n^2$  for low energies. The  $n(E_{0n}) \propto \sqrt{E_{0n}}$  corresponds to the limiting case of a second fixed wall enclosing the cavity for a confined particle (infinite square box problem in quantum mechanics [272]). Since those reconstructed cavities with “overhanging cliffs” cannot represent physical solutions, we constrain the applicability of our inverse method here for rotation parameters  $C$  equal or lower than  $C = C_{\text{crit}}$ , where  $C_{\text{crit}}$  is the highest rotation coefficient for which the “overhanging cliffs” behavior does not arise. That defines the range of applicability of this method for the imperfect draining vortex with  $m = 10$ . For other  $m$  values, a different range in  $C$  needs to be further established.

It is the first few modes that produce the non-monotonic behavior on the energy dependence of the cavity width. Suppose we want to recover the monotonic behavior of the effective reconstructed cavity. In that case, we can try repeating the inverse method, but this time neglecting the first mode into the inverse BS rule. Depending on the rotation parameter  $C$ , we might even need to go further and neglect a couple of first modes instead. Then, in this way, we recover the monotonic behavior of the reconstructed cavity width, although we lift our potential minimum  $E_{\text{min}}$ .

Finally, we can now test the accuracy of the reconstructed effective potentials to reproduce the transmission curves used as input for their reconstruction and whether it can approximately predict the same resonant peaks from the original curves. For this goal, we use the same numerical scheme used for the original energy-dependent potentials, but now replacing the analytical potential defined in Eq. (8.7) with the effective WKB-equivalent potential. The results are shown in Fig. 8.3, where we compare the original transmissions

from the energy-dependent potentials (solid lines), with the ones reconstructed from our inverse method (dashed lines). Notice the good agreement between the transmission curves and the reproduction of the location and width of the resonant peaks from the original energy-dependent potential for  $C = 0$  and  $C = 0.1$ .

For rotations above the working limit threshold of our method, such as  $C = 0.2 \geq C_{\text{crit}}$  for instance, the curves with “overhanging cliffs” forbid us from interpolating the potentials to run the reconstruction of the transmission. As discussed previously, however, we can circumvent this problem by neglecting the first mode. This way we re-obtain a functional inverse reconstructed potentials. Those potentials have their minimum  $E_{\text{min}}$  vertically lifted upwards, decreasing the accuracy of their reconstruction for energies around the first considered mode.

Since the reconstruction of higher modes also depends on the lower modes, the inaccuracy does not go away completely for higher energy modes. To illustrate that, we present the WKB-equivalent potentials in the bottom panel of Fig. 8.2 for  $m = 10$  and  $C = 0.2$ . Here we contrast the reconstructed potential possessing “overhanging cliffs” (red dashed curve) with its regularized version obtained by inputting all modes but the fundamental one in the inversion formulas (black dashed curve). Finally, we also compute the associated reconstructed transmission for this case. This result is represented by the green dashed curve in Fig. 8.3. We can see the accuracy loss when comparing this reconstructed transmission with the exact one (green solid curve).

#### 8.4.2.2 Dependency on the angular parameter $m$

Now, we investigate the impact of different angular momentum parameters  $m$  in our inverse method. In Fig. 8.4, we contrast the WKB-equivalent potentials, reconstructed by employing our inverse techniques, and the associated family of energy-dependent potentials for a certain range of energy values. The comparison between the transmissions computed from these energy-dependent potentials and their corresponding WKB-equivalent potentials are shown

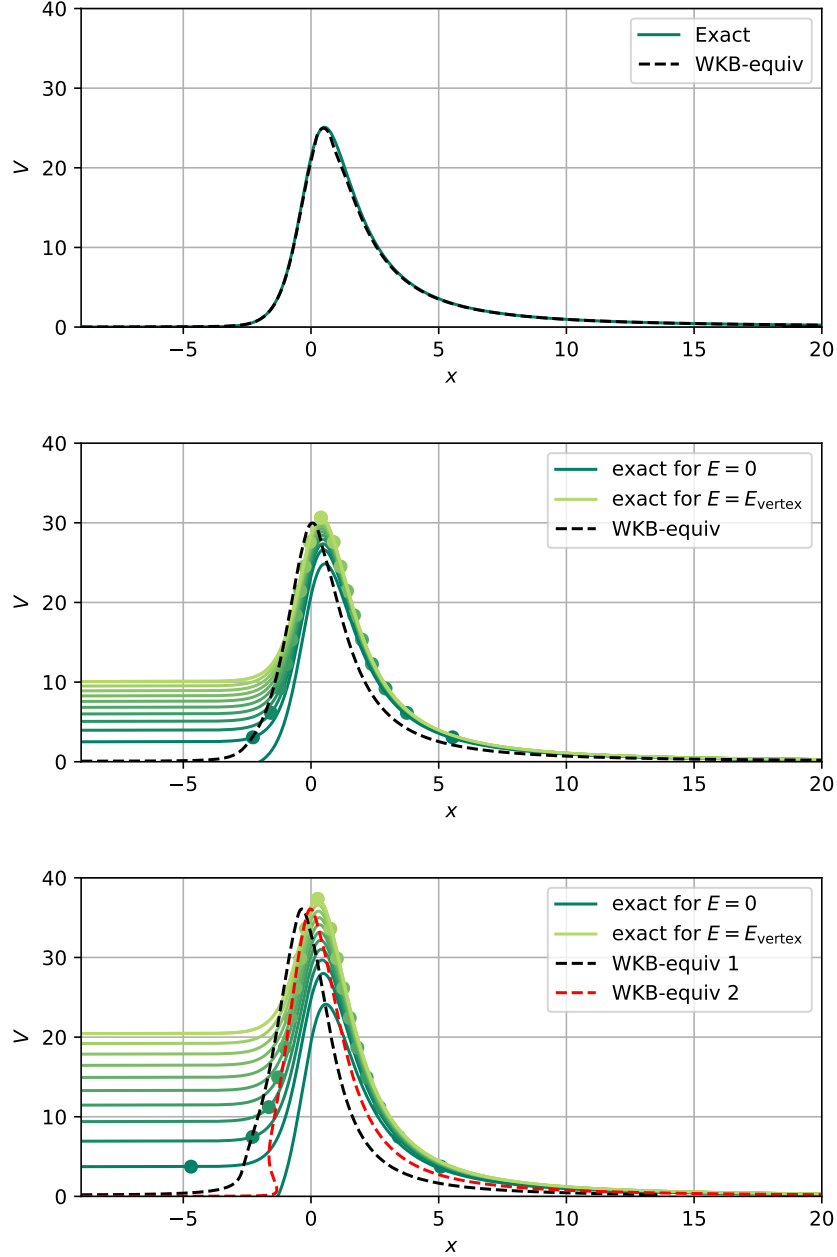


Figure 8.2: In the three panels, we show the WKB-equivalent potential reconstructed by the inverse method presented in this framework for  $m = 10$  and  $C = 0, C = 0.1$  and  $C = 0.2$ , respectively. The solid colored lines are the original energy-dependent potentials from Eq. (8.7) for a range of energies from  $E = 0$  to  $E = E_{\text{vertex}}$ . A pair of colored dots mark the intersection of each  $V(x, E)$  curve with the horizontal line placed at its associated energy value  $E$ . The color scheme is defined by a green-yellow transition from the lowest energy value to the highest. In the bottom panel, with  $C = 0.2$ , the red-dashed curve (WKB-equiv 2) represents the reconstructed potential by taking into account all energy modes. The regularized version of the WKB-equivalent potential (WKB-equiv 1), obtained by dismissing the fundamental mode in the inverse reconstruction, is represented by the black-dashed curve.

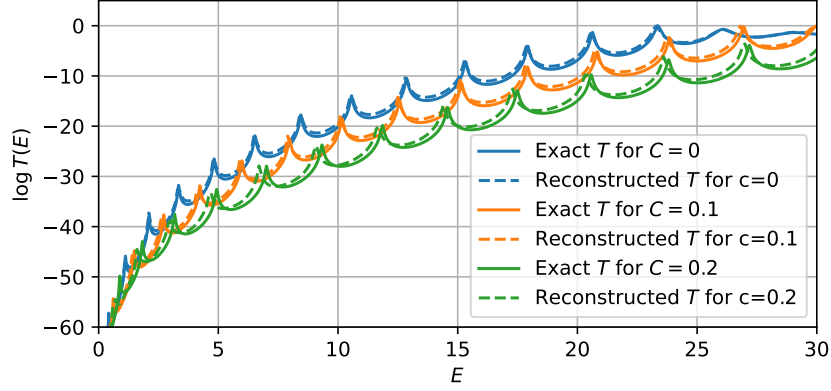


Figure 8.3: Here we show a comparison between the original transmissions, calculated from the energy-dependent potentials (solid colored line) in Eq. (8.7), and the reconstructed transmissions calculated from the WKB-equivalent potentials in Fig. 8.2 (colored dashed lines).

in Fig. 8.5.

As discussed in chapter 6 for the non-rotating case,  $m$  controls the height of the potential barrier. Hence, a larger value of  $m$  implies a larger number of resonant quasi-stationary modes, and accordingly, a higher overall accuracy for the reconstruction. For the more general rotating case, a similar qualitative behavior is expected. We illustrate this in Fig. 8.4, where one can see the impact of the absolute value of  $m$  for the height of the reconstructed potentials (read  $E_{\text{vertex}}$ ); and in the associated number of resonant peaks for the transmission curves in Fig. 8.5. In terms of the reconstruction's overall quality, we see a considerable difference in the accuracy of the reconstructed transmissions when comparing results for  $m = 10$  with the ones for  $m = 5$ . This is expected because the underlying WKB theory should become more accurate for large values of  $m$ .

Furthermore, an additional analysis that can only be carried out when we consider rotating regimes concerns applying our inverse method to investigate the scattering of counter-rotating waves, rather than co-rotating ones. For non-zero rotating parameter  $C$ , the incident acoustic waves can be both oriented in the vortex's rotating/absorbing direction or, oppositely, in a contrary direction. Those scenarios correspond to co-rotating and counter-rotating waves, respectively. Co-rotating waves are represented by a positive angular momentum  $m$ ,

while counter-rotating waves have negative  $m$ . So far, we have only considered the co-rotating regime. Considering the counter-rotating regime is interesting because it can lead to instabilities, especially if large  $m$  modes are excited.

Looking at Eq. (8.7), we can see that the term coupling the energy dependence to the potential consists of a linear product between  $m$  and  $C$ . In all other terms,  $m$  appears squared, so there is no special role played by its sign. The effect of the  $m$ 's sign only concerns the energy-dependent term, and it corresponds to two aspects; first for  $m > 0$ , increasing the size increment of the potential barriers with  $E$  (which is also amplified for larger  $|m|$  values); second for  $m < 0$ , “pulling down” the potential curves as the energy increases. We illustrate this qualitative discussion in the last two panels of Fig. 8.4, where we present the results of the inverse method’s application for two distinct scenarios for  $C = 0.1$ , namely  $m = -10$  (counter-rotating regime) and  $m = 10$  (co-rotating regime).

For the first scenario, the amplification of all the potential barrier’s heights implies an overall increase of our WKB-equivalent potential’s height. Since all  $V_{\max}$  are pushed upwards, it is expected that  $E_{\text{vertex}}$  goes in the same direction. For the second scenario, however,  $E_{\text{vertex}}$  is pushed down just like all the other turning points for any  $E$ . That behavior opposes the co-rotating waves. The reconstructed transmissions associated with both scenarios discussed here are depicted in fig. 8.5, where we compare them with their corresponding original transmission.

#### 8.4.2.3 Dependency of reflectivity $K$

Finally, we now apply the two approaches introduced in Sec. 8.3 for inferring the reflectivity parameter at the boundary condition in  $x_0$ . We expect in advance that both presented methods for the reconstruction of the boundary condition fail around energies close to  $E_{\max} = E_{\text{vertex}}$ , which defines the range of applicability for our reconstruction. In Fig. 8.6 and Fig. 8.7 we show the results of both approaches for reconstructing some injected reflectivity functions  $K(E)$ . The expected breakdown of our method is indicated by the orange-shaded

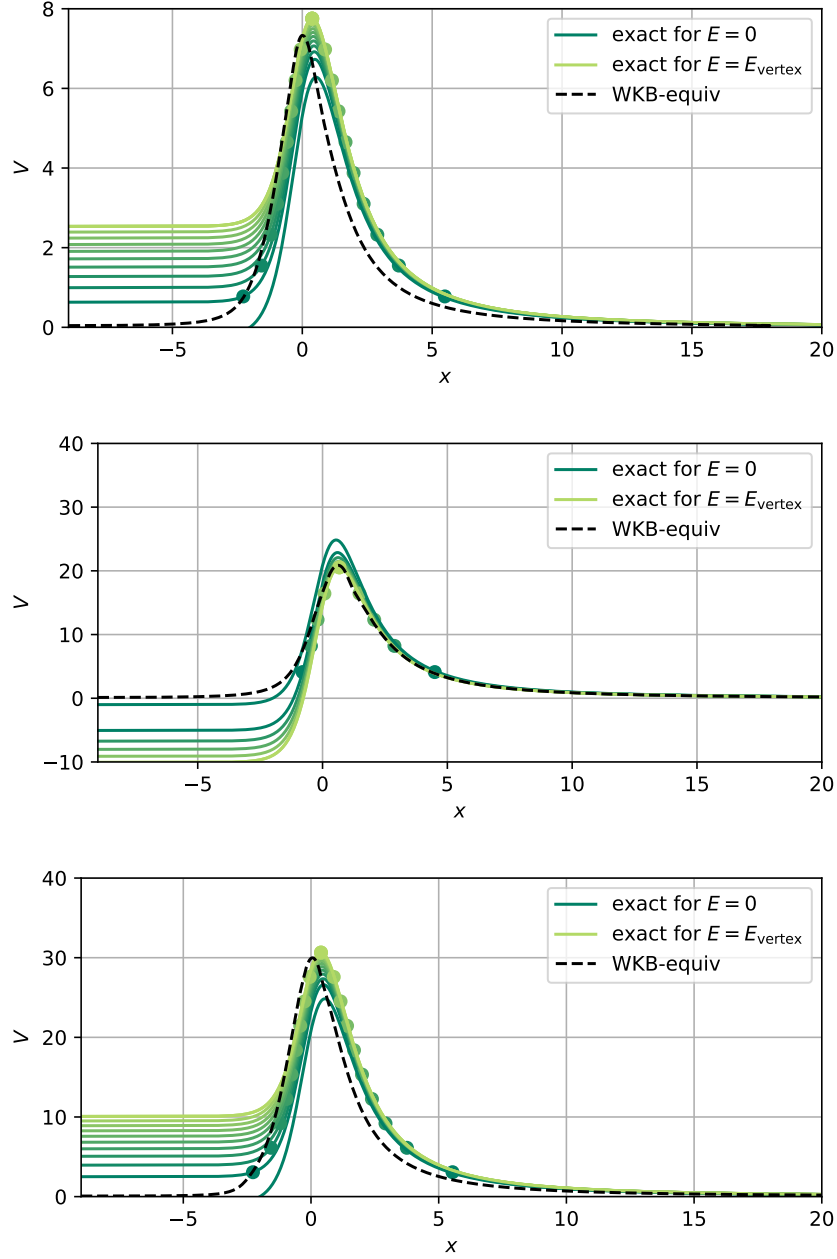


Figure 8.4: In the three panels, we show the WKB-equivalent potential reconstructed by the inverse method presented in this framework for  $C = 0.1$  and  $m = 5, m = -10$ , and,  $m = 10$ , respectively. They are represented as black dashed curves. The solid colored lines are the original energy-dependent potentials from Eq. (8.7) for a range of energies from  $E = 0$  to  $E = E_{\text{vertex}}$ . A pair of colored dots mark the intersection of each  $V(x, E)$  curve with the horizontal line placed at its associated energy value  $E$ . The color scheme is defined by a green-yellow transition from the lowest energy value to the highest.

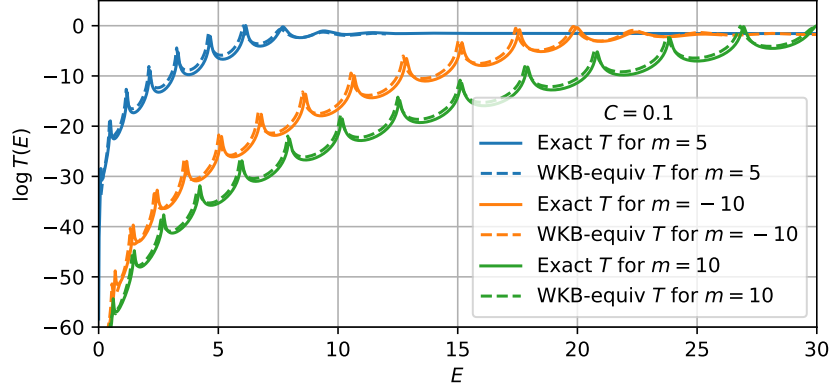


Figure 8.5: Here we show a comparison between the original transmissions, calculated from the energy-dependent potentials (solid colored line) in Eq. (8.7), and the reconstructed transmissions calculated from the WKB-equivalent potentials in Fig. 8.4 (colored dashed lines).

area. To focus on the properties of  $K$  when applying the inverse method, we fix our model to  $m = 10$  and a rotation profile specified by  $C = 0.01$ . Figure 8.6 contains reflectivity functions plateauing at two different values of  $K$ ; one for low asymptotic energy and the other one for higher asymptotic energy. The physical motivation for this step transition in  $K$  comes from the analogy between  $K$  with the vortex’s overall behavior for the reflectivity coefficient  $R$ . Likewise, we show in Fig. 8.7 how effectively our inference methods tackle reflectivity functions with local valleys in the core-reflectivity. Those local valleys are physically motivated by the idea of a scattering core with intrinsic resonant tunneling properties, in analogy with the vortex itself. All those injected reflectivities, although physically motivated by general qualitative assumptions, are only models to demonstrate the capabilities of the method. It is outside the scope of this framework to derive the core reflectivity functions from a first-principle perspective, as this would depend on the specific physical properties of the example.

To finish our discussion, we analyze the systematic error associated with the outlined approaches for reconstructing the boundary reflectivity  $K(E)$ . As we discussed in our earlier analysis in Sec. 8.3, the approach based on the envelope’s average was originally more reliable and flexible. This technique remained accurate with no regard to the rotation parameter



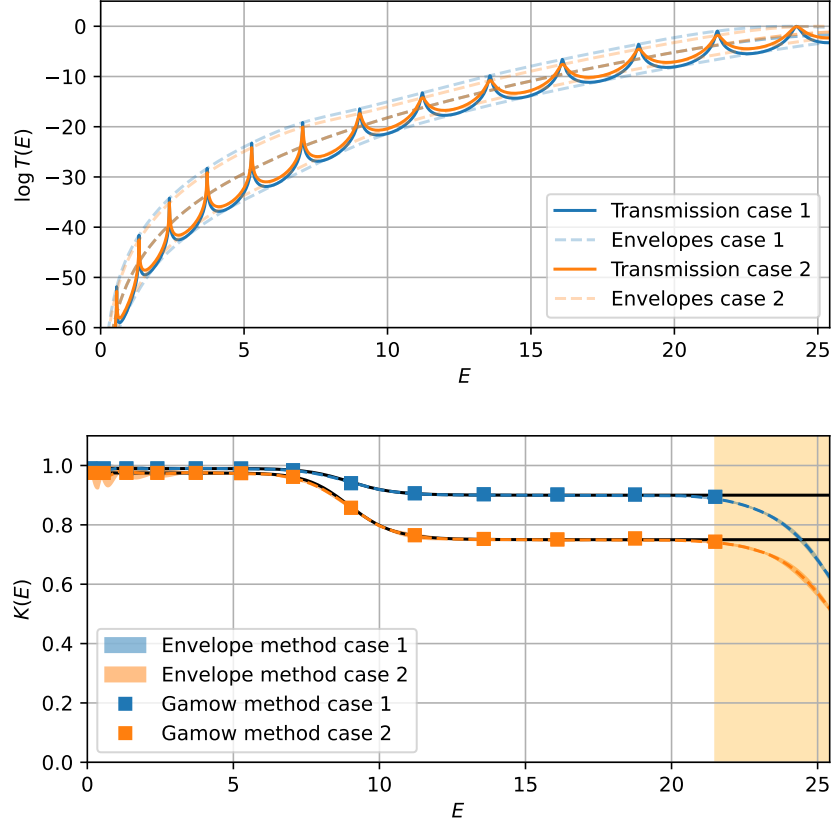


Figure 8.6: In the upper panel we show the transmission for the two reflectivity cases (cases 1 and 2), including their envelopes and the average between them. The injected reflectivity is represented in the lower panel by the solid black line. We also present the final results of our method inference for those two reflectivities by using both the Gamow method (colored squares) and the envelopes' technique (colored dashed lines). These two cases considered here consisted of two plateau-dominated models for the reflectivity, representing transitions from a low-energy plateau to another plateau for higher energies.

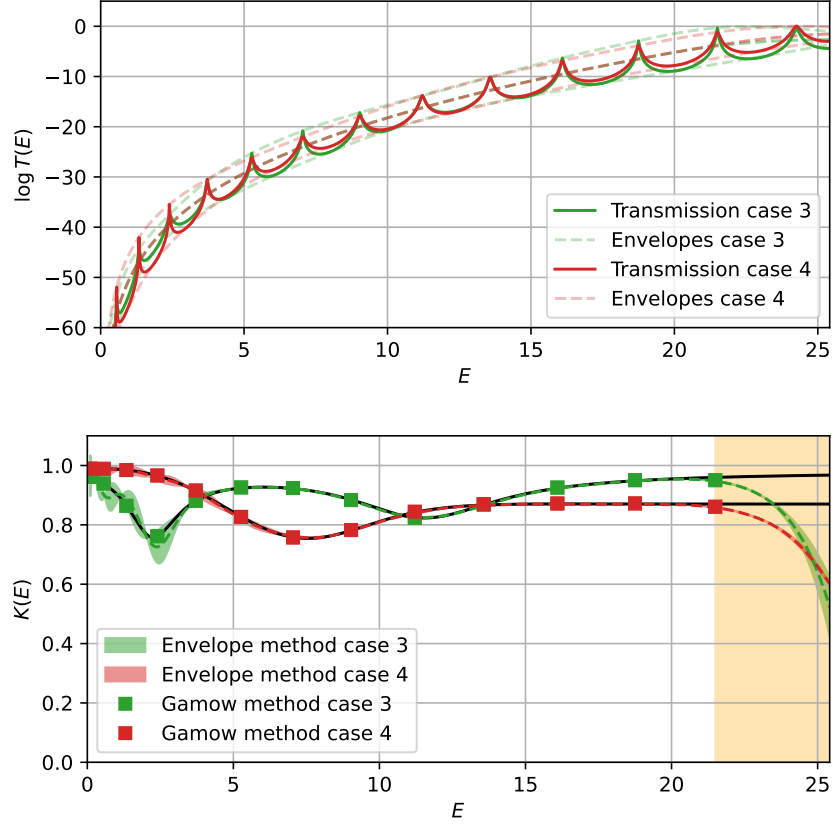


Figure 8.7: In the upper panel, we show the the transmission for the two reflectivity cases (cases 3 and 4), including their envelopes and the average between them. The injected reflectivity is represented in the lower panel by the solid black line. We also present the final results of our method inference for those two reflectivities by using both the Gamow method (colored squares) and the envelopes' technique (colored dashed lines). These two cases considered here consisted of reflectivity models with some local valleys due to possible core-resonant effects.

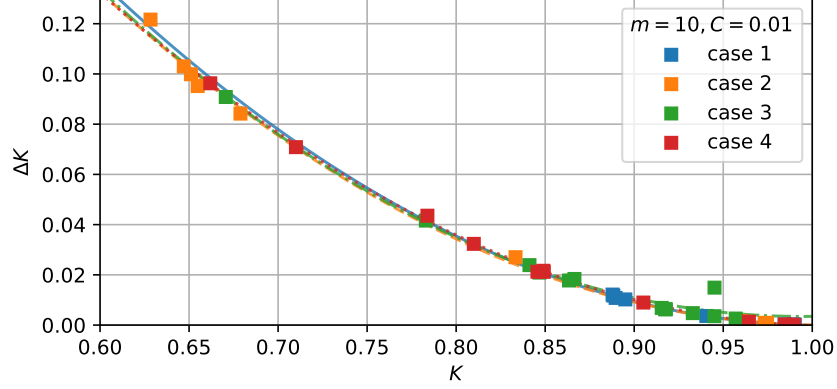


Figure 8.8: Here we show the deviations on the reflectivity  $\Delta K(E_n)$  inferred by the Gamow points for the four cases shown in Fig. 8.6 and in Fig. 8.7. Those deviations are obtained by the difference between  $K^{\text{Gamow}}(E_n)$  and the reflectivity  $K^{\text{envelope}}(E)$  predicted by the envelopes approach. For each scenario, the fitting curve for the associated data with the quadratic expansion in Eq (8.2) is shown.

and the absolute value of the reflectivity  $K$ , as long as  $E < E_{\text{vertex}}$ . In fact, this method even provides us with the reference values for the reflectivity  $K$  that are also used to correct the Gamow method (see Eq. (8.6)). As we mentioned in Sec. 8.3, we exploit the systematic error introduced by the interpolation to evaluate the systematic errors of this method. Our results are depicted as the colored areas in Fig. 8.6 and Fig. 8.7.

Meanwhile, for the “Gamow method”, we noticed that as we decreased the value of the injected reflectivity, it showed an approximately quadratic deviation from the values obtained by the envelope method. This is exactly what we expected from the discussion in Sec. 8.3. Therefore, the correction proposed by Eq. (8.2) allows us to circumvent this limitation and refine our findings to obtain the precise reconstruction of the reflectivities we see in Fig. 8.6 and Fig. 8.7. For each case, we have fitted the deviation data for  $\Delta K(E_n)$  with the quadratic correction in Eq. (8.5). The resulting fits are represented by the colored curves plotted in Fig. 8.8. Notice the approximate convergence between all of those fitting curves. This validates the point we made in Sec. 8.3 that the corrections would not depend on the energy, but only on the absolute value of  $K^{\text{Gamow}}$ .

## 8.5 Conclusions

In this chapter, we extended the WKB-based framework presented in Ref. [2] to study the inverse problem of certain types of energy-dependent potentials with energy-dependent boundary conditions. The input for the inverse method is the transmission through the potential. If it admits resonance features, they can be related to quasi-stationary states of a potential well, and the transmission through a potential barrier and an energy-dependent boundary condition.

Until recently, the inverse WKB methods have been applied to energy-independent potentials Refs. [212, 122, 213, 237, 214, 127, 125, 130, 129, 2] . From Ref. [3] it is known that the construction of isospectral, energy-independent potentials can be possible from bound states and transmissions of energy-dependent ones. This assumes the validity of the WKB approximation in the form of the Bohr-Sommerfeld rule and Gamow formula for two turning-point potentials, respectively.

By applying it to an imperfect draining vortex [48], we explicitly demonstrated how the inverse method can be used to find energy-independent potentials that are isospectral (within the validity of the WKB approximation and for three turning points), which we verified by computing the transmission of the inverse potential numerically. Moreover, our approach also allows the reconstruction of energy-dependent boundary conditions, which we explicitly demonstrated. The latter is highly non-trivial in the inverse problem, because computing its impact on the transmission relies, in general, on the knowledge of the underlying potential. Our method can bypass this limitation by using the reconstructed potential as a placeholder.

The reconstruction of energy-dependent boundary conditions can be a very interesting tool when applied to experimental measurements of transmissions of applicable analog gravity systems. Here one might not know a priori the right boundary conditions, or simply want to verify the experimental setup and underlying assumptions. For example, the boundary condition could effectively describe internal degrees of freedom, e.g., absorption lines of the

core. We have demonstrated that the model-independent reconstruction of such absorption features can be possible.

The methods discussed here are not limited to analog gravity systems. Systems with similar phenomenology have been suggested in a scenario with astrophysical exotic compact objects. Such objects can, in principle, admit quasi-stationary states and could reveal themselves in terms of so-called gravitational wave echoes after the merger of two such objects. Here the boundary condition is highly speculative and not well understood since different models exist (see Ref. [104] for a review of such systems).

Finally, it has recently been suggested that the high-frequency content of the black hole ringdown can be associated with their respective greybody factors [273, 274, 275, 276]. If this identification is robust in measurable frequency ranges, applying the inverse method, i.e., as presented in this work or in Ref. [129], could also be possible for gravitational wave observations. The connection of quasi-normal modes and greybody factors within WKB theory in this context has recently been discussed in Ref. [277].

# Chapter 9

## Final Remarks

### 9.1 Conclusions

Throughout this thesis, we introduced the direct and the inverse problems in perturbation theory for the scattering of astrophysical ultracompact objects and their analog systems, focusing especially on the last ones. The availability of data from lab-controlled experiments on the scattering study of those tabletop experiments provided the theoretical motivation for establishing this preference. By setting up a specific model of an analog gravity system to black holes and exotic compact objects consisting of an imperfect draining vortex in a bathtub, we have employed a cinematic modified model for describing the core reflectivity properties of this system. For such a goal, the usual procedure for the description of exotic compact objects was imported from the astrophysical case, providing us with a possible and physically well-justified analog model for ECOs. As we explained in chapter 3, this procedure consisted of adopting a model-dependent reflectivity parameter established as a boundary condition just above the 'would-be' event horizon.

After introducing our cinematical model for the analog ECO, we described its acoustic perturbation theory in linear order, and we derived some important results concerning its direct problem in scattering theory. Among those results, some of the most important ones were the echoes in the ringdown wave signal measured by an observer far away from this

relaxing scattering source. Another interesting result obtained for an imperfect draining vortex was the scattering properties of those systems, namely the cross-section and reflective coefficients. We have inferred from those results an attenuated global behavior, as a consequence of the reflective boundary condition at their core. At the same time, we have noticed that the cross-section presented an enhanced absorption of waves for some specific frequencies, which are visible through the presence of narrow spectral lines in the transmission spectrum. That was the core reflectivity's signature. As we have explained, those specific resonant frequencies are the trapped quasinormal modes, our quasibound states of these systems.

Finally, from the cross-section coefficients, numerically obtained in the previous sections, we have developed a novel nonparametric method that allowed us to reconstruct the effective perturbation potential in terms of semiclassical WKB formulas. In Chapter 5, we introduced this semianalytical method, deriving its general inverse formulas, which we used in the following applications. In Chapter 6, we then applied this method for reconstructing the effective perturbation potential governing the scattering properties of the non-rotating analog IDV model.

When considering extending the application of our developed inverse method for rotating scenarios of the analog model, we faced the difficulty imposed by the fact that the rotation parameter couples an energy dependence to our effective scattering potential. We then addressed this problem in a general way in chapter 7, showing that we can actually apply the same inverse WKB formulas to the scattering coefficients and the spectra of energy-dependent potentials in some scenarios. This application led us to an effective reconstructed and energy-independent potential, which we called 'WKB-equivalent potential'. This potential reproduced the exact physical quantities that were used for its reconstruction. "For example, we reconstructed an associated effective potential barrier when we started initially with the cross-section. Meanwhile, in the case where the spectrum was the quantity provided, we reconstructed an effective WKB-equivalent cavity. Both effective potential barriers and

cavities reproduced the same results that were used as input for their definition in our inverse method. We illustrated how the method worked with two insightful toy models, the modified energy-dependent quadratic potential and the modified energy-dependent Pösch-Teller potential.

Furthermore, a physical approximation of some critical values from the energy-dependent potentials was also discussed. For the cases of energy-dependent cavities, this critical value was the asymptotic behavior of the potentials, while for barriers, this value consisted of the energy level in which the energy-varying turning points encounter themselves. Both those critical values, which we named energy vertex, were imprinted in the effective WKB-equivalent potential reconstructed by our inverse method.

Finally, with that novel extension of the method for energy-dependent potentials, we applied our inverse method, in chapter 8, for the effective potentials from rotating analog models. As the main result of this application, we derived an effective WKB-equivalent potential that reproduced with accurate precision the original cross-section curves used as input for their reconstruction. The resonant peaks of our final approximate results agreed well with the original ones. An additional application of our method for reconstructing the reflective boundary condition was discussed in chapter 6 for constant core reflectivities. This discussion was presented again in chapter 7, but this time for the more general case of energy-dependent reflectivity parameters. Lastly, the effective potential maximum was also comparable to the vertex of the energy-dependent potential barriers.

Finally, we can assert that the inverse method we presented in this thesis achieved a successful application when employed for analog gravity systems, from the theoretical and computational perspectives. From the theoretical point of view, we provided a technique that reconstructed important dynamical information about the underlying physical systems in terms of a set of physical observables that are, in principle, available to be obtained. The cross-section curves and reflection coefficients are quantities measurable by lab-controlled experiments. Meanwhile, from the computational point of view, we have derived a simple



and cheap mathematical technique that allows us to tackle the inverse problem of scattering with good accuracy.

From the paradigm of the physics of analog gravity systems, when we investigate these systems, we not only tackle their specific physical intricacies but also grasp important insights and a great deal of qualitative knowledge on the astrophysical system that motivates the analogy. That is the main motivation behind the inverse problem for analog gravity systems we carried out throughout this thesis.

We conclude this text by posing some future perspectives on this study. From our last chapter, the application we considered consisted of extending the inverse method we developed for the rotating analog gravity system obtained from an imperfect draining vortex in a bathtub. Among the many motivations for this work, a recent paper [120] on an experimental result obtained by the Gravity Group from Nottingham reported the experimental detection of the fluid analogy to the spacetime twisting effect produced by rotating black holes. This astonishing analog effect was measured in a liquid helium fluid under extremely low temperatures. Physically, it is impossible to approach this fluid's description in terms of a classical fluid approximation, since quantum effects play a major role in their dynamics. So, in principle, although we gain an extremely better approximation for the hypothesis of a fluid with null viscosity, we lose the description in terms of the classical hydrodynamical equations. Accordingly, we might no longer have a linear wave equation using the WKB method. One of our future perspectives is to tackle the problem of analog systems with quantum vortices in the low-temperature regime. When we are addressing this problem, we will eventually check the possibility and the conditions for a semi-classical approximation, for which the inverse formulas can be appropriately used. This future investigation, however, will depend on the material conditions for its proper development.

# Bibliography

- [1] Saulo Albuquerque, Iarley P. Lobo, and Valdir B. Bezerra. “Massless Dirac perturbations in a consistent model of loop quantum gravity black hole: quasinormal modes and particle emission rates”. In: *Class. Quant. Grav.* 40.17 (2023), p. 174001. DOI: 10.1088/1361-6382/ace7a8. arXiv: 2301.07746 [gr-qc].
- [2] Saulo Albuquerque et al. “Inverse problem of analog gravity systems”. In: *Phys. Rev. D* 108.12 (2023), p. 124053. DOI: 10.1103/PhysRevD.108.124053. arXiv: 2309.11168 [gr-qc].
- [3] Saulo Albuquerque, Sebastian H. Völkel, and Kostas D. Kokkotas. “Inverse problem in energy-dependent potentials using semi-classical methods”. In: (Apr. 2024). arXiv: 2404.11478 [hep-ph].
- [4] Saulo Albuquerque et al. “Inverse problem of analog gravity systems II: rotation and energy-dependent boundary conditions”. In: (June 2024). arXiv: 2406.16670 [gr-qc].
- [5] Einstein A. “On the General Theory of Relativity”. In: *Sitzungsber. Preuss. Akad. Wiss. Berlin (Math. Phys.)* (Nov. 1915), pp. 778–786.
- [6] Albert Einstein. “The field equations of gravitation”. In: *Sitzungsber. Preuss. Akad. Wiss. Berlin (Math. Phys.)* 1915 (1915), pp. 844–847.
- [7] Albert Einstein. “On the electrodynamics of moving bodies”. In: *Annalen Phys.* 17 (1905), pp. 891–921. DOI: 10.1002/andp.200590006.
- [8] Anatoli Vankov. “Explanation of the Perihelion Motion of Mercury from General Relativity Theory”. In: *The General Science Journal* (Jan. 2011), Research Papers–Relativity Theory/Download/3213. URL: <https://hal.archives-ouvertes.fr/hal-00828384>.
- [9] Arthur Stanley Eddington. “The deflection of light during a solar eclipse”. In: *Nature* 104.2615 (1919), pp. 372–372.
- [10] Robert V Pound and Glen A Rebka Jr. “Gravitational red-shift in nuclear resonance”. In: *Physical Review Letters* 3.9 (1959), p. 439.
- [11] RFC Vessot and MW Levine. “A test of the equivalence principle using a space-borne clock”. In: *General relativity and gravitation* 10.3 (1979), pp. 181–204.

- [12] Clifford M Will. “Finally, results from gravity probe-b”. In: *arXiv preprint arXiv:1106.1198* (2011).
- [13] Roy P. Kerr. “Gravitational field of a spinning mass as an example of algebraically special metrics”. In: *Phys. Rev. Lett.* 11 (1963), pp. 237–238. DOI: 10.1103/PhysRevLett.11.237.
- [14] Kendrick M Smith, Oliver Zahn, and Olivier Dore. “Detection of gravitational lensing in the cosmic microwave background”. In: *Physical Review D* 76.4 (2007), p. 043510.
- [15] Ludovic Van Waerbeke et al. “Detection of correlated galaxy ellipticities on CFHT data: first evidence for gravitational lensing by large-scale structures”. In: *Arxiv preprint astro-ph/0002500* (2000).
- [16] David J Bacon, Alexandre R Refregier, and Richard S Ellis. “Detection of weak gravitational lensing by large-scale structure”. In: *Monthly Notices of the Royal Astronomical Society* 318.2 (2000), pp. 625–640.
- [17] Leonardo Ferreira et al. “Panic! At the Disks: First Rest-frame Optical Observations of Galaxy Structure at  $z > 3$  with JWST in the SMACS 0723 Field”. In: *arXiv preprint arXiv:2207.09428* (2022).
- [18] LIGO Scientific et al. “Tests of general relativity with GW150914”. In: *Physical review letters* 116.22 (2016), p. 221101.
- [19] B. P. Abbott et al. “Observation of Gravitational Waves from a Binary Black Hole Merger”. In: *Phys. Rev. Lett.* 116.6 (2016), p. 061102. DOI: 10.1103/PhysRevLett.116.061102. arXiv: 1602.03837 [gr-qc].
- [20] B. P. Abbott et al. “GW170814: A Three-Detector Observation of Gravitational Waves from a Binary Black Hole Coalescence”. In: *Phys. Rev. Lett.* 119.14 (2017), p. 141101. DOI: 10.1103/PhysRevLett.119.141101. arXiv: 1709.09660 [gr-qc].
- [21] B. P. Abbott et al. “GWTC-1: A Gravitational-Wave Transient Catalog of Compact Binary Mergers Observed by LIGO and Virgo during the First and Second Observing Runs”. In: *Phys. Rev. X* 9.3 (2019), p. 031040. DOI: 10.1103/PhysRevX.9.031040. arXiv: 1811.12907 [astro-ph.HE].
- [22] R. Abbott et al. “GWTC-2: Compact Binary Coalescences Observed by LIGO and Virgo During the First Half of the Third Observing Run”. In: *Phys. Rev. X* 11 (2021), p. 021053. DOI: 10.1103/PhysRevX.11.021053. arXiv: 2010.14527 [gr-qc].
- [23] R. Abbott et al. “Tests of general relativity with binary black holes from the second LIGO-Virgo gravitational-wave transient catalog”. In: *Phys. Rev. D* 103.12 (2021), p. 122002. DOI: 10.1103/PhysRevD.103.122002. arXiv: 2010.14529 [gr-qc].

- [24] R. Abbott et al. “GWTC-3: Compact Binary Coalescences Observed by LIGO and Virgo During the Second Part of the Third Observing Run”. In: (Nov. 2021). arXiv: 2111.03606 [gr-qc].
- [25] R. Abbott et al. “Tests of General Relativity with GWTC-3”. In: (Dec. 2021). arXiv: 2112.06861 [gr-qc].
- [26] Pau Amaro-Seoane et al. “Laser Interferometer Space Antenna”. In: (Feb. 2017). arXiv: 1702.00786 [astro-ph.IM].
- [27] LIGO Scientific Collaboration, Virgo Collaboration, et al. “GW190521: a binary black hole merger with a total mass of 150  $M$ ”. In: *Physical review letters* 125.10 (2020).
- [28] Stephen W Hawking. “Particle creation by black holes”. In: *Euclidean quantum gravity*. World Scientific, 1975, pp. 167–188.
- [29] Yakov B. Zel’dovich. “Generation of Waves by a Rotating Body”. In: *ZhETF Pisma Redaktsiiu* 14 (1971), pp. 270–272.
- [30] W. G. Unruh. “Experimental black hole evaporation”. In: *Phys. Rev. Lett.* 46 (1981), pp. 1351–1353. DOI: 10.1103/PhysRevLett.46.1351.
- [31] Matt Visser. “Acoustic propagation in fluids: An Unexpected example of Lorentzian geometry”. In: (Nov. 1993). arXiv: gr-qc/9311028.
- [32] Matt Visser. “Acoustic black holes: horizons, ergospheres and Hawking radiation”. In: *Classical and Quantum Gravity* 15.6 (1998), pp. 1767–1791. DOI: 10.1088/0264-9381/15/6/024. URL: <https://doi.org/10.1088%2F0264-9381%2F15%2F6%2F024>.
- [33] Emanuele Berti, Vitor Cardoso, and José P. S. Lemos. “Quasinormal modes and classical wave propagation in analogue black holes”. In: *Phys. Rev. D* 70 (12 2004), p. 124006. DOI: 10.1103/PhysRevD.70.124006. URL: <https://link.aps.org/doi/10.1103/PhysRevD.70.124006>.
- [34] Matt Visser. “Some general bounds for one-dimensional scattering”. In: *Physical Review A* 59.1 (1999), pp. 427–438. DOI: 10.1103/physreva.59.427. URL: <https://doi.org/10.1103%2Fphysreva.59.427>.
- [35] L. J. Garay et al. “Sonic Analog of Gravitational Black Holes in Bose-Einstein Condensates”. In: *Phys. Rev. Lett.* 85 (22 2000), pp. 4643–4647. DOI: 10.1103/PhysRevLett.85.4643. URL: <https://link.aps.org/doi/10.1103/PhysRevLett.85.4643>.

- [36] L. J. Garay et al. “Sonic black holes in dilute Bose-Einstein condensates”. In: *Phys. Rev. A* 63 (2 2001), p. 023611. DOI: 10.1103/PhysRevA.63.023611. URL: <https://link.aps.org/doi/10.1103/PhysRevA.63.023611>.
- [37] Carlos Barceló, Stefano Liberati, and Matt Visser. “Towards the Observation of Hawking Radiation in Bose–Einstein Condensates”. In: *International Journal of Modern Physics A* 18.21 (2003), pp. 3735–3745. DOI: 10.1142/S0217751X0301615X.
- [38] Carlos Barceló, S. Liberati, and Matt Visser. “Probing semiclassical analog gravity in Bose-Einstein condensates with widely tunable interactions”. In: *Phys. Rev. A* 68 (5 2003), p. 053613. DOI: 10.1103/PhysRevA.68.053613. URL: <https://link.aps.org/doi/10.1103/PhysRevA.68.053613>.
- [39] Petr O. Fedichev and Uwe R. Fischer. “Gibbons-Hawking Effect in the Sonic de Sitter Space-Time of an Expanding Bose-Einstein-Condensed Gas”. In: *Phys. Rev. Lett.* 91 (24 2003), p. 240407. DOI: 10.1103/PhysRevLett.91.240407. URL: <https://link.aps.org/doi/10.1103/PhysRevLett.91.240407>.
- [40] L. J. Garay et al. “Hawking Radiation in an Atomic Bose-Einstein Condensate”. In: *Physical Review Letters* 85 (2000), pp. 4643–4647. DOI: 10.1103/PhysRevLett.85.4643.
- [41] Theo Torres et al. “Analogue Black Hole Spectroscopy; or, how to listen to dumb holes”. In: *Classical and Quantum Gravity* 36 (2019), p. 194002. DOI: 10.1088/1361-6382/ab3abe.
- [42] Jeff Steinhauer. “Observation of self-amplifying Hawking radiation in an analog black hole laser”. In: *Nature Phys.* 10 (2014), p. 864. DOI: 10.1038/NPHYS3104. arXiv: 1409.6550 [cond-mat.quant-gas].
- [43] Jeff Steinhauer. “Observation of quantum Hawking radiation and its entanglement in an analogue black hole”. In: *Nature Phys.* 12 (2016), p. 959. DOI: 10.1038/nphys3863. arXiv: 1510.00621 [gr-qc].
- [44] Jeff Steinhauer. “Observation of quantum Hawking radiation and its entanglement in an analogue black hole”. In: *Nature Physics* 12 (2016), pp. 959–965. DOI: 10.1038/nphys3863.
- [45] Theo Torres et al. “Rotational superradiant scattering in a vortex flow”. In: *Nature Physics* 13.9 (Sept. 2017), pp. 833–836. DOI: 10.1038/nphys4151.
- [46] Sam Patrick et al. “Backreaction in an Analogue Black Hole Experiment”. In: *Physical Review Letters* 126 (2021), p. 041105. DOI: 10.1103/PhysRevLett.126.041105.

- [47] Theo Torres et al. “Quasinormal Mode Oscillations in an Analogue Black Hole Experiment”. In: *Phys. Rev. Lett.* 125.1 (2020), p. 011301. DOI: 10.1103/PhysRevLett.125.011301. arXiv: 1811.07858 [gr-qc].
- [48] Theo Torres, Sam Patrick, and Ruth Gregory. “Imperfect draining vortex as analog extreme compact object”. In: *Phys. Rev. D* 106.4 (2022), p. 045026. DOI: 10.1103/PhysRevD.106.045026. arXiv: 2204.10139 [gr-qc].
- [49] Vitor Cardoso and Paolo Pani. “Tests for the existence of black holes through gravitational wave echoes”. In: *Nature Astron.* 1.9 (2017), pp. 586–591. DOI: 10.1038/s41550-017-0225-y. arXiv: 1709.01525 [gr-qc].
- [50] Vitor Cardoso, Emmanuele Berti, and Paolo Pani. “Observational signatures of horizonless ultracompact objects”. In: *Classical and Quantum Gravity* 33.17 (2016), p. 174001. DOI: 10.1088/0264-9381/33/17/174001.
- [51] Luís Felipe Longo Micchi, Niayesh Afshordi, and Cecilia Chirenti. “How loud are echoes from exotic compact objects?” In: *Phys. Rev. D* 103 (4 2021), p. 044028. DOI: 10.1103/PhysRevD.103.044028. URL: <https://link.aps.org/doi/10.1103/PhysRevD.103.044028>.
- [52] Vitor Cardoso et al. “Gravitational-wave signatures of exotic compact objects and of quantum corrections at the horizon scale”. In: *Physical Review D* 94.8 (Oct. 2016). ISSN: 2470-0029. DOI: 10.1103/physrevd.94.084031. URL: <http://dx.doi.org/10.1103/PhysRevD.94.084031>.
- [53] Vitor Cardoso and Paolo Pani. “Testing the nature of dark compact objects: a status report”. In: *Living Reviews in Relativity* 22.1 (July 2019). ISSN: 1433-8351. DOI: 10.1007/s41114-019-0020-4. URL: <http://dx.doi.org/10.1007/s41114-019-0020-4>.
- [54] Vania Vellucci, Edgardo Franzin, and Stefano Liberati. “Echoes from backreacting exotic compact objects”. In: *Phys. Rev. D* 107 (4 2023), p. 044027. DOI: 10.1103/PhysRevD.107.044027. URL: <https://link.aps.org/doi/10.1103/PhysRevD.107.044027>.
- [55] Vitor Cardoso et al. “Exotic compact objects and how to quench their ergoregion instability”. In: *Physical Review D* 90.12 (2014), p. 124077. DOI: 10.1103/PhysRevD.90.124077.
- [56] Vitor Cardoso and Paolo Pani. “Ultra-compact objects and the fate of the light ring instability”. In: *Physical Review D* 95.12 (2017), p. 124056. DOI: 10.1103/PhysRevD.95.124056.

- [57] Steve K. Chung and Vitor Cardoso. “Gravitational wave echoes from interacting quantum fields”. In: *Physical Review D* 105.12 (2022), p. 124043. DOI: 10.1103/PhysRevD.105.124043.
- [58] Elisa Maggio et al. “Ergoregion instability of exotic compact objects: Electromagnetic and gravitational perturbations and the role of absorption”. In: *Physical Review D* 99.6 (Mar. 2019). ISSN: 2470-0029. DOI: 10.1103/physrevd.99.064007. URL: <http://dx.doi.org/10.1103/PhysRevD.99.064007>.
- [59] Zachary Mark et al. “A recipe for echoes from exotic compact objects”. In: *Physical Review D* 96.8 (Oct. 2017). ISSN: 2470-0029. DOI: 10.1103/physrevd.96.084002. URL: <http://dx.doi.org/10.1103/PhysRevD.96.084002>.
- [60] Elisa Maggio, Maarten van de Meent, and Paolo Pani. “Extreme mass-ratio inspirals around a spinning horizonless compact object”. In: *Phys. Rev. D* 104 (10 2021), p. 104026. DOI: 10.1103/PhysRevD.104.104026. URL: <https://link.aps.org/doi/10.1103/PhysRevD.104.104026>.
- [61] Luis Longo Micchi, Niayesh Afshordi, and Cecilia Chirenti. “Can we “hear” echoes from Exotic Compact Objects?” In: *APS April Meeting Abstracts*. Vol. 2021. APS Meeting Abstracts. Jan. 2021, S17.008, S17.008.
- [62] R. Ruffini and S. Bonazzola. “Gravitational Stability of Scalar Matter”. In: *Physical Review* 187.5 (1969), pp. 1767–1783. DOI: 10.1103/PhysRev.187.1767.
- [63] E. Seidel and W.-M. Suen. “Boson Stars: Gravitational Equilibria of Self-Interacting Scalar Fields”. In: *Physical Review Letters* 66.13 (1991), pp. 1659–1662. DOI: 10.1103/PhysRevLett.66.1659.
- [64] Philippe Jetzer. “Boson stars in general relativity”. In: *Physics Reports* 220.4 (1992), pp. 163–227. DOI: 10.1016/0370-1573(92)90123-H.
- [65] Franz E. Schunck and Andrew R. Liddle. “Boson stars: Stability, formation and evolution”. In: *Physical Review D* 56.2 (1997), pp. 762–771. DOI: 10.1103/PhysRevD.56.762.
- [66] Franz E. Schunck and Eckehard W. Mielke. “New dimensions for boson stars”. In: *Classical and Quantum Gravity* 20.20 (2003), R301–R356. DOI: 10.1088/0264-9381/20/20/201.
- [67] Carlos A. R. Herdeiro, Eugen Radu, and Helgi F. Rúnarsson. “Proca Stars: Gravitating Bose-Einstein condensates of massive spin 1 particles”. In: *Physical Review D* 94.6 (2016), p. 063001. DOI: 10.1103/PhysRevD.94.063001.

- [68] Richard Brito et al. “Proca stars with nonminimal coupling to curvature”. In: *Physical Review D* 94.2 (2016), p. 024003. DOI: 10.1103/PhysRevD.94.024003.
- [69] Vitor Cardoso, Edgardo Franzin, and Paolo Pani. “Gravitational wave signatures of exotic compact objects and of quantum corrections at the horizon scale”. In: *Physical Review D* 93.10 (2016), p. 104044. DOI: 10.1103/PhysRevD.93.104044.
- [70] G. Y. Rainich. “Some properties of spheres of uniform density in general relativity”. In: *Physical Review* 24.4 (1924), pp. 372–376. DOI: 10.1103/PhysRev.24.372.
- [71] S. Chandrasekhar. *An Introduction to the Study of Stellar Structure*. University of Chicago Press, 1939.
- [72] Steven Weinberg. *Gravitation and Cosmology: Principles and Applications of the General Theory of Relativity*. Wiley, 1972.
- [73] H. A. Buchdahl. “Relativistic Stars in an Asymptotically Minkowski Space”. In: *Physical Review* 116.4 (1959), pp. 1027–1034. DOI: 10.1103/PhysRev.116.1027.
- [74] Jahed Abedi, Hannah Dykaar, and Niayesh Afshordi. “Echoes from the abyss: Evidence for Planck-scale structure at black hole horizons”. In: *Physical Review D* 96.8 (2017), p. 082004. DOI: 10.1103/PhysRevD.96.082004.
- [75] Juan Carlos Bustillo, Paolo Pani, and Vitor Cardoso. “Gravitational wave echoes from black hole area quantization”. In: *Physical Review D* 102.4 (2020), p. 044039. DOI: 10.1103/PhysRevD.102.044039.
- [76] Elisa Maggio. *Probing new physics on the horizon of black holes with gravitational waves*. 2022. arXiv: 2211.16900 [gr-qc].
- [77] A. Ali et al. *Quantum Characteristics Near Event Horizons*. 2024. arXiv: 2401.12028 [quant-ph].
- [78] Sumanta Chakraborty et al. “Implications of the quantum nature of the black hole horizon on the gravitational-wave ringdown”. In: *Phys. Rev. D* 106 (2 2022), p. 024041. DOI: 10.1103/PhysRevD.106.024041. URL: <https://link.aps.org/doi/10.1103/PhysRevD.106.024041>.
- [79] Theo Torres et al. “Observation of superradiance in a vortex flow”. In: *Nature Phys.* 13 (2017), pp. 833–836. DOI: 10.1038/nphys4151. arXiv: 1612.06180 [gr-qc].
- [80] Theo Torres. “Estimate of the superradiance spectrum in dispersive media”. In: *Phil. Trans. Roy. Soc. Lond. A* 378.2177 (2020), p. 20190236. DOI: 10.1098/rsta.2019.0236. arXiv: 2003.02230 [gr-qc].



- [81] Karl Schwarzschild. “Über das Gravitationsfeld einer Kugel aus inkompressibler Flüssigkeit nach der Einsteinschen Theorie”. In: *Sitzungsberichte der königlich preußischen Akademie der Wissenschaften zu Berlin* (1916), pp. 424–434.
- [82] Tullio Regge and John A Wheeler. “Stability of a Schwarzschild singularity”. In: *Physical Review* 108.4 (1957), p. 1063.
- [83] Roy P Kerr. “Gravitational field of a spinning mass as an example of algebraically special metrics”. In: *Physical review letters* 11.5 (1963), p. 237.
- [84] Ezra T Newman et al. “Metric of a rotating, charged mass”. In: *Journal of mathematical physics* 6.6 (1965), pp. 918–919.
- [85] H. Reissner. “Über die Eigengravitation des elektrischen Feldes nach der Einsteinschen Theorie”. In: *Annalen der Physik* 355.9 (Jan. 1916), pp. 106–120. DOI: 10.1002/andp.19163550905.
- [86] G. Nordström. “On the Energy of the Gravitation field in Einstein’s Theory”. In: *Koninklijke Nederlandse Akademie van Wetenschappen Proceedings Series B Physical Sciences* 20 (Jan. 1918), pp. 1238–1245.
- [87] James M Bardeen, Brandon Carter, and Stephen W Hawking. “The four laws of black hole mechanics”. In: *Communications in mathematical physics* 31.2 (1973), pp. 161–170.
- [88] Jacob D Bekenstein. “Black holes and entropy”. In: *JACOB BEKENSTEIN: The Conservative Revolutionary*. World Scientific, 2020, pp. 307–320.
- [89] Subrahmanyan Chandrasekhar and Subrahmanyan Chandrasekhar. *An introduction to the study of stellar structure*. Vol. 2. Courier Corporation, 1957.
- [90] J Robert Oppenheimer and Hartland Snyder. “On continued gravitational contraction”. In: *Physical Review* 56.5 (1939), p. 455.
- [91] Roger Penrose. “Gravitational collapse and space-time singularities”. In: *Physical Review Letters* 14.3 (1965), p. 57.
- [92] Roger Penrose, Reinhard Genzel, and Andrea Ghez. *The Nobel Prize in Physics 2020*. 2020.
- [93] M Oda et al. “X-ray pulsations from Cygnus X-1 observed from Uhuru”. In: *The Astrophysical Journal* 166 (1971), p. L1.
- [94] H Tananbaum et al. “Observation of a correlated X-ray transition in Cygnus X-1”. In: *The Astrophysical Journal* 177 (1972), p. L5.

- [95] A Eckart et al. “Stellar orbits near Sagittarius A”. In: *Monthly Notices of the Royal Astronomical Society* 331.4 (2002), pp. 917–934.
- [96] S Gillessen et al. “The orbit of the star S2 around SGR A\* from very large telescope and keck data”. In: *The Astrophysical Journal* 707.2 (2009), p. L114.
- [97] Event Horizon Telescope Collaboration. “First Sagittarius A\* Event Horizon Telescope Results. II. EHT and Multiwavelength Observations, Data Processing, and Calibration”. In: *Astrophysical Journal Letters* (2022). ISSN: 2041-8205. DOI: 10.3847/2041-8213/ac6675. URL: <http://hdl.handle.net/10150/665353>.
- [98] GC Bower. “Focus on First Sgr A\* Results from the Event Horizon Telescope”. In: *The Astrophysical Journal Letters* 930.2 (2022).
- [99] Jahed Abedi, Hannah Dykaar, and Niayesh Afshordi. “Echoes from the Abyss: Tentative evidence for Planck-scale structure at black hole horizons”. In: *Phys. Rev. D* 96.8 (2017), p. 082004. DOI: 10.1103/PhysRevD.96.082004. arXiv: 1612.00266 [gr-qc].
- [100] Subrahmanyan Chandrasekhar, Valeria Ferrari, and Roland Winston. “On the non-radial oscillations of a star - II. Further amplifications”. In: *Proceedings of the Royal Society of London. Series A: Mathematical and Physical Sciences* 434.1892 (1991), pp. 635–641. DOI: 10.1098/rspa.1991.0117. URL: <https://royalsocietypublishing.org/doi/abs/10.1098/rspa.1991.0117>.
- [101] K. D. Kokkotas. “Pulsating relativistic stars”. In: *Les Houches School of Physics: Astrophysical Sources of Gravitational Radiation*. Sept. 1995, pp. 89–102. arXiv: gr-qc/9603024.
- [102] Kazuhiro Tominaga, Motoyuki Saijo, and Kei-ichi Maeda. “Gravitational waves from a test particle scattered by a neutron star: Axial mode case”. In: *Phys. Rev. D* 60 (1999), p. 024004. DOI: 10.1103/PhysRevD.60.024004. arXiv: gr-qc/9901040.
- [103] V. Ferrari and K. D. Kokkotas. “Scattering of particles by neutron stars: Time evolutions for axial perturbations”. In: *Phys. Rev. D* 62 (2000), p. 107504. DOI: 10.1103/PhysRevD.62.107504. arXiv: gr-qc/0008057.
- [104] Vitor Cardoso and Paolo Pani. “Testing the nature of dark compact objects: a status report”. In: *Living Rev. Rel.* 22.1 (2019), p. 4. DOI: 10.1007/s41114-019-0020-4. arXiv: 1904.05363 [gr-qc].
- [105] Albert Einstein. “Näherungsweise Integration der Feldgleichungen der Gravitation”. In: *Sitzungsberichte der Königlich Preussischen Akademie der Wissenschaften zu Berlin* (1916), pp. 688–696.

- [106] LIGO Scientific Collaboration, Virgo Collaboration, KAGRA Collaboration, et al. “Observation of Gravitational Waves from Two Neutron Star–Black Hole Coalescences”. In: *Astrophysical Journal Letters* 915.1 (2021).
- [107] LIGO Scientific Collaboration, Virgo Collaboration, et al. “GW190425: Observation of a Compact Binary Coalescence with Total Mass similar to  $3.4 M_{\odot}$ ”. In: *Astrophysical Journal Letters* 892.1 (2020).
- [108] B. P. Abbott et al. “Tests of General Relativity with GW150914”. In: *Phys. Rev. Lett.* 116 (22 2016), p. 221101. DOI: 10.1103/PhysRevLett.116.221101. URL: <https://link.aps.org/doi/10.1103/PhysRevLett.116.221101>.
- [109] R. Abbott et al. “Tests of general relativity with binary black holes from the second LIGO-Virgo gravitational-wave transient catalog”. In: *Physical Review D* 103.12 (2021). DOI: 10.1103/physrevd.103.122002. URL: <https://doi.org/10.1103/2Fphysrevd.103.122002>.
- [110] B. P. Abbott et al. “GW151226: Observation of Gravitational Waves from a 22-Solar-Mass Binary Black Hole Coalescence”. In: *Phys. Rev. Lett.* 116 (24 2016), p. 241103. DOI: 10.1103/PhysRevLett.116.241103. URL: <https://link.aps.org/doi/10.1103/PhysRevLett.116.241103>.
- [111] B. P. Abbott et al. “GW170608: Observation of a 19 Solar-mass Binary Black Hole Coalescence”. In: *The Astrophysical Journal* 851.2 (2017), p. L35. DOI: 10.3847/2041-8213/aa9f0c. URL: <https://doi.org/10.3847/2F2041-8213/2Faa9f0c>.
- [112] Ya. B. Zel’dovich. “Generation of Waves by a Rotating Body”. In: *JETP Letters* 14 (1971), p. 180.
- [113] Ya. B. Zel’dovich. “Amplification of Cylindrical Electromagnetic Waves Reflected from a Rotating Body”. In: *JETP* 35 (1972), p. 1085.
- [114] S. W. Hawking. “Particle Creation by Black Holes”. In: *Commun. Math. Phys.* 43 (1975). Ed. by G. W. Gibbons and S. W. Hawking. [Erratum: *Commun.Math.Phys.* 46, 206 (1976)], pp. 199–220. DOI: 10.1007/BF02345020.
- [115] William G. Unruh and Ralf Schutzhold. “On the universality of the Hawking effect”. In: *Phys. Rev. D* 71 (2005), p. 024028. DOI: 10.1103/PhysRevD.71.024028. arXiv: [gr-qc/0408009](https://arxiv.org/abs/gr-qc/0408009).
- [116] Jeff Steinhauer. “Experimental observation of Hawking radiation”. In: *Nature Physics* 12 (2016), pp. 959–965. DOI: 10.1038/nphys3863.

- [117] Carlos Barceló, Stefano Liberati, and Matt Visser. “Quantum simulation of black holes in a charged Bose-Einstein condensate”. In: *Physical Review A* 68.5 (2003), p. 053613. DOI: 10.1103/PhysRevA.68.053613.
- [118] Oren Lahav et al. “Observation of an analogue black hole in a Bose-Einstein condensate”. In: *Physical Review Letters* 105.24 (2010), p. 240401. DOI: 10.1103/PhysRevLett.105.240401.
- [119] Sam Patrick and Silke Weinfurter. “Superradiance in dispersive black hole analogues”. In: *Phys. Rev. D* 102 (8 2020), p. 084041. DOI: 10.1103/PhysRevD.102.084041. URL: <https://link.aps.org/doi/10.1103/PhysRevD.102.084041>.
- [120] Patrik Švančara et al. “Rotating curved spacetime signatures from a giant quantum vortex”. In: *Nature* 628 (Mar. 2024), pp. 1–5. DOI: 10.1038/s41586-024-07176-8.
- [121] Francesco Belgiorno et al. “Analog Hawking radiation in an optical system”. In: *Physical Review Letters* 105.20 (2010), p. 203901. DOI: 10.1103/PhysRevLett.105.203901.
- [122] K. Chadán and P. C. Sabatier. *Inverse problems in quantum scattering theory*. Second. Texts and Monographs in Physics. New York: Springer-Verlag, 1989. ISBN: 0-387-18731-6. DOI: 10.1007/978-3-642-83317-5. URL: <http://www.springer.com/us/book/9783642833199>.
- [123] W. R. Gilks, S. Richardson, and D. J. Spiegelhalter, eds. *Markov Chain Monte Carlo in Practice*. London: Chapman and Hall/CRC, 1996.
- [124] Gregory F. Cooper and Edward Herskovits. “A Bayesian method for the induction of probabilistic networks from data”. In: *Machine Learning* 9.4 (1992), pp. 309–347. DOI: 10.1007/BF00994110.
- [125] Sebastian H. Völkel and Kostas D. Kokkotas. “Wormhole Potentials and Throats from Quasi-Normal Modes”. In: *Class. Quant. Grav.* 35.10 (2018), p. 105018. DOI: 10.1088/1361-6382/aabce6. arXiv: 1802.08525 [gr-qc].
- [126] Sebastian H. Völkel and Kostas D. Kokkotas. “A Semi-analytic Study of Axial Perturbations of Ultra Compact Stars”. In: *Class. Quant. Grav.* 34.12 (2017), p. 125006. DOI: 10.1088/1361-6382/aa68cc. arXiv: 1703.08156 [gr-qc].
- [127] Sebastian H. Völkel and Kostas D. Kokkotas. “Ultra Compact Stars: Reconstructing the Perturbation Potential”. In: *Class. Quant. Grav.* 34.17 (2017), p. 175015. DOI: 10.1088/1361-6382/aa82de. arXiv: 1704.07517 [gr-qc].

- [128] Sebastian H. Völkel. “Inverse spectrum problem for quasi-stationary states”. In: *J. Phys. Comm.* 2.2 (2018), p. 025029. DOI: 10.1088/2399-6528/aaeee2. arXiv: 1802.08684 [quant-ph].
- [129] Sebastian H. Völkel, Roman Konoplya, and Kostas D. Kokkotas. “Inverse problem for Hawking radiation”. In: *Phys. Rev. D* 99.10 (2019), p. 104025. DOI: 10.1103/PhysRevD.99.104025. arXiv: 1902.07611 [gr-qc].
- [130] Sebastian H. Völkel and Kostas D. Kokkotas. “On the Inverse Spectrum Problem of Neutron Stars”. In: *Class. Quant. Grav.* 36.11 (2019), p. 115002. DOI: 10.1088/1361-6382/ab186e. arXiv: 1901.11262 [gr-qc].
- [131] K. Schwarzschild. “Über das Gravitationsfeld eines Massenpunktes nach der Einsteinschen Theorie”. In: *Sitzungsberichte der Königlich Preussischen Akademie der Wissenschaften* (1916), pp. 189–196.
- [132] K. Schwarzschild. “Über das Gravitationsfeld einer Kugel aus inkompressibler Flüssigkeit nach der Einsteinschen Theorie”. In: *Sitzungsberichte der Königlich Preussischen Akademie der Wissenschaften* (1916), pp. 424–434.
- [133] Alejandro Cárdenas-Avendaño and Carlos F. Sopuerta. “Testing gravity with Extreme-Mass-Ratio Inspirals”. In: (Jan. 2024). arXiv: 2401.08085 [gr-qc].
- [134] Lorenzo Pompili et al. *Laying the foundation of the effective-one-body waveform models SEOBNRv5: improved accuracy and efficiency for spinning non-precessing binary black holes*. 2023. arXiv: 2303.18039 [id='gr-qc' full\_name='GeneralRelativityandQuantumC Truealt\_name = Nonein\_archive =' gr-qc'is\_general = Falsedescription = "GeneralRelativityand
- [135] Tullio Regge and John A. Wheeler. “Stability of a Schwarzschild singularity”. In: *Phys. Rev.* 108 (1957), pp. 1063–1069. DOI: 10.1103/PhysRev.108.1063.
- [136] Frank J. Zerilli. “Effective potential for even parity Regge-Wheeler gravitational perturbation equations”. In: *Phys. Rev. Lett.* 24 (1970), pp. 737–738. DOI: 10.1103/PhysRevLett.24.737.
- [137] Jon Mathews. “Gravitational Oscillations of a Collapsing Star”. In: *Phys. Rev.* 128 (1962), pp. 2464–2475. DOI: 10.1103/PhysRev.128.2464.
- [138] Vitor Cardoso. “Quasinormal Modes and Gravitational Radiation in Black Hole Space-times”. PhD thesis. Instituto Superior Técnico, Universidade Técnica de Lisboa, 2004. URL: <https://inspirehep.net/literature/650051>.
- [139] Frank J. Zerilli. “Gravitational field of a particle falling in a Schwarzschild geometry analyzed in tensor harmonics”. In: *Phys. Rev. D* 2 (1970), pp. 2141–2160. DOI: 10.1103/PhysRevD.2.2141.

- [140] Marc Davis et al. “Gravitational Radiation from a Particle Falling Radially into a Schwarzschild Black Hole”. In: *Phys. Rev. Lett.* 27 (1971), pp. 1466–1469. DOI: 10.1103/PhysRevLett.27.1466.
- [141] S. Iyer and C. M. Will. “Black-hole normal modes: A WKB approach. I. Foundations and application of a higher-order WKB analysis of potential-barrier scattering”. In: *Physical Review D* 35.12 (1987), pp. 3621–3631. DOI: 10.1103/PhysRevD.35.3621. URL: <https://doi.org/10.1103/PhysRevD.35.3621>.
- [142] Bernard F. Schutz and Clifford M. Will. “Black hole normal modes: A semianalytic approach”. In: *Astrophys. J. Lett.* 291 (1985), pp. L33–L36. DOI: 10.1086/184453.
- [143] Peter Anninos et al. “Collision of two black holes”. In: *Phys. Rev. Lett.* 71 (18 1993), pp. 2851–2854. DOI: 10.1103/PhysRevLett.71.2851. URL: <https://link.aps.org/doi/10.1103/PhysRevLett.71.2851>.
- [144] Saul A Teukolsky. “Perturbations of a rotating black hole. I. Fundamental equations for gravitational, electromagnetic, and neutrino-field perturbations”. In: *The Astrophysical Journal* 185 (1973), pp. 635–647.
- [145] Richard H Price. “Nonspherical perturbations of relativistic gravitational collapse. II. Integer-spin, zero-rest-mass fields”. In: *Physical Review D* 5.10 (1972), p. 2439.
- [146] S Chandrasekhar. “The solution of Maxwell’s equations in Kerr geometry”. In: *Proceedings of the Royal Society of London. A. Mathematical and Physical Sciences* 349.1659 (1976), pp. 571–575.
- [147] S Chandrasekhar. “The solution of Dirac’s equation in Kerr geometry”. In: *Proceedings of the Royal Society of London. A. Mathematical and Physical Sciences* 349.1659 (1976), pp. 571–575.
- [148] Norbert Bodendorfer, Fabio M Mele, and Johannes Münch. “A note on the Hamiltonian as a polymerisation parameter”. In: *Classical and Quantum Gravity* 36.18 (2019), p. 187001. DOI: 10.1088/1361-6382/ab32ba. URL: <https://doi.org/10.1088/1361-6382/ab32ba>.
- [149] Abhay Ashtekar and Jerzy Lewandowski. “Quantum theory of geometry: I. Area operators”. In: *Classical and Quantum Gravity* 14.1A (1997), A55–A81. DOI: 10.1088/0264-9381/14/1a/006. URL: <https://doi.org/10.1088/0264-9381/14/1a/006>.
- [150] Abhay Ashtekar and Jerzy Lewandowski. “Background independent quantum gravity: a status report”. In: *Classical and Quantum Gravity* 21.15 (2004), R53–R152. DOI: 10.1088/0264-9381/21/15/r01. URL: <https://doi.org/10.1088/0264-9381/21/15/r01>.

- [151] Carlo Rovelli and Lee Smolin. “Discreteness of area and volume in quantum gravity”. In: *Nuclear Physics B* 442.3 (1995), pp. 593–619. DOI: 10.1016/0550-3213(95)00150-q. URL: <https://doi.org/10.1016%2F0550-3213%2895%2900150-q>.
- [152] Carlo Rovelli and Lee Smolin. “Loop space representation of quantum general relativity”. In: *Nuclear Physics B* 331.1 (1990), pp. 80–152.
- [153] Carlo Rovelli. “Zakopane lectures on loop gravity”. In: *PoS QGQGS2011* (2011). Ed. by John Barrett et al., p. 003. DOI: 10.22323/1.140.0003. arXiv: 1102.3660 [gr-qc].
- [154] Norbert Bodendorfer, Fabio M Mele, and Johannes Münch. “Effective quantum extended spacetime of polymer Schwarzschild black hole”. In: *Classical and Quantum Gravity* 36.19 (2019), p. 195015.
- [155] Pawel O Mazur and Emil Mottola. “Gravitational vacuum condensate stars”. In: *Proceedings of the National Academy of Sciences* 101.26 (2004), pp. 9545–9550.
- [156] Franz E Schunck and Eckehard W Mielke. “General relativistic boson stars”. In: *Classical and Quantum Gravity* 20.20 (2003), R301–R356.
- [157] Michael S Morris and Kip S Thorne. “Wormholes in spacetime and their use for interstellar travel: A tool for teaching general relativity”. In: *American Journal of Physics* 56.5 (1988), pp. 395–412.
- [158] Samir D Mathur. “The fuzzball proposal for black holes: An elementary review”. In: *Fortschritte der Physik: Progress of Physics* 53.7–8 (2005), pp. 793–827.
- [159] Abhay Ashtekar, Tomasz Pawłowski, and Parampreet Singh. “Quantum nature of the big bang: improved dynamics”. In: *Physical Review D* 74.8 (2006), p. 084003.
- [160] Vitor Cardoso, Edgardo Franzin, and Paolo Pani. “Is the gravitational-wave ringdown a probe of the event horizon?” In: *Physical Review Letters* 116.17 (2016), p. 171101.
- [161] Josef Lense and Hans Thirring. “Über den Einfluss der Eigenrotation der Zentralkörper auf die Bewegung der Planeten und Monde nach der Einsteinschen Gravitationstheorie”. In: *Physikalische Zeitschrift* 19 (1918), pp. 156–163.
- [162] Roger Penrose. “Gravitational collapse: The role of general relativity”. In: *Rivista del Nuovo Cimento* 1 (1969), pp. 252–276.
- [163] J. B. Hartle. “Slowly rotating relativistic stars. I. Equations of structure”. In: *Astrophysical Journal* 161 (1973), pp. 111–126.

- [164] Nicola Franchini. “Slow rotation black hole perturbation theory”. In: *Phys. Rev. D* 108 (4 2023), p. 044079. DOI: 10.1103/PhysRevD.108.044079. URL: <https://link.aps.org/doi/10.1103/PhysRevD.108.044079>.
- [165] E. Arias et al. *Analogue spacetimes: The first thirty years*. 2013.
- [166] Mauricio Richartz et al. “Superradiant scattering of dispersive fields”. In: *Classical and Quantum Gravity* 30 (Apr. 2013). DOI: 10.1088/0264-9381/30/8/085009.
- [167] Vitor Cardoso et al. “Rotational superradiance in fluid laboratories”. In: *Physical Review Letters* 117 (July 2016). DOI: 10.1103/PhysRevLett.117.271101.
- [168] Mauricio Richartz et al. “Rotating black holes in a draining bathtub: Superradiant scattering of gravity waves”. In: *Physical Review D* 91 (Nov. 2014). DOI: 10.1103/PhysRevD.91.124018.
- [169] Elisa Maggio, Paolo Pani, and Valeria Ferrari. “Exotic compact objects and how to quench their ergoregion instability”. In: *Phys. Rev. D* 96 (10 2017), p. 104047. DOI: 10.1103/PhysRevD.96.104047. URL: <https://link.aps.org/doi/10.1103/PhysRevD.96.104047>.
- [170] Caio F. B. Macedo et al. “Spectral lines of extreme compact objects”. In: *Phys. Rev. D* 98 (10 2018), p. 104034. DOI: 10.1103/PhysRevD.98.104034. URL: <https://link.aps.org/doi/10.1103/PhysRevD.98.104034>.
- [171] Peter James Nee, Sebastian H. Völkel, and Harald P. Pfeiffer. “Role of black hole quasinormal mode overtones for ringdown analysis”. In: *Phys. Rev. D* 108.4 (2023), p. 044032. DOI: 10.1103/PhysRevD.108.044032. arXiv: 2302.06634 [gr-qc].
- [172] Paolo Pani et al. “Perturbations of slowly rotating black holes: Massive vector fields in the Kerr metric”. In: *Physical Review D* 86.10 (Nov. 2012). ISSN: 1550-2368. DOI: 10.1103/physrevd.86.104017. URL: <http://dx.doi.org/10.1103/PhysRevD.86.104017>.
- [173] C. V. Vishveshwara. “Scattering of Gravitational Radiation by a Schwarzschild Black-hole”. In: *Nature* 227 (1970), pp. 936–938. DOI: 10.1038/227936a0.
- [174] Barry Wardell. *Self-force: Computational Strategies*. Jan. 2015. ISBN: 978-3-319-18334-3. DOI: 10.1007/978-3-319-18335-0.
- [175] Emanuele Berti, Vitor Cardoso, and Andrei O Starinets. “Quasinormal modes of black holes and black branes”. In: *Classical and Quantum Gravity* 26.16 (July 2009), p. 163001. ISSN: 1361-6382. DOI: 10.1088/0264-9381/26/16/163001. URL: <http://dx.doi.org/10.1088/0264-9381/26/16/163001>.



- [176] Emanuele Berti, Vitor Cardoso, and Paolo Pani. “Breit-Wigner resonances and the quasinormal modes of anti-de Sitter black holes”. In: *Phys. Rev. D* 79 (10 2009), p. 101501. DOI: 10.1103/PhysRevD.79.101501. URL: <https://link.aps.org/doi/10.1103/PhysRevD.79.101501>.
- [177] Vitor Cardoso. *Quasinormal Modes and Gravitational Radiation in Black Hole Spacetimes*. 2004. arXiv: gr-qc/0404093 [gr-qc].
- [178] Frank J. Zerilli. “Gravitational Field of a Particle Falling in a Schwarzschild Geometry Analyzed in Tensor Harmonics”. In: *Phys. Rev. D* 2 (10 1970), pp. 2141–2160. DOI: 10.1103/PhysRevD.2.2141. URL: <https://link.aps.org/doi/10.1103/PhysRevD.2.2141>.
- [179] Marc Davis et al. “Gravitational Radiation from a Particle Falling Radially into a Schwarzschild Black Hole”. In: *Phys. Rev. Lett.* 27 (21 1971), pp. 1466–1469. DOI: 10.1103/PhysRevLett.27.1466. URL: <https://link.aps.org/doi/10.1103/PhysRevLett.27.1466>.
- [180] Nicola Franchini and Sebastian H. Völkel. “Testing General Relativity with Black Hole Quasi-Normal Modes”. In: (May 2023). arXiv: 2305.01696 [gr-qc].
- [181] E. W. Leaver. “An Analytic Representation for the Quasi-Normal Modes of Kerr Black Holes”. In: *Proceedings of the Royal Society of London. Series A, Mathematical and Physical Sciences* 402.1823 (1985), pp. 285–298. ISSN: 00804630. URL: <http://www.jstor.org/stable/2397876> (visited on 06/11/2024).
- [182] R. A. Konoplya. “Quasinormal behavior of themml:math xmlns:mml=”http://www.w3.org/1998/M. display=”inline” mml:miD/mml:mi/mml:math-dimensional Schwarzschild black hole and the higher order WKB approach”. In: *Physical Review D* 68.2 (2003). DOI: 10.1103/physrevd.68.024018. URL: <https://doi.org/10.1103/2Fphysrevd.68.024018>.
- [183] Sai Iyer and Clifford M. Will. “Black-hole normal modes: A WKB approach. I. Foundations and application of a higher-order WKB analysis of potential-barrier scattering”. In: *Phys. Rev. D* 35 (12 1987), pp. 3621–3631. DOI: 10.1103/PhysRevD.35.3621. URL: <https://link.aps.org/doi/10.1103/PhysRevD.35.3621>.
- [184] R A Konoplya, A Zhidenko, and A F Zinhailo. “Higher order WKB formula for quasinormal modes and grey-body factors: recipes for quick and accurate calculations”. In: *Classical and Quantum Gravity* 36.15 (2019), p. 155002. DOI: 10.1088/1361-6382/ab2e25. URL: <https://doi.org/10.1088/1361-6382/ab2e25>.
- [185] Adriano Testa and Paolo Pani. “Analytical template for gravitational-wave echoes: signal characterization and prospects of detection with current and future interferom-

- eters”. In: *Phys. Rev. D* 98.4 (2018), p. 044018. DOI: 10.1103/PhysRevD.98.044018. arXiv: 1806.04253 [gr-qc].
- [186] G. Wentzel. “Eine Verallgemeinerung der Quantenbedingungen für die Zwecke der Wellenmechanik”. In: *Zeitschrift für Physik* 38.6 (1926), pp. 518–529. DOI: 10.1007/BF01397171.
  - [187] H. A. Kramers. “Wellenmechanik und halbzahlige Quantisierung”. In: *Zeitschrift für Physik* 39 (1926), pp. 828–840.
  - [188] L. Brillouin. “La mécanique ondulatoire de Schrödinger une méthode générale de résolution par approximations successives”. In: *Comptes Rendus* 183 (1926), pp. 24–26.
  - [189] L. Brillouin. “Remarques sur la mécanique ondulatoire”. In: *J. de Physique* 7 (1926), pp. 353–368.
  - [190] J. Liouville. “Sur le développement des fonctions et séries”. In: *Journal de Mathématiques Pures et Appliquées* 1 (1837), pp. 16–35.
  - [191] G. Green. “On the motion of waves in a variable canal of small depth and width”. In: *Transactions of the Cambridge Philosophical Society* 6 (1837), pp. 457–462.
  - [192] H. Jeffreys. “On Certain Approximate Solutions of Linear Differential Equations of the Second Order”. In: *Proceedings of the London Mathematical Society* 23 (1925), pp. 428–436. DOI: 10.1112/plms/s2-23.1.428.
  - [193] Bernard F. Schutz and Clifford M. Will. “Black Hole Normal Modes: A Semianalytic Approach”. In: *The Astrophysical Journal* 291 (1985), pp. L33–L36. DOI: 10.1086/184453. URL: <https://doi.org/10.1086/184453>.
  - [194] S. Iyer and C. M. Will. “Black-hole normal modes: A WKB approach. I. Foundations and application of a higherorder WKB analysis of potential-barrier scattering”. In: *Phys. Rev. D* 35 (1987), pp. 3621–3631. DOI: 10.1103/PhysRevD.35.3621.
  - [195] S. Iyer. “Black-hole normal modes: A WKB approach. II. Schwarzschild black holes”. In: *Phys. Rev. D* 35 (1987), pp. 3632–3636. DOI: 10.1103/PhysRevD.35.3632.
  - [196] K. D. Kokkotas and B. F. Schutz. “Black-hole normal modes: A WKB approach. III. The Reissner-Nordström black hole”. In: *Phys. Rev. D* 37 (1988), pp. 3378–3387. DOI: 10.1103/PhysRevD.37.3378.
  - [197] E. Seidel and S. Iyer. “Black-hole normal modes: A WKB approach. IV. Kerr black holes”. In: *Phys. Rev. D* 41 (1990), pp. 374–382. DOI: 10.1103/PhysRevD.41.374.

- [198] J. L. Dunham. “The Wentzel-Brillouin-Kramers Method of Solving the Wave Equation”. In: *Phys. Rev.* 41 (1932), pp. 713–720. DOI: 10.1103/PhysRev.41.713.
- [199] K. D. Kokkotas. “Normal modes of the Kerr black hole”. In: *Class. Quant. Grav.* 8 (1991), pp. 2217–2224. DOI: 10.1088/0264-9381/8/12/006.
- [200] Sebastian H. Völkel. “On the Gravitational Wave Spectrum of Compact Relativistic Objects”. PhD thesis. U. Tübingen, 2020. DOI: 10.15496/publikation-42527.
- [201] C.M. Bender, S. Orszag, and S.A. Orszag. *Advanced Mathematical Methods for Scientists and Engineers I: Asymptotic Methods and Perturbation Theory*. Advanced Mathematical Methods for Scientists and Engineers. Springer, 1999. ISBN: 9780387989310. URL: <https://books.google.it/books?id=-yQXwhE6iWMC>.
- [202] Boris Karnakov and Vladimir Krainov. *WKB Approximation in Atomic Physics*. Mar. 2013. ISBN: 978-3-642-31557-2. DOI: 10.1007/978-3-642-31558-9.
- [203] C. M. Bender and S. A. Orszag. *Advanced Mathematical Methods for Scientists and Engineers*. McGraw-Hill, 1978.
- [204] G. Gamow. “Zur Quantentheorie des Atomkernes”. In: *Zeitschrift für Physik* 51.3-4 (Mar. 1928), pp. 204–212. DOI: 10.1007/BF01343196.
- [205] M. W. Cole and R. H. Good. “Determination of the shape of a potential barrier from the tunneling transmission coefficient”. In: *Phys. Rev. A* 18 (3 1978), pp. 1085–1088. DOI: 10.1103/PhysRevA.18.1085. URL: <https://link.aps.org/doi/10.1103/PhysRevA.18.1085>.
- [206] John C. Lazenby and David J. Griffiths. “Classical inverse scattering in one dimension”. In: *American Journal of Physics* 48.6 (June 1980), pp. 432–436. ISSN: 0002-9505. DOI: 10.1119/1.11998. eprint: [https://pubs.aip.org/aapt/ajp/article-pdf/48/6/432/8499804/432\\\_1\\\_online.pdf](https://pubs.aip.org/aapt/ajp/article-pdf/48/6/432/8499804/432\_1\_online.pdf). URL: <https://doi.org/10.1119/1.11998>.
- [207] Sohang C. Gandhi and Costas J. Efthimiou. “Inversion of Gamow’s formula and inverse scattering”. In: *American Journal of Physics* 74.7 (July 2006), 638–643. ISSN: 1943-2909. DOI: 10.1119/1.2190683. URL: <http://dx.doi.org/10.1119/1.2190683>.
- [208] V.S. Popov, V.D. Mur, and A.V. Sergeev. “Quantization rules for quasistationary states”. In: *Physics Letters A* 157.4 (1991), pp. 185–191. ISSN: 0375-9601. DOI: [https://doi.org/10.1016/0375-9601\(91\)90048-D](https://doi.org/10.1016/0375-9601(91)90048-D). URL: <https://www.sciencedirect.com/science/article/pii/037596019190048D>.

- [209] Subrahmanyan Chandrasekhar, Valeria Ferrari, and John Edwin Enderby. “On the non-radial oscillations of a star. III. A reconsideration of the axial modes”. In: *Proceedings of the Royal Society of London. Series A: Mathematical and Physical Sciences* 434.1891 (1991), pp. 449–457. DOI: 10.1098/rspa.1991.0104. URL: <https://royalsocietypublishing.org/doi/abs/10.1098/rspa.1991.0104>.
- [210] K. D. Kokkotas. “Axial modes for relativistic stars”. In: *Mon. Not. Roy. Astron. Soc.* 268 (1994), p. 1015.
- [211] Vitor Cardoso et al. “Light rings as observational evidence for event horizons: long-lived modes, ergoregions and nonlinear instabilities of ultracompact objects”. In: *Phys. Rev. D* 90.4 (2014), p. 044069. DOI: 10.1103/PhysRevD.90.044069. arXiv: 1406.5510 [gr-qc].
- [212] J. A. Wheeler. *Studies in Mathematical Physics: Essays in Honor of Valentine Bargmann*. Princeton Series in Physics. Princeton University Press, 2015, pp. 351–422. ISBN: 9780608066288. URL: <https://press.princeton.edu/titles/861.html>.
- [213] J. C. Lazenby and D. J. Griffiths. “Classical inverse scattering in one dimension”. In: *American Journal of Physics* 48 (June 1980), pp. 432–436. DOI: 10.1119/1.11998.
- [214] S. C. Gandhi and C. J. Efthimiou. “Inversion of Gamow’s formula and inverse scattering”. In: *American Journal of Physics* 74 (2006), pp. 638–643. DOI: 10.1119/1.2190683. eprint: quant-ph/0503223.
- [215] K. F. Riley, M. P. Hobson, and S. J. Bence. *Mathematical Methods for Physics and Engineering: A Comprehensive Guide*. 3rd ed. Cambridge University Press, 2006, ”1193–1194”. DOI: 10.1017/CB09780511810763.
- [216] W. Pauli. “Zur Quantenmechanik des magnetischen Elektrons”. In: *Zeitschrift für Physik* 43.9-10 (1927), pp. 601–623. DOI: 10.1007/bf01397326.
- [217] N Rosen and Philip M Morse. “On the vibrations of polyatomic molecules”. In: *Physical Review* 42.2 (1932), p. 210.
- [218] LI Schiff, H Snyder, and J Weinberg. “On the existence of stationary states of the mesotron field”. In: *Physical Review* 57.4 (1940), p. 315.
- [219] VA Rizov, H Sazdjian, and Ivan T Todorov. “On the relativistic quantum mechanics of two interacting spinless particles”. In: *Annals of Physics* 165.1 (1985), pp. 59–97.
- [220] Hagop Sazdjian. “Relativistic wave equations for the dynamics of two interacting particles”. In: *Physical Review D* 33.11 (1986), p. 3401.

- [221] H Sazdjian. “The scalar product in two-particle relativistic quantum mechanics”. In: *Journal of mathematical physics* 29.7 (1988), pp. 1620–1633.
- [222] J Mourad and H Sazdjian. “The two-fermion relativistic wave equations of constraint theory in the Pauli–Schrödinger form”. In: *Journal of Mathematical Physics* 35.12 (1994), pp. 6379–6406.
- [223] J Formanek, RJ Lombard, and J Mareš. “Wave equations with energy-dependent potentials”. In: *Czechoslovak journal of physics* 54.3 (2004), pp. 289–315.
- [224] J Garcia-Martinez et al. “Exactly solvable energy-dependent potentials”. In: *Physics Letters A* 373.40 (2009), pp. 3619–3623.
- [225] RJ Lombard, J Mareš, and C Volpe. “Wave equation with energy-dependent potentials for confined systems”. In: *Journal of Physics G: Nuclear and Particle Physics* 34.9 (2007), p. 1879.
- [226] O Langueur, M Merad, and B Hamil. “DKP equation with energy dependent potentials”. In: *Communications in Theoretical Physics* 71.9 (2019), p. 1069.
- [227] Axel Schulze-Halberg and Özlem Yeşiltaş. “Generalized Schrödinger equations with energy-dependent potentials: Formalism and applications”. In: *Journal of Mathematical Physics* 59.11 (2018).
- [228] Axel Schulze-Halberg. “Higher-order Darboux transformations and Wronskian representations for Schrödinger equations with quadratically energy-dependent potentials”. In: *Journal of Mathematical Physics* 61.2 (2020).
- [229] Jorge A. Borrego-Morell, Cleonice F. Bracciali, and Alagacone Sri Ranga. “On an Energy-Dependent Quantum System with Solutions in Terms of a Class of Hypergeometric Para-Orthogonal Polynomials on the Unit Circle”. In: *Mathematics* 8.7 (2020). ISSN: 2227-7390. URL: <https://www.mdpi.com/2227-7390/8/7/1161>.
- [230] Kostas D. Kokkotas and Bernd G. Schmidt. “Quasinormal modes of stars and black holes”. In: *Living Rev. Rel.* 2 (1999), p. 2. DOI: 10.12942/lrr-1999-2. arXiv: gr-qc/9909058.
- [231] Hans-Peter Nollert. “TOPICAL REVIEW: Quasinormal modes: the characteristic ‘sound’ of black holes and neutron stars”. In: *Class. Quant. Grav.* 16 (1999), R159–R216. DOI: 10.1088/0264-9381/16/12/201.
- [232] Emanuele Berti, Vitor Cardoso, and Andrei O. Starinets. “Quasinormal modes of black holes and black branes”. In: *Class. Quant. Grav.* 26 (2009), p. 163001. DOI: 10.1088/0264-9381/26/16/163001. arXiv: 0905.2975 [gr-qc].

- [233] R. A. Konoplya and A. Zhidenko. “Quasinormal modes of black holes: From astrophysics to string theory”. In: *Rev. Mod. Phys.* 83 (2011), pp. 793–836. DOI: 10.1103/RevModPhys.83.793. arXiv: 1102.4014 [gr-qc].
- [234] Carlos Barcelo, Stefano Liberati, and Matt Visser. “Analogue gravity”. In: *Living Rev. Rel.* 8 (2005), p. 12. DOI: 10.12942/lrr-2005-12. arXiv: gr-qc/0505065.
- [235] A. Sommerfeld. “Zur Quantentheorie der Spektrallinien”. In: *Annalen der Physik* 356.17 (1916), pp. 1–94. DOI: <https://doi.org/10.1002/andp.19163561702>.
- [236] G. Gamow. “Zur Quantentheorie des Atomkernes”. In: *Z. Phys.* 51 (1928), pp. 204–212. DOI: 10.1007/BF01343196.
- [237] Dennis Bonatsos, C. Daskaloyannis, and Kostas D. Kokkotas. “WKB equivalent potentials for  $q$  deformed harmonic and anharmonic oscillators”. In: *J. Math. Phys.* 33 (1992), pp. 2958–2965. DOI: 10.1063/1.529565.
- [238] K. D. Kokkotas. “Quasinormal modes of the Kerr-Newman black hole”. In: *Nuovo Cim. B* 108 (1993), pp. 991–998. DOI: 10.1007/BF02822861.
- [239] R. A. Konoplya. “Quasinormal behavior of the  $d$ -dimensional Schwarzschild black hole and higher order WKB approach”. In: *Phys. Rev. D* 68 (2003), p. 024018. DOI: 10.1103/PhysRevD.68.024018. arXiv: gr-qc/0303052.
- [240] R. A. Konoplya, A. Zhidenko, and A. F. Zinhailo. “Higher order WKB formula for quasinormal modes and grey-body factors: recipes for quick and accurate calculations”. In: *Class. Quant. Grav.* 36 (2019), p. 155002. DOI: 10.1088/1361-6382/ab2e25. arXiv: 1904.10333 [gr-qc].
- [241] Pöschl, G. and Teller, E. “Bemerkungen zur Quantenmechanik des anharmonischen Oszillators”. In: *Z. Phys.* 83 (1933), pp. 143–151. DOI: 10.1007/BF01331132.
- [242] B. M. Karanakov and V. P. Krainov. *WKB Approximation in Atomic Physics*. Springer-Verlag Berlin Heidelberg, 2013. DOI: 10.1007/978-3-642-31558-9.
- [243] J. Formánek, R.J. Lombard, and J. Mareš. “Wave Equations with Energy-Dependent Potentials”. In: *Czechoslovak Journal of Physics* 54.3 (Mar. 2004), 289–316. ISSN: 0011-4626. DOI: 10.1023/b:cjop.0000018127.95600.a3. URL: <http://dx.doi.org/10.1023/B:CJOP.0000018127.95600.a3>.
- [244] Shihai Dong, Wen-Chao Qiang, and Jesús García Ravelo. “Analytical approximations to the Schrodinger equation for a second Poschl-Teller-like potential with centrifugal term”. In: *International Journal of Modern Physics A - IJMPA* 23 (Apr. 2008), pp. 1537–1544. DOI: 10.1142/S0217751X0803944X.

- [245] Shihai Dong and Jesús García Ravelo. “Exact solutions of the Schrodinger equation with the Pöschl-Teller like potential”. In: *Modern Physics Letters B - MOD PHYS LETT B* 23 (Feb. 2009), pp. 603–606. DOI: 10.1142/S0217984909018047.
- [246] Bahram Mashhoon. “Quasinormal modes of a black hole”. In: *3rd Marcel Grossmann Meeting on the Recent Developments of General Relativity*. 1982.
- [247] Valeria Ferrari and Bahram Mashhoon. “Oscillations of a Black Hole”. In: *Phys. Rev. Lett.* 52.16 (1984), p. 1361. DOI: 10.1103/PhysRevLett.52.1361.
- [248] Richard H. Price and Gaurav Khanna. “Gravitational wave sources: reflections and echoes”. In: *Class. Quant. Grav.* 34.22 (2017), p. 225005. DOI: 10.1088/1361-6382/aa8f29. arXiv: 1702.04833 [gr-qc].
- [249] Mario Novello, Mat Visser, and E Volovik Grigory. *Artificial black holes*. Hackensack, NJ: World Scientific, 2002.
- [250] Grigory E Volovik. *The Universe in a helium droplet*. Oxford, UK: Oxford University Press, 2003.
- [251] William G. Unruh and Ralf Schützhold. *Quantum Analogues: From Phase Transitions to Black Holes and Cosmology*. Berlin: Springer, 2007.
- [252] H. S. Vieira and Kostas D. Kokkotas. “Quasibound states of Schwarzschild acoustic black holes”. In: *Phys. Rev. D* 104.2 (2021), p. 024035. DOI: 10.1103/PhysRevD.104.024035. arXiv: 2104.03938 [gr-qc].
- [253] H. S. Vieira, Kyriakos Destounis, and Kostas D. Kokkotas. “Slowly-rotating curved acoustic black holes: Quasinormal modes, Hawking-Unruh radiation, and quasibound states”. In: 105.4, 045015 (Feb. 2022), p. 045015. DOI: 10.1103/PhysRevD.105.045015. arXiv: 2112.08711 [gr-qc].
- [254] H. S. Vieira, Kyriakos Destounis, and Kostas D. Kokkotas. “Analog Schwarzschild black holes of Bose-Einstein condensates in a cavity: Quasinormal modes and quasibound states”. In: *Phys. Rev. D* 107 (10 2023), p. 104038. DOI: 10.1103/PhysRevD.107.104038. URL: <https://link.aps.org/doi/10.1103/PhysRevD.107.104038>.
- [255] Leonardo Solidoro et al. “Quasinormal modes in semi-open systems”. In: (June 2024). arXiv: 2406.11013 [gr-qc].
- [256] Francesco Del Porro, Stefano Liberati, and Marc Schneider. “Tunneling method for Hawking quanta in analogue gravity”. In: (June 2024). arXiv: 2406.14603 [gr-qc].

- [257] Germain Rousseaux et al. “Observation of negative phase velocity waves in a water tank: A classical analogue to the Hawking effect?” In: *New J. Phys.* 10 (2008), p. 053015. DOI: 10.1088/1367-2630/10/5/053015. arXiv: 0711.4767 [gr-qc].
- [258] L.-P. Euvé et al. “Observation of Noise Correlated by the Hawking Effect in a Water Tank”. In: *Phys. Rev. Lett.* 117 (12 2016), p. 121301. DOI: 10.1103/PhysRevLett.117.121301. URL: <https://link.aps.org/doi/10.1103/PhysRevLett.117.121301>.
- [259] Juan Ramón Muñoz de Nova et al. “Observation of thermal Hawking radiation and its temperature in an analogue black hole”. In: 569.7758 (May 2019), pp. 688–691. DOI: 10.1038/s41586-019-1241-0. arXiv: 1809.00913 [gr-qc].
- [260] Victor I. Kolobov et al. “Observation of stationary spontaneous Hawking radiation and the time evolution of an analogue black hole”. In: *Nature Physics* 17.3 (Jan. 2021), pp. 362–367. DOI: 10.1038/s41567-020-01076-0. arXiv: 1910.09363 [gr-qc].
- [261] F. Belgiorno et al. “Hawking Radiation from Ultrashort Laser Pulse Filaments”. In: 105.20, 203901 (Nov. 2010), p. 203901. DOI: 10.1103/PhysRevLett.105.203901. arXiv: 1009.4634 [gr-qc].
- [262] Philbin, Thomas G. and Kuklewicz, Chris and Robertson, Scott and Hill, Stephen and König, Friedrich and Leonhardt, Ulf. “Fiber-optical analogue of the event horizon”. In: *Science* 319 (2008), pp. 1367–1370. DOI: 10.1126/science.1153625. arXiv: 0711.4796 [gr-qc].
- [263] O. Lahav et al. “Realization of a sonic black hole analogue in a Bose-Einstein condensate”. In: *Phys. Rev. Lett.* 105 (2010), p. 240401. DOI: 10.1103/PhysRevLett.105.240401. arXiv: 0906.1337 [cond-mat.quant-gas].
- [264] Vitor Cardoso et al. “Detecting Rotational Superradiance in Fluid Laboratories”. In: *Phys. Rev. Lett.* 117 (27 2016), p. 271101. DOI: 10.1103/PhysRevLett.117.271101. URL: <https://link.aps.org/doi/10.1103/PhysRevLett.117.271101>.
- [265] . “Magnonic Analog of Black- and White-Hole Horizons in Superfluid  $^3\text{He}-B$ ”. In: *Phys. Rev. Lett.* 123 (16 2019), p. 161302. DOI: 10.1103/PhysRevLett.123.161302. URL: <https://link.aps.org/doi/10.1103/PhysRevLett.123.161302>.
- [266] Samuel L. Braunstein et al. “Analogue simulations of quantum gravity with fluids”. In: *Nature Reviews Physics* 5.10 (16 Oct. 2023), pp. 612–622. DOI: 10.1038/s42254-023-00630-y. arXiv: 2402.16136 [gr-qc]. URL: <https://link.aps.org/doi/10.1103/PhysRevLett.123.161302>.



- [267] B. Carter. “Axisymmetric Black Hole Has Only Two Degrees of Freedom”. In: *Phys. Rev. Lett.* 26 (16 1971), pp. 331–333. DOI: 10.1103/PhysRevLett.26.331. URL: <https://link.aps.org/doi/10.1103/PhysRevLett.26.331>.
- [268] S. W. Hawking. “Black holes in general relativity”. In: *Commun. Math. Phys.* 25 (16 1972), pp. 152–166. DOI: 10.1007/BF01877517. URL: <https://link.aps.org/doi/10.1103/PhysRevLett.25.152>.
- [269] D. C. Robinson. “Uniqueness of the Kerr black hole”. In: *Phys. Rev. Lett.* 34 (16 1975), pp. 905–906. DOI: 10.1103/PhysRevLett.34.905. URL: <https://link.aps.org/doi/10.1103/PhysRevLett.34.905>.
- [270] . *The Kerr Spacetime: Rotating Black Holes in General Relativity*. Ed. by David L. Wiltshire, Matt Visser, and Susan M. Scott. Vol. 123. Cambridge University Press, 2009, p. 161302. ISBN: 9780521885126. DOI: 10.1103/PhysRevLett.123.161302. URL: <https://link.aps.org/doi/10.1103/PhysRevLett.123.161302>.
- [271] V. S. Popov, V. D. Mur, and A. V. Sergeev. “Quantization rules for quasistationary states”. In: *Physics Letters A* 157 (16 1991). Ed. by David L. Wiltshire, Matt Visser, and Susan M. Scott, pp. 185–191. DOI: 10.1016/0375-9601(91)90048-D. URL: <https://link.aps.org/doi/10.1103/PhysRevLett.123.161302>.
- [272] David J. Griffiths. *Introduction to Quantum Mechanics*. Ed. by David L. Wiltshire, Matt Visser, and Susan M. Scott. 3rd. Vol. 123. See Chapter 2 for the infinite square well problem. Pearson Education, 2018, p. 161302. ISBN: 978-1107189638. DOI: 10.1103/PhysRevLett.123.161302. URL: <https://link.aps.org/doi/10.1103/PhysRevLett.123.161302>.
- [273] Naritaka Oshita. “Greybody Factors Imprinted on Black Hole Ringdowns: an alternative to superposed quasi-normal modes”. In: *Phys. Rev. Lett.* 123 (16 Sept. 2023). Ed. by David L. Wiltshire, Matt Visser, and Susan M. Scott, p. 161302. DOI: 10.1103/PhysRevLett.123.161302. arXiv: 2309.05725 [gr-qc]. URL: <https://link.aps.org/doi/10.1103/PhysRevLett.123.161302>.
- [274] Kazumasa Okabayashi and Naritaka Oshita. “Greybody Factors Imprinted on Black Hole Ringdowns. II. Merging Binary Black Holes”. In: *Phys. Rev. Lett.* 123 (16 Mar. 2024). Ed. by David L. Wiltshire, Matt Visser, and Susan M. Scott, p. 161302. DOI: 10.1103/PhysRevLett.123.161302. arXiv: 2403.17487 [gr-qc]. URL: <https://link.aps.org/doi/10.1103/PhysRevLett.123.161302>.
- [275] Romeo Felice Rosato, Kyriakos Destounis, and Paolo Pani. “Ringdown stability: greybody factors as stable gravitational-wave observables”. In: *Phys. Rev. Lett.* 123 (16 June 2024). Ed. by David L. Wiltshire, Matt Visser, and Susan M. Scott, p. 161302. DOI: 10.1103/PhysRevLett.123.161302. arXiv: 2406.01692 [gr-qc]. URL: <https://link.aps.org/doi/10.1103/PhysRevLett.123.161302>.

- [276] Naritaka Oshita, Kazufumi Takahashi, and Shinji Mukohyama. “(In)stability of the black hole greybody factors and ringdowns against a small-bump correction”. In: *Phys. Rev. Lett.* 123 (16 June 2024). Ed. by David L. Wiltshire, Matt Visser, and Susan M. Scott, p. 161302. DOI: 10.1103/PhysRevLett.123.161302. arXiv: 2406.04525 [gr-qc]. URL: <https://link.aps.org/doi/10.1103/PhysRevLett.123.161302>.
- [277] R. A. Konoplya and A. Zhidenko. “Correspondence between grey-body factors and quasinormal modes”. In: *Phys. Rev. Lett.* 123 (16 June 2024). Ed. by David L. Wiltshire, Matt Visser, and Susan M. Scott, p. 161302. DOI: 10.1103/PhysRevLett.123.161302. arXiv: 2406.11694 [gr-qc]. URL: <https://link.aps.org/doi/10.1103/PhysRevLett.123.161302>.